ATMOSPHERIC CORROSION OF AA2024 IN OCEAN

WATER ENVIRONMENTS

BY

SARAH JANE MARIE GLANVILL

A thesis submitted to the University of Birmingham for the degree of

DOCTOR OF PHILOSOPHY

School of Metallurgy and Materials

College of Engineering and Physical Sciences

University of Birmingham

February 2018

UNIVERSITY OF BIRMINGHAM

University of Birmingham Research Archive

e-theses repository

ABSTRACT

Observations of atmospheric corrosion on aluminium alloy AA2024-T3 were made within droplets of NaCl solution and simulated ASTM ocean water. High speed *in-situ* synchrotron X-ray tomography has been used to observe the initiation and propagation of corrosion sites. Tomographic scans had a temporal resolution of 300 s per full tomographic scan, providing a non-destructive visualisation of corrosion. Sites initiate at numerous surface morphologies, including at intermetallic inclusions, under surface deposits and salt crystals, and also at sites with no obvious micron-scale microstructural features. It was observed that corrosion sites grow discontinuously and inhomogeneously when conditions are constant, consistent with bursts of dissolution followed by some repassivation.

The nature of corrosion products was investigated with Raman spectroscopy and EDX. The dominant corrosion product was Dawsonite for both droplet solutions, however the distribution of corrosion products differed between the two types of droplet. NaCl droplets spread more, resulting in fewer, larger corrosion sites. ASTM ocean water droplets showed multiple small corrosion sites within the droplet owing to the presence of Hydrotalcite around the droplet perimeter.

Corrosion development under wet-dry cycling conditions was different for NaCl and ASTM ocean water droplets. Under NaCl droplets, no growth or initiation was observed during "dry" phases. However, ASTM ocean water remains partially wet in "dry" periods as some of the salt constituents in ASTM ocean water remain hydrated. As a consequence, corrosion site growth is able to continue.

Dedicated to my family and friends.

'An understanding of the natural world and what's in it is a source of not only a great curiosity but great fulfilment.' David Attenborough

'When life gets your down, you know what you gotta do? Just keep swimming.' Dory

ACKNOWLEDGEMENTS

First of all I would like to thank my supervisor Professor Alison Davenport who has shown a tremendous amount of patience and belief in me, and without whom this PhD may never had been started, let alone finished. Words are not enough to express my gratitude for everything she has done for me.

I would also like to thank my co-supervisor Professor Trevor Rayment, who has given me invaluable advice and guidance, especially with work on Tomography.

Thank you to Mark Basham my Diamond Light Source supervisor for his time and technical input on tomography analysis.

To all my colleagues; Steven, George, Sophie, Angus, Berenika, Andy, Flaviu, Qi, Haval, Liya and Majid. The help, support and memories I have gained from you will stay with me forever. Without you all as friends, as well as colleagues I have no doubt I would not have obtained the level of knowledge I have today. Thank you.

Thank you to Andrew du Plessis for the initial guidance and data to analyse when I first started this PhD.

I'm particularly thankful to my parents for their constant and undying support in everything that I've done over my time at Birmingham.

And finally to my grandad Keith B. Glanvill in honour of his memory. Thank you for teaching me curiosity.

Contents

ACRONYMS

Abbreviations:

µm	Micrometre
3D	Three Dimensional
AA	Aluminium Alloy
ASTM	American Society For Testing And Materials
CBM	Condition Based Maintenance
CCD	Charge Coupled Device
CDD	Chloride Deposition Density
D	Dry
DCLS	Direct Classical Least Square
DRH	Deliquescent Relative Humidity
EDX	Energy Dispersive Spectroscopy
E_{pit}	Critical Pitting Potential
ERH	Efflorescence
FIB	Focus Ion Beam SEM
FTIR	Fourier-Transform Infrared Spectroscopy
GD	Grinding Direction
GIXRD	Grazing Angle XRD
GIXRD	Gracing Angle X-Ray Diffraction
GPB	Guinier-Preston-Bagaryatsky
H14	Work Hardening
IGC	Intergranular Corrosion
IR	Infra-Red
L	Longitudinal
LT	Long Transverse
mins	Minutes
O	Ocean
ORR	Oxygen Reduction Reaction
OW	Ocean Water
PCA	Principle Component Analysis
PFZ	Precipitate Free Zones
PHM	Prognostic Health Management
RD	Rolling Direction
RH	Relative Humidity
S	Short
SEM	Scanning Electron Microscope
SSSS	Supersaturated Solid Solution
ST	Short Transverse
STP	Standard Temperature and Pressure
T	Transverse
TOW	Time Of Wetness
T-5	Temper And Number Designation

W	Wet
XMT	X-Ray Microtomography
XRD	X-Ray Diffraction
XXXX	Aluminium Series

Equations:

F	Faradays Constant
$[C]$	Concentration
$M_{\{Cl\}}$	Molar mass Cl
E_{pit}	Critical Pitting Potential
Δh	Difference In Distance
Δt	Difference In Time
i	Current Density
M	Molar Mass
n	Oxidation State
V	Volume
ρ	Density

1.   INTRODUCTION

The Al-Cu-Mg alloy 2024 is widely used in the aerospace industry because of its high strength relative to other aluminium alloys. It is, however, also susceptible to atmospheric corrosion while in service.

Whilst the corrosion of AA2024-T3 has been extensively studied, in order to investigate corrosion mechanisms and provide better corrosion prediction models, most studies have investigated corrosion under full immersion conditions, e.g. [1-9] and relatively little work has been done on atmospheric corrosion [10-13].

Atmospheric conditions often arise when an electrolyte layer forms after salts have deposited as aerosols on the metal surface. These salts will deliquesce, i.e. draw in moisture, when the relative humidity increases above their deliquescence relevant humidity (DRH), which is specific to each salt species, and form highly concentrated salt solutions. Under atmospheric conditions there is generally considered to be a three phase boundary region where the metal, solution and air are all in close proximity. Cathodic reactions are most likely to happen at this boundary region as atmospheric O_2 is required [14]. The size of the droplet can therefore affect corrosion.

It is well established that S-phase (Al_2CuMg) particles are common sites for initiation in both atmospheric and full immersion conditions [2, 3, 5]. These particles are initially anodic, owing to selective dissolution of Mg and Al [15]. This partially de-alloys the surrounding matrix, giving this area a lower potential

1

[5, 16]. The Cu rich remnant is cathodic with respect to the matrix and results in the formation of a localised galvanic cell, promoting initiation of further corrosion in these locations [1, 15].

X-ray microtomography (XMT) is a useful tool for *in-situ* studies of early corrosion stages under atmospheric conditions because XMT is a non-destructive technique that allows for three-dimensional (3D) observations and analysis of surface morphologies such as intermetallic particles and sites of corrosion. Corrosion occurring via this method can be viewed *in-situ* (during exposure) and *ex-situ (post exposure).*

Previous tomography-based experiments have provided a spatial resolution sufficient to resolve intergranular corrosion fissures as they grow over intervals of hours [17-20]. However, most have observed corrosion under full-immersion or are potentiodynamically driven by *in-situ* electrochemistry. Advancements in synchrotron XMT have allowed for an improvement in data capture time. This improvement allows time dependant *in situ* measurements which permit the visualisation of initiation and propagation of corrosion under atmospheric conditions [19, 20]. The initial exposure of samples to a steady state RH found the main corrosion site grew discontinuously. Initiation occurred at various features such as intermetallic particles, sub-micron heterogeneities and under surface deposits. H_2 evolution is seen evolving at the mouth of corrosion sites as they initiate.

Previous work carried out on AA2024 and other aluminium alloys in realistic service conditions show corrosion damage accumulation is greater when RH is

not fixed than that found when RH is fixed [21-23]. XMT was used to improve the knowledge associated with the kinetics of corrosion occurring during fluctuation in RH. Corrosion damage was found to be different than under steady state conditions. The dissimilar deliquescent relative humidity of constituent salts found in ocean water result in continuous initiation of corrosion salts in both wet and dry humidities. Whereas corrosion process under NaCl droplets was halted in dry conditions. The initial stages of high or low humidity resulted concentrated salt solutions and salt crystals facilitated corrosion sites to initiate. The corrosion sites that initiated in high chloride concentrations proceeded to grow as salt solutions became more dilute.

Corrosion products have previously been identified within corrosion sites [12, 22, 24]. However, investigations have not yet identified corrosion products over an entire atmospheric droplet. Investigations found Dawsonite to be the dominant corrosion product formed in cathodic regions under both NaCl and ASTM ocean water droplets. Anodic regions of NaCl droplets also saw the presence of Dawsonite. Under anodic regions of ASTM ocean water droplets other corrosion products were identified these included Felsöbányaite and Hydrotalcite.

The aims of this thesis are to compare the kinetics of atmospheric corrosion of AA2024-T3 under NaCl and ASTM ocean water droplets. In particular initiation and growth will be studied by using a high temporal resolution XMT during the early stages of steady state and during wet-dry cycling exposure. The chemistry of atmospheric corrosion under the two solutions will be examined by the analysis of corrosion products with Raman spectroscopy and EDX. Mechanistic

and chemical information will be valuable for developing corrosion prediction

models to underpin condition-based maintenance (CBM) of aircraft [25-27].

2. LITERATURE REVIEW

2.1 Aircraft Management

2.2 Maintenance Intervals

Aeroplanes are exposed to many different environments across the globe. In countries which are warm with high humidity levels and with their airports near to the sea, aeroplanes are particularly susceptible to corrosion [21]. The most significant problems with corrosion arise when aeroplanes are on the ground, where they experience ambient temperatures and humidities. Further issues arise, during flight, with external temperatures from -20 to -56° C [28], where corrosion processes may be reduced or stopped until thawing creates highly concentrated and aggressive chloride solutions within already established corrosion sites [21].

Sustained localised corrosion can result in the formation of fissures with high localised stress intensities where fatigue can jeopardise structural reliability [29-31]. Aeroplanes must therefore be monitored for corrosion and fatigue periodically to ensure they remain safe during use. A balance must be found by which optimal maintenance intervals are achieved: long enough to be cost effective, and frequent enough to be safe.

Condition-based maintenance (CBM) is used, where planes are assessed on the ground before being removed from service for more extensive tests if required. Needing to remove planes from service for long durations of time is very costly, but is essential to ensure that structural integrity is maintained [25-27].

Prognostic health management (PHM) [32-38] is now being brought in, to increase safety and decrease cost [32]. This is done by using sensors on planes to provide real time data [33]. Data collected includes accumulation of salt deposits, time of wetness (TOW) and temperature. This accumulation of environment data collected from sensors is used to provide data from which accelerated lab based testing can be used to predict optimum length of maintenance intervals [39, 40]. High quality data is needed to predict the safest and most cost effective intervals for maintenance cycles [34].

2.3 Aluminium Alloy (AA)2024

2.3.1 Introduction

Aluminium is the metal in the highest abundance in the earth's crust making up approximately 8% (by weight) [41-44]. Due to aluminium's high strength-to-weight ratio it is used in a broad range of applications where both tensile and compressive strength are required. AA2024 is a wrought 2XXX series aluminium alloy engineered to exploit age hardening [42]. A process accidental discovered by Alfred Wilm during the search for a replacement of brass in the automotive industry. This discovery resulted in the development of 'Duralumin' an AlCu alloy which is a precursor to the 2XXX series of aluminium alloys for use in aerospace applications in more recent times [42]. AA2024-T3 (or T351) (Al-Cu-Mg) is a widely-used high strength aircraft alloy. The addition of alloying elements copper and magnesium through precipitation hardening improves the mechanical properties of AA2024-T3 by impeding the motion of dislocations [42]. As well as this, alloying elements drastically increases the alloys vulnerability to corrosion when exposed to the atmosphere which in turn

increase it susceptibility in fatigue [29, 30, 42, 45]. These are considerable drawbacks for an alloy with its intended use in the aerospace industry.

Thermomechanical processing leads to improvements of mechanical properties of the parent material [46]. Heat treatment at high temperatures promotes the incorporation of alloying elements into a solid state solution. Once alloying elements are dissolved, application specific heat treatments can take place. T3 and T351 are standard aerospace grade EN 515 temper treatments that involves solution heat treatment followed by stretching and ageing. This specific heat treatment takes place at approximately 500 to 550 °C and is followed by quenching to obtain a supersaturated solid solution (SSSS) [42, 47-49]. Controlled decomposition of the alloying elements takes place at room temperature (natural ageing). For T3 and T351 specific cold working follows the quenching process [42, 50, 51]. The chemical composition of AA2024-T3 in wt% is given in Table 2-1.

Table 2-1 Composition limits of AA2024-T3 in wt% [52].

Wt%	Cu	Mg	Mn	Fe	Si	Zn	Cr	Ti	Other (total)	Al
Min	3.8	1.2	0.30	0.0	0.0	0.0	0.0	0.0	0.0	Bal
Max	4.9	1.8	0.90	0.50	0.25	0.10	0.10	0.15	0.15	Bal

2.3.2 *The Metallurgy of AA2024*

The presence of alloying and impurity elements in AA2024 results in a heterogeneous microstructure with precipitates on different length scales. Three types of precipitate particles are observed:

- Constituent intermetallic particles

- Dispersoid particles

- Strengthening particles

These particles are developed during either alloy manufacture or the precipitation hardening processes.

The largest precipitates are constituent intermetallic particles [15]. The most common are S-phase Al_2CuMg and Al_6(Fe, Mn) [3, 47, 53, 54]), their size range from 1-10 µm in diameter [6, 15]. The S-phase particles are highly electrochemically active both as cathodes (after they dealloy producing copper-rich surfaces) and can be sites at which corrosion initiates [15]. S-phase particles are round and regular in shape. Other Cu rich θ-phase (Al_2Cu) can also be found in AA2024 [55]. Al_6(Fe, Mn) particles can leave areas susceptible to fatigue and are irregular and larger in size then S-phase particles. Al_6(Fe, Mn) are less cathodically active than S and θ-phase [15, 55, 56].

Dispersoid particles, are smaller, ranging from 0.05 – 0.5 µm [57] and are not as electrochemically active so do not pose a risk to the material's integrity [6]. Two

types are formed during the homogenization of the ingot: $Al_{20}Cu_2Mn$ and

$Al_2(MnFe)_3Si$ [49, 58]. They serve to retard the recrystallisation and grain growth

during processing and heat treatment of the alloy [42, 50, 51].

The smallest precipitates are the strengthening particles. These can be up to

0.1 µm. These are Cu and Mg atoms which have formed within grains in

localised concentrations. They act to reduce movement along slip planes and

directly obstruct dislocations [57, 59, 60]. These particles develop as a result of

aging of the SSSS.

Precipitate hardening is a process by which precipitates, which form in the

metal matrix, increase the yield strength of a component by directly obstructing

movement of dislocations [42]. Precipitations result in the well-established

microstructures observed in AA2024. The decomposition process is complex

and involves multiple stages. This process starting from the SSSS is

summarised as follows:

SSSS →GPB zones → S'' → S' Phase → S Phase (Al_2CuMg)
[54, 61, 62]

Following the quenching of the SSSS the formation of agglomerates happens via diffusion. GPB (Guinier-Preston-Bagaryatsky) zones are the location where Cu and Mg atoms cluster whilst being fully coherent with the metal matrix and form in disks on the (100) aluminium (FCC) planes [13, 63]. These lead to the formation of metastable semi coherent S´ on dislocations [64, 65]. Zones which are semi coherent with the metal matrix are where stable S phase is precipitated.
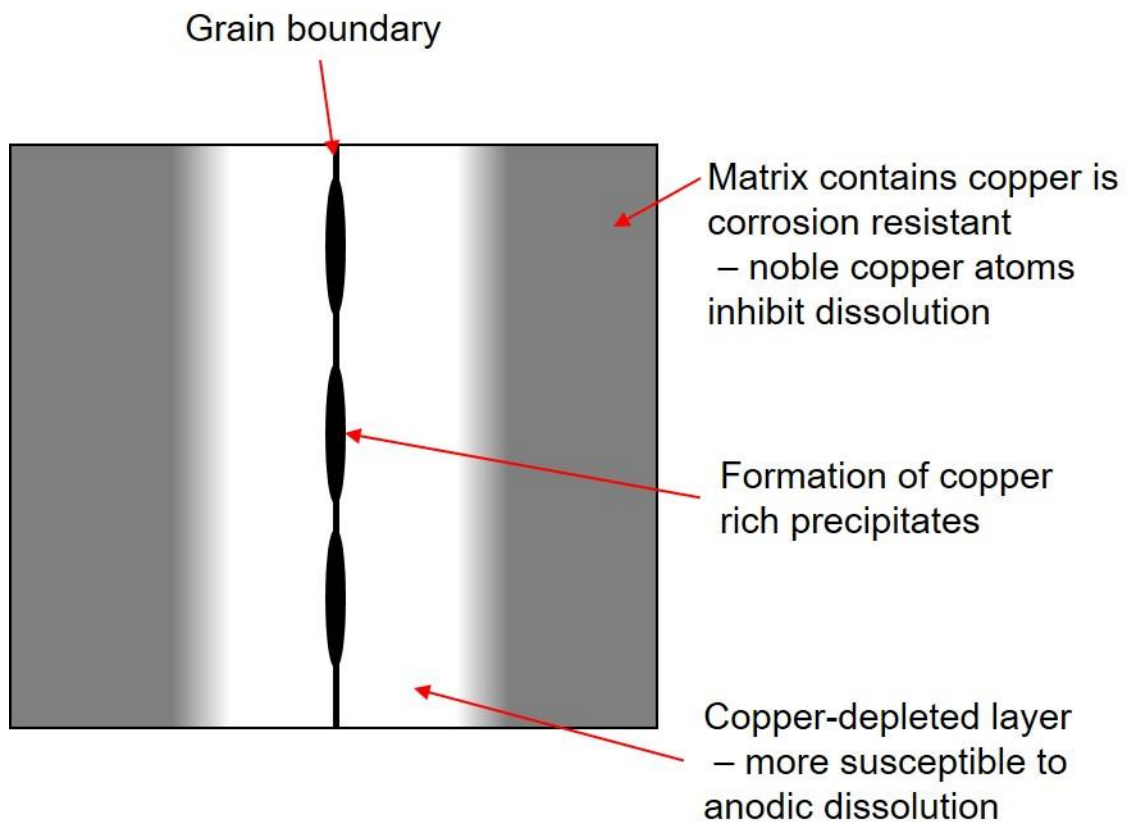
Figure 2-1 Formation of precipitate free zones of AA2024 (PFZ) adapted from [60].

Local concentrations of alloying elements forming along grain boundaries create precipitate free zones (PFZ) [42, 47]. Although not desirable, all alloys in which

precipitation has occurred PFZ will be present. The regions form to a smaller extent following natural ageing. An electrochemical gradient is formed in these regions as they are often depleted in copper compared to the grain boundaries as shown in Figure 2-1 [47].

2.4 Corrosion of AA2024 Under Full Immersion

2.4.1 Introduction

AA2024 naturally forms as insulating passive film of Al_2O_3 which ranges in thickness from 1 to 5 nm [42]. This layer forms naturally in the presence of water according to Equation 2-1. The passive film is an insulator, so is a poor cathode. Unfortunately the presence of precipitate particles under the surface disrupts the passive film, allowing for the movement of electrons which leaves it vulnerable to corrosion. This is due to the passive film being thinner and more conductive over these sites [2, 3, 5].

$$2Al(s) + 3H_2O\ (l) \rightarrow Al_2O_3\ (s) + 6H^+(aq) + 6e^- \qquad \textbf{Equation 2-1}$$
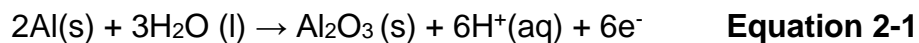
2.4.2 Stability of the Passive Film in Wet Environments

Owning to its amphoteric nature this passive film is stable in aqueous solutions of a pH range 4.5-8.8 as shown by Pourbaix in Figure 2-2 [1, 42, 50, 66].
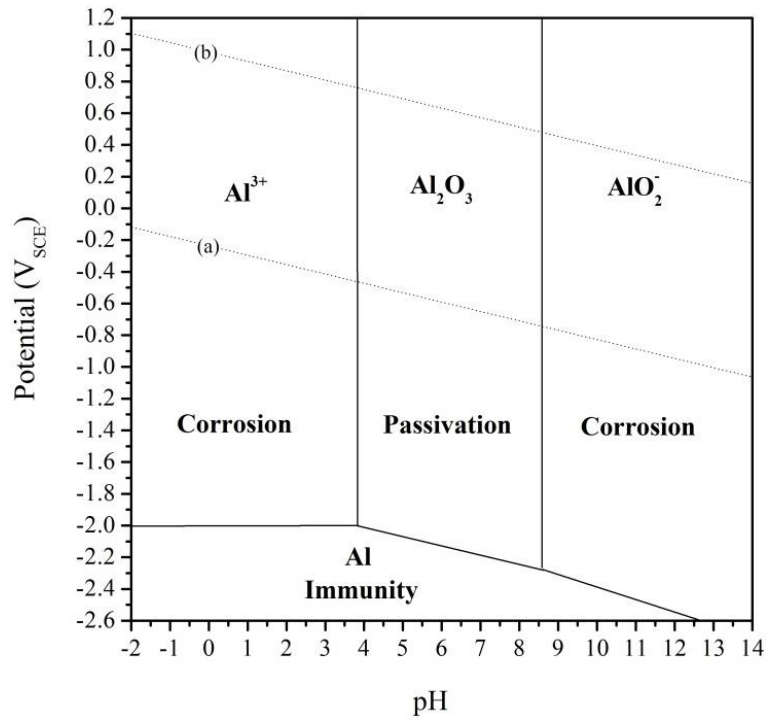
Figure 2-2 Pourbaix diagram showing conditions of corrosion, passivation, and corrosion of aluminium at 25 °C. Line indicated by (b) refers to the reaction $H_2 \leftrightarrow 2H^+ + 2e^-$ line indicated by (a) refers to $2H_2O \leftrightarrow O_2 + 4H^+ - 4e^-$ [67] p.172.

In acidic conditions Al_2O_3 will dissolve as stated in Equation 2-2 [60, 66, 68, 69]:

$$Al_2O_3 + 6H^+ \rightarrow 2Al^{3+} + 3H_2O$$ **Equation 2-2**
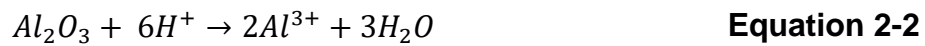
In alkaline conditions Al_2O_3 will dissolve as stated in Equation 2-3 [60, 66, 68, 69]:

$$Al_2O_3 + 3H_2O + 2OH^- \rightarrow 2Al(OH)_4^-$$ **Equation 2-3**
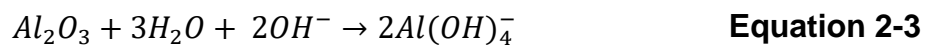
Attack on the passive film in highly acidic or alkaline solutions will lead to the rapid dissolution of the underlying aluminium.

Acidic conditions lead to anodic dissolution of aluminium as stated in Equation 2-4 [60, 66, 68, 69]:
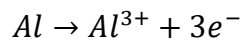
$$Al \rightarrow Al^{3+} + 3e^-$$ **Equation 2-4**

Alkaline conditions lead to cathodic dissolution aluminium will dissolve as stated in Equation 2-5 [60, 66, 68-71]:
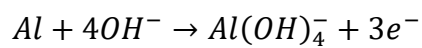
$$Al + 4OH^- \rightarrow Al(OH)_4^- + 3e^-$$ **Equation 2-5**

2.4.3 Localised Corrosion of AA2024

Localised corrosion is the breakdown of the protective passive film leading to accelerated dissolution at a discrete site. A common form of localised corrosion is pitting [1, 72]. In corrosion pits, anodic dissolution of the metal leads to a build-up of metal ions.

Subsequently, hydrolysis occurs and generates H^+ which will cause the local pH to drop.

The hydrolysis reaction is given by Equation 2-6

$$Al^{3+} + H_2O \rightarrow AlOH^{2+} + H^+ \qquad\qquad \textbf{Equation 2-6}$$

This further increases the rate of dissolution. The high metal cation concentration generated from the anodic reaction causes the electromigration of Cl⁻ from the bulk solution to be drawn in and balance charge within the pit [73, 74]. The additional presence of Cl⁻ further favours the dissolution of the metal over the formation on the passive film, by inhibiting regrowth [1]. Sustained pit propagation can be maintained if the rate of metal ion production inside the pit is greater than the rate of escape [75, 76]. In order for the anodic processes to continue, the electrons that are generated must also be consumed via two cathodic reactions.

The oxygen reduction reaction as stated in Equation 2-7:

$$O_2 + 2H_2O + 4e^- \rightarrow 4OH^- \qquad\qquad \textbf{Equation 2-7}$$

The hydrogen evolution reaction as stated in Equation 2-8:

$$2H^+ + 2e^- \rightarrow H_2 \qquad\qquad \textbf{Equation 2-8}$$

Formation of hydrogen bubbles has been observed during active corrosion on AA2024 [6, 19, 20, 77].

2.4.3.1 Metastable Pitting

Metastable pitting can be used to describe the early stages of pitting [1, 76, 78]. Were small pits grow for limited periods then repassivate. Unless these pits become sufficiently large enough to sustain their own growth, sites will die and resultantly not transition into stable pits. Many reasons for premature pit death have been hypothesised in the literature. Multiple faults in the passive film due to alloying may attribute to the occurrence of metastable pitting [75, 78]. In the presence of ions such as Cl^- repassivation of these flaws is decelerated allowing for pits to initiate [79-81]. In the event of initiation the passive film can behave simply as a cover, blocking the escape of metal ions allowing for acidification within the pit to happen. However if cathodic events happen locally to the corrosion site such as hydrogen evolution, this can be enough to clear the mouth of the site allowing the aggressive environment within to be evacuated. This would result in a higher number of metal ions escaping the site rather than being produced allowing the site to passivate [80] [76].

Electrochemical studies have measured this phenomenon [80]. Metastable pitting events appear as oscillations of current below that of pitting potential [1, 76, 82]. Indications of these oscillations is a precursor to stable pitting events occurring.

2.4.3.2 Stable Pitting

Metastable and stable pits initiate via the same manner [78, 80]. The transition of metastable pits forming stable pits happens if the environment within pits is sufficiently aggressive to prevent repassivation, i.e. a non-neutral pH. Factors such as this are dependent on metal ion concentration, Cl^- concentration,

temperature, and surface roughness [1]. Using electrochemical measurements in 2D pits this is described as the Critical Pitting Potential (E_{pit})[1, 75]. Criterion for this transition in pure aluminium that pitting potential must be higher than *ix*. i ≤10^{-2} A/cm^2, with *x* being pit depth, and i being pit current density [75, 80].

Once pitting is stable, the pit will act as a net anode and draw current from cathodically charged regions [42, 66, 74, 83-85]. An autocatalytic process occurs which self-sustains the corrosion site, with low pH maintained due to continued release of metal ions and the resulting hydrolysis. This leads to the electromigration of Cl$^-$ in order to maintain charge balance. The presence of both H$^+$ and Cl$^-$ contributes to preventing repassivation (shown in Figure 2-3).
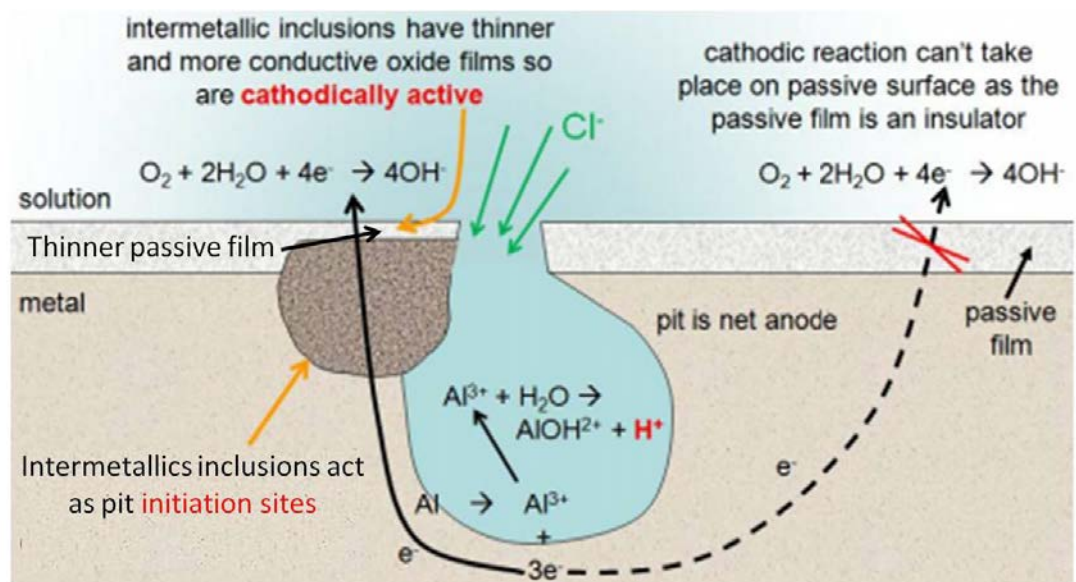
Figure 2-3 – Mechanisms of pitting corrosion of AA2024 under full immersion conditions adapted from: [60]

2.4.4 Intergranular Corrosion (IGC)

Intergranular Corrosion (IGC) is a form of local attack of grain boundaries [86]. IGC usually initiate in pits, although can initiate at surface defects, or at the surface in the case where grain boundaries are seen to intersect. PFZ in AA2024 close to grain boundaries are depleted in copper due to the age-hardening process [21, 42, 66] (Shown in Figure 2-1). These regions are small and lower in electrochemical potential in comparison to the copper-rich matrix, making these regions more susceptible to anodic dissolution [46, 47, 87, 88]. The copper rich phases which have formed along grain boundaries become the net cathodes driving anodic dissolution at the grain boundaries [47, 68, 89].

IGC sites are typically narrow due to the nano-scale nature of the PFZ but can penetrate up to 1 mm into the metal surface. The difficulty in detecting and measuring these sites makes them of huge interest to corrosion investigations as they increase the alloys susceptibility to stress corrosion cracking in its working environment [90]. The tip of intergranular fissures can result in areas of high stress concentrations this increase in stress intensity can result in premature failure [90, 91].

Growth rates of IGC are difficult to measure due to complex metallographic geometry of which propagation follows. IGC has been measured using radiography [6, 92-95], foil penetration [4, 96, 97], FIB SEM [10, 11], microtomography (XMT) corrosion experiments [17, 98-100] as well as metallographic sectioning [21, 91, 101].
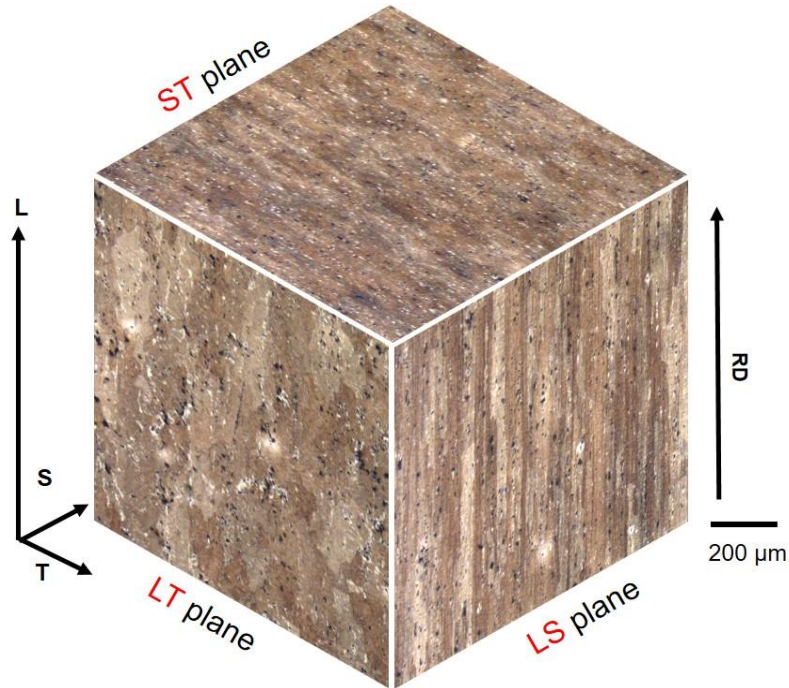
Figure 2-4 Optical microscopy shows grain size of longitudinal (L), long transverse (LT) and short transverse (ST) planes of AA2024-T3 in the orientation used in this body of work. Rolling direction (RD) is indicated with an arrow. Directionality is indicated with L = longitudinal, S = short and T = transverse.

Propagation rates of IGC favour metallographic directionality geometry [47, 94]. Typical grain sizes are shown in Figure 2-4. Preferential attack along longitudinal (L) and long transverse (LT) directions have been found over that of the short transverse (ST) direction under droplet experiments [20]. Agreeing with full immersion experiments where growth in L and transverse (T) direction was seen [83, 92]. Under stresses applied parallel to L and T direction, growth was fastest in L and T and occurred on the flat faces of elongated grains when stress was applied [90].

2.4.5 Trenching and Grooving
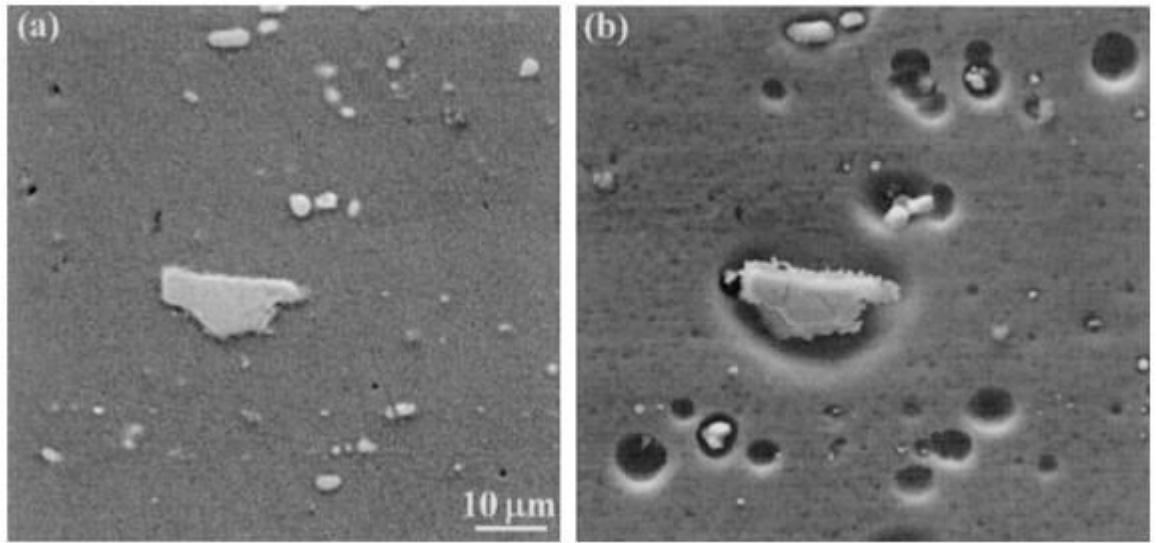
Figure 2-5 SEM of a typical surface on AA2024 (a) before and (b) after immersion in 0.5 M NaCl. Showing an example of cathodic behaviour around constituent particles taken from [55].

Trenching, sometimes referred to as grooving, is a form of alkaline dissolution of AA2024 passive film and matrix [6, 55, 102, 103]. This is the process by which slightly acidic (pH 5 which has the lowest rate of dissolution) and alkaline conditions result in a uniform dissolution. This dissolution happens around cathodically active particles due to a strong pH gradient caused by the high production of OH^- [103]. This leaves these particles proud from the metal surface with a trench or grooved region as shown in Figure 2-5. This trenching behaviour varies between species of intermetallic particles when exposed to low Cl^- concentration solutions. S-phase Al_2CuMg and Al_2Cu particles being most susceptible, followed by $Al_6(Fe, Mn)$ [103]. This trenching behaviour can be also seen under pure water droplet as pH changes establish roles of alkalinisation due to the oxygen reduction reaction [102].

19

2.4.6 Corrosion Product Precipitation

The presence and production aluminium oxy-hydroxides is well established in the field of aluminium corrosion [104-109]. Under atmospheric exposure aluminium's passive film itself can grow and transform into various products such as Boehmite ($Al_2O_3 \cdot H_2O$) Bayerite ($Al_2O_3 \cdot 3H_2O$) which have their own solubility at different potentials as shown in Figure 2-6. The migration of the acidic (Al^{3+}) ions towards the alkaline (OH^-), generated during corrosion, results in the precipitation of several of insoluble corrosion products when they come into contact with one another.
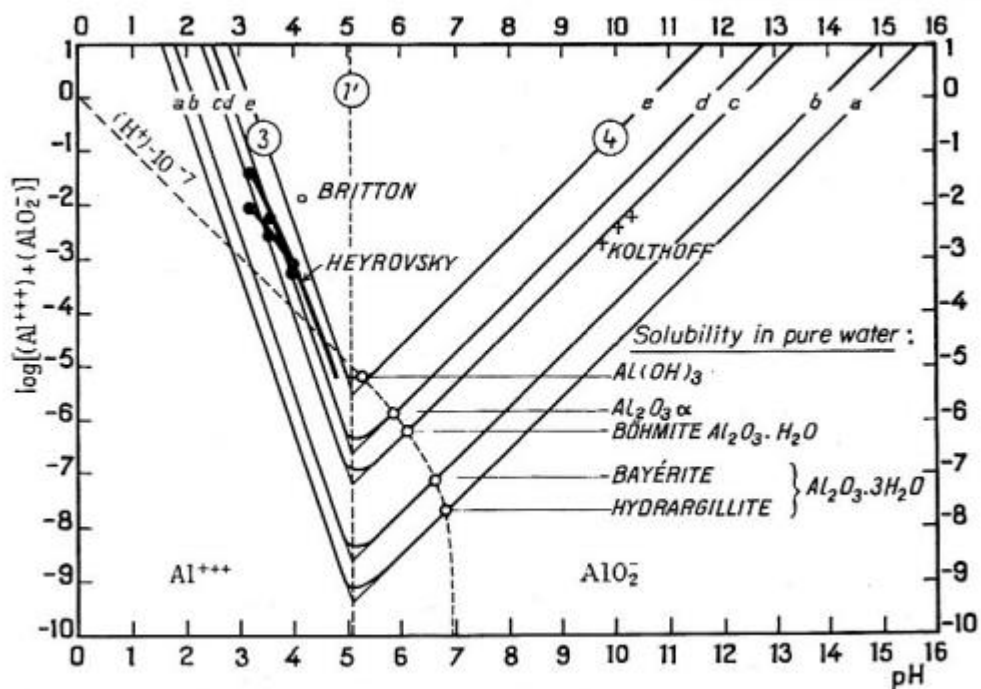
Figure 2-6 influence of pH on the solubility of Al_2O_3 and its hydrates at 25°C. [67] p. 174

The most obvious indicator that corrosion has occurred is therefore the existence of corrosion products. Their presence and patterns of deposition can indicate anodic corrosion processes like IGC, which would otherwise be hard to see. Corrosion product rings are where gradients in pH from anodic and cathodic regions result in no surface attack at pH 5, this highlights anodic sites with unattacked zones surrounded by rings of corrosion product as regions collide [8, 110] .

Corrosion product processes simultaneously affect corrosion rates once precipitated. Due to introduction of a porous substance to the metal surface the movement of ions in solution can be slowed. Longer durations of exposure leads to a build-up of corrosion products and thus reduce the rate of corrosion. As well as this physical barrier, the corrosion products' electrolyte constituents can become absorbed in corrosion products. This is demonstrated with NaCl droplets. Na is incorporated into corrosion products reducing the volume of electrolyte [108].

Corrosion products give an insight into the thermodynamics of the corrosion system being analysed. The resultant precipitate chemistry can be used to assess the environment which a material has been exposed. Reflecting atmospheric constituents found, be that a coastal or industrial atmosphere such as constituent salts, sulphates, gaseous concentration or even pH and temperature [12, 104, 108, 111, 112]. The resultant chemical makeup of corrosion products is therefore not simple and varies among corrosion studies.

Multiple techniques have been used in order to identify corrosion products. The most common being X-ray diffraction (XRD) [12, 55, 106, 111, 112]. However this technique provides issues when evaluating corrosion under droplets as regional information cannot be obtained. Samples must be processed for measurements in lab based experiments. Similar issues arise when using FT-IR techniques. Grazing angle XRD (GIXRD) [108] has been able to study droplets. However the issue regarding small regional changes occurring within the droplet will be generalised once again when data is collected. Region information of basic chemistry can be obtained using EDX. Many studies have used EDX to evaluate the whereabouts of common elements and their roles in corrosion. The migration of Cl^- towards regions of high H^+ has been shown by finding Cl^- within corrosion sites on aluminium alloys [8, 11, 112]. Despite improving the information regionally, only knowing single elements reduces the usefulness of this technique. Many conclusions are reached based on assumptions and usually neglect the impact on the environment such as aggressive salt anions, cations, temperature and pH when considering the corrosion products. For example deductions of Diaspore - AlOOH and Gibbsite $Al(OH)_3$ are common when elemental Al and O are detected. Raman, a technique widely used to provide information on chemical structure and physical form has capabilities of both detecting and denoting compounds to regions. Most commonly used in mineral studies to monitor the composition of bauxites for sourcing aluminium [107]. The three principle oxyhydroxides investigated are Gibbsite γ-$Al(OH)_3$, Boehmite - γ-AlOOH and Diaspore α – AlOOH. As well as being used to evaluated the adherence and adsorption of Chromate and

Hydrotalcite aluminium coatings [109, 113-116]. These oxyhydroxides correlate with corrosion products previously shown on aluminium with both chemical accuracy and special resolution for atmospheric studies [108, 109, 117, 118]. Unless simply acknowledging the presence of corrosion products, several methods used in conjunction with one another are best for compound confirmation. The use of multiple techniques have allowed for the identification of corrosion products such as Dawsonite under single salt solutions such as NaCl [108, 112, 117]. A review of corrosion products after exposure to various chloride containing environments for aluminium alloys can be found in Table 2-2.

Table 2-2 Literature matrix of Aluminium Corrosion Products

Material	Corrosion Product	Solution	Method	Reference
AA2024-T3	• $[Mg_{1-x}Al_x(OH)_2]^{x+}Cl^-_x \cdot_m H_2O$ • Brucite • $Al(OH)_3$	Salt lake environments	XRD	[111]
AA7075-T6 AA2024-T3	• Cu_2O	NaCl	XRD	[55]
AA2024-T3 AA6061-T6 AA7075-T6	• Al, O	NaCl	EDX	[110]
AA2024 AA7075	• γ-$Al(OH)_3$ • α-$Al_2O_3 \cdot 3H_2O$ • Al, O, S, Ca, Na, Si	Costal Urban Industrial	SEM XRD EDS	[12]
AA2024-T3 AA7075-T6	• Cl, O, Cu	NaCl	EDS	[8]
AA2024-T3	• Cu_2O • Al Oxide	Bare Al metal Treated Al - $NaVO_3$, and V_2O_3	Raman	[109]
AA2024	• AlOOH • Boehmite	Sea water	FIB SEM	[10]
AA2024	• Cu_2O • Al, Cl, O	Sea water	FIB SEM	[11]
AA2024	• Boehmite • Hydrotalcite coating	NaCl	XANES	[115]
AA2024-T3 AA6061-T6 AA7075-T6	• AlOOH • $Al(OH)_3$	NaCl	EDX	[110]
AA2024-T3	• Pseudoboehmite	Electro chemical cell 0.5M NaCl	IR Raman AFM	[118]

Continued from previous page:

99.95% Aluminium	• Bayerite • Gibbsite • Dawsonite	Aqueous NaCl	Raman	[117]
99.999% Aluminium	• Al, O, Na, Cl • Bayerite • Bischofite • Mendozite • Dawsonite	NaCl Na$_2$SO$_4$ AlCl MgCl$_2$	EDX XRD	[112]
AA1050	• Bayerite • Aluminium Hydroxide • Basal aluminite	NaSO$_4$/NaCl	Raman	[119]
AA1100	• Dawsonite	NaCl	FTIR Raman	[108]
AA1100 AA6061	• Al, Na, O, S, Cl, • (Cl and S inside pits) • Aluminium hydroxide • Aluminium carbonate • Basic aluminium sulphate • Dawsonite	Environmental Japan	EDX IR	[24]
AA6016	• Dawsonite • Aluminium Chloride	HCl 16 wt %, saturated AlCl$_3$, salt fog, NaCl	FTIR	[120]
AA1100 AA6061	• Dawsonite • Basic aluminium sulphate • Al, Na, O, S, Cl	Simulated marine environments	FTIR EDX	[22]
AA1100	• Dawsonite	NaCl	GIXRD FTIR Raman	[108]
AA1100 AA6061	• Al(OH)CO$_3$, Al2(SO$_4$)$_3$·17H$_2$O, Al(OH)$_3$ and Al$_2$O$_3$	Miyakojima, 2 km far from the North Pacific Ocean	FTIR EDX	[121]
Aluminium Powder	• Bayerite	Water immersion	IR Raman	[122]
Mineral Studies	• Gibbsite • Bayerite • Diaspore • Boehmite		Raman	[107]
Mineral Studies	• Dawsonite		Raman	[123]
Mineral Studies	• Hydrotalcite		Raman	[124]

2.5 Atmospheric Corrosion

Atmospheric corrosion takes place when localised or general corrosion occurs under thin layers of electrolyte which form on a metal surface in the form of droplets [68]. These droplets contain salts which create a conductive electrolyte which catalyse corrosion [68]. Droplets have a restricted volume with high concentrations of aggressive salts which cause localised corrosion.
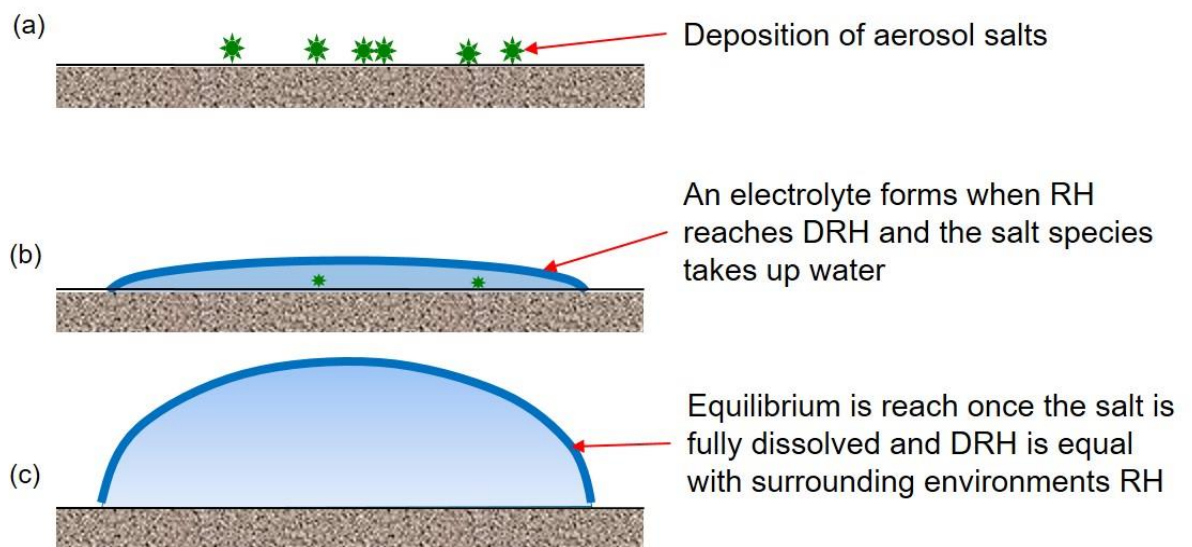
Figure 2-7 Deliquescence of an aerosol salt on a metal surface. (a) shows the deposition of aerosol salts. (b) shows these salts taking up water to form a thin solution droplet. (c) shows the equilibrium once RH reaches DRH and the salt aerosols are fulling dissolved.

2.5.1 Deposition of Salts

The deposition of aerosol salts primarily come from marine sources via wave crashing [125, 126] and ocean winds [125]. They also originate from industrial and rural sources. In these environments aerosol can arise from factory emissions and road salts [127].

An electrolyte layer forms when atmospheric aerosols deposit salt on a surface (as shown in Figure 2-7 (a)). Droplets can form either via direct solution transfer by rain or sea spray or rely on phenomenon of salts called deliquescence which is the process by which a substance absorbs enough moisture to dissolve itself.

2.5.2   Deliquescence

Salts deliquesce when the relative humidity ((RH) [128]) increases above their deliquescent relative humidity (DRH). DRH is specific to individual salt species. Above its DRH a specified salt will take up water to form a thin, concentrated and corrosive salt solution droplet when compared with a bulk solutions as shown in Figure 2-7 (b) [129]. At equilibrium, the concentration of a salt solution is determined by the humidity of its surrounding environment. This is caused by the water activity of the salt surface attaining equilibrium with that of the atmosphere [130, 131]. A RH above a salts DRH will continue to draw moisture reducing the salt concentration. A RH below the DRH will result in the salt losing moisture. This is known as 'efflorescence' relative humidity (ERH) [132]. If a salts DRH and environmental RH are equal it is said to be saturated. At which point an equilibrium of water activity is reached between the two phases, salt deposit and humid air. For example NaCl has a DRH of ~75% RH and will form a saturated droplet at this RH [133].

Under atmospheric conditions where the solution layer is discontinuous, there is a three-phase boundary; the metal, solution and air. The cathodic reactions such as oxygen reduction (**Equation 2-7**) most likely happen in this region. The size of the droplet can therefore affect corrosion. Two other key parameters are salt density (mass per unit area - CDD) and RH. The RH will determine the

concentration and consequently the height of the electrolyte. For a fixed droplet size and RH, a higher salt density will give a thicker droplet. As solution concentration does not change, the total amount of conductance through the droplet will increase, allowing a higher current (lower IR drop) and thus higher current (increased corrosion rate) [134]. The concentration determines the viscosity of the solution, affecting the ion transport within the droplet concentration [128, 132]. As salt containing droplets have the ability to gain and lose moisture in a given humidity the droplet has an oxygen consumption profile, allowing for an anodic inner zone and a cathodic outer zone [14]. This dependence on size dramatically changes corrosion behaviour when comparing bulk and thin electrolyte media [67].

2.5.3 Wet Dry Cycling

Fluctuations in RH are natural and should be considered when assessing corrosion damage for aircraft as they are thought to worsen corrosion [21, 135-137]. Humidity will cycle through an aerosol's ERH and DRH which will simultaneously affect a salt droplet's height, area and CDD. These periods of change can be described as 'wet' and 'dry' cycles. As the RH falls below the ERH a droplet will lose water to the atmosphere, a 'dry' cycle and transition to 'wet' once RH is raised to the salts DHR. In dry periods the droplet will reduce in height and diameter. During a wet periods the droplet height will increase. The height of a droplet is important as it can change the dynamics of the three phase boundary [138]. A higher droplet allows for easier diffusion of O_2 into the droplet at its edges [139]. A thinner droplet allows for a shorter diffusion pathway across the entire droplet subsequently is then controlled by the rate

that O_2 can dissolve into the droplet. Furthermore thinner droplets are not limited to O_2 diffusion at its edges, but establish diffusion across its entire surface increasing the amount available for oxygen reduction to help drive anodic reactions [13]. During wet and dry cycles a droplets viscosity and water activity will also vary concurrently effecting the rate of corrosion. As a droplet dries its chloride concentration will increase along with viscosity and solution conductance. Under a regime where ion concentration is high the concentration of free ions reduces and results in a drop in conductivity however due to an increase in viscosity as the droplet saturates [140]. This lower water activity reduces the mobility of ions within the solution increasing resistance slowing the reaction rates under a drying droplet. Despite all this the growth of the passive film will cease to occur under saturated droplets due to its inability to reform with no free water. For passivation O_2 needs adsorbs onto the metal surface deprotonation removes an H^+. The inability for re-passivation to occur in a high chloride environment with an easy access of O_2 is likely to lead to initiation. Phases of saturation can happen during both wet and dry cycles as a salt passes through their DHR and EHR thought to promote growth and initiation [135-137].

It has been proposed that wet dry cycling is worse than thin aggressive electrolyte as corrosion processes are not continuous [13, 21, 22, 135-137, 141]. Multiple methods have been used to assess wet dry cycling and its effects of corrosion rates on numerous aluminium alloys.

Drip testing of NaCl crystal on AA4043 has been carried out. NaCl crystals are dried and deposited on the metal surface. Pure water was then dripped close to them to form highly concentrated solutions with varying wetness times. Most corrosion attack was seen under the most concentrated near the edges of the wet regions where the droplet spread [142].

Acid rain testing on AA2024-T3 higher rates of corrosion in wet periods [143]. Agreeing with findings on 99.999% aluminium where the early stages of wetting have shown increased corrosion rates [141].

Splash zone tests carried out by Ul-Hamid in iron containing aluminium showed splatter zones are more corrosive compared to atmospheric conditions. This was attributed to humidity variations and high Cl^- concentrations during alternating wet dry cycles [144].

2.5.3.1 Influence of Salt Species

Different salt species have an effect on corrosion processes. Examples of constituents studies include, NaCl [55, 110, 115], $MgCl_2$ [112], Na_2SO_4 [112, 119, 145] and ocean water [10, 11].

The effects of aggressive salts has been studied on aluminium in the absence of CO_2 and found ordered from least aggressive to most aggressive as:

$MgCl_2 \cdot 6H_2O < AlCl_3 \cdot 6H_2O < Na_2SO_4 < NaCl$ [112]
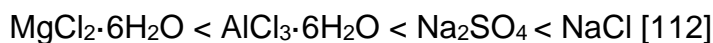
Ocean water standards contain a mixture of these salts and contains a mixture of anions such as Cl^- and SO_4^{2-} and cations Mg^{+2}, Ca^{+2} and Na^+. The equivalent is found in aluminium, whereby a mechanism of competitive migration reduces

the effect of aggressive Cl^- ions. This has been found in aluminium where pit initiation has been inhibited in the presence of sulphate ions [22]. AA6XXX series using ocean water [22] established the role of SO_4^{2-} reducing Cl^- the migration by using ocean water solution with and without sulphate ions. Using EDX sulphur had accumulated in corrosion products on the metal surface. The DHR of ocean water is effected by its salt species 29% for $CaCl_2 \cdot 6H_2O$, 33% for $MgCl_2 \cdot 6H_2O$, 75% for $NaCl$, 93% for $Na_2SO_4 \cdot 10H_2O$, 98% for $CaSO_4 \cdot 2H_2O$ (20°C) and 90% for $MgSO_4 \cdot 7H_2O$, respectively [133]. Sodium sulphate a component of ocean water is a known inhibitor. It can form easily in ocean water as it effloresces from solutions at 90% RH [24]. It is therefore important to consider anion and cation species when considering corrosion.

2.5.4 Secondary Spreading

Secondary spreading is the formation of thin regions or micro droplets of solution which fall outside the perimeter of atmospheric droplets. The phenomenon has been seen on alloys such as zinc and steel and aluminium [108, 136, 146, 147]. Due to the amphoteric nature of aluminium mechanisms proposed by other studies of spreading on different metals cannot be made.
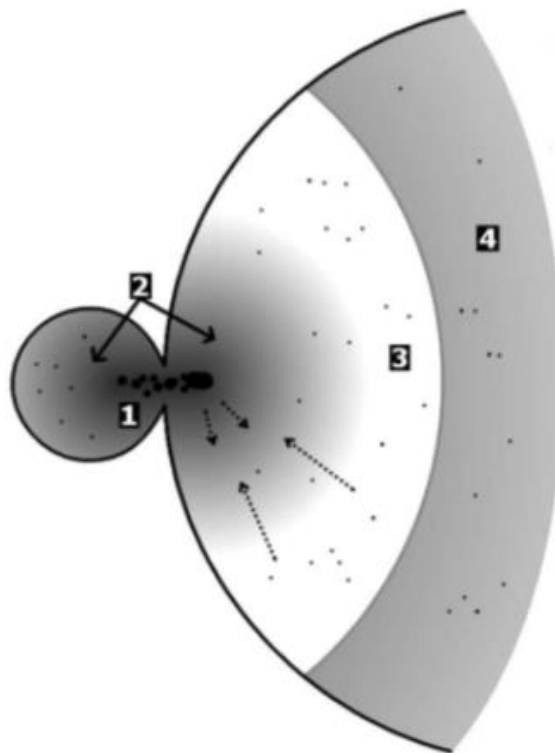
Figure 2-8 schematic representation of a secondary droplet taken from [136]. Severe corrosion attack occurs at region 1 near the edge of the droplet. Region 2 is covered in corrosion product. Region 3 is the primary cathodic region. Dotted arrows indicate ion transport between the anode and cathode regions.

Once corrosion initiates local chemical conditions rapidly evolve to govern the kinetics of the corrosion processes. The corrosion site establishes the production of metal ions and thin edges of the droplet the cathodic reaction of oxygen reduction. This cathodic region is associated the spreading or micro droplet region [108, 136, 146]. The mechanism thought to promote the growth of secondary spreading is proposed by Morton in AA7075 in NaCl whereby cathodic reactions produces OH^- ions. Cations present in the solution such as Na^+ are attracted towards these negative anions [136]. These ions diffuse towards the edge of the droplet where with their high ion content begin to absorb water and form secondary spreading/microdroplets as shown in Figure 2-8. A mechanism similar to this was proposed in $MgCl_2$ solutions in an Al-Mg-Si alloy [148] and on steel [149].

2.6   Atmospheric Corrosion of AA2024

2.6.1   Introduction

The difference in corrosion mechanisms of AA2024 under full immersion and atmospheric conditions does not differ hugely. The presence of intermetallic particles still plays the role of initiations sites. This has been seen in most cases where atmospheric corrosion is investigated [15, 73, 150, 151].

2.6.2   Early Methods of Testing

Early experiments of atmospheric corrosion focused on the analysis of long term based exposure of samples of clad AA2024 [12]. Samples were used to determine the different effects of urban and industrial environments [127]. Industrial environments were found to have greater weight loss than that in urban surroundings.

A method for simulating environments close to atmospheric conditions is through thin electrolyte layer [13]. A limit at which O_2 reduction under 3% NaCl solution determines the rate of corrosion has been established using variable electrolyte thickness. The height of the electrolyte was found to be between 100-200 µm above which O_2 reduction was not a factor in driving corrosion. O_2 reduction was also found to be inversely proportional to corrosion rate. This is a good way to distinguish between the corrosion driving forces in atmospheric corrosion and that found under full immersion conditions [13]. A problem with this method is that it does not directly simulate different behaviours of that associated with a droplet media, as it assumes a layer of constant thickness.

Looking at artificially applied droplets is a method that can be used to simulate real atmospheric corrosion conditions [10, 11, 19, 20]. Development of corrosion has been investigated using FIB and SEM to study the corrosion under droplets of simulated ocean water. Another development in aluminium corrosion has been analysed using x-ray microtomography (XMT). XMT can capture simulated atmospheric corrosion data with *in situ*, three-dimensional imaging. Tomography methods have looked at the evolution of corrosion of samples with a NaCl salt crystal in 100% relative humidity.

Both methods have found corrosion attack at both clusters and individual intermetallic particles [10, 11, 19, 20]. Dealloying of these intermetallic particles from the matrix was seen using destructive methods such as slicing the samples, where striations in particles were then exposed and observed using FIB and SEM. The classification of these particles was; Cu, Mg and Fe [10, 11]. It is therefore predominantly concluded that intermetallic particles stabilise pitting through supplying a cathodic pathway through the aluminium's passive film, allowing for adjacent attack [2, 3, 5].

At some point during the corrosion process propagation switches from grain boundary attack to intergranular corrosion (IGC) this process is little understood [19, 20]. The method of tomography, which in this case is time dependent, with rest time between scans of 30-35 mins which allowed for corrosion sites to be monitored during their growth under the metal surface. It was thought that clusters of intermetallic particles stabilised the growth of IGC sites [10, 152]. It was found that this IGC growth was influenced by grain orientation in the longitudinal direction. Fast-acquired tomography data captured the H_2 evolution

as a function of time. H_2 has been seen evolving from corrosion sites previously under full immersion [3, 153], but its relation to growth had not been captured. H_2 seen evolving from initiated sites, and has been associated with the onset of corrosion, as it shows a cathodic reaction is taking place. Time dependent measurements were taken as the corrosion site grew, and it was seen that H_2 bubbles evacuate from its mouth also grew overtime. Very little has been concluded from the sighting of H_2 apart from its presence and growth with time [20].

2.6.1 Summary of Atmospheric Corrosion

Despite these difference in electrolyte behaviour between full immersion and atmospheric droplets, studies of atmospheric corrosion of AA2024 are limited. With most studies focusing on long term atmospheric exposure, weight loss measurements with inconstant conditions. Little work has been done under droplets to study corrosion kinetics in order to understand corrosion processes due to difficulties viewing corrosion optically. Tomography has added insight to growth and propagation of IGC over 30-35 mins and 4-12 hour intervals [19, 20], however highly temporally resolved information of corrosion propagation is yet to be achieved.

2.7 X- ray Microtomography (XMT)

2.7.1 Introduction

X-ray Tomography (XMT) is a technique used to display real time and 3D observation of through solid objects using X-rays. Tomography can be in both labs and at synchrotron X-ray sources [154-159].

This method is useful as it allows measurements to be taken 'in-situ'. This means corrosion can be monitored in the presence of an aqueous environment, unlike other methods such as electron tomography. X-ray tomography is a non-destructive method that can allow you to view the extent of corrosion under the surface.

2.7.2 Synchrotrons Sources for X-ray Tomography

A synchrotron is characterised by its ability to produce highly parallel and narrow beams of X-rays with high intensity [155, 160]. They provide X-rays with exceptional flux and consistency when compared to laboratory based sources [161]. Allowing for faster data acquisition times and better spatial resolution than lab based sources [155].
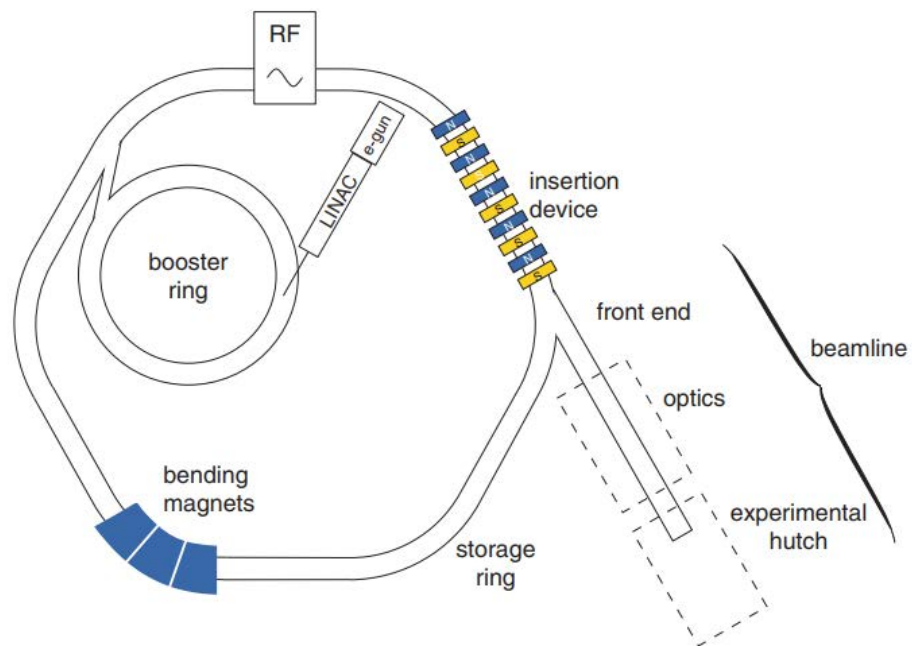
Figure 2-9 Schematic of important components of a modern 3rd generation synchrotron source [161]

3rd generation synchrotrons consist of five main components. These are outlined in Figure 2-9. An Electron gun generates electrons by a process known as thermionic emission. These electrons are then accelerated by LinAc; a linear accelerator. Electrons are accelerated to an energy of approximately 100 MeV. Electrons go on to enter a booster ring where they are accelerated further before they enter the storage ring.

The storage ring is a polygon made up of magnets which deflect the electrons around it. Unlike the booster ring, the storage ring is required to have a constant current. This is done by periodically inserting electrons from the booster ring to

the storage ring as electrons are lost by general use or from colliding with gases which remain in the rings vacuum.

X-ray beams are formed tangentially when electrons 'are deflected by 'superbend' magnets and give off energy as they change direction [162]. This radiation is directed frontward as an X-ray beam towards a beam line. This X-ray beam with high flux and brightness arrives from the insertion device as 'pink beam'. Pink beam has a wide range of wavelengths and can be tailored using a monochromator. Monochromators use Si (111) crystals aligned to specific angles [163]. Using Braggs law specific wavelengths can be selected.

Higher flux achieved by synchrotrons results in faster acquisition time and more accurate temporally resolved true *in-situ* measurements [164].

X-rays generated and tailored to wavelength selected via attenuation. The level of attenuation is determined by the absorption coefficients of the chosen material. This is calculated by using Beer-Lambert's law of attenuation [161, 165].
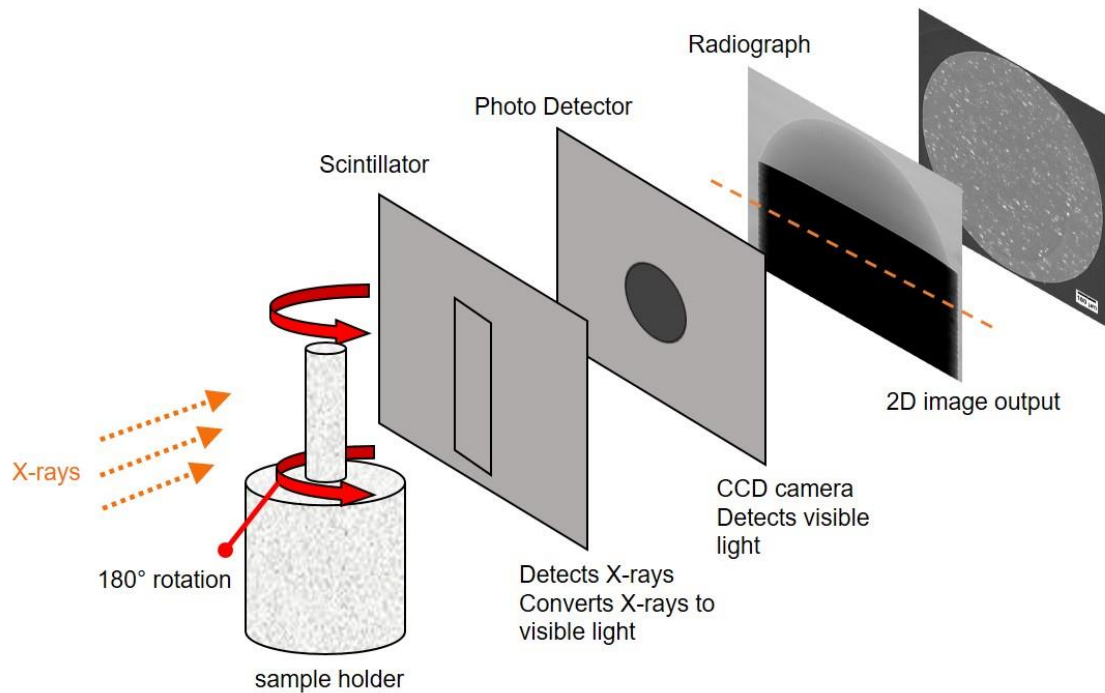
Figure 2-10 schematic diagram illustrating the process of image collection in synchrotron XMT

Figure 2-10 shows the process of image collection for synchrotron XMT. To obtain an image on a beam line X-rays of the selected wave length are passed through the sample. A scintillator is placed behind the sample to collects X-rays which have not been fully attenuated. The scintillator converts these X-rays into visible light which are then magnified by an objective lens. A high speed charge coupled device (CCD) camera is then used to capture 2D images known as radiographs (also referred to as projections). Flat field and dark field corrections are then made to radiographs. Due to distortions in the beam (flat field) and the detector (dark field) radiographs may initially be misrepresented. Radiographs are processed in order to correct any distortions after they are collected as shown in **Equation 2-9**.

$$\text{Corrected image} = \frac{\text{Transmitted data-dark field}}{\text{flat field-dark field}} \qquad \textbf{Equation 2-9}$$

A series of radiographs which are taken as the sample rotates from 0-180° are then reconstructed via one of two methods, back filter projection or gridding reconstruction algorithms in order to achieve a three dimensional tomogram [166].

2.7.3 In-Situ Visualisation of Corrosion

Corrosion propagation in aluminium alloys under electrolyte layers can be investigated using *in situ* synchrotron XMT. XMT is a non-destructive imaging method in which a series of one-dimensional radiographs are captured during the rotation of a sample through 180° [156]. These radiographs are then reconstructed (pieced back together using a specially gridding [166] or filtered-back projection algorithm [167]) to build a three-dimensional image of the sample.

This method is useful as it allows for measurements to be taken *in situ* since x-rays can penetrate metal and solution. This means corrosion can be monitored in the presence of an aqueous environment, unlike other methods such as electron tomography.

However drawbacks of XMT should be considered when interpreting tomography data. Temporal and spatial resolution are limited and varied depending on sample size and density. Trade-offs for some applications where larger samples are required results in longer data collection time or a reduction

in spatial resolution. Smaller samples generally result in better spatial resolution. Higher density samples will require a smaller sample size. Other limitation of XMT include beam hardening, ring artefacts [99] and effects of beam radiation on corrosion droplet solutions such as hydrolysis of water [168]. During radiolysis products produced include oxidising agents such as; HO_2, H^+, O_2, OH^- and H_2O_2 and reducing agents such as; H_2, H^{2-} and H^- [168-170]. These products are thought to accelerate corrosion process while fundamentally not changing them. Tomography also does not provide chemical analysis of the system tested, however is a tool to highlight density in 3D.

2.8 Summary

Localised corrosion of AA2024 has generally been carried out under full immersion conditions. AA2024 undergoes corrosion which is usually localised and takes place rapidly. Localised corrosion poses the highest risk of damage accumulation to AA2024. However, less work has been performed on atmospheric corrosion of AA2024.

The environment variables in which atmospheric corrosion takes place such as temperature, RH and time of exposure largely affect corrosion processes. This is well researched in other alloys, however not much has been investigated on AA2024.

The most useful mechanistic insight to atmospheric corrosion kinetics has been carried out by XMT. Nevertheless through current methods temporal resolution does not compliment well known electrochemical measurements under full immersion with visual examples of atmospheric corrosion events and morphology.

Mechanisms of corrosion have been carried out under at length under steady state conditions however do not fully consider the effects atmospheric conditions have on localised corrosion. A key characteristic of many of these studies is that they use single salts to assess corrosion damage. Very little atmospheric accelerated testing is done using ocean water substitutes. Features of atmospheric corrosion such as trenching/grooving as well as secondary spreading and the formation of corrosion products can be a useful tool for accessing corrosion damage. The aim of this thesis by means of XMT

and lab based atmospheric corrosion experiments is to further knowledge of atmospheric corrosion behaviour on AA2024 under ASTM ocean water droplets.

3. EXPERIMENTAL METHOD

3.1 Material Overview

AA2024-T3 and AA1050-H14 were supplied by Future Metals UK, Winson plc, and Hydro Aluminium Rolled Products. There experimental details are shown in Table 3-1.

Table 3-1 Aluminium Alloys used within this body of work

Material	Form	Supplier	Processing [42]	Experiments
AA2024-T3	Plate	Future Metals UK	T-3	Tomography
AA2024-T3	Plate	Winson plc	T-3	Lab Based
AA1050A	Sheet	Hydro Aluminium Rolled Products	H14	Lab Based

3.1.1 Characterisation of AA2024-T3 Plate
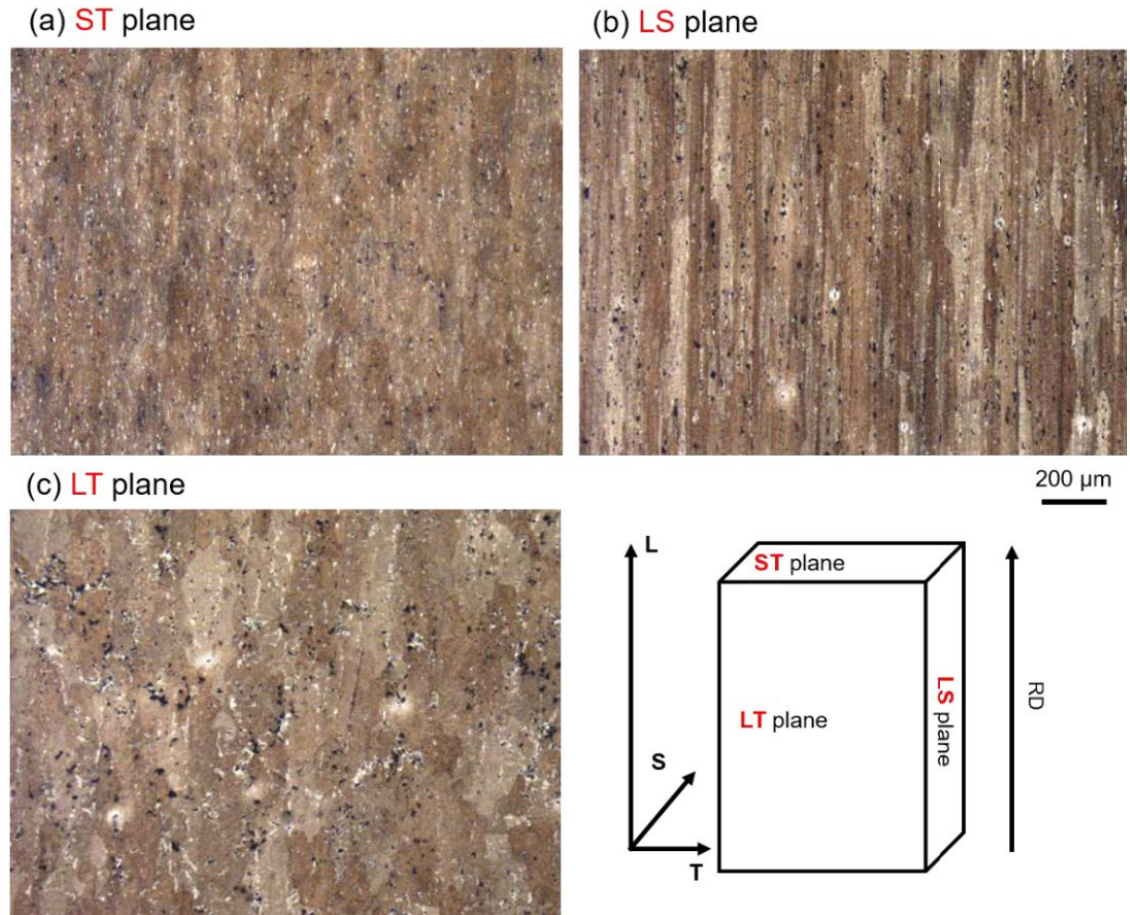
Figure 3-1 Optical microscope image of etched mirror polished AA2024-T3 plate. Surface polished with 0.04 µm diamond paste (MetPrep LTD) and then etched with Kellers reagent. Metallography of three directional planes (a) ST plane, (b) LS plane and (c) LT plane are presented along with an arrow to indicate the rolling direction.

Figure 3-1 displays an AA2024-T3 plate supplied for tomography experiments which was polished to mirror finish using 0.04 µm diamond paste (MetPrep LTD) and rinsed with methanol before being etched using Kellers reagent [171] for 2 minutes. Directionality of grains along with intermetallic particle (seen as black and white speckles) can be seen throughout the metal surface. Rolling direction is highlighted by elongated grains created by means of a cold working process as a part of the T3 age precipitation procedure.

(a) element	weight %	atomic %	(b) element	weight %	atomic %	(c) element	weight %	atomic %	(d) element	weight %	atomic %	(e) element	weight %	atomic %
Al	120.11	83.95	Al	115.3	82.63	Al	139.29	86.68	Al	127.67	86.69	Al	133.56	87.82
Cu	14.23	4.22	Cu	13.35	4.04	Cu	13.16	3.48	Cu	9.78	2.82	Cu	9.95	2.68
C	4.58	7.19	C	5.7	9.12	C	5.38	7.51	C	5.21	7.95	C	4.98	7.35
Fe	4.16	1.41	Fe	3.89	1.34	Mg	2.27	1.56	Mn	2.27	1.71	Mg	2.48	1.82
Mn	3.84	1.32	Mn	3.15	1.2	Mn	0.97	0.3	Mg	0.95	0.32	Mn	1.05	0.34
Mg	1.12	0.87	Mg	1.14	0.91	O	0.44	0.46	O	0.45	0.51	totals	151.65	100
O	0.58	0.68	O	0.57	0.68	totals	161.5	100	Totals	146.33	100			
Si	0.53	0.36	Si	0.26	0.18									
Totals	149.16	100	Totals	143.98	100									

Figure 3-2 SEM of AA2024-T3 mirror polished plate. Surface polished with 0.04 µm diamond paste (MetPrep LTD). Red arrows highlight intermetallic particles (a)-(e) measured with Energy Dispersive X-ray Spectroscopy (EDX).

Figure 3-2 shows SEM images mirror polished AA2024-T3 plate shown in Figure 3-1. The surface polished with 0.04 µm diamond paste (MetPrep LTD) then rinsed with methanol was then measured with EDX point measurements according to section 3.4.1. Analysis of the intermetallic particles (a)-(e) are shown in the table form. Examination showed these particles to be rich in varying quantities of Cu, Mg and Fe. Particles (a) and (b) were rich in both Cu, Fe. Particles (c)-(e) where rich in Cu, Mg without the presence of Fe.

3.2   Salt Droplets

ASTM substitute ocean water was made in accordance to standard D114-98,
"Standard Practice for the Preparation of Substitute Ocean Water" without the
addition of NaF and pH corrected to 8.2 [172]. NaCl (Sigma Aldrich) and other
salts (shown in Table 3-2) were dried at 3 ±3.0 % RH using silica gel orange
(Sigma Aldrich) for a minimum of 24 hours prior to weight measurements.
Relative humidity was measured during drying using an EasyLog EL-USB-2-
LCD, Lascar Electronics Ltd with an accuracy ±3.0 %RH. The salts are then
mixed with de-ionised water (>15 MΩ·cm) in accordance with the standard.

Table 3-2 Salt compound composition used for the preparation of ASTM ocean water [172].

Salt Compound	Concentration (g/L)	DRH % at 25°C [133]
NaCl	24.53	75
$MgCl_2$	5.20	33
Na_2SO_4	4.09	90
$CaCl_2$	1.16	29
$NaHCO_3$	0.695	N/A
KBr	0.201	81
H_3BO_3	0.101	N/A
$SrCl_2$	0.025	71

The initial CDD (mass of chloride per unit area – chloride deposition density) of each droplet was calculated using **Equation 3-1**. For tomography droplets, the volume is calculated using the diameter of the pin sample and is fixed. For lab based droplets, the area is measured by optical microscopy directly after the droplet is deposited and calculated using Fiji (freeware) [173].

$$\text{CDD} = \frac{\text{n}V M_{\{Cl\}}[C]}{A}$$

Equation 3-1

n – *number of Cl$^-$ per molecule*

V – *volume of droplet at deposition (µl)*

$M_{\{Cl\}}$ – *molar mass of chloride(g mol^{-1})*

[C] – *concentration of solution deposition (moles)*

A – *area of deposited droplet (cm^2)*

3.3 Synchrotron Experiments

3.3.1 Material

A 10mm AA2024-T3 plate was supplied by Future Metals UK (Table 3-3). Pin samples (1 mm diameter) for X-ray microtomography (XMT) measurements were machined from the middle of the plate, with their long axis parallel to the rolling direction, as shown in Figure 3-3.

Table 3-3 Composition of AA2024-T3 (Future Metals UK)

	Si	Fe	Cu	Mn	Mg	Zn	Cr	Ti	Others
Cast Analysis Weight %	Max 0.5	Max 0.5	3.8-4.9	0.3-0.9	1.2-1.8	Max 0.25	Max 0.01	0.15	0.02

3.3.2 Tomography Sample Preparation

Prior to each experiment the top surface (ST in Figure 3-1) of the pins (shown in was dry-polished with SiC paper. The samples were passed over P800 and P1200 grit (MetPrep LTD) for three unidirectional passes, then passed over P4000 grit for six unidirectional passes. Samples were then rinsed with methanol, and left to passivate for one hour before applying a salt droplet.

Tomographic sample cells were designed based on modifications made to cells used by Connolly et al [17] and Knight [20]. A schematic of the cell used for both steady state and wet dry cycling experiments is shown in Figure 3-3. A droplet is deposited on the polished pin surface 10 minutes after drying had taken place. Filter paper soaked in saturated KCl with additional KCl crystals are used to control the relative humidity at 85% [133] was placed inside the silicone tubing (versilic) and sealed with an AA1XXX stopper and petrolatum tape. During wet to dry cycle the tube is then replaced by a tube containing a silica gel orange (Sigma Aldrich) sphere to achieve 3 ±3.0% RH. Due to the size of the cells estimates of RH had to be made from lab based measurements taken from within larger desiccators monitored using an EasyLog EL-USB-2-LCD, Lascar Electronics Ltd. RH (with an accuracy ±3.0 %RH) was measured at ~3 ±3.0%.
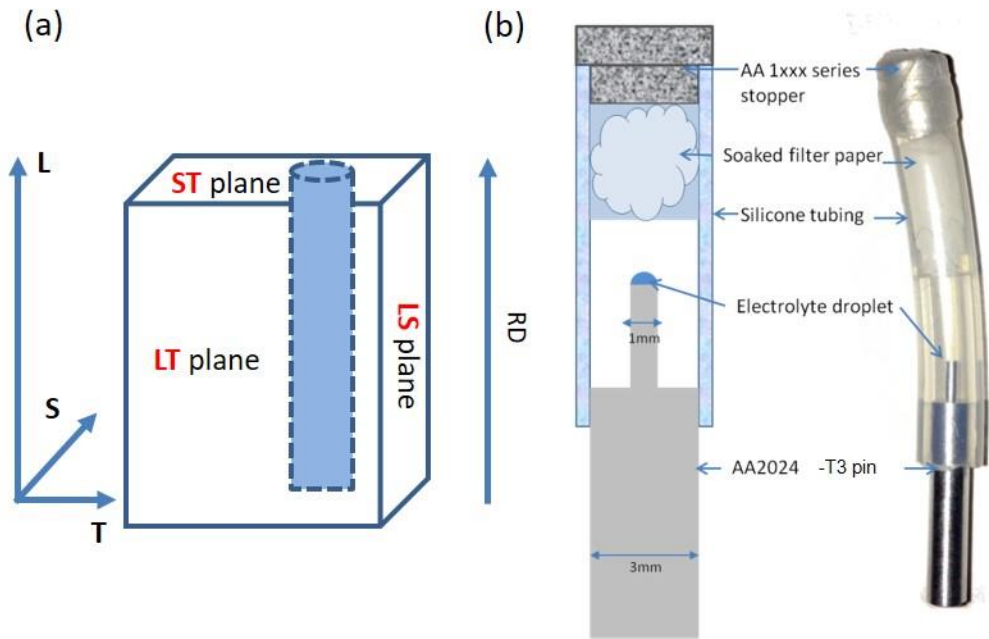
Figure 3-3 (a) the sample holder used for synchrotron tomography experiments, illustrating the cell used for maintaining relative humidity. (b) The location of the machined pins relative to the AA2024-T3 plate rolling direction (RD), TRD = transverse rolling direction, PRD = perpendicular to rolling direction, L = longitudinal, ST = short transverse, and LT = long transverse. Tomographic stage set up at Swiss Light Source - TOMCAT.

3.3.3   Tomography Experimental Conditions

3.3.3.1 Steady State

Two solutions were used: NaCl (Sigma Aldrich) to make up a saturated NaCl solution (6.1 M), and substitute ASTM ocean water made according to ASTM standards (D 1141 – 98), without the addition of trace NaF. Experimental conditions are shown in Table 3-4. An Eppendorf research plus microlitre pipette was used to deposit 0.2 µL ± 0.04 µL of the chosen solution on top of the polished pin (as specified in 3.3.2) surface giving a chloride deposition density CDD as shown in Table 3-4.

Table 3-4 – Salt droplet, chloride deposition density (CDD) and relative humidity used for the two samples tested.

Sample	Salt Droplet	CDD $\mu g/cm^2$	Relative humidity maintained by KCl [133]
1	ASTM standards (D 1141 – 98), without the addition of trace NaF	1400	85 %
2	6.1 M NaCl	5400	85 %

3.3.3.2 Wet Dry Cycling Tomography Experiments

Two solutions were used: NaCl (Sigma Aldrich) to make up a NaCl solution (0.5 M), and substitute ASTM ocean water made according to ASTM standards (D 1141 – 98), without the addition of trace NaF. An Eppendorf research plus microlitre pipette was used to deposit 0.2 µL ± 0.04 µL of the chosen solution on top of the polished pin surface (as specified in 3.3.2) giving a CDD shown in Table 3-5 along with the experimental exposures.

Table 3-5 Salt droplet, chloride deposition density (CDD) and relative humidity used for the two samples tested.

Sample	Salt Droplet	CDD $\mu g/cm^2$	Relative humidity maintained by KCl [133]
1	ASTM standards (D 1141 – 98), without the addition of trace NaF.	1400	85 %
2	0.5 M NaCl	500	85 %

Timing and data collection measurements for both salts tested are shown in Figure 3-4 and Figure 3-5. Figure 3-4 shows the wet dry cycles and scans associated to the ASTM ocean water droplet. Figure 3-5 shows the wet dry cycles and scans associated to the NaCl droplet. D is used to define dry phases of the experiment. W is used to define the 'wet' phases of the experiment. E is used to describe the End scan of each experiment. O indicates ASTM ocean water droplets and Na indicates NaCl droplets. The number associated to either D or W refers to the tomographic scan number which was taken in series. Orange is used to also indicate 'dry' phase, and blue used to indicate 'wet' phases. Each tomographic scan is 300 s in duration. This time is measured from the start of each scan. Each sample was exposed to 85% RH for 12 h before tomographic scanning began. The new scanning phase is undertaken during the first hour in which the RH is changed.

During wet to dry cycle, silica gel orange (Sigma Aldrich) spheres are placed in the silicone tubing used to achieve 3 ±3 % RH. There was a 5 minute interval between the RH being changed and the first tomographic scan initiating.
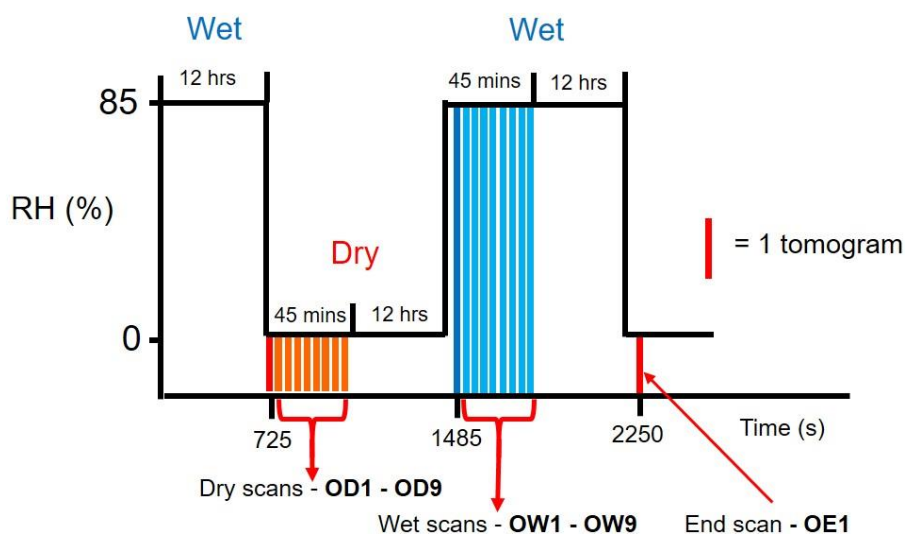
Figure 3-4 A schematic of time vs humidity for a wet and dry cycle experments for an ASTM ocean water droplet at a temperature of 21±2 °C . Humidty is cycled from 85% relative humidity to 0% relative humidity. Lines indicate the number of tomographic scans completed during each dry phase of the cycle along with the duration of the block of scans and the total time of corrosion. Each scan represents 300s of data collection. The red line indicates the interval before RH was changed before dry scan were initiated. Orange lines indicate of the scans during the visulisation of the corrosion in the dry environment. The labels designated to dry scans are – OD1 to OD9. A dark blue line indicates the interval the RH was changed to wet before scanning. Light blue lines signify scans carry out during the wet phase. Labels designated to wet scans are – OW1 – OWD. The last scan is labeled OE1.
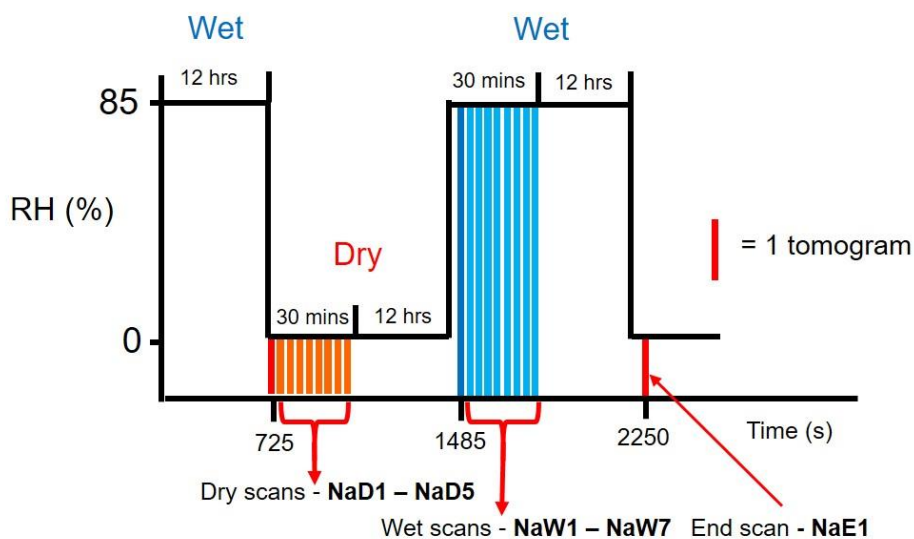
Figure 3-5 A schematic of time vs humidity for a wet and dry cycle experments for a NaCl droplet at a temperature of 21±2 °C . Humidty is cycled from 85% relative humidity to 0% relative humidity. Lines indicate the number of tomographic scans completed during each dry phase of the cycle along with the duration of the block of scans and the total time of corrosion. The red line indicates the interval before RH was changed before dry scan were initiated Orange lines indicate of the scans during the visulisation of the corrosion in the dry environment. The labels designated to dry scans are – NaD1 to NaD5 A dark blue line indicates the interval the RH was changed to wet before scanning. Light blue lines signify scans carry out during the wet phase. Labels designated to wet scans are – NaW1 – NaD7. The last scan is labeled NaE1

3.3.4 Beam Line Set Up

X-ray tomography measurements were carried out at the TOMCAT beamline at the Swiss Light Source (SLS) [174]. Pins were set up in cells, as shown in Figure 3-5. There was an interval of five minutes between the application of the droplet and the start of the first scan. The temperature of the experimental hutch was 21 ± 2 °C. Measurements were made with an X-ray energy of 21.9 keV selected by a double multi-layer monochromator. The sample was placed 25 mm from the detector (PCO.2000, PCO AG, Kelheim, Germany), X-rays were then converted into visible light by a 20 µm LuAg scintillator. The corresponding images were magnified with a x10 optic onto the detector giving a pixel size of 0.74 µm, and actual voxel volume of 0.406 µm^3 (as verified in section Appendix 1 Figure 9-2). A series of radiographs (projections) were collected as the sample rotated through 180° about the vertical axis. 1201 projections were collected with a 160 ms total exposure time, giving a data collection time of 300 s per tomogram. Raw projections (radiographs) were collected as .tif image files. Three dimensional tomograms were then reconstructed using a gridding method algorithm developed at TOMCAT [166].

3.3.5 Tomography Data Analysis

ImageJ [175] and Fiji software (freeware) [173] alongside Avizo FEI 8 were used for subsequent image processing. Files collected post data reconstructed were in .DMP file format (specific to the tomcat bean line). .DMP files were resaved to .tif format via a Fiji macro script (found in Appendix 1 section - 9.1.1 Figure 9-1). This script used an input file location along with a brightness and contract level which can be altered in the script before saving the files in a

desired location. The resaved .tif files are then manipulated in Fiji to reduce their working size. This is done by opening .tif files as 'image sequences' and cropping any unwanted regions of air and the pin sample. Cropping was done using the 'Duplicate' function within Fiji and data is resaved as 'image stacks'. Reopened files are then used to analyse selected data in 2D vertical and horizontal slices. 3D analysis can be done by saving cropped files in the AmiraMesh format for use in the Avizo FEI program.

(a) Metal line measurements
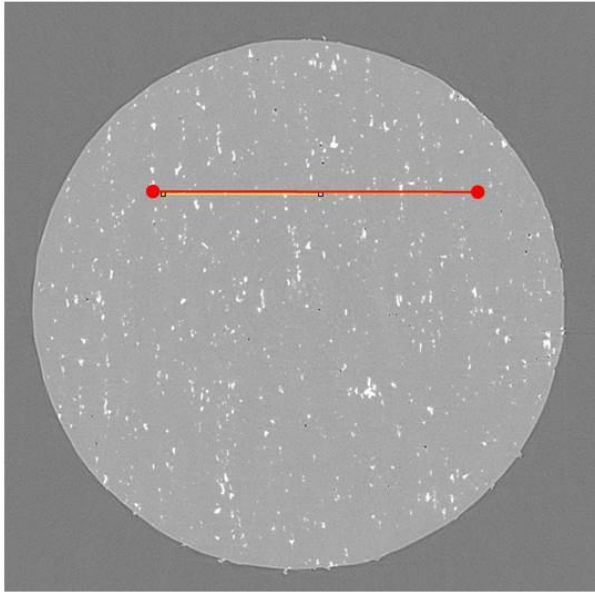
(b) Average = 162.3   σ = 8.9
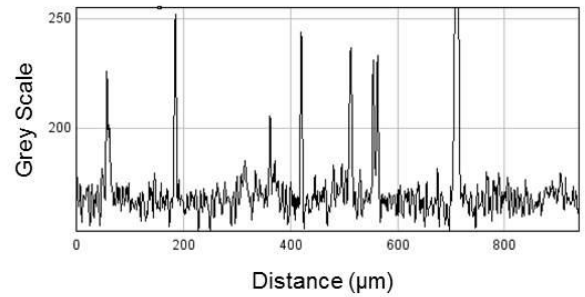
(c) Signal from metal line measurement applied to 'Magic wand' tool
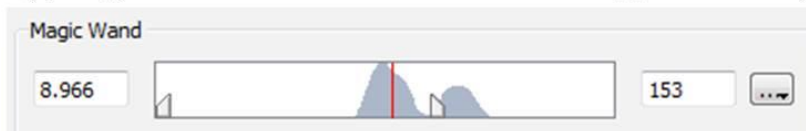
(d) Corrosion site
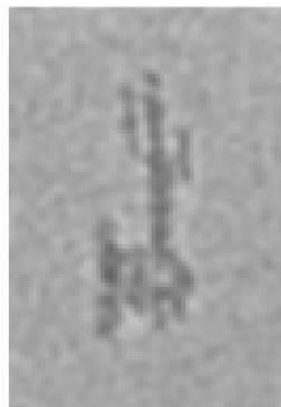
Avg − σ = 153
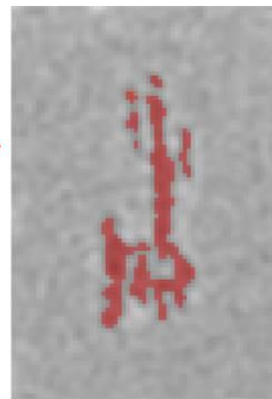
Figure 3-6 schematic of the calculated grey scale threshold settings used for volume segmentation measurements in Avizo FEI. (a) a line scan of the metal surface measured in Fiji. (b) an illustration of the line scan, shown with an average of the data collected and its derived standard deviation given as σ. (c) indicate the settings which are then applied to the 'Magic wand' tool. (d) the application of the calculated grey scale value to pixels are shown in red.
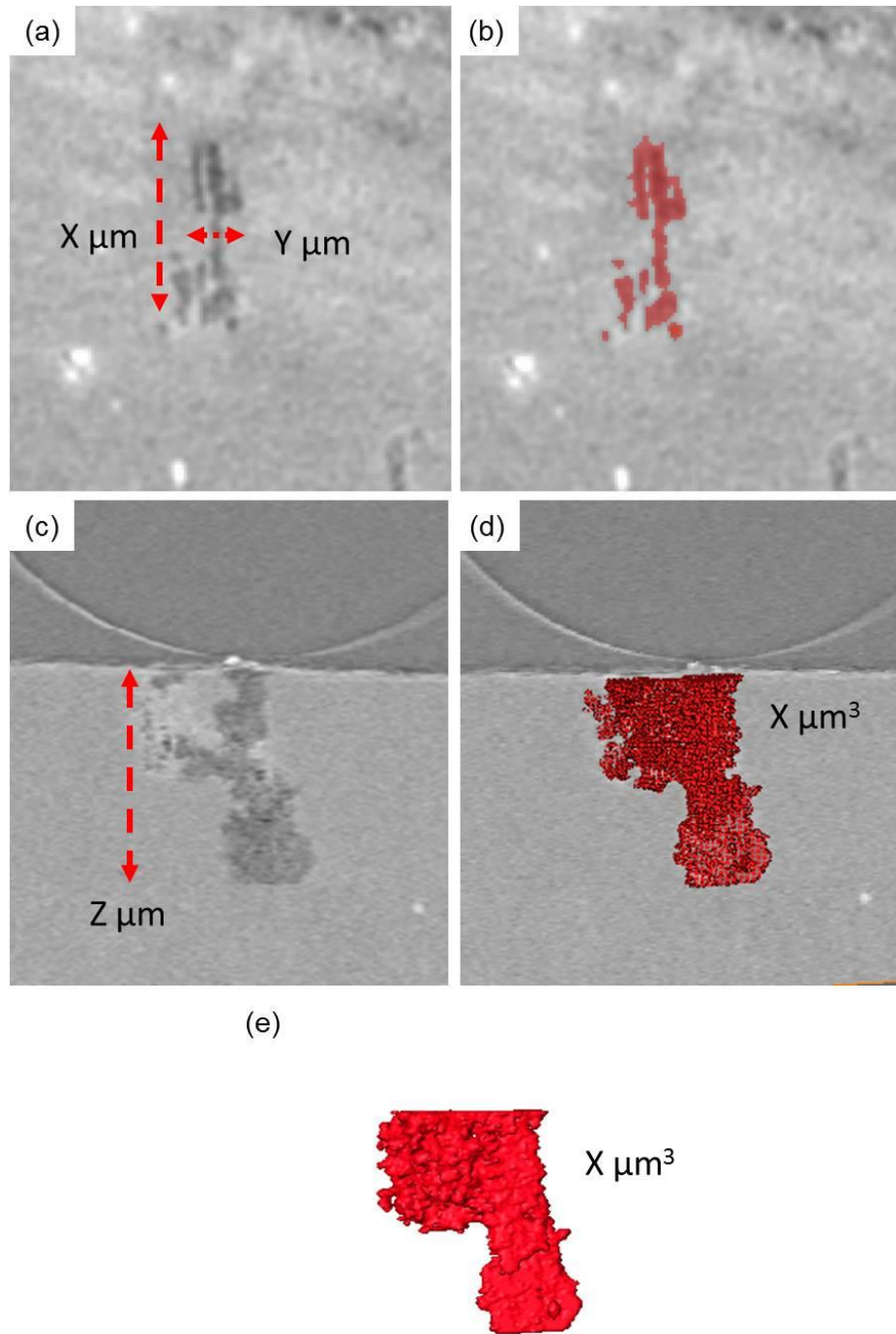
Figure 3-7 (a) and (c) the length depth and width measurements indicated as X, Y and Z of a visible fissure. (b) and (d) the segmentation process used for tomographic 3D measurements of a visible fissure. (e) shows the completed 3D segmentation once pixels have been selected used to calculate volume loss in μm^3.

3.3.5.1 Segmentation and Measurements

Avizo FEI is used for 3D analysis and the segmentation process used for quantifying corrosion volume loss. Segmentation of samples was done in Avizo FEI by assigning pixels of a calculated grey scale value as shown in Figure 3-6. Using the 'Magic wand' tool and a grey scale values which was predetermined in Fiji (as shown in Figure 3-6) selects pixels within the selected range. The working grey scale value is used to assign pixels as 'metal loss'. An average value is taken from a line measurement of the metal surface demonstrated in Figure 3-6 (a). This includes the white intermetallic (higher density) particles and black voids (lower density). The average of this line measurement is used to derive a standard deviation (σ) as shown in Figure 3-6 (b). The standard deviation is then subtracted from the average value from the line scan of the metal. The figure generated is then applied to the 'Magic wand' tool settings in (c) and shown as a selected value of pixels in (d) in red. This process is done to avoid human error and variation being applied to the analysis of all tomography data sets.

The segmentation and depth, width, and corrosion site length measurement processes is outlined in Figure 3-7. Avizo FEI is used to measure volume and present 3D images of IGC and pitted sites as shown in Figure 3-7 (d) and (e). This was done by using segmentation labels, shown in (b) (d) and (e) using calculated grey scale (shown in Figure 3-6). Due to the nature of the analysis by way of using a predetermined grey scale value, measurements were set the same for every sample allowing for a single measurement of volume to be made. Voxel counting was done using material statistics within Avizo FEI. Fiji is

used to measure the width X μm, length Y μm and depth Z μm of corrosion sites by eye shown in Figure 3-7 (a) and (c). Measurements were made 6 times and then averaged to give values used.

Time lapse imaging of H_2 bubbles was done using an Infinity 2 microscope with a x10 lens looking top down on samples.

3.4 Lab Based Experiments

3.4.1 Material

A 2x100x100 cm AA2024-T3 plate (Alcoa Europe) was supplied by Winson plc with composition detailed in Table 3-6. Samples (2 cm by 2 cm) were cut from the middle of the plate, with their long axis parallel to the rolling direction, as shown in Figure 3-8.

Table 3-6 – Composition of AA2024-T3 (Alcoa Europe) [176]

	Si	Fe	Cu	Mn	Mg	Zn	Cr	Ti	Others
Cast Analysis Weight %	0.08	0.22	4.6	0.7	1.5	0.11	0.01	0.03	0.02

A 1 m^2 (2 mm) AA1050A- H14 1 mm sheet (Hydro Aluminium Rolled Products) with composition detailed in Table 3-7. Samples (2 cm by 2 cm) were cut from the middle of the plate as shown in Figure 3-9.

Table 3-7 – Composition of the AA1050A- H14 (Hydro Aluminium Rolled Products)

	Si	Fe	Cu	Mn	Mg	Zn	Ti	Al	Others
Cast Analysis Weight %	0.04	0.36	0.001	0.003	1.5	000	0.001	99.58	0.02

3.4.1.1 Lab Based Sample Preparation
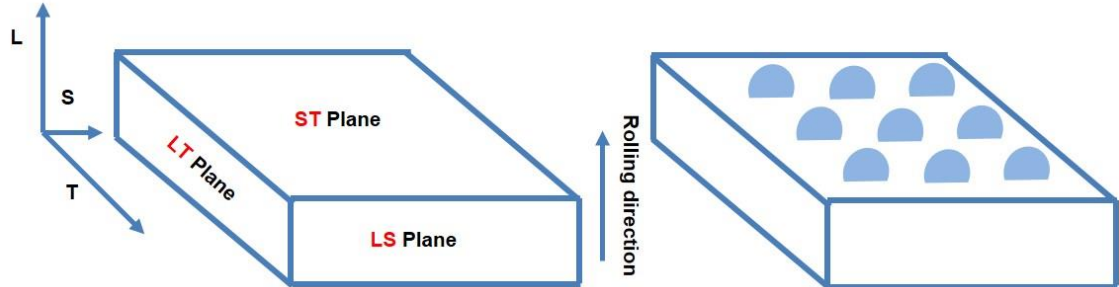
Figure 3-8 Sample set up of AA2024-T3 plate for atmospheric exposure. ST, LT, and LS planes along with rolling direction are shown. Droplets were deposited on the ST plane as shown.
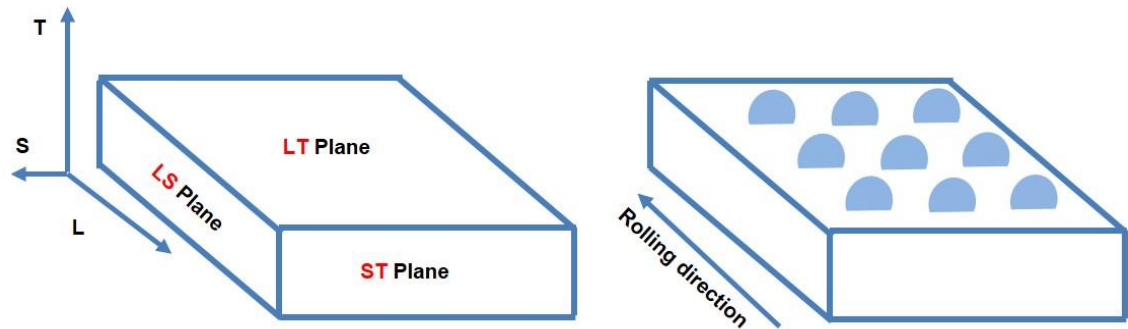
Figure 3-9 Sample set up AA1050 aluminium alloy sheet for atmospheric experiments. LT, LS, and ST planes along with rolling direction are shown. Droplets were deposited on the LT plane as shown.

Samples (2 cm by 1.5 cm) were cut from the middle of the plate as shown in

Figure 3-8 and Figure 3-9.

Prior to each experiment, the top surface of the plate and sheet samples were

polished with SiC paper and methanol. The samples were passed over P800

grit (MetPrep LTD) and rinsed clean with methanol. Samples were then left for

30 minutes to passivate before droplets were deposited. P800 was chosen to promote the atmospheric corrosion of AA2024-T3 used.

3.4.2 Lab Based Experimental Conditions

3.4.2.1 Lab Based Experiments

The solutions used were: NaCl (Sigma Aldrich) to make up a 1 M NaCl solution and substitute ASTM ocean water made according to ASTM standards (D 1141 – 98)[172]. An Eppendorf research plus microlitre pipette was used to deposit 2 µL ± 0.04 µL of each solution on top of the polished sample surface giving chloride deposition density CDD as shown in Table 3-8. The RH of 85% was maintained by KCl and the RH of 98% was maintained by K_2SO_4 [133] within sealed desiccators. Temperature (with an accuracy ±0.5 °C) and humidity (with an accuracy ±3.0 %RH) during exposure was monitored using an EasyLog EL-USB-2-LCD, Lascar Electronics Ltd.).

Table 3-8 Salt droplet, chloride deposition density (CDD) and relative humidity used for the three samples tested and presented.

Sample	Salt Droplet	CDD $\mu g/cm^2$	Relative Humidity (RH)	Test Duration
NaCl droplet on AA2024-T3	1 M NaCl	1000	85 ±3 %	4 weeks
ASTM ocean water droplet on AA2024-T3	ASTM standards (D 1141 – 98)	430	85 ±3 %	4 weeks
NaCl droplet on AA1050	ASTM standards (D 1141 – 98)	430	98 ±3 %	8 weeks

3.4.3 Sample Preparation for Imaging

For Raman measurements samples shown in Figure 3-8 and Figure 3-9 were rinsed and dried following atmospheric exposure outlined in Table 3-8, methanol was used to remove any residual salts.

After exposure corrosion environments shown in Table 3-8 each samples corrosion products were removed by immersed in 70% nitric acid for two minutes. Samples were then polished for 6 minutes with OP-S colloidal suspension (Struers) and water.

3.4.1 Sample Imaging

SEM images of samples were made on a Jeol 6060LV and used a 10 mm working distance and an accelerating voltage of 10 kV. Optical microscopy was done using Leica DMLM microscope and a Leica DFC 420 digital camera. A Schott KL 1500 LCD cold light source was used to illuminate samples from side on.

3.4.1 Raman Microscopy

Raman microscopy was used to identify corrosion products prior to washing outlined in 3.4.3. Point measurements and mapping were performed on a typical example of one of the 9 droplets on a corroded sample. The machine used was a Renishaw InVia spectrometer with confocal microscope. The excitation wavelength was 488 nm with an approximate 1 mW focus through a 20x super long working distance objective. This gave a spot size of approximately 10 μm.

3.4.1.1 Point Measurements

Point measurements where collected using a 448 nm laser with approximately 20mW power, 2 second exposure and 25 accumulations. The data range was measured from 0–1600 cm^{-1}, and then truncated at 100 cm^{-1} then baseline subtracted (polynomial) to remove any fluorescence.

3.4.1.2 Raman Mapping

Mapping data was collected using a 448 nm laser with approximately 20mW power, 10 second exposure and 2 accumulations per point. Map resolutions were set per sample. NaCl droplet on AA2024-T3 sample was set up to take 14690 data points at a step size of 28 μm by 28 μm. AA2024-T3 ASTM ocean water was set up to take 10584 points at a step size of 28 μm by 28 μm. The data range was measured from 0–1600 cm^{-1}, and then truncated at 100 cm^{-1} then baseline subtracted to remove any fluorescence.

Two types of Raman maps were generated by Wire™ 4.0 (Windows based Raman environment – Renishaw plc 2002) software principle component analysis (PCA) and direct classical least square analysis (DCLS).

3.4.1.3 Principal Component Analysis Mapping

Raman maps of the droplets were loaded into Wire™ software where PCA maps of potential phases were constructed by machine identification of consistent patterns of peaks within the data set. Potential phases of interest that were identified were then compared to spectra of know compounds it identify the phases present. Components found in the sample were used to generate a map using DCLS.

3.4.1.4 DCLS Mapping

DCLS mapping is used to assigns a score to each spectrum in the dataset based on how well it correlates with a particular standard spectrum. This score is then used to generate a pixel value, allowing an image to be generated where intensity corresponds to goodness of fit calculated from the least squares algorithm. These are then exported as a BMP. image.

3.4.1.5 Control Standards

Standards from RRUFF [177] and measured standards along a standard for Hydrotalcite (Sigma Aldrich CAS Number: 11097-95-9) can be found in Appendix 2 section - 9.2.1. A standard for Dawsonite was synthesised following protocol Appendix 2 section - 9.2.1 [178]. These standards were selected based on finding from literature reviews in Table 2-2.

3.4.1.6 Raman Data Averaging

BMP images files are produced from DCLS maps. Each pixels grey scale intensity from 0-255 was set in Wire™ using the LUT (look up table) controls set at 5%-95% of the histogram of distribution of intensity. Grey scale values set in BMP images are then used to average and normalise all data points and plot Raman shift *vs.* intensity using the Matlab Script found in Appendix 3 - Matlab Scripts section 9.3.1.

3.4.2 SEM, EDX and Optical Procedures

Corrosion products in droplets were investigated with the use of SEM, EDX, optical microscopy (Leica DFC420), grazing angle XRD and FTIR.

SEM and EDX measurements of droplets were made on Jeol 6060LV. EDX measurements used a 10 mm working distance and an accelerating voltage of 10 kV.

Optical microscopy was used to assess corrosion site number. Corrosion sites where counted if sites were above 10 μm in length in one direction and deeper than 3 μm.

3.4.3 XRD Sample Preparation and Measurements

A Bruker D8 Advanced X-ray powder diffractometer was used to gather grazing angle XRD patterns of an entire corroded droplet of one 1000 μg/cm^2 NaCl and one 450 μg/cm^2 ASTM ocean water on AA2024-T3 samples held at 85% and 30 ^{o}C for 4 weeks as shown in Table 3-8. Cu K-α with a wavelength of 0.15418 nm was used. The incident angle was fixed at 1 degree and incident beam stepped at 0.02 degrees taking 1645 steps per scan, data was then monochromated. Standards used were Dawsonite: [179], Felsöbányaite: [180] and Hydrotalcite [181].

3.4.4 FTIR Sample Preparation and Measurements

FTIR test were prepared by scraping corrosion products off using a glass slide off 12 NaCl droplets with an average CDD of 5000 μg/cm^2 and 12 ASTM ocean water droplets with an average CDD of 450 μg/cm^2 on AA2024-T3 samples as shown in Figure 3-8 following exposure at 85% and 30 ^{o}C for 4 weeks shown in

Table 3-8. Corrosion products were collected and then suspended in KBr, which was dried overnight at 120°C. 300 mg of KBr was used per 3 g of samples collected. Samples were then measured using a Thermo Scientific Nicolet 8700 Model 912A0685.

3.4.5 Salt Droplet Quantification

A Rigaku Miniflex 600 x-ray powder diffractometer was used to gather XRD patterns of dried salts of ASTM ocean water gathered by drying 50 mL of solution at 80 °C for 30 minutes. Cu K-α with a wavelength of 0.15418 nm was used. θ – 2 theta geometry was stepped at 0.02 degrees. A Si holder was used and subtracted from patterns collected. Standards were gathered from the ICDD PDF2 database [181].

4. THE INITIATION OF ATMOSPHERIC CORROSION

4.1 Introduction

The corrosion of aluminium and its alloys has been extensively studied in order to improve corrosion resistance, and contribute to the body of knowledge which is applied to life cycle planning models. Most of the published work has studied corrosion in full immersion environment [1, 72-74]. However, much less work has been carried out in atmospheric conditions under salt droplets [15, 73, 112, 150, 151, 182].

XMT provides a non-destructive way of visualising atmospheric corrosion. Under *in-situ* conditions in previous studies, this method is usually carried out over hourly time intervals due to the length of data collection. The data collection time is usually dictated by the resolution required to visualise small scale features such as IGC which can only be observed with sub-micron resolution. Particular attention has been paid to initiation and growth propagation of IGC between AA2024-T3 and AA7050 over hourly intervals of growth [19, 20, 92, 99, 100].

The initiation of corrosion in AA2024-T3 is most commonly associated intermetallic particles [1, 15, 183], due to the presence of a thinner passive film [73, 86, 151]. However faults such as voids in the passive film have also been shown to act as initiation sites for corrosion [184, 185].

Visualisation of intermetallic particles and H_2 evolution has been achieved with current XMT techniques. Tomography has enable corrosion sites to be observed at intermetallic particles and intermetallic particles clusters which are

seen clearly due to phase contrast, along with the evolution of H_2 bubbles from growing corrosion sites [19]. However, these observations have been made in minutes and hours following corrosion events and did not capture initiation in real time.

In this chapter, high speed *in-situ* synchrotron X-ray tomography has been used to observe the initiation and propagation of atmospheric corrosion on aluminium alloy AA2024-T3. The technique used to collect tomographic scans allowed for a temporal resolution of 300 s per full tomographic reconstruction.

4.2 Results

4.2.1 Preliminary Observations of Corrosion in Tomographic Projections
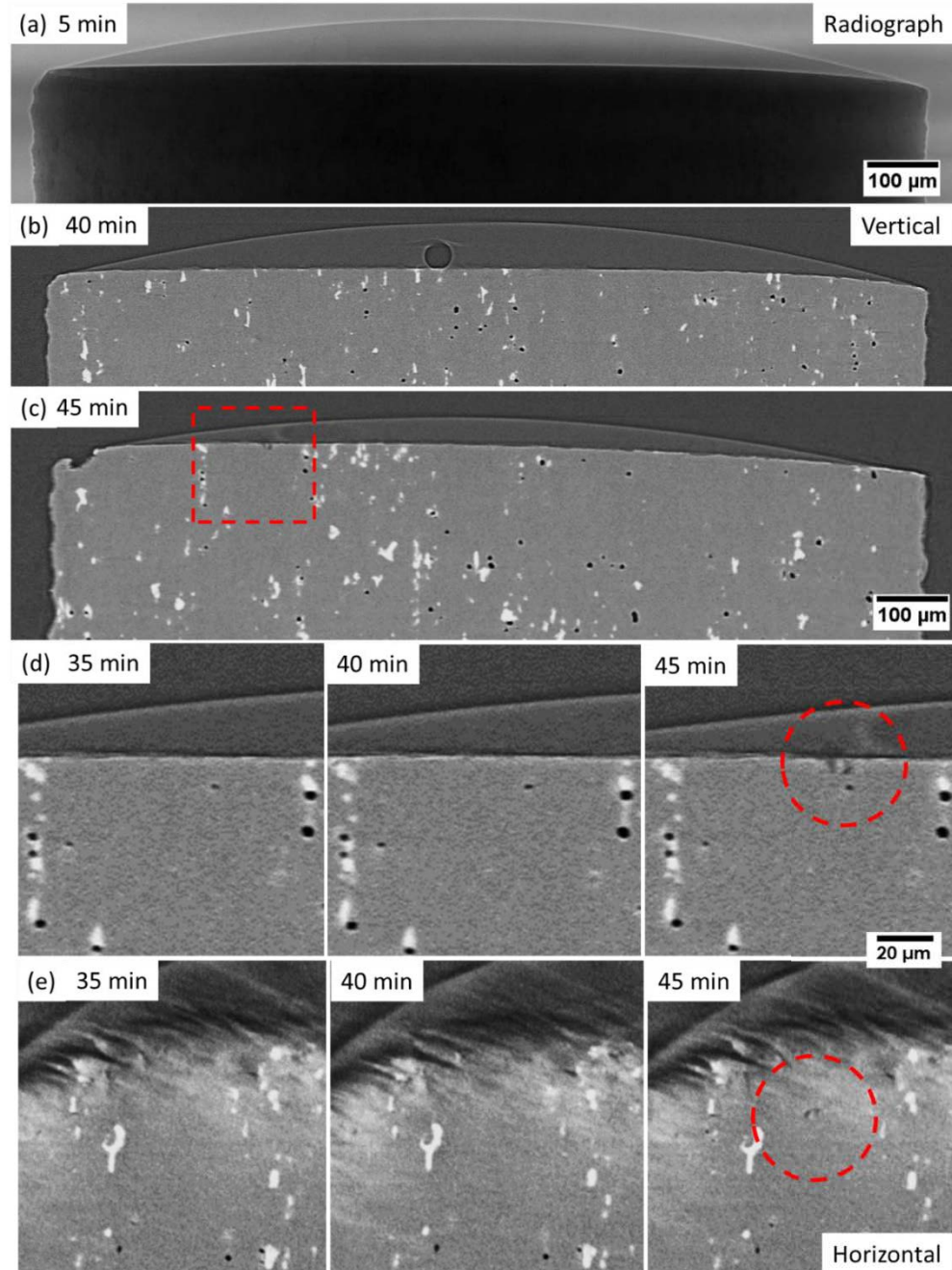
Figure 4-1 - Evolution of corrosion on a 1 mm diameter AA2024-T3 pin exposed to a 0.2 μL droplet of ASTM standard (D 1141 – 98) ASTM ocean water (without NaF), with conditions shown in Table 3-4 giving a CDD of ~1400 μg/cm^2 at a temperature of 21 ± 2 °C and 85% RH: (a) radiograph at the start of the experiment, (b) vertical section through the first sighting of H$_2$ at 40 minutes, (c) vertical section through the pin at the location of the first corrosion site (red square) at 45 minutes, (d) higher resolution vertical sections of the location of the corrosion site in (b) before initiation (35 and 40 minutes), and after initiation (45 minutes, red circles), and (e) horizontal sections of the tomograms shown in (d) intersecting the location of the localised corrosion site (red circle). Broken red circles highlight the location of the initiation site.

Figure 4-1 shows the evolution of a corrosion site on a 1 mm diameter AA2024-T3 sample exposed to a 0.2 µL droplet of ASTM standard ASTM ocean water (without NaF), giving a CDD of approximately 1400 µg/cm^2 (shown in Table 3-4). The sample was then kept at a temperature of 21 ± 2 °C and a relative humidity of 85% (KCl). The sample was scanned at five minute intervals, until beam was lost at 45 minutes. Figure 4-1 (a) shows a projection (radiograph) of the sample in which both the droplet and pin can be observed. The bright outline is a result of slight phase contrast enhancement. Figure 4-1 (b) shows a vertical section of the tomogram five minutes before any corrosion sites can be detected. White intermetallic particles, black voids and a bubble, assumed to be H$_2$, can be seen. Figure 4-1 (c) shows the vertical section in which the first corrosion site can be identified. Figure 4-1 (d) and (e) show an enlarged higher resolution image of the outlined region in Figure 4-1 (c). The image at 35 and 40 minutes are identical, showing the reproducibility of the image. The image at 45 minutes shows two dark areas just beneath the surface, which are assumed to be different parts of a localised corrosion site. These two dark regions are recurrent in horizontal sections at 45 minutes. Detailed examination of the initiation site looking through both vertical (Figure 4-1 (d)) and horizontal (Figure 4-1 (e)) sections did not reveal any visible intermetallic particle from which the site may have initiated. The presence of bubbles within the droplet should be noted, shown clearly at 40 minutes and assumed as hydrogen. The bubble appears to have no spatial relation to a corrosion site and therefore it is feasible that this bubble could be a result of 'beam damage' where X-rays interact with

the solution droplet producing radiolysis products; one of which is known to be
H$_2$ [168].
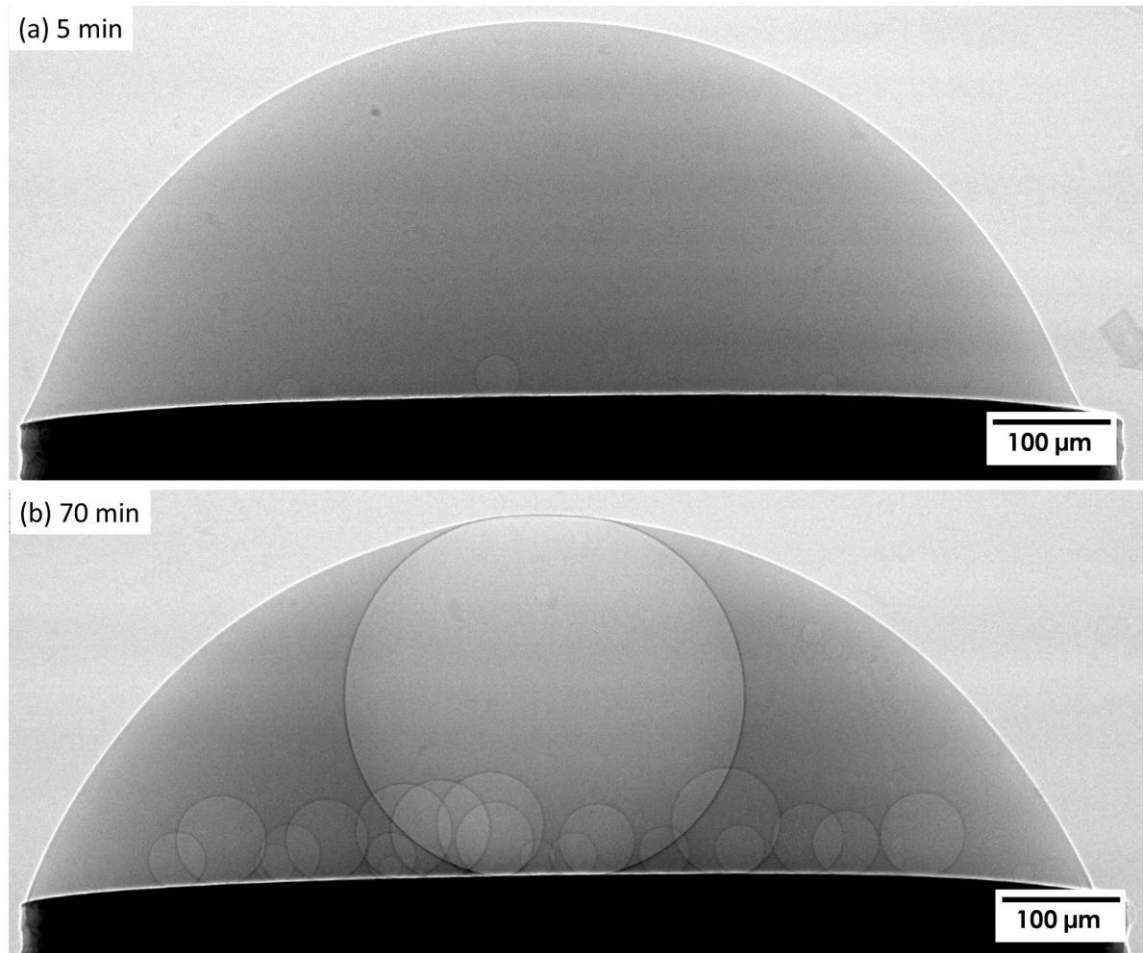
Figure 4-2 - Radiographs showing the evolution of hydrogen on a 1 mm diameter AA2024-T3 pin with a
0.2 µL droplet of NaCl with a CDD of ~ 5400 µg/cm^2 at a temperature of 22 ± 2 °C and 85% shown in Table
3-4: (a) 5 minutes and (b) 70 minutes.

Figure 4-2 shows the evolution of a corrosion site on a 1 mm diameter AA2024-
T3 sample exposed to a 0.2 µL droplet of 6.1 M NaCl giving a CDD of
approximately 5400 µg/cm^2. The sample was then kept at a temperature of 21 ±
2 °C and a relative humidity of 85% (KCl) (a) shows a projection: in this image,
a dark outline of the pin sample can be identified; on top of this NaCl salt

solution droplet. The first bubbles can be seen on the surface from the first scan at five minutes. Figure 4-2 (b) shows the same sample after 70 minutes of exposure. There was a large increase in the number and size of bubbles in this droplet. Time lapse optical microscopy of an identical pin under the same conditions was set up in the lab in order to study bubble formation in the absence of x-ray radiation. H_2 initially evolved at 7 minutes on average in lab samples. Only one H_2 bubble could be seen in the *ex-situ* sample after 70 minutes, 100 μm in diameter. The differences in H_2 productions between lab and XTM experiments could be attributed to beam damage.
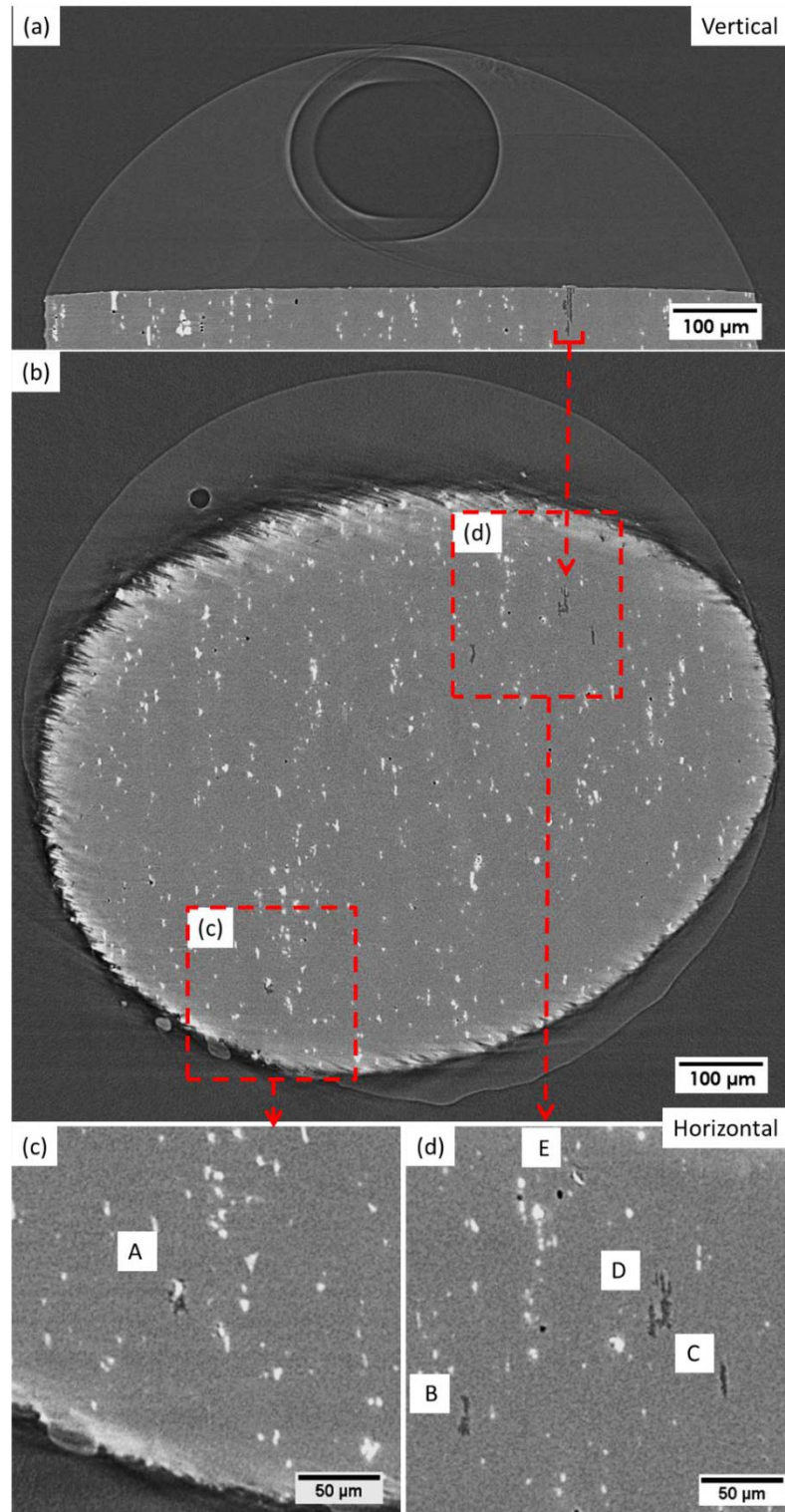
Figure 4-3 – Sections of tomograms generated from radiographs shown in Figure 4-2 taken during a synchrotron experiment. Five corrosion sites were identified in the last 5 minutes of the 120 minute scan. The sample was a 1 mm diameter AA2024-T3 pin exposed to a 0.2 µL droplet of NaCl, giving a CDD of ~ 5400 µg/cm^2 at a temperature of 22 ± 2 °C shown in Table 3-4. (a) shows a vertical section though the largest corrosion site, and (b) top down view of all corrosion sites. (c) and (d) are magnifications of the corrosion sites in (c) and (d). Corrosion sites in (c) and (d) are labelled A-E.

Figure 4-3 shows tomographic sections of the NaCl droplet sample after 120 minutes of exposure. Figure 4-3 (a) shows a sequence of vertical sections through the largest of all the corrosion sites present on the sample and a large H_2 bubble can be seen within the droplet. Figure 4-3 (b) shows a horizontal section through Figure 4-3 (a) which reveals both metal and droplet, showing corrosion sites and a smaller H_2 bubble. Figure 4-3 (b) also shows that the top of the sample is not flat so the horizontal section does not include a full cross section of the sample surface: both metal and droplet can be seen. Large amounts of H_2 are present in this droplet after 120 minutes shown as a large bubble. This appears to differ from the situation of many bubbles shown at 70 minutes in Figure 4-2. However, a radiograph shows a 2D image through the entire sample, displaying all bubbles on top of the pin in one image, unlike the tomogram which shows one 2D section. H_2 may also have left the droplet or combined further expanding the central bubble shown in Figure 4-3 (a). Figure 4 (c) and (d) show enlargements of sections shown in (b) in which corrosion sites are labelled A-E. The evolution of these sites is described in detail below.

4.2.2 Initiation and Growth
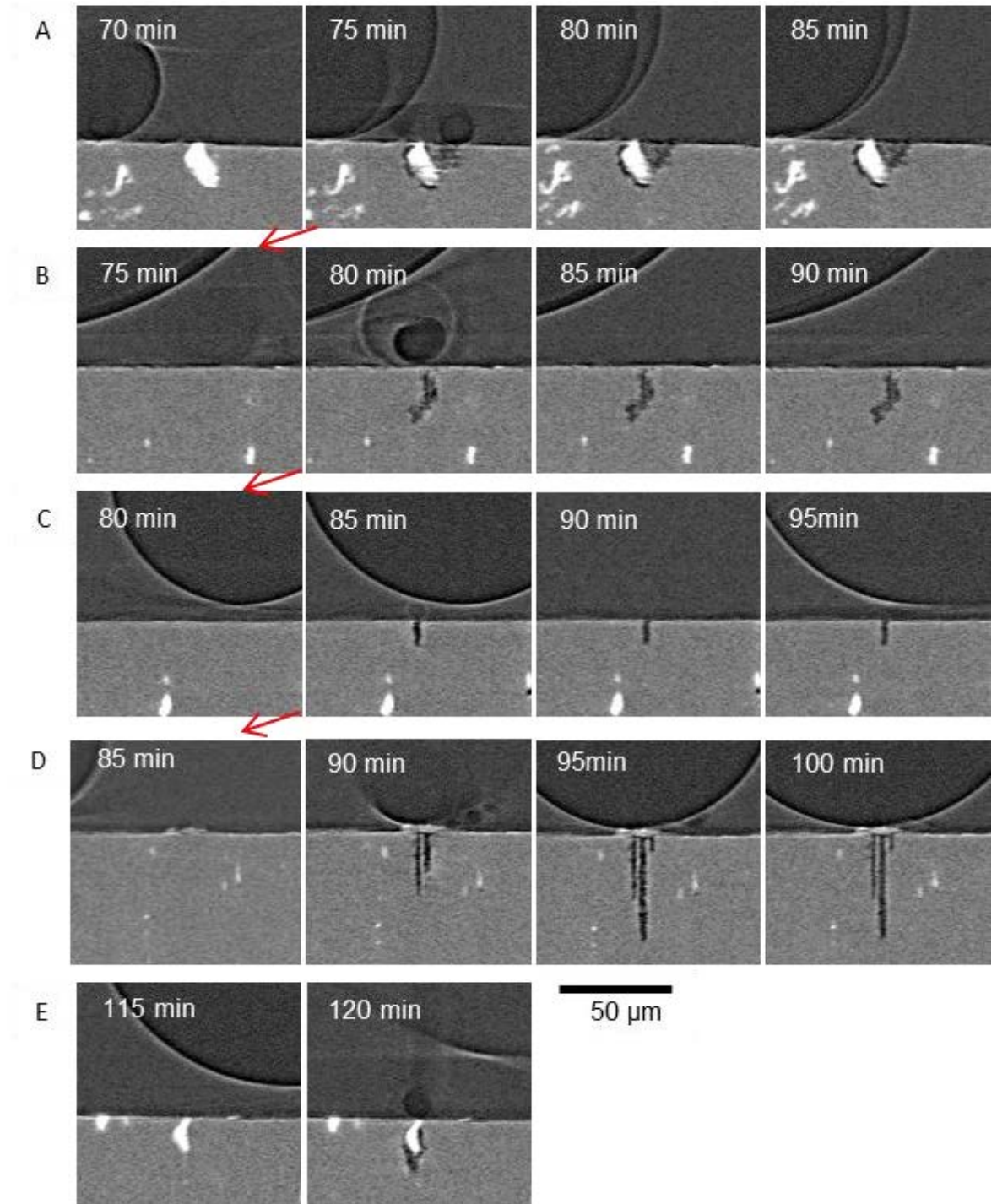
Figure 4-4 – A series of tomograms taken during a synchrotron experiment showing the evolution of corrosion sites from Figure 4-3 on a 1 mm diameter AA2024-T3 pin exposed to a 0.2 µL droplet of NaCl giving a CDD of ~ 5400 µg/cm^2 at a temperature of 22 ± 2 ^{o}C (shown in Table 3-4). Corrosion sites are shown in rows A-E, and present growth of an individual corrosion site. For each site, the second image in the series shows the sites initiation. Red arrows indicate that the sites initiated sequentially at 5 minutes.

Figure 4-4 contains a series of tomograms from the NaCl sample showing the growth of each of the sites identified in Figure 4-3 . Each row in Figure 4-4 shows individual corrosion sites on the same sample. The time increments of the 5 minute scans permit both the initiation and growth of corrosion to be captured. It can be seen that the sites initiate sequentially, with A starting at 75 minutes, B at 80 minutes, C at 85 minutes and D at 90 minutes. Site D grows until 115 minutes, whereupon E is then seen to initiate at 120 minutes. In each case, the second image in the sequence shows the first sign of corrosion. The first image shows the initiation site prior to the development of corrosion. In all cases a H_2 bubble accompanies each corrosion site. The third image in each sequence shows that each site ceases to grow at the same point in time and the bubble present at initiation leaves the surface of the site although the large bubble remains on site D. Only site D continues to grow after the first signs of corrosion.
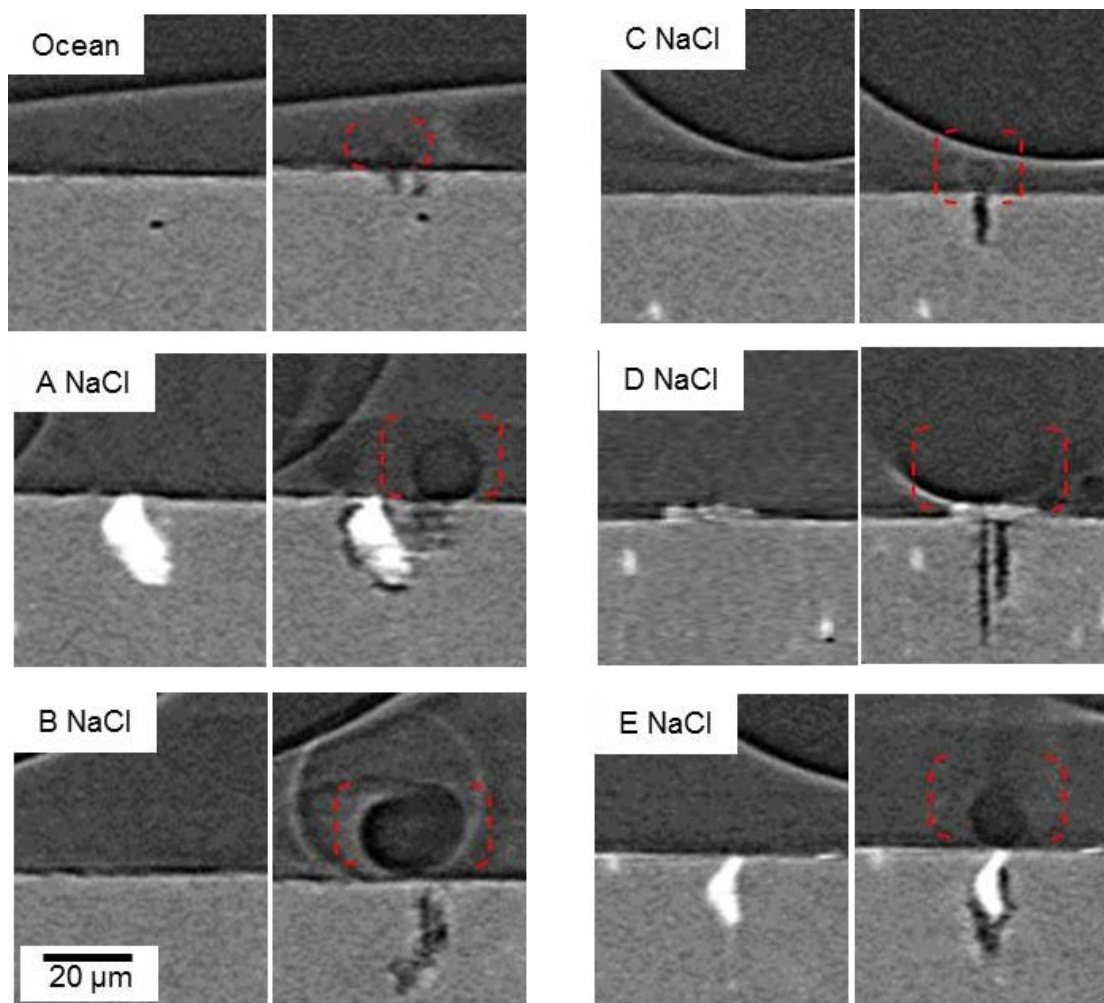
Figure 4-5 - A series of tomograms taken during a synchrotron experiment showing the evolution of corrosion on a 1 mm diameter AA2024-T3 pin. A-E were exposed to a 0.2 μL droplet of NaCl Figure 4-2, giving a CDD of ~ 5400 g/cm^2 (shown in Table 3-4). 'Ocean' shows (site from Figure 4-1) a 0.2 μL droplet of ASTM standard (D 1141 – 98) ASTM ocean water without the addition of NaF, giving a CDD of ~ 1400 μg/cm^2. Samples were exposed at a temperature of 22 ± 2°C. Vertical sections of all individual sites taken from the same sample at 120 minutes.

Figure 4-5 shows the ASTM ocean water site from Figure 4-1 and five sites A-E

from the NaCl sample shown in Figure 4-3. Each corrosion site is coupled with

the evolution of an H_2 bubble (highlighted by red dotted brackets). Sites A and E

show the initiation of corrosion at bright intermetallic particles. In the case of site

A and E a crevice can be seen around the intermetallic particles and extents out

into the metal matrix. Site D Initiates under a deposit on the surface which may

act as a crevice. Sites B, C and ASTM ocean water do not appear to have

initiated at any visible microstructural feature. However, it is worth noting that

the 0.74 μm pixel size will limit the visibility of any submicron heterogeneities in

the matrix.
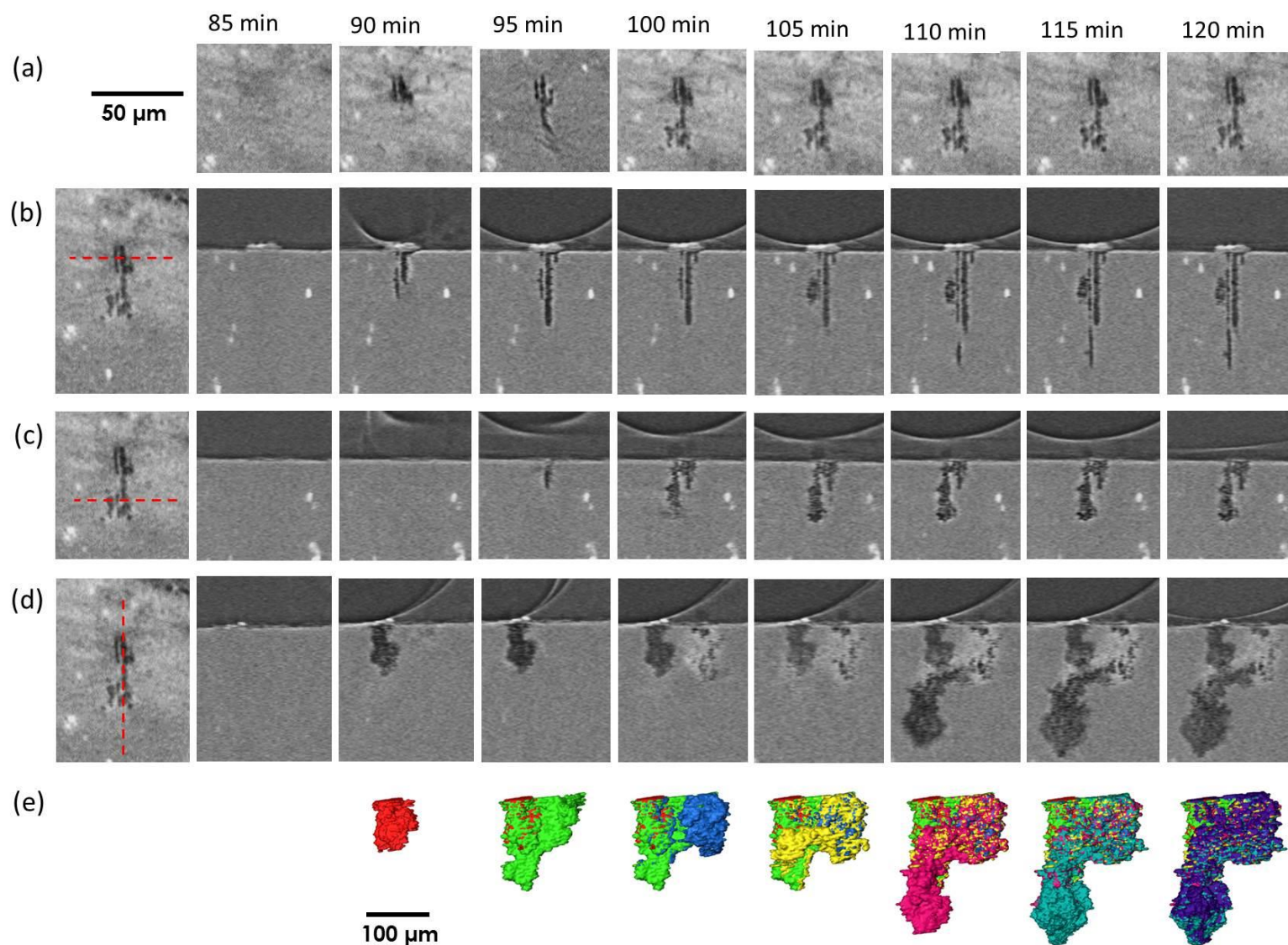
Figure 4-6 – Development of site D in Figure 4-4, showing the extended growth of the site at 5 minute intervals. (a) vertical sections of the corrosion site at time intervals shown. (b)–(d) show time series of horizontal sections at the location indicated in the first column by a dotted red line Row (e) shows volume renderings of site D (Figure 5). Each colour change reveals the addition of metal loss at each time interval.

Figure 4-6 shows a series of tomogram sections of site D from Figure 4-4 from the NaCl sample. The first column of images shows a horizontal section of the region at which corrosion originates. Each row (b)-(d) then shows the growth of each specific section in time. The final row shows a 3D rendering of D where the material loss in each sequential five-minute period is shown via the use of the addition of a different colour.
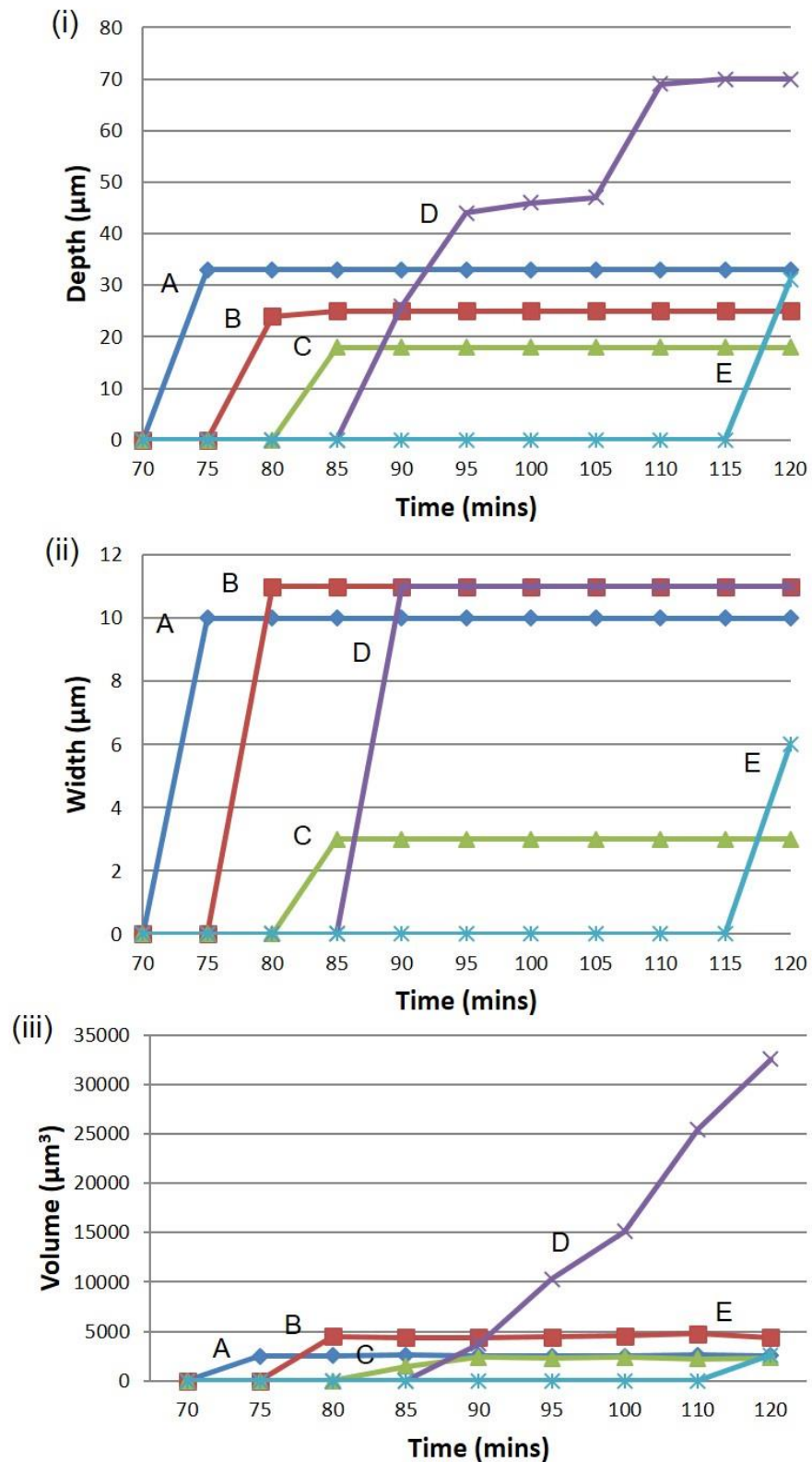
Figure 4-7 – A series of graphs showing how an individual corrosion site mouth widths, depths and volumes change with time. (a) – (e) correspond to the sites in Figure 4-4. (i) shows growth in depth against time, (ii) shows growth of width against time, and (iii) shows growth of volume against time.

Figure 4-7 illustrates the growth profile of individual sites on the NaCl sample first shown in Figure 4-3. Figure 4-7 (i) shows the evolution of depth in the longitudinal (L) direction for each individual corrosion site on the sample. The L direction is parallel to the rolling direction of the sample. Figure 4-8 (ii) shows how the width in the transverse (T) direction changes over time, and Figure 4-8 (iii) shows the increase in volume of each site in μm^3, measured using Avizo FEI. Each corrosion site is labelled A to E, as in Figure 4-3. The sites appear to grow sequentially: when a new site is established, the previous one stops growing in depth, width and volume.

4.2.3 Current Density
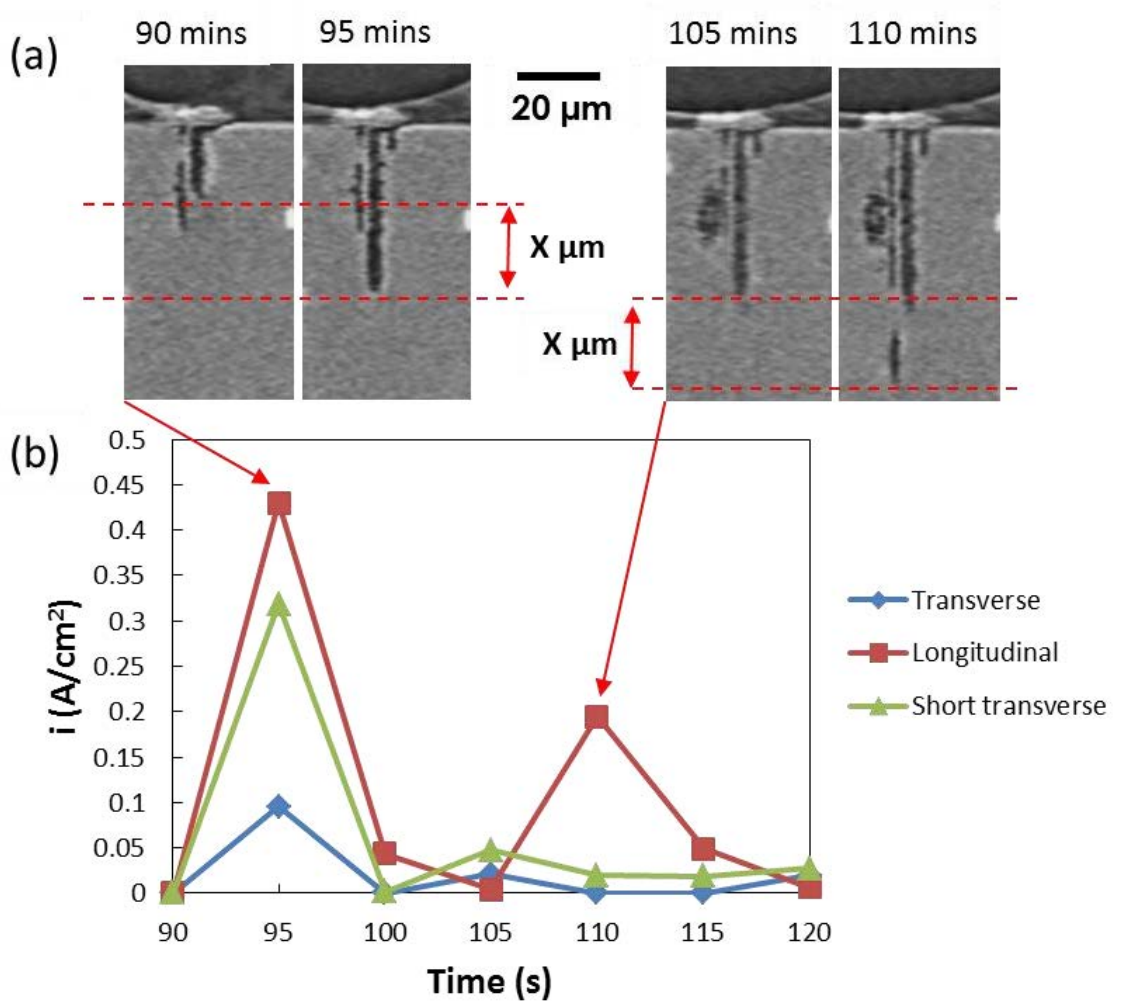
Figure 4-8 - A graph and schematic showing the current density of site D shown in Figure 4-3, Figure 4-4 and Figure 4-5 as it grows in time and how measurements were made. (a) shows how measurements in the longitudinal (L) directions were made (b) shows the current density generated from these measurements.

Figure 4-8 shows the largest corrosion site (D) observed under the NaCl droplet. Growth in each direction, longitudinally (L), short transverse (ST) and transverse (T), was measured using Fiji in each scan. (a) shows the total increase in depth (L), thickness of the site (T) and length (ST) throughout the experiment. The difference in growth of the site between scans can be

quantified to give a growth rate in different directions. This directional growth was then used to calculate an average current density which is presented in (b).

Equation 4-1 has been used to estimate the average current density of the largest corrosion site on the NaCl sample found in Figure 4-6, where n is the number of electrons generated by the corrosion process (aluminium oxidation state); $n = 3$, F is Faradays constant; $F = 96484$ C mol^{-1}, ρ is density of aluminium; $\rho = 2.7$ g/cm^3, M is the molar mass of aluminium; $M = 26.962$ g, Δt is the difference in time derived from the time taken to perform a full tomogram; Δt = 300 s and Δh μm is the changing variable of distance measured with Fiji and and example in the L direction shown by X μm in Figure 4-8 (a).

$$i = \frac{nF\rho}{M} \times \frac{\Delta h}{\Delta t}$$ **Equation 4-1**

4.3 Discussion

4.3.1 Corrosion Initiation Sites

Initiation of corrosion can occur at intermetallic inclusions due the presence of a thinner and more conductive passive film [73, 86, 151]. Furthermore intermetallic inclusions are usually cathodic in comparison to the metal matrix, resulting in the formation of a galvanic couple which promotes initiation in these regions [1, 15, 183]. The need for intermetallic particles in the role of initiation sites, however, is not always necessary. Oxide films are not uniform and pre-existing crystallographic flaws can also result in initiation. These flaws cause a tunnelling effect in the presence on Cl⁻, whereby Cl⁻ is adsorbed into these small regions where an autocatalytic development of corrosion sites is created. Regions become acidified due to the local accumulation of hydrolysing Al^{3+} [186]. Observations of nanoscale voids as nucleation sites for corrosion in aqueous and Cl⁻ solutions show similar autocatalytic processes as crystallographic flaws [184].

From Figure 4-4, it can be seen that early time growth after initiation is fast. A new site can be seen within the five-minute time interval, between which each new scan was taken.

Figure 4-5 shows the five sites that have initiated on the NaCl sample and the single site from the ocean water. One site (site NaCl D) initiated at a deposit on the surface. Initiation here would be expected as a crevice will also be created [75, 76].

On the NaCl sample two sites have initiated at intermetallic particles. This is to be expected if the particles are S phase as they are more cathodically active, however identification of which species of intermetallic particle is not possible using tomography. It can be hypothesised that de-alloying of Mg from these particles if they are S phase, will create a small crevice which reduce the rate that metal ions can escape within the site, resulting in a generation of H^+ by hydrolysis, which reduces the local pH. Due to the local cathodic particles, the potential for corrosion in these areas will increase, which in turn draws current and thus promotes corrosion [1, 2, 5, 15, 16, 183].

Two other sites have initiated where there is no clearly visible heterogeneity. This may, however, be due to the resolution limitation of tomography, as a site may initiate at an intermetallic particle that is < 1 μm in size, which will not be clearly visible *via* the tomography method used in this experiment with a resolution limit of 0.74 µm. Sites can initiate in nanoscale voids and flaws in the passive oxide film on aluminium [184, 186].

4.3.2 Metastable Pits

From Figure 4-4, it is clear that only one site grows at a time. Site A as shown in Figure 4-3 (c), formed at 75 minutes, and grows until site B forms at 80 minutes. This is a fast process which takes less than 5 mins. This process may occur due to the drawing of cathodic current to the one site [78, 134]. This is as expected since there are two stages of pitting: metastable and stable. Sites usually form sequentially during the metastable pitting stage, which has been seen from electrochemical measurements. A pit transitions to a 'stable' pit only if it can maintain the environment, where the amount of metal ions produced is

greater than metal ions lost. This will create an environment with a low pH promoting metal loss [75, 78, 80]. At this point the environment in one pit is aggressive enough to prevent re-passivation [1].

This transition from metastable, to stable pitting event is known as the critical pitting potential (E_{pit}) as suggested by Galvele [80]. Metastable and stable pitting measurements of AA2024-T3 suggest similar high current density upon initiation as calculated by Galvele, however lower current is measured once a pit sustains itself as stable. These observations indicate that the complexity of the pitting volume caused by the microstructure of AA2024-T3 combined with overpotentials ultimately determines if a pit becomes stable

Features such as these are shown during the initiation of sites in Figure 4-5. Pits are all seen to initiate paired with a H_2 bubble which then disappears. The indication of H_2 bubble upon initiation shows a burst of cathodic reaction to allow high current density to sustain a small pit. The loss of this bubble could in turn cause the site to re-passivate as ions are allowed to more easily diffuse from the site. The H_2 bubble or pit mouth obstruction such as a pit cover or surface deposit will act to reduce diffusion of ions from the active site. A stable pit was attained under a surface deposit as shown in Figure 4-6. An obstruction of the site mouth will interrupt diffusion of ions in and out of the pit [78]. A retention of H^+ will reduce of the internal pH required for a pit to stabilise without the prerequisite of having a high anodic current density [78].

4.3.3   Time Sequence of Corrosion Sites

The initiation of a pit will lead to a drop in open circuit potential as the corrosion

rate increases leading to individual sites developing one at a time [60].

Sequential pitting has been captured (Figure 4-3). As one pit is seen growing

and then dying, another starts and takes the cathodic current from the first, thus

causing the previously growing pit to die until site D (as seen in Figure 4-4) at

90 minutes establishes stable growth.

4.3.4   Stable Corrosion Site Growth

From Figure 4-6, the growth of the largest site is seen to be irregular and

random, with bursts of growth in varying directions with the most growth

occurring along the longitudinal orientation. The observation that longitudinal (L)

and long transverse (LT) growth rates are faster than that of the short

transverse (ST) orientation, agrees with previous tomographic work [20].

Growth similar to this can be seen in Figure 4-8, where corrosion current

density can be directly correlated to velocity.

Growth rates are highly dependent on crystallographic orientation. It has

previously been shown using XMT that the ST growth rates are the slowest

when compared to other metallographic orientations such as L and T. This is

due to mechanical processing [17, 19, 20, 98].

Figure 4-8 shows how 300 s resolved scans can been used to measure the

directional growth of the largest corrosion site, as seen in Figure 4-8. The fast

scanning method has allowed for estimates of current density to be derived.

The current densities have been calculated for the largest site, as seen in

Figure 4-3 site (d) the highest current density for this site was 0.44 A/cm^2. The data collection method averages the first and last radiographs to form the reconstructed data tomograms shown. The current density could therefore be higher, as growth during the scan may have taken in >300 s as tomograms reconstructions are averaged.

Higher current density has been recorded in 2D pits on high purity Al in the range of 18-30 A/cm^2 [4, 96, 187]. Galvele likewise states stable pits grow at approximately 10 A/cm^2 [75], but initiation of sites can occur at current densities as low as 0.1 A/cm^2 [78]. Metastable pitting is therefore seen occurring at lower currently densities than those generated by 2D depth measurements.

4.3.5 Cathodic Reaction and Beam Effects

Both of the droplets presented here contained gas bubbles, which are assumed to be H$_2$. H$_2$ evolution (**Equation 4-2**) is one of two cathodic reactions occurring during the corrosion of Al (the other is the O$_2$ reduction reaction). Once a site has been established *via* dissolution, it can grow, drawing cathodic current from all the active sites in the droplet, typically intermetallic particles [134]. The interfacial corrosion potential drops during the growth of a pit. This potential drop and drawing of current will generate more active sites and, in turn, generate more H$^+$, causing the pH to drop. This drop in potential and pH favours the evolution of H$_2$ [80, 188]. Despite O$_2$ reduction being the dominant cathodic reaction, the evolution of H$_2$ can be observed evolving upon initiation and has been imaged previously [4, 20]. H$_2$ evolution has been seen using electrochemical measurements under high potentials [4].
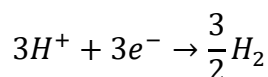
$$3H^+ + 3e^- \rightarrow \frac{3}{2}H_2 \qquad\qquad \textbf{Equation 4-2}$$

There is a difference in H_2 seen in the lab and *in situ* experiments. Although the time to first bubble for lab and in situ experiments under the same conditions was similar, the retention within the droplet and the volume of H_2 bubbles after this point differs, as seen in Figure 4-2. The lab sample still evolves H_2, but the bubbles in the lab are smaller and are released from the sample surface. In tomography samples, the bubbles are seen growing in proximity to corrosion sites, as seen in Figure 4-5, as well as growing to a larger size and remaining within the droplet. This difference may be caused by the X-rays, which are known to cause radiolysis of water and the formation of radiolysis products [168]. These can be oxidising agents and reducing agents such as H_2 that could help explain the presence of more H_2 within the droplet for these two experiments. Other radiolysis products include oxidising agents such as; HO_2, H^+, O_2, OH^- and H_2O_2 and reducing agents such as; H_2, H^{2-} and H^- [168-170]. Presence of these species are likely to accelerate corrosion processes and thus should be considered when assessing corrosion damage on the samples. It is likely these considerations imply that the hydrogen seen by XMT is greater than or equal to that resulting from **Equation 4-2.**

The volume (measured with Avizo FEI) of aluminium loss is then used to calculate the volume of hydrogen that could be produced, assuming hydrogen evolution is the only cathodic reaction. The volume of H_2 bubbles was calculated by measuring bubble diameter shown in Figure 4-9. As tomographic reconstructions are an average of 300s any fast-moving growth of H_2 can be shown as swirls. Measurements are taken from the largest diameter in tomograms. H_2 bubbles were assumed to be perfectly spherical.
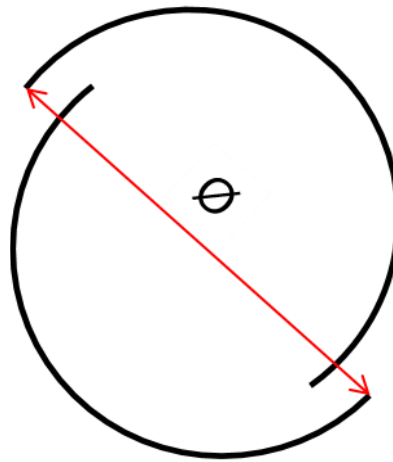
Figure 4-9 diameter measurements from an illustration of a growing bubble regularly seen in tomographic reconstructions used to calculate volume. The measurement made is highlighted by a red arrow.

(a)

Molar volume of Al = $V = \dfrac{M}{\rho}$

Molar volume of Al = $10 \ cm^3 \ mol^{-1}$

Molar volume of any gas at STP = $22400 \ cm^3$

$Al \rightarrow Al^{3+} + 3e^-$ 1.5:1
$3H^+ + 3e^- \rightarrow 3/2H_2$ H_2:Al
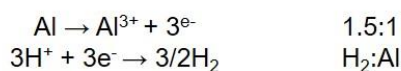
H_2/Al volume constant = $2240 \times 1.5 = 3360$

(b)
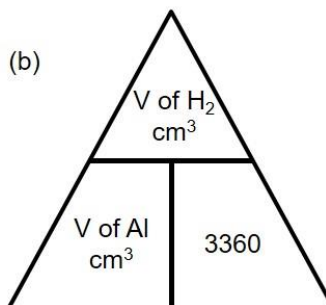
Figure 4-10 (a) shows the method used to calculate a volume constant using the molar volume of aluminium and of gas at standard temperature and pressure (STP). (b) shows a formula triangle demonstrating inputs of volumes of aluminium and H_2 measured to calculate theoretical values of volumes of Al and H_2 produced.

H_2 volume production and aluminium volume loss were calculated via a volume constant as shown in Figure 4-10 (a). The molar volume of Al is calculated; V = volume, M = atomic weight (27 g/mol) and ρ = density (2.7 g/cm^3) giving a volume of 10 cm^3/mol. This volume is divided by the molar volume of any gas at STP (22400cm^3) to give a value of 2240. This is then multiplied by the number of H_2 atoms generated by the dissolution of Al (which was found as every Al atom will produce 1.5 H_2 atoms) which equates to 3360. This volume constant is then used to convert either measured H_2 evolved upon initiation or aluminium volume loss measured as shown in Figure 4-10 (b) as a formula triangle, by

either dividing or multiplying this constant from measured values. To calculate

theoretical value of H_2 from volume loss measured. Aluminium volume is

multiplied by 3360. To calculate theoretical value of aluminium dissolved from a

H_2 bubble volume generated above the corroded site measured is then divided

by 3360.

Table 4-1 shows measured volumes of hydrogen and aluminium metal loss

from the sites highlighted in Figure 4-3. The volume of hydrogen measured from

bubbles are highlighted in Figure 4-5. It is shows that hydrogen evolution

directly evolved from the anodic sites is as low as 0.01% and as high as 3.4% of

the cathodic reaction taking place. Consideration of the effect of beam damage,

indicates that these figures must be regarded as upper limits in each case.

Table 4-1 – Measured aluminium and H_2 volume corrosion site and the % of O_2 reduction and H_2 evolution per site growth (values have been rounded to the nearest 100).

Corrosion site	Volume of Al loss observed (μm^2)	Volume of H_2 observed (μm^3)	% of cathodic O_2 reduction	% H_2 evolution
A	2500	1300	99.985	0.015
B	4500	4100	99.972	0.027
C	1500	200	99.997	0.003
D	15100	1731000	96.535	3.465
E	2600	900	99.990	0.010

4.4 Conclusions

X-ray micro tomography was used for the visualisation of corrosion of aluminium and has been achieved *in-situ*.

1. Corrosion sites seen initiating at intermetallic particles, surface deposits and no resolvable microstructure.

2. At any one time only one pit can be seen growing.

3. Initiation was observed to be associated with a H_2 bubble at the mouth of the corrosion pit.

4. Pit growth observed over successive scans shows only a part of the pit grows over time. Local growth is at a high rate corresponding to 0.44 A/cm^2.

5. H_2 was observed both prior to and during growth of pits. (Some of this H_2 could be contributed to x-ray interaction)

6. An estimate of the total amount of H_2 evolved was less than the amount that could be generated by the corrosion observed. A tiny fraction of the H_2 evolved, confirming O_2 reduction to be the major cathodic reaction occurring.

5. INVESTIGATIONS INTO THE CORROSION PRODUCTS FORMED UNDER ATMOSPHERIC CORROSION OF AA2024-T3

5.1 Introduction

Aluminium hydrates are expected to precipitate at pH 5 and below as the passive film of aluminium and its alloys becomes unstable and the production of Al^{3+} increases [67]. Corrosion products are consequently precipitated between anode and cathode as Al^{3+} migrate towards OH^- rich cathodic regions in order to maintain charge balance [189]. The corrosion products thought to commonly form on aluminium are Boehmite (γ-AlO(OH)) [118] Nordstrandite (Al(OH)$_3$) and Bayerite (β-Al(OH)$_3$) [105], due to the presence of elemental aluminium and oxygen identified by methods such as EDX. Despite this being a well-accepted process, the integration of other anions and cations found in atmospheric salts in corrosion products of aluminium is commonly over looked.

Analysis of corrosion products on a small scale, within corrosion sites has been carried out in the past. Corrosion products formed following exposure to atmospheric marine environments on AA1100 and AA6061, were analysed using EDX and chlorine and oxygen along with small amounts of sulphur were found within corrosion sites. FTIR confirmed these regions to be basic aluminium sulphate [12, 22, 24]. Anions from the atmosphere such as chloride and sulphates are therefore incorporated into corrosion products in corrosion sites in these instances. However, in all cases these investigations have not considered the distribution of corrosion precipitates in entire atmospheric droplets.

Other methods such as grazing incident X-ray diffraction (GIXRD) and FTIR on AA1050 exposed to NaCl have identified the corrosion product Dawsonite $(NaAlCO_3(OH)_2)$ on a larger scale in solution droplets. EDX mapping showed a distribution of Na within droplets where Dawsonite was precipitated. Dawsonite was confirmed using FTIR combined with knowledge of the location of Na from EDX measurements. The movement of Na^+ towards cathodic regions is shown to contribute to charge balance along with the well-established movement of Al^{3+} to these regions to form Dawsonite. The role of corrosion products were shown to hinder corrosion rates due to the movement of Na^+ ions [108].

Different atmospheric environments have been shown to affect the composition of corrosion products formed. However, little work has been done on how the migration of different ions species in these environments governs the composition of corrosion products precipitated under a corroding OW droplets. The focus of this chapter is to identify and develop a better understanding of the corrosion products and their formation in relation to anodic and cathodic regions as they are formed during atmospheric corrosion. NaCl and ASTM ocean water atmospheric droplets will be used analysed the effect that their constituent ions have on corrosion and whether they are incorporated into corrosion products formed. The distribution of precipitates within a corroded droplet will be analysed using various methods, including droplet mapping, EDX, XRD and FTIR.

5.2 Results

5.2.1 NaCl and ASTM Ocean Water Droplet Chemistry
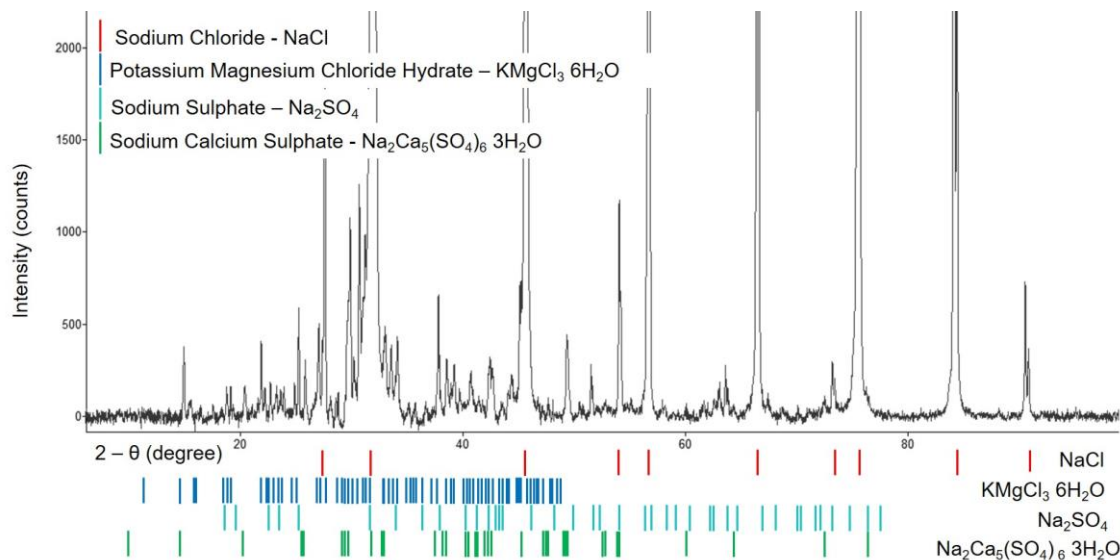
Figure 5-1 An XRD pattern of ASTM ocean water salts after drying (protocol shown in section 3.4.5). Coloured bars indicate dominant peaks of compounds cystals formed following drying. Database used for analysis of salt cystals – ICDD PDF2 [181].

Figure 5-1 shows an XRD pattern of ASTM ocean water salt solution after drying in an 80 °C oven (shown in section 3.4.5). The dominant peaks are from sodium chloride (NaCl). The second strongest peaks are from potassium magnesium chloride hydrate ($KMgCl_3$ $6H_2O$), third sodium sulphate (Na_2SO_4) and finally sodium calcium sulphate ($Na_2Ca_5(SO_4)_6$ $3H_2O$). It is to be noted sodium sulphate can form in both anyhydrous and decahydrate forms. However which form was not specified by the data base used.
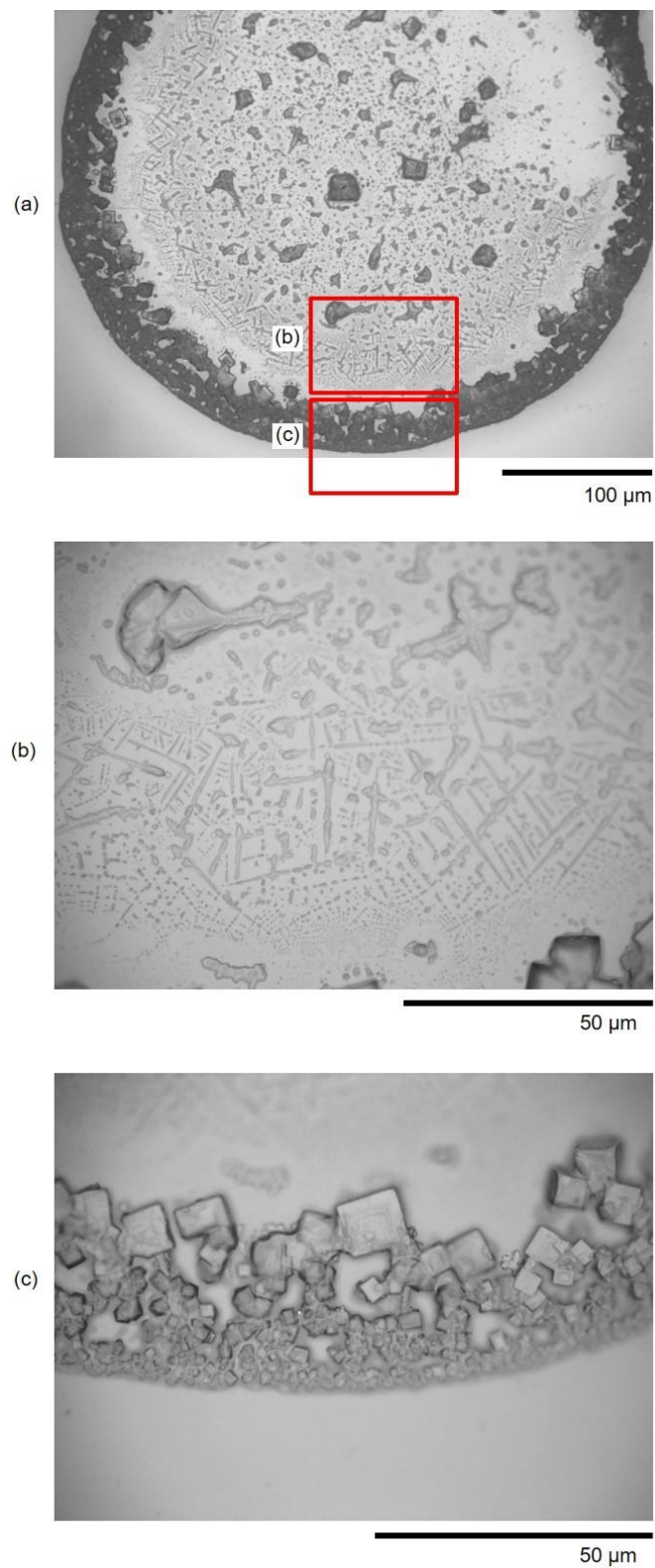
Figure 5-2 A 2.00 ± 0.04 µL ASTM ocean water droplet dried on a glass slide at 3 ± 3% RH at room temperature 22 ± 3 °C. (a), (b) and (c) show different length scales of salt crystals distributed within the dried droplet.

Figure 5-2 shows a typical example taken from a six droplet array 2.00 ±

0.04 µL ASTM ocean water droplet on a glass slide. The droplet has been dried

at room temperature 22 ± 3 °C. Image (a) shows a large region of the droplet.

Regions of different crystal shapes and types can be seen. Image (b) shows the

middle of the dried droplet where sharp and elongated dendritic shaped crystals

increasing in size from the edge towards the centre can be seen. Image (c)

shows the edge of the droplet region where cubic crystals can be seen.

Figure 5-3 shows a typical example taken from a six-droplet array of the dried

droplet shown in Figure 5-2. (a) shows an optical image of the dried droplet

followed images for three spectroscopic regions labelled, 'Region 1', 'Region 2'

and 'Region 3'. The three regions shown maps gathered by Raman PCA

analysis (shown in section 3.4.1.3). The spectra from those regions with pixels

with grey scale values above a 250 threshold are then summed and averaged.

The average Raman spectrum from each region plotted is shown in (b). In the

graphs plotted in Figure 5-3 (b), Region 1 Averaged shows a sharp peak at

995 cm^{-1} along with a broader feature between 1050 - 1200 cm^{-1}, which

contains a second sharp peak at 1110 cm$^{-1.}$ These peaks are primarily found at

the edge of the dried droplet. Region 2 Averaged shows a lower intensity peak

at 995cm^{-1} and a strong peak at 1050 cm^{-1}. These peaks are primarily found at

the edge and middle of the dried droplet. The broad peak from 1050 - 1200 cm^{-1}

in Region 1 Averaged is shown again but at higher intensity. Region 3 Averaged

shows the broad peak seen in both previous averaged spectrum in the range

1050 - 1200 cm^{-1} with the highest intensity peak at 1110 cm^{-1} without any

additional peaks. These peaks are primarily found in the middle and outside of the dried droplet.

(a)

Dried Ocean Water Droplet

Region 1

Region 2

Region 3

(b)

Region 1 Averaged

Region 2 Averaged

Region 3 Averaged

Intensity

Raman Shift (cm^{-1})
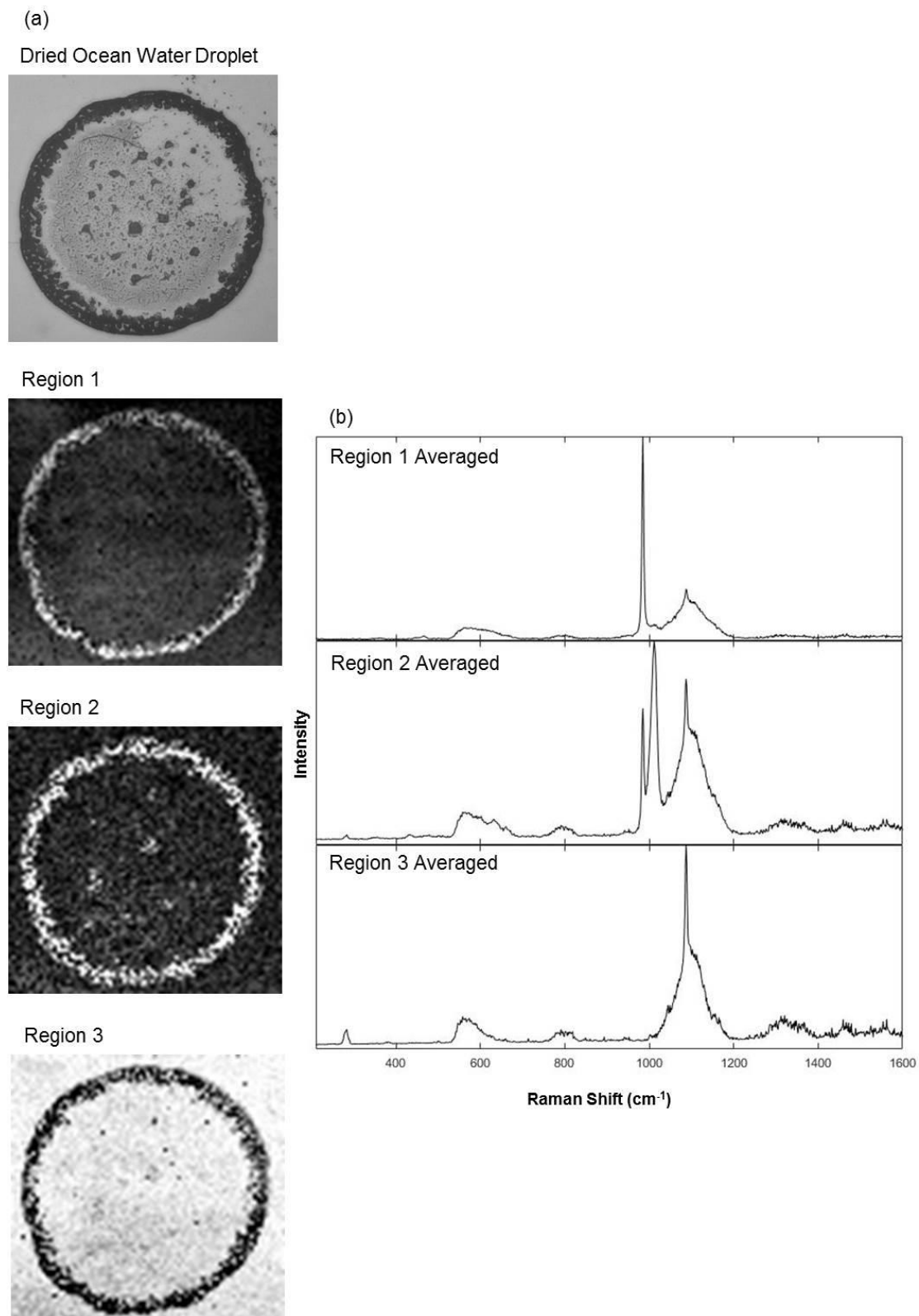
Figure 5-3 A series of images of data from sample shown in Figure 5-2. (a) shows an optical image of the dried salt droplet followed intensity maps generated by PCA (shown in section 3.4.1.3). (b) shows a plot of the average (via method in section 3.4.1.6) data of Raman spectra from regions above a 250 grey scale threshold shown in (a).

102
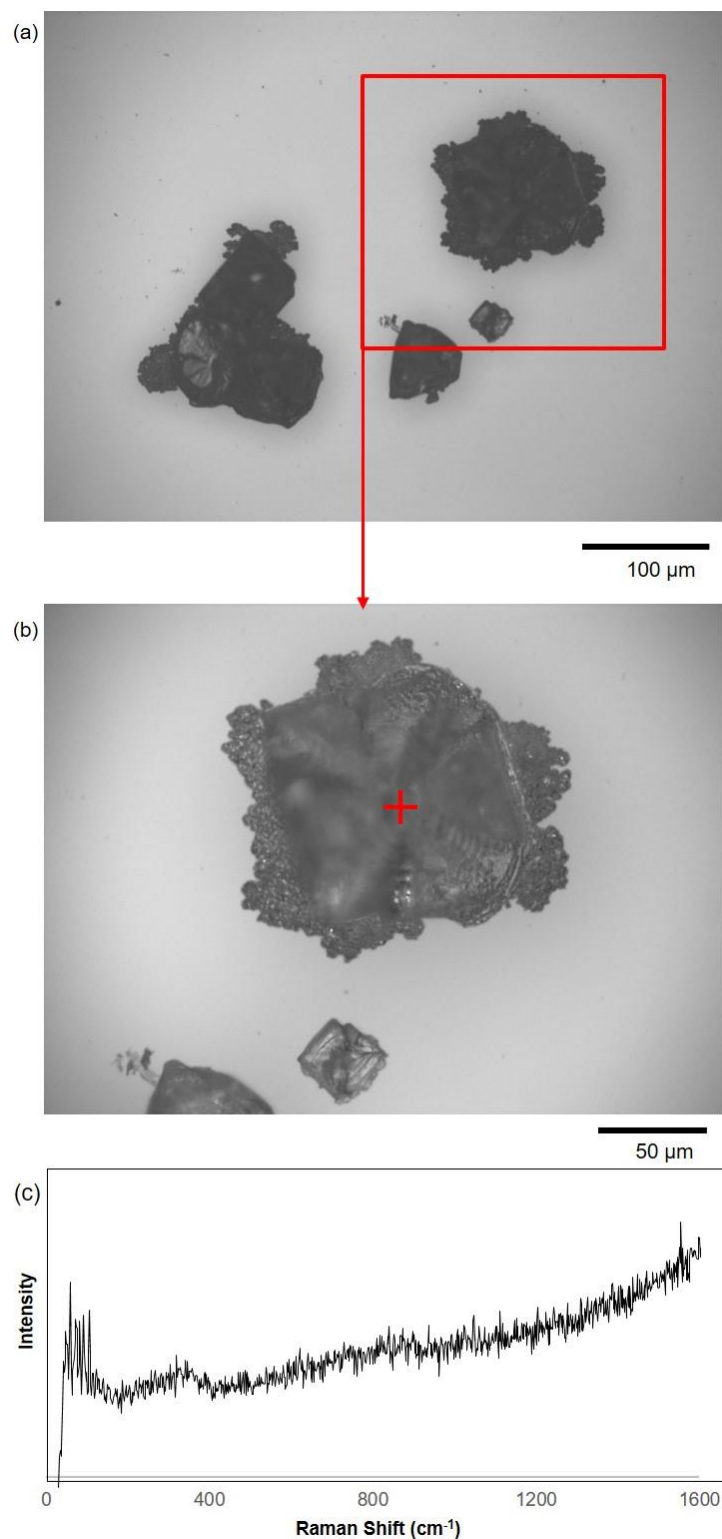
Figure 5-4 Shows the precipitates from a 2.00 ± 0.04 µL 1M NaCl droplet on a glass slide after being dried at 3 ± 3% RH at room temperature 22 ± 3 ℃. (a) and (b) different length scales of salt crystals distributed within the dried droplet. A red cross indicates the region at which a Raman spectrum was collected. (c) shows the Raman spectrum gathered from the point measurement shown in (b).

Figure 5-4 shows a typical example taken from a six-droplet array of 2.00 ±
0.04 µL NaCl droplets on a glass slide after being dried at 3 ± 3% RH at room
temperature 22 ± 3 °C. Figure 5-4 (a) and (b) show images of salt crystals over
different length scales within the dried droplet. Figure 5-4 image (a) shows the
distribution of the NaCl salt crystals as the droplet has dried. Figure 5-4 (b)
shows a magnified image of the main bulk of salt formed by drying the droplet.
Figure 5-4 (c) shows a Raman point measurement taken from the cross
highlighted in (b) on a dried crystal. The baseline of the Raman spectrum is
shown to slightly increase. However, no significant peaks are seen.

Data collected of dried salts is to be used as standards when mapping Raman
data of atmospheric droplets, to ensure peaks of corrosion products are not
mistaken for dried salts. Additional standards have either been measured or
collected from the RRUFF database and are shown in Appendix 2 in Figure 9-4
and Figure 9-3.

5.2.2 Observations of Corrosion on AA2024-T3
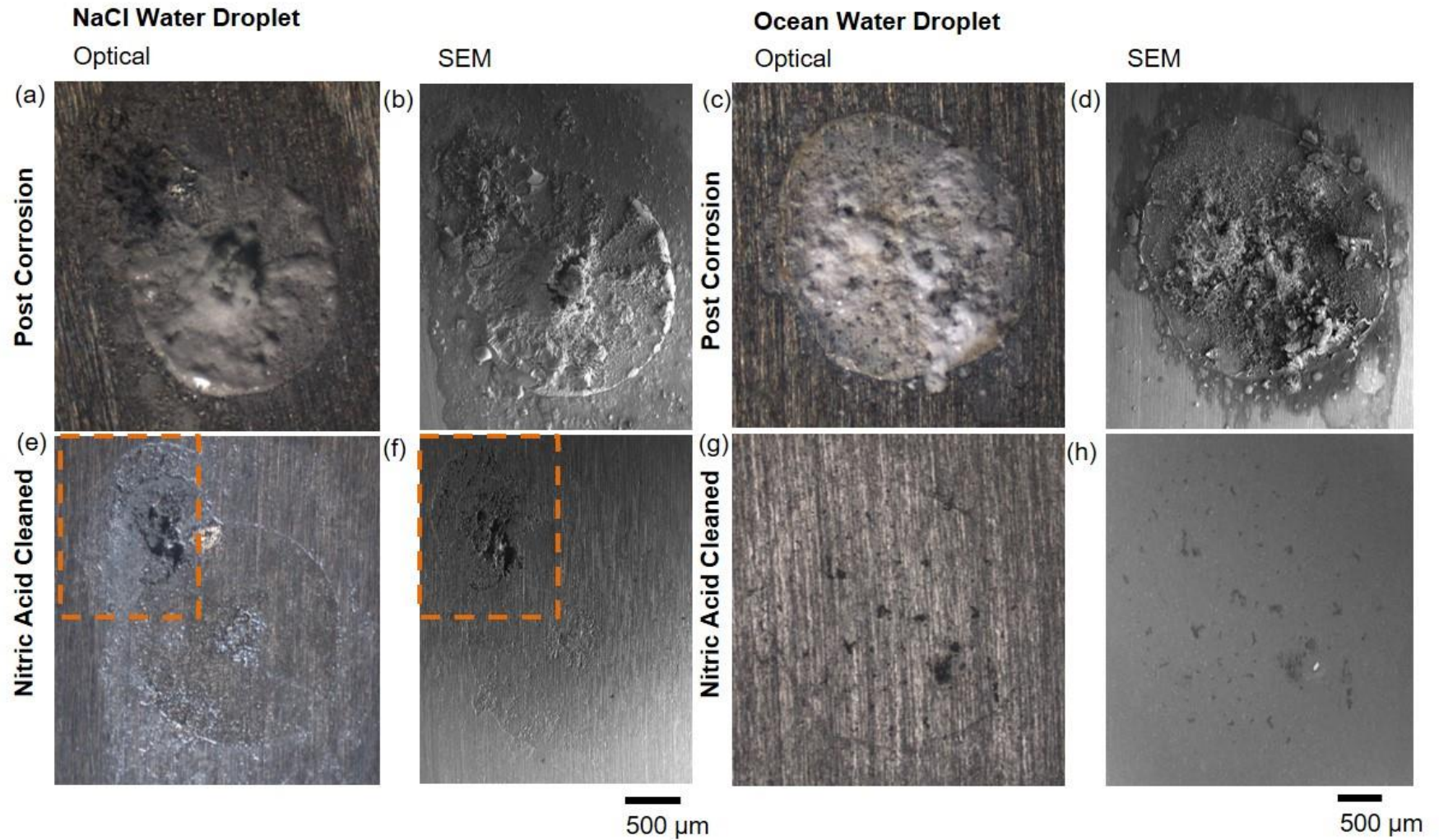
Figure 5-5 a series of micrographs of corroded 2.00 ± 0.04 µL , 1000 µg/cm^2 CDD NaCl and 430 µg/cm^2 CDD ASTM ocean water droplets on AA2024-T3 corroded at 85 ± 3% RH and at 30 ± 1 °C for 4 weeks (shown in Table 3-8). Microscope images (a) and (c). An optical microscope images following immersion nitric acid (following protocol in 3.4.3) (e) and (g). SEM images after exposure (b) and (d), and SEM images of each sample immersion in 70% nitric acid (f) and (h) NaCl. SEM using secondary electron and ASTM ocean water using back scatter to image the sample. The largest NaCl droplet corrosion site is highlighted with an orange box.

Figure 5-5 shows representative droplets of the sample set of 9 measured of a 1000 μg/cm^2 CDD NaCl and a 430 μg/cm^2 CDD ASTM ocean water droplet corroded at 85 ± 3% RH and at 30 ± 1 °C for 4 weeks. The image presents preliminary observations of samples both optically and by SEM before and after cleaning in 70% nitric acid. A corrosion site on the NaCl droplet is seen in top left corner, highlighted with an orange box. This is the dark region of the unwashed sample and is made clearer after nitric acid cleaning. Corrosion sites under the ASTM ocean water droplet occurs scattered at various locations within the droplets original footprint.

5.2.3 Visualisation of Corrosion and Corrosion Products on AA2024-T3
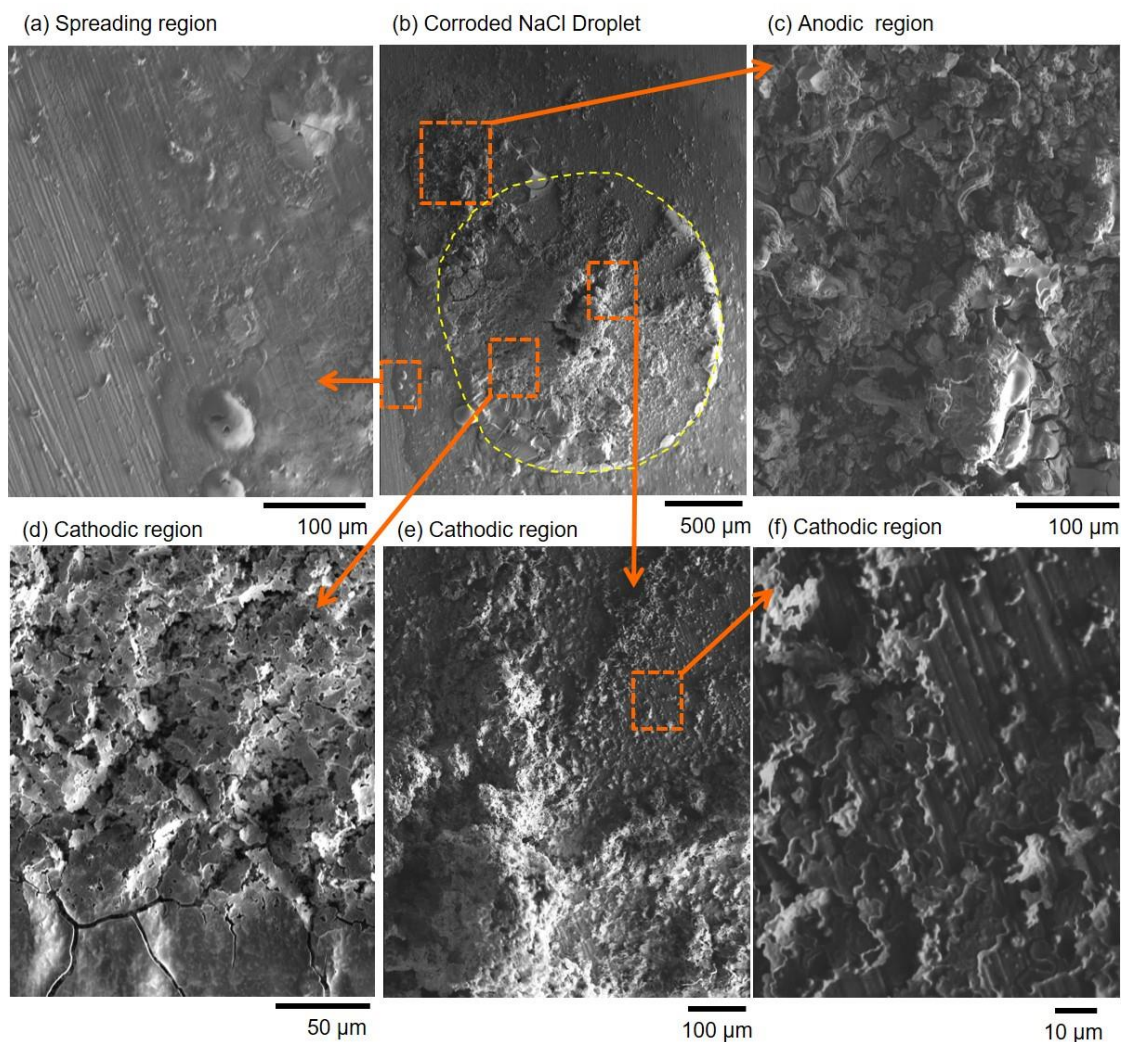
Figure 5-6 shows a series of SEM images using secondary electrons to view a 2.00 ± 0.04 μL, 1000 μg/cm² CDD NaCl droplets on AA2024-T3 shown in Figure 5-5, corroded at 85 ± 3% RH and at 30 ± 1 °C (shown in Table 3-8). The corroded droplet has been rinsed and dried following protocol in section 3.4.3. Orange boxes outline different regions including, (a) the droplet spreading region, the original footprint of the deposited droplet is shown with a dotted yellow line in (b), and corrosion products (c-f) at various length scales.

Figure 5-6 shows a series of SEM images at different length scales of the NaCl droplet shown in Figure 5-5. SEM images were taken following Raman mapping scans to ensure there is no carbon contamination. The corrosion products can be seen on the surface of the bulk material in (c), (d), (e) and (f). Regions of interest can be seen on different length scales and are highlighted by orange boxes. The original droplet area is highlighted by a yellow dotted line in image

(b). (c) shows that the corrosion products are coarse, and non-uniform in appearance. The region labelled as the spreading region (a), shows a thin smooth uniform layer of corrosion product outside the original boundary where the droplet was deposited. Spreading is defined as the area outside the original perimeter of the droplet where corrosion processes have occurred before the droplet was dried. Three other regions of corrosion products are highlighted (e-f) in the main body of the originally deposited droplet. Corrosion products are seen to vary in height and thickness. (d) shows corrosion products that have formed a dry connected bulk, but break into angular subdivisions as thickness reduces. (e) and (f) show similar thick corrosion product material along a thin spreading of the same angular like particles as seen in (e).

(a) Edge of droplet   (b) Corroded NaCl Droplet   (c) Cathodic region

(d) Anodic region   50 µm   (e) Anodic region   500 µm   (f) Anodic region region   100 µm

200 µm   100 µm   50 µm
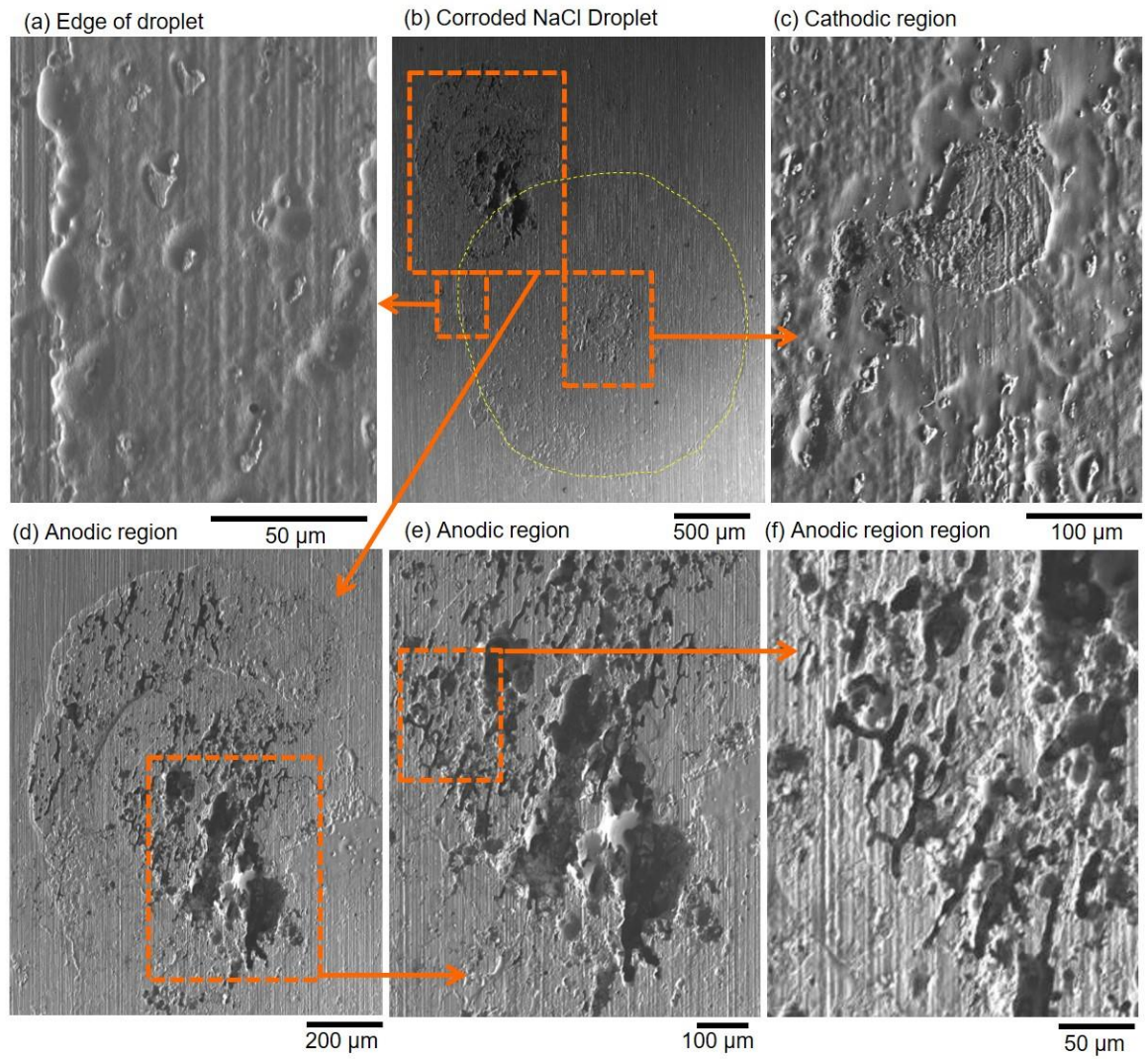
Figure 5-7 shows a series of SEM images using secondary electrons to view the A 1000 µg/cm^2 CDD NaCl droplet corroded on AA2024-T3 at 85 ± 3% RH and at 30 ± 1 °C 4 weeks (shown in Table 3-8) of Figure 5-6 after immersion in nitric acid following protocol in section 3.4.3. Orange boxes outline different regions including the (a) edge region, (b) The original footprint of the deposited droplet shown with a dotted yellow line (c) the middle of the droplet and (d-f) the corroded region at different length scales.

Figure 5-7 shows the surface morphology of the NaCl droplet from Figure 5-5 after being immersed in nitric acid. The entire droplet highlighted by a yellow dotted line can be seen in (b) and regions of interest are highlighted by orange boxes. Image (a) shows the edge of the spreading region. A height change at the edge of this area can be seen along with elevated particles, expected to be intermetallic particles, where uniform dissolution of the metal has occurred under the droplet. Image (c) shows the middle of the droplet. A reduction in surface height and intermetallic particles are seen on the matrix surface. Images (d – f) show the corroded region in different length scales intersecting the main body and outside of the original droplet. Wide corrosions sites 110 μm across at their widest section are seen alongside small thin corrosion sites 5 μm in width are observed.
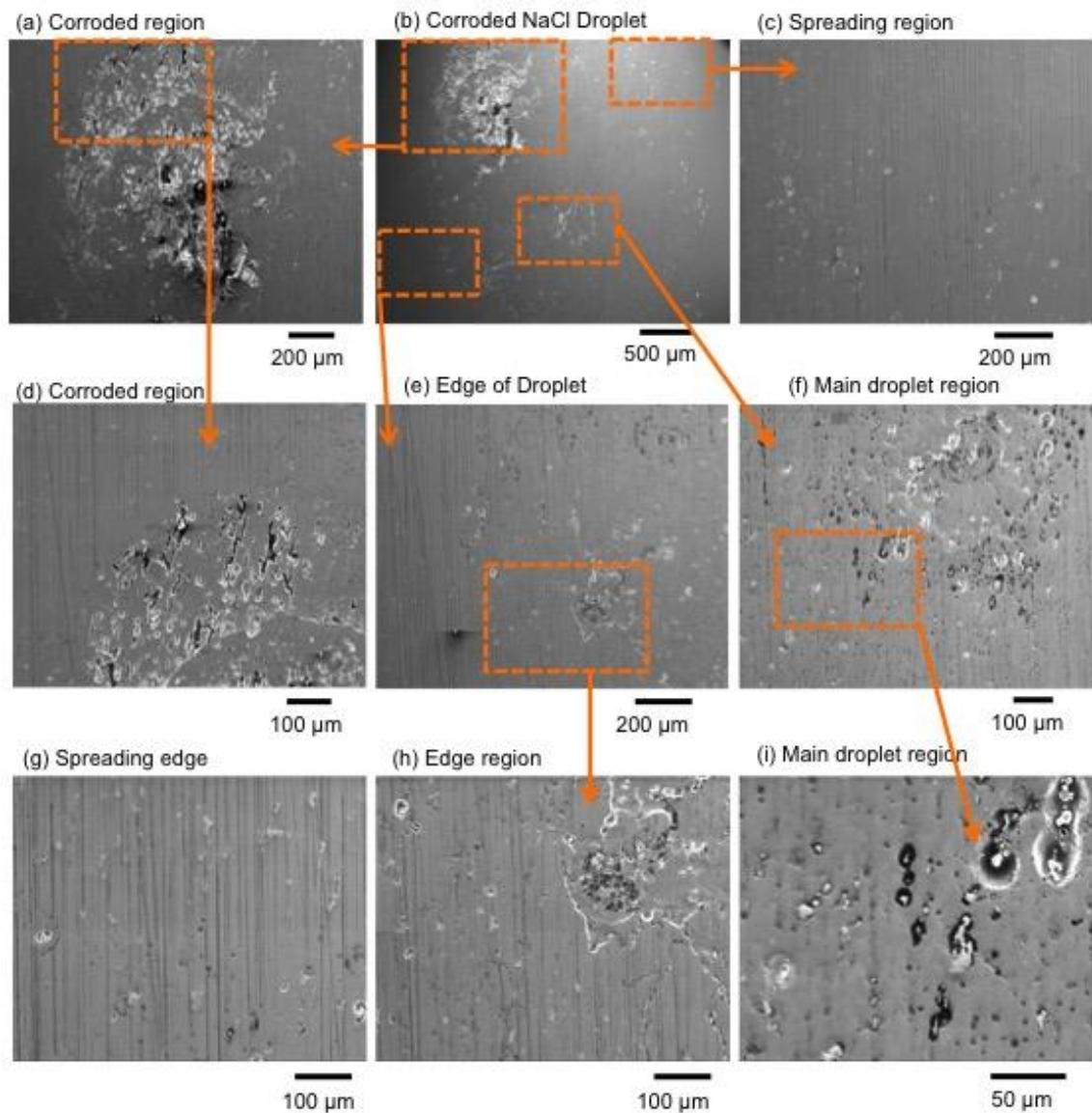
Figure 5-8 shows a series of SEM images using secondary electrons to view of experimental droplet from Figure 5-6 and Figure 5-7. A 1000 µg/cm^2 CDD NaCl droplet corroded on AA2024-T3 at 85 ± 3% RH and at 30 ± 1 ^{o}C 4 weeks (shown in Table 3-8) after minutes of immersion in nitric acid and following polishing with OP-S and water (procedure shown in section 3.4.3). Orange boxes outline different regions including the edge region (e), corroded regions (a, b, d) and the cathodic region at various length scales (c, e, f, g, h, i).

Figure 5-8 shows a series of SEM images of NaCl droplets which have been corroded at 85 ± 3% RH and at 30 ± 1 °C for 4 weeks after immersion nitric acid and polishing with OP-S and water. The polishing was done to reveal a clearer view of features such as cathodic grooving. Figure 5-8 (b) shows the entire NaCl droplet post polishing. Regions of interest are highlighted using orange boxes. (c) and (g) shows the area at which the spreading region stops. (a) and (d) show regions where corrosion sites can be seen. (e) and (h) shows the edge of the droplet where a change in the surface height can be observed. The inside of the droplet being lower suggests uniform dissolution of the metal. (f) and (i) show the main body of the droplet where grooving around intermetallic particles can be seen.

(a) Spreading region (b) Corroded Ocean Droplet (c) Cathodic region

(d) Cathodic and anodic region 100 µm (e) Anodic region 500 µm (f) Edge region

50 µm 10 µm 20 µm

10 µm
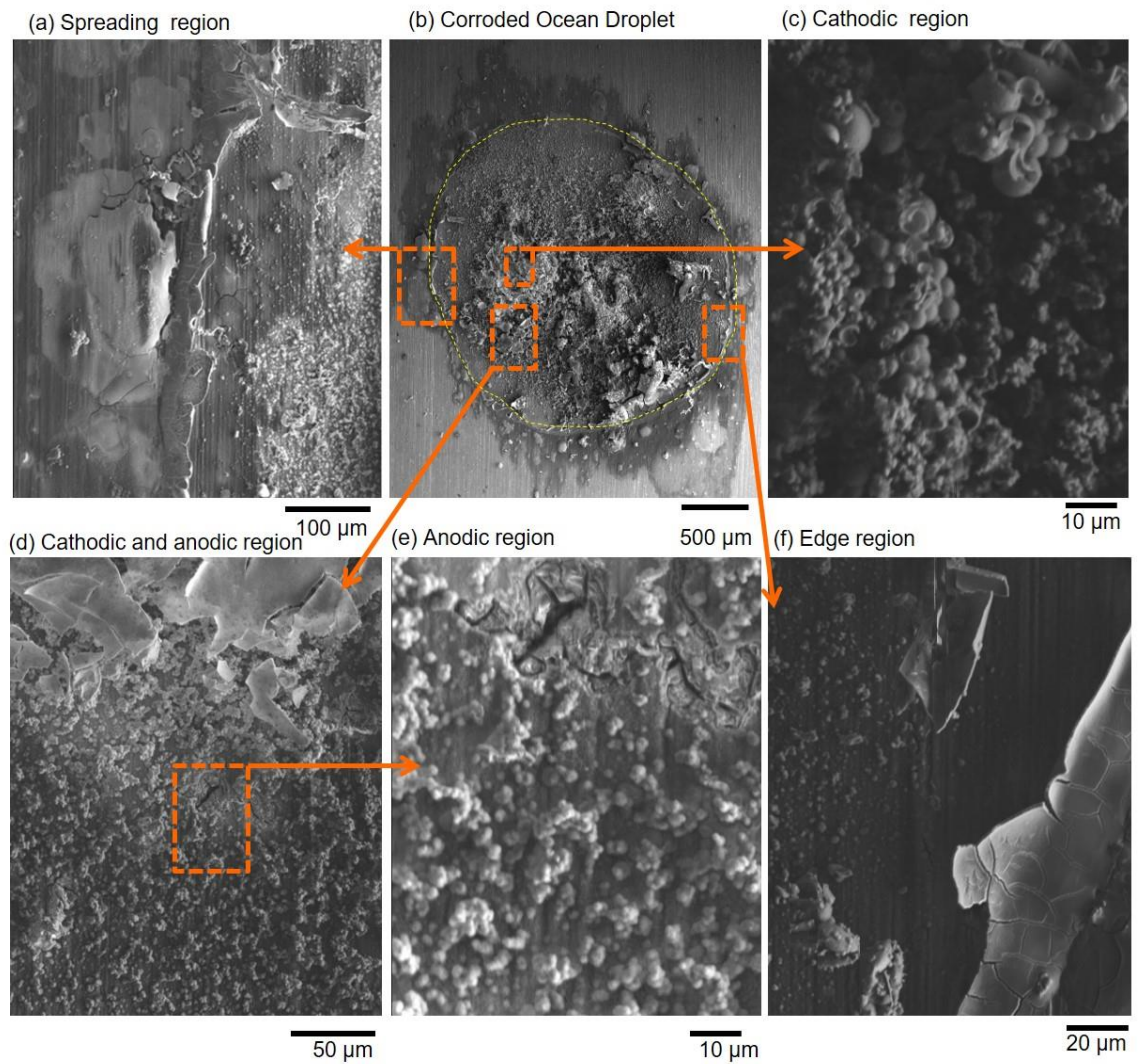
Figure 5-9 a series of SEM images using secondary electrons to view a 430 µg/cm^2 CDD ASTM ocean water droplet as shown in Figure 5-5 on AA2024-T3 at 85 ± 3% RH and at 30 ± 1 $^{\circ}$C for 4 weeks (shown in Table 3-8). The droplets have been rinsed and dried using methanol. Orange boxes out line different regions including (a) the spreading region, (b) the corroded droplet region shown with a dotted yellow line, (c-e) the corrosion products at various length scales and (f) the droplet edge.

Figure 5-9 shows a SEM images of the ASTM ocean water droplet which was introduced in Figure 5-5. Image (b) shows the main body of the droplet. Regions of interest are highlighted with orange boxes. A yellow dotted line outlines the original perimeter of the deposited droplet. Figure 5-9 (a) shows the edge of the spreading region where a thin layer of uniform dried corrosion product can be observed. Image (c) shows a highly magnified image of corrosion products in the middle of the droplet. The corrosion products are smooth and spherical. Images (d –f) display the main body of the originally deposited droplet, there is a variety of thickness in corrosion products, moreover a corrosion sites can be observed. Corrosion products have varying textures, from smooth and flat bulk like morphologies (d), to smooth and spherical (e), as well as flat structures at the edge of the droplet as seen in (f).

(a) Edge region (b) Corroded Ocean Droplet (c) Anodic region (d) Anodic region (e) Anodic region (f) Anodic region
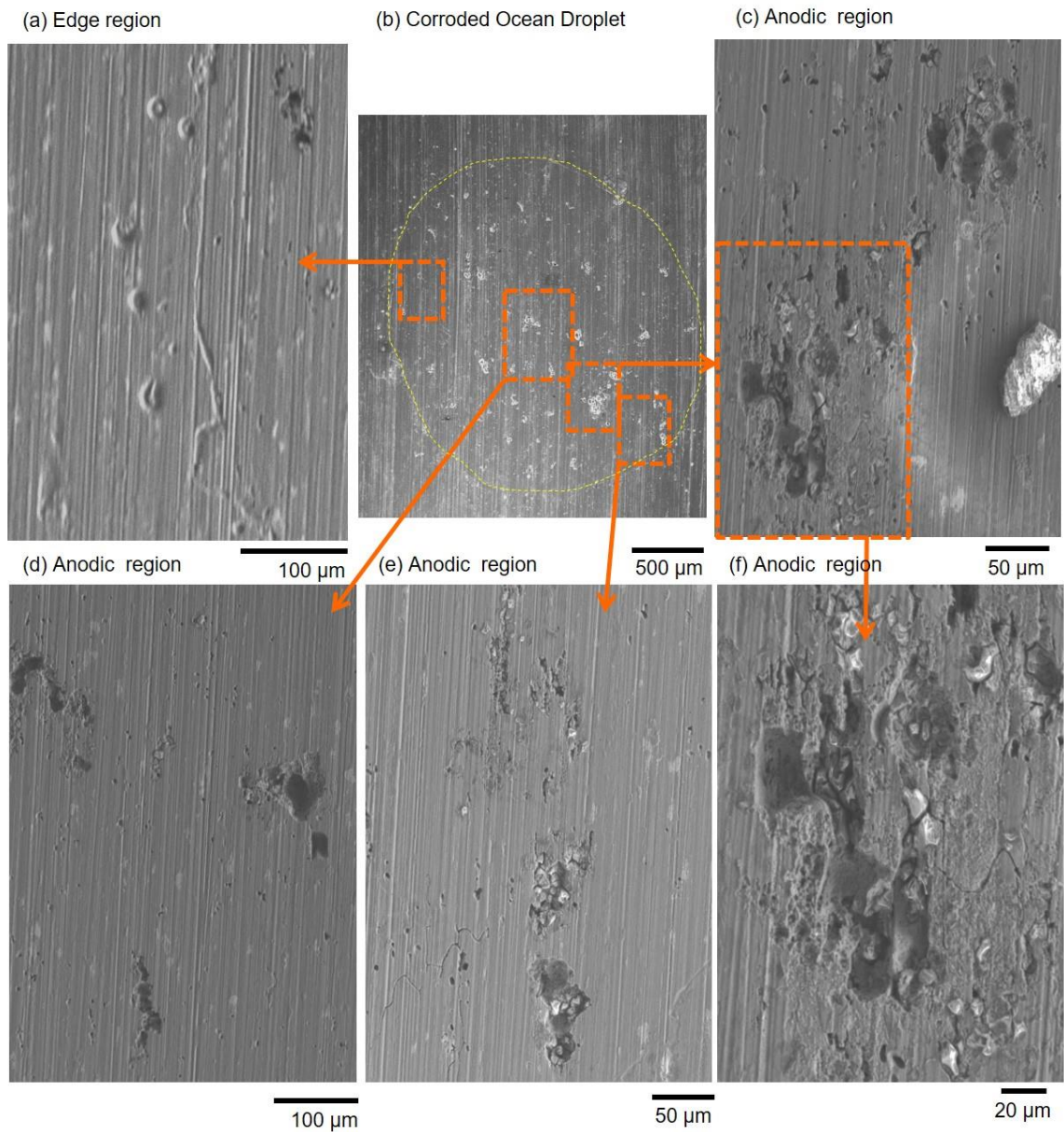
Figure 5-10 shows a series of SEM images using secondary electrons to view corrosion under an 430 µg/cm^2 CDD ASTM ocean water droplet (Figure 5-5(c)), on AA2024-T3 exposed at 85 ± 3% RH and at 30 ± 1 °C for 4 weeks (shown in Table 3-8) after immersion in nitric acid (procedure shown in section 3.4.3). Orange boxes outline different regions including (a) the edge region, (b- f) the corroded regions at various length scales. The original perimeter of the deposited droplet is shown in (b) with a dotted yellow line.

Figure 5-10 shows the surface morphology of the sample shown in Figure 5-9 after being immersed in 70% nitric acid introduced in Figure 5-5. Image (b) shows a SEM backscatter electron image of the entire corroded droplet; dark regions show anodic corroded sites. Image (a) shows the edge of the deposited droplet region. Where holes can be seen outside the edge of the droplet, made visible by a change in height. This feature shows that uniform dissolution is occurring at the edge of the droplet region where intermetallic particles may have been removed from the metal surface leaving round holes. Images (c - f) show corrosion sites at varying length scales. There are multiple corrosion sites distributed within the confines of the originally deposited droplet (b).

(a) Corroded Ocean Droplet (b) Edge region Droplet edge

500 µm 50 µm

(c) Spreading region (d) Middle of Droplet

50 µm 100 µm

(e) Middle of Droplet

S Phase

Iron containing

10 µm
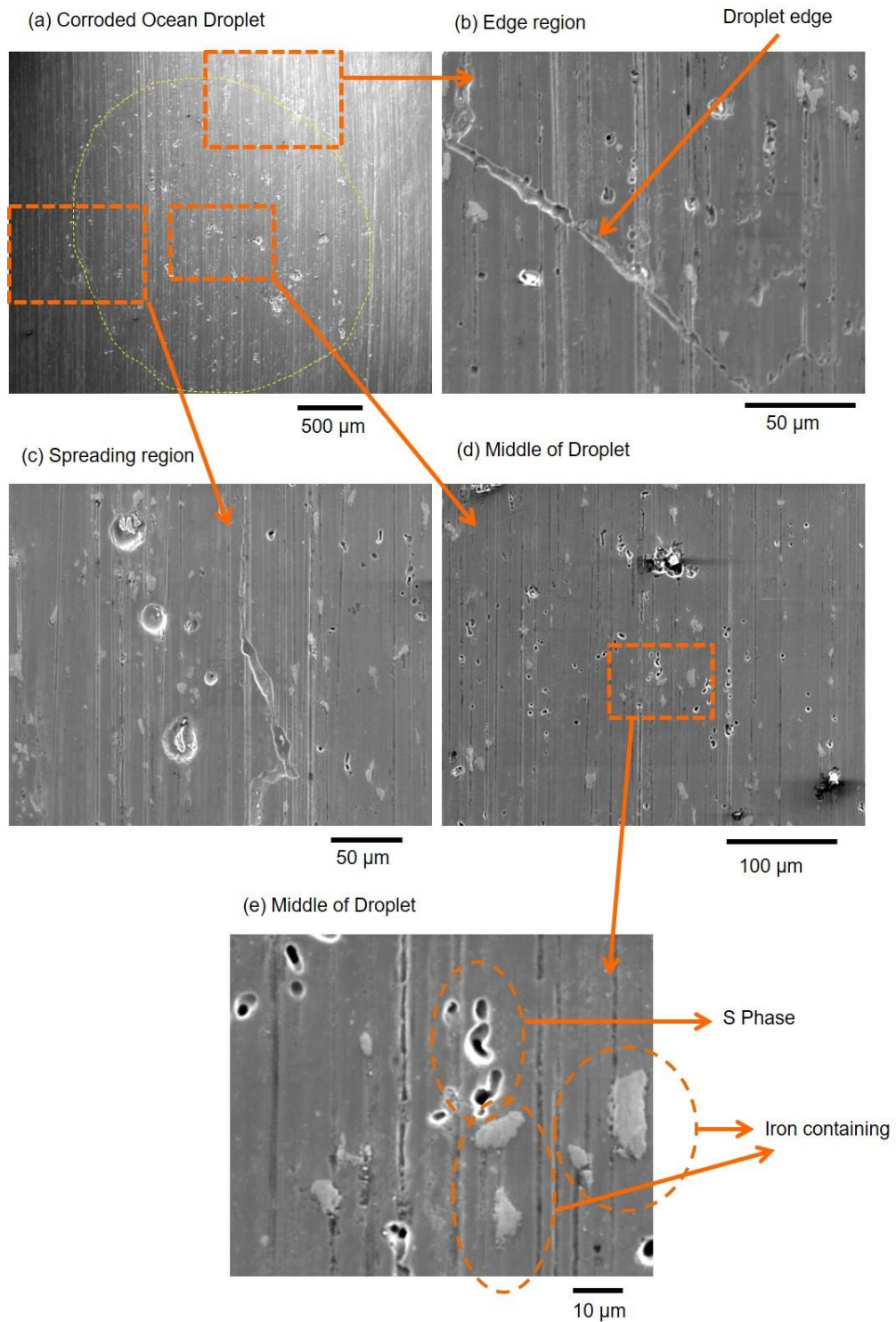
Figure 5-11 shows a series of SEM images using back scatter electrons to view of 430 µg/cm^2 CDD ASTM ocean water droplet from Figure 5-5, on AA2024-T3 exposed at 85 ± 3% RH and at 30 ± 1 °C for 4 weeks (shown in Table 3-8) after immersion in nitric acid and after polishing using OP-S and water (procedure shown in section 3.4.3). Orange boxes outline different regions including (a) the corroded droplet, (b) edge region highlighted by a yellow dotted line, (d) the spreading region, (e-f) the middle of the droplet.

117

Figure 5-11 shows a series of back scatter electron SEM images of corrosion induced by the ASTM ocean water droplets introduced in Figure 5-5. The sample has been submerged in nitric acid and polished with OP-S and water (procedure shown in section 3.4.3). (a) shows the entire droplet region. (b) shows the edge of the droplet where a height difference between the inside of the droplet and the spreading region is observed, this is indicated with an arrow. (c) shows the spreading region where the edge of the droplet and exposed intermetallic particles can be seen. (d) and (e) shows the main surface beneath the original foot print of the deposited droplet shown with a yellow dotted line. Dark regions show holes were intermetallic particles have been dislodged from the surface. (e) shows a magnified region of (d) where the smooth-edged hole indicates where S phase particles used to reside, which have fallen out following trenching around the particles. Less cathodically active and unattached iron-containing particles are also highlighted.
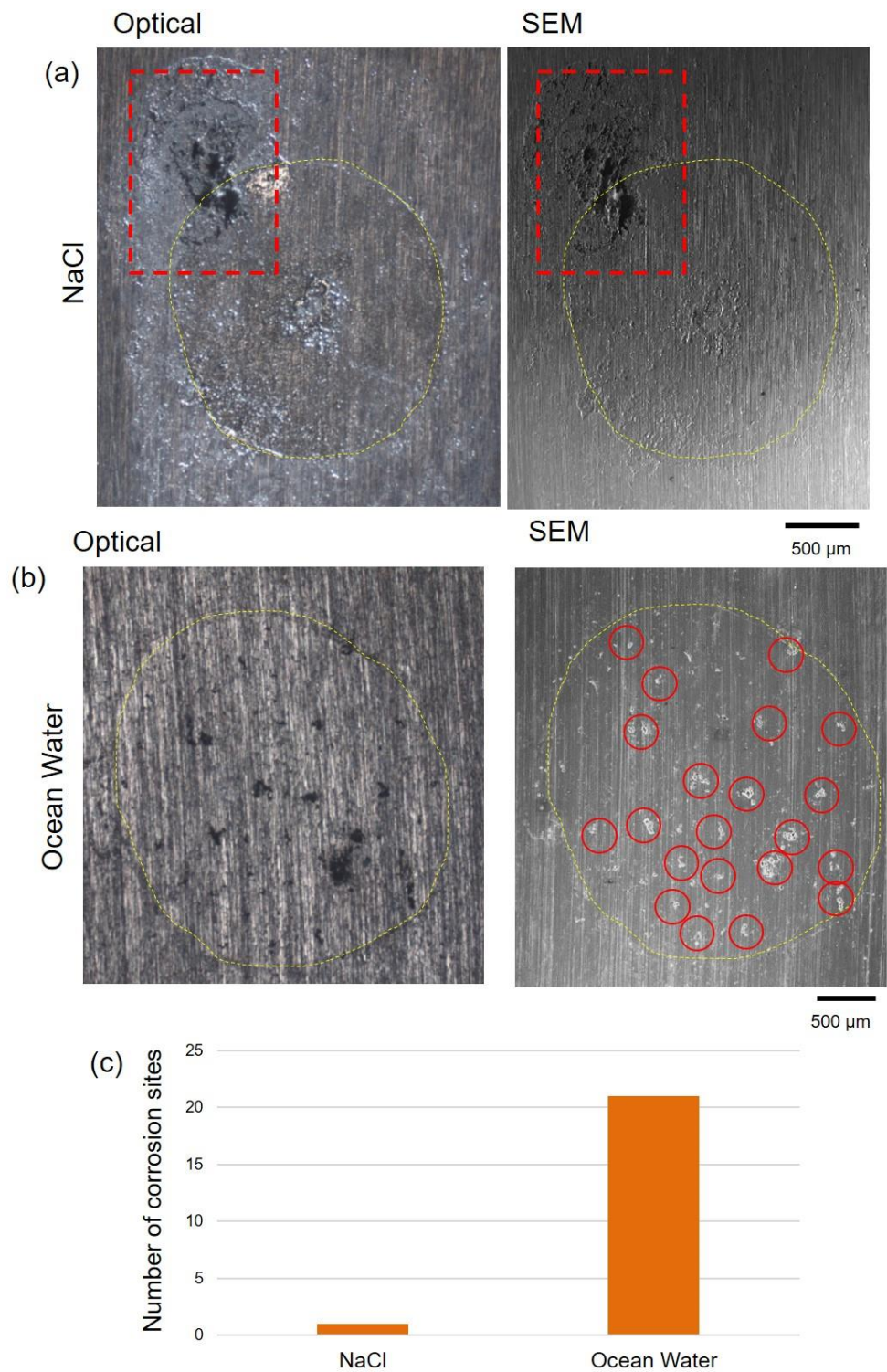
Figure 5-12 micrographs of droplets introduced in Figure 5-5 of (a) a corroded 2.00 ± 0.04 µL, 1000 µg/cm^2 CDD NaCl corrosion site is highlighted by a red box and (b) a 430 µg/cm^2 CDD ASTM droplet both on AA2024-T3 exposed at 85 ± 3% RH and at 30 ± 1 °C for 4 weeks (shown in Table 3-8) corrosion sites are highlighted by red circles (shown in Figure 5-7). The original droplet area is highlighted by a yellow dotted line. An optical microscope (left) and secondary electron SEM (right) images are taken after immersion in nitric acid. (c) bar chart showing the number of corrosion sites (corrosion sites counted must be above 10 µm as shown in section 3.4.2.

119

Figure 5-12 shows micrographs for the corroded NaCl droplet in (a) and ASTM droplet water droplets in (b) shown from Figure 5-5. Each sample in Figure 5-12 has been washed with nitric acid to reveal anodic sites beneath the corrosion products. Figure 5-12 (c) shows a bar chart of the number of anodic sites found on each NaCl and ASTM ocean water sample shown. Sites were identified using optical microscopy and counted if they were above 10 µm in length in one direction and deeper than 3 µm (shown in section 3.4.2). Only one corrosion site was found under the NaCl droplet and is highlighted by a red box, whereas 22 anodic sites were found on the sample with the ASTM ocean water droplet, highlighted by red circles after the 4 weeks exposure. These droplets were typical of sample size of 9 NaCl and 9 ASTM ocean water droplet observed in the same sample set. Each NaCl droplet would contain a single and large corrosion site intersecting both the main droplet and a spread region, whereas ASTM ocean water droplets contained multiple droplets confined to the originally deposited droplet footprint.

5.2.4 Raman Point Measurements on Corroded AA2024-T3
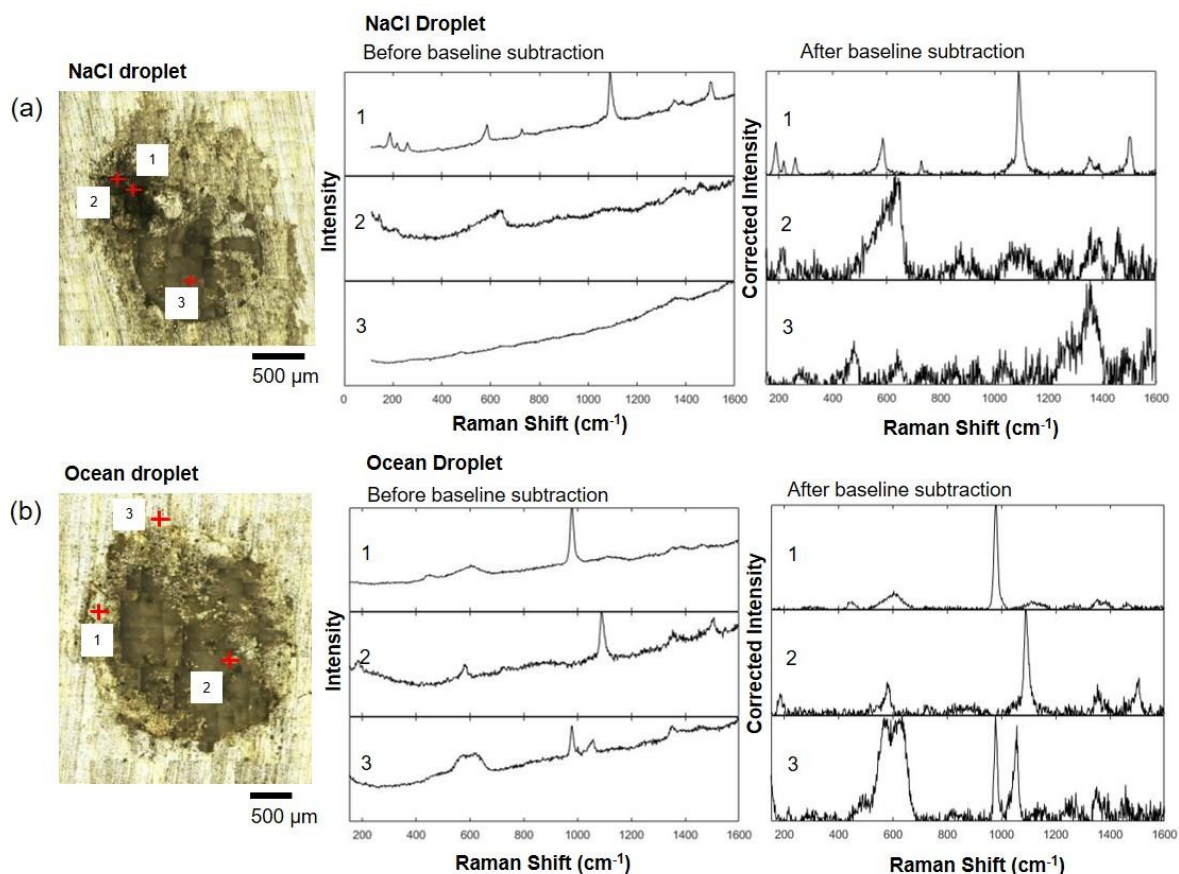
Figure 5-13 A pair of optical mosaic images constructed for Raman mapping and a series of graphs presenting Raman spectrum. 1000 µg/cm^2 NaCl (a) and 430 µg/cm^2 ASTM ocean (b) droplets on AA2024-T3 exposed at 85 ± 3% RH and at 30 ± 1 °C for 4 weeks (Table 3-8) shown in Figure 5-5. Optical and SEM images of these samples are shown in Figure 5-5. The graphs on the left show Raman spectra collected with a 488 nm laser, from point measurements labelled 1-3 and are representative spectrum from regions outlined by initial PCA (section 3.4.1.3) labelled 1-3 on the optical images. The graphs on the left show data as collected and graphs on the right show the data points after baseline subtractions (section 3.4.1.1).

Figure 5-13 shows optical images and Raman spectra data from NaCl and ASTM ocean water droplet introduced in Figure 5-5. The location of the point scans is indicated by red crosses in the optical images and labelled 1-3 in both salt droplets. Point measurements were selected based on collective regions highlighted by PCA, typical spectra from these regions are then used to plot spectra labelled 1-3. The graph plotted to the left shows data following initial

collection. The baseline in all 6 cases is seen to steadily increase showing fluorescence. The graph plotted to the right shows data after truncation and baseline subtraction to remove fluorescence (shown in section 3.4.1.1). Spectra taken from the NaCl droplet following baseline subtraction show clear peaks of varying intensities. NaCl point measurement 1 shows a spectrum similar to the Raman signals given by the compound Dawsonite (standard found in section 9.2.1). NaCl point measurement 2 shows a spectrum with a main peak at 630 cm^{-1}. NaCl point measurement 3 shows a spectrum with the highest intensity peak at 1350 cm^{-1}. Raman spectra collected from point measurements on a 430 μg/cm^2 ASTM ocean water droplet are indicated on the optical image and labelled 1-3. The associated spectra are labelled 1-3. ASTM ocean water point measurement 1 shows a strong peak at 980 cm^{-1}. ASTM ocean water point measurement 2 shows similar Raman signals given by the compound Dawsonite. ASTM ocean water point measurement 3 shows multiple strong peaks. The same 980 cm^{-1} peak is seen in a similar manner to measurement 1. Additional peaks are seen at 550 cm^{-1}, 630 cm^{-1}, and 1100 cm^{-1}.

5.2.5 Raman Component Mapping of AA2024-T3
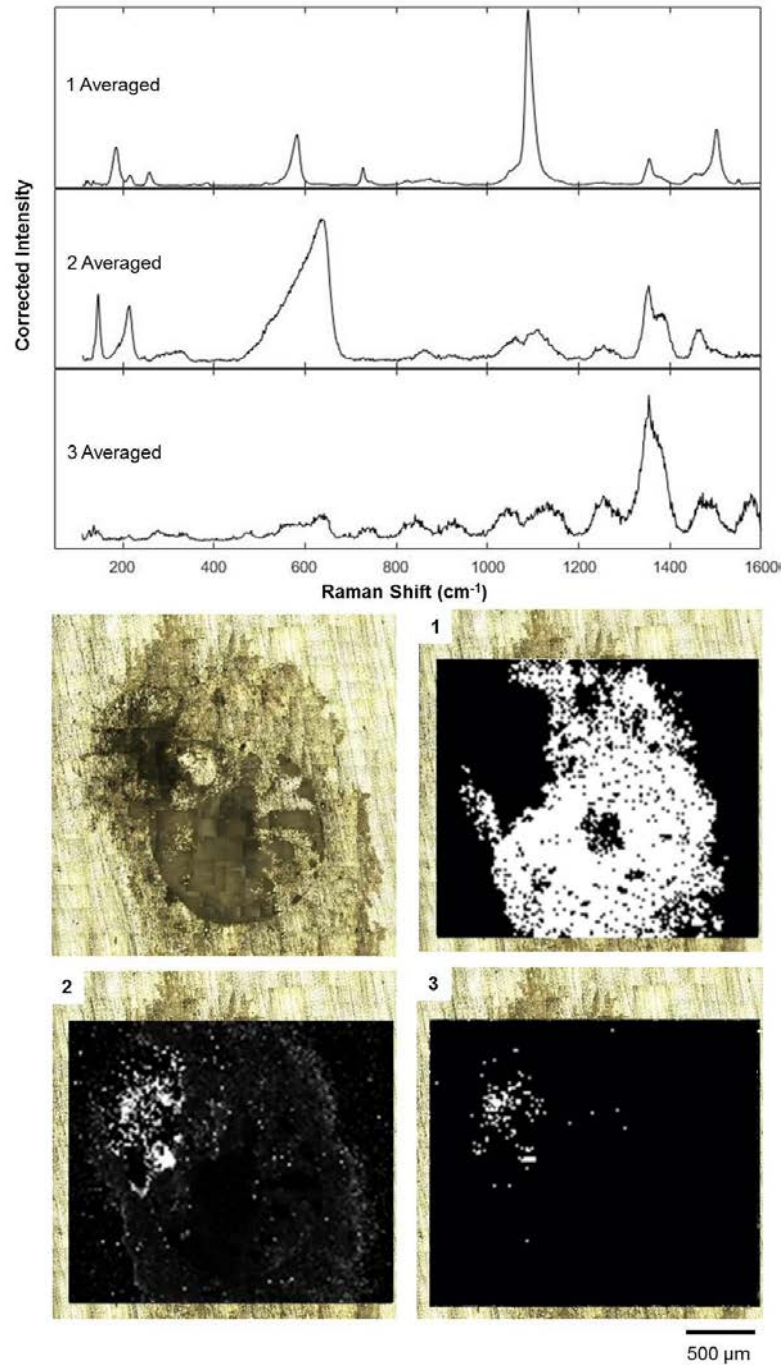
Figure 5-14 Raman shift signals of corroded 1000 µg/cm^2 NaCl droplet on AA2024-T3 exposed at 85 ± 3% relative humidity and at 30 ± 1 °C for 4 weeks (shown in Table 3-8) introduced in Figure 5-5. Raman data was collected with a 488 nm laser and data has been baseline subtracted as shown in Figure 5-13. The black and white overlays show mapping of the characteristic spectra of regions highlighted using PCA. White pixels show locations PCA has correlation (as shown in section 3.4.1.3). Data points for averaging are taken from the maps at a colour intensity of 255 from the mapped images. Map 1 data points are summed and averaged (shown in section 3.4.1.6) to generate '1 Averaged'. Map 2 data points are summed and averaged to generate '2 Averaged'. Map 3 data points are summed and averaged to generate '3 Averaged'.

Figure 5-14 shows data from a NaCl droplet on AA2024-T3 introduced in Figure 5-5 and Figure 5-13. The graphs at the top show Raman maps of the 3 main components. The spectra in data maps shown are averaged from data points above a 250 threshold. Main peaks in spectrum Averaged 1 are: 190 cm^{-1}, 590 cm^{-1} and 1100 cm^{-1}, these features are found in the regions where all corrosion products are deposited apart from the location where the corrosion site is found and are shown with SEM in Figure 5-7. The main peaks from Averaged 2 are: 160 cm^{-1}, 210 cm^{-1} and 630 cm^{-1}, these spectra are found where the corrosion site is seen, as shown by SEM Figure 5-7 and Figure 5-8. The main peak from averaged 3 is 1350 cm^{-1}.
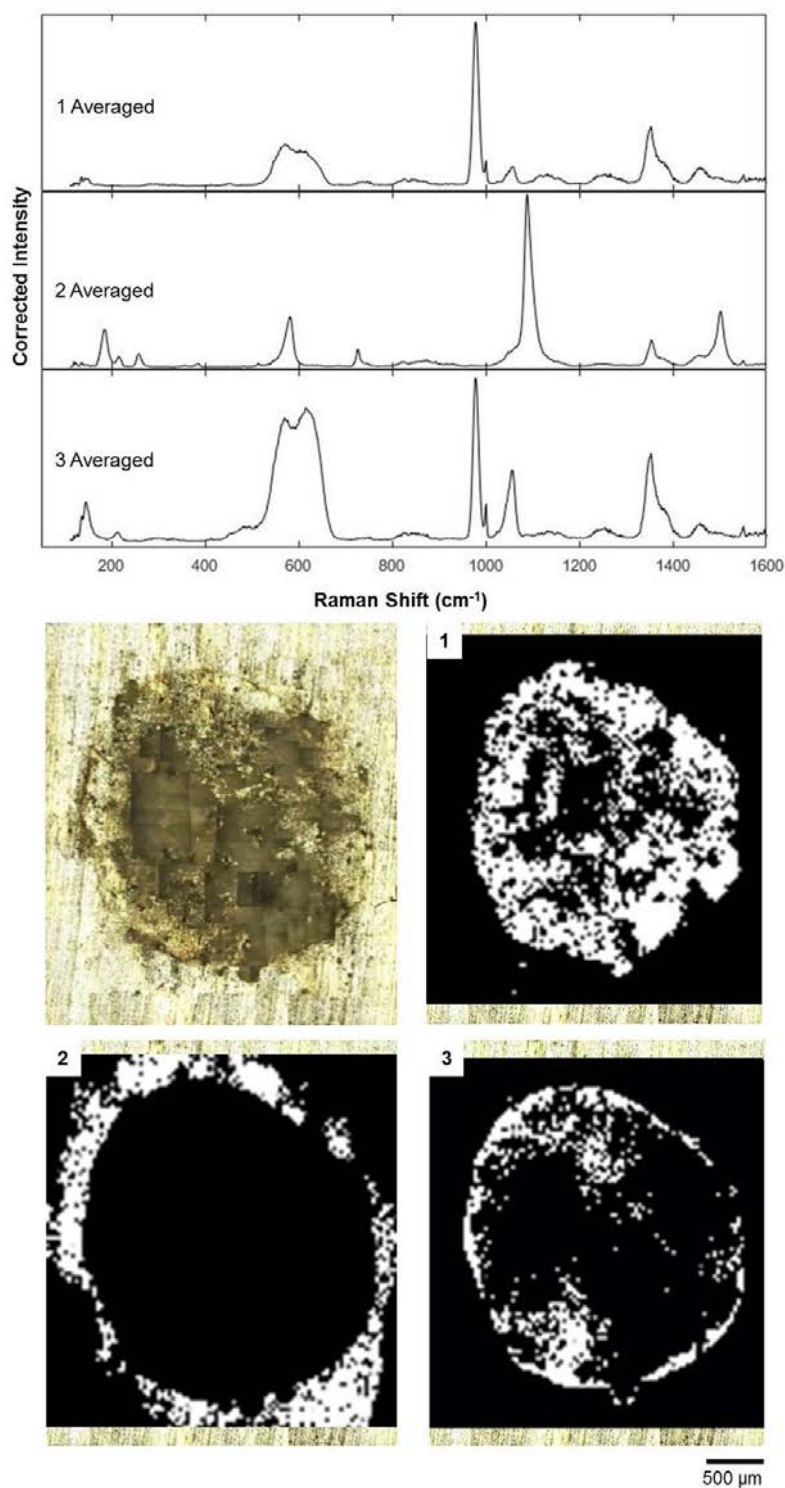
Figure 5-15 images of corroded 430 µg/cm^2 CDD ASTM ocean water droplets on AA2024-T3 exposed at 85 ± 3% RH and at 30 ± 1 °C for 4 weeks (shown in Table 3-8). Raman data was collected with a 488 nm laser and data has been baseline subtracted as shown in Figure 5-13. The black and white overlays show mapping of the characteristic spectra of regions highlighted using PCA. White pixels show locations PCA has emphasised (section 3.4.1.3). Data points for averaging are taken from the maps at a colour intensity of 250 from the mapped images. Map 1 data points are summed and averaged to generate '1 Averaged'. Map 2 data points are summed and averaged to generate '2 Averaged'. Map 3 data points are summed and averaged to generate '3 Averaged'.

Figure 5-15 shows data from an ASTM ocean water droplet shown in Figure 5-5 and Figure 5-13 . The graphs plot the three main components of the Raman signals identified. In the data maps shown, the spectra are averaged from data points above a 250 threshold. Main peaks in Averaged spectrum 1 are: 540 cm^{-1}, 630 cm^{-1}, and 990 cm^{-1}, these spectra are found only inside the middle of the originally deposited droplet. The same region corrosion sites were shown by SEM as shown by Figure 5-10 and Figure 5-12. The main peaks from Averaged 2 are: 190 cm^{-1}, 590 cm^{-1} and 1100 cm^{-1}, these spectra are found in the spreading region outside the original footprint of the deposited droplet. The main peaks from Averaged 3 are 150 cm^{-1}, 990 cm^{-1}, 1090 cm^{-1}, 1450 cm^{-1} and a double peak at 570 cm^{-1} and 630 cm^{-1}. These spectra are found within the perimeter of the interior of the droplet.

Corrosion product spectrum found under the NaCl droplet show two clear regions are highlighted by three different spectra in Figure 5-14. The largest is Average 1 and is shown to be over the entire body of the initial droplet region and the spreading region. Two other spectra, Average 2 and 3 are seen located in the same region at the corrosion site. A similar spectrum predicted to be Dawsonite is seen on both samples; Average 1 in the NaCl Figure 5-14, and Average 2 in the ASTM ocean water sample seen in Figure 5-14. The ASTM ocean water sample shows differences in corrosion products in the main droplet body and the spreading region.
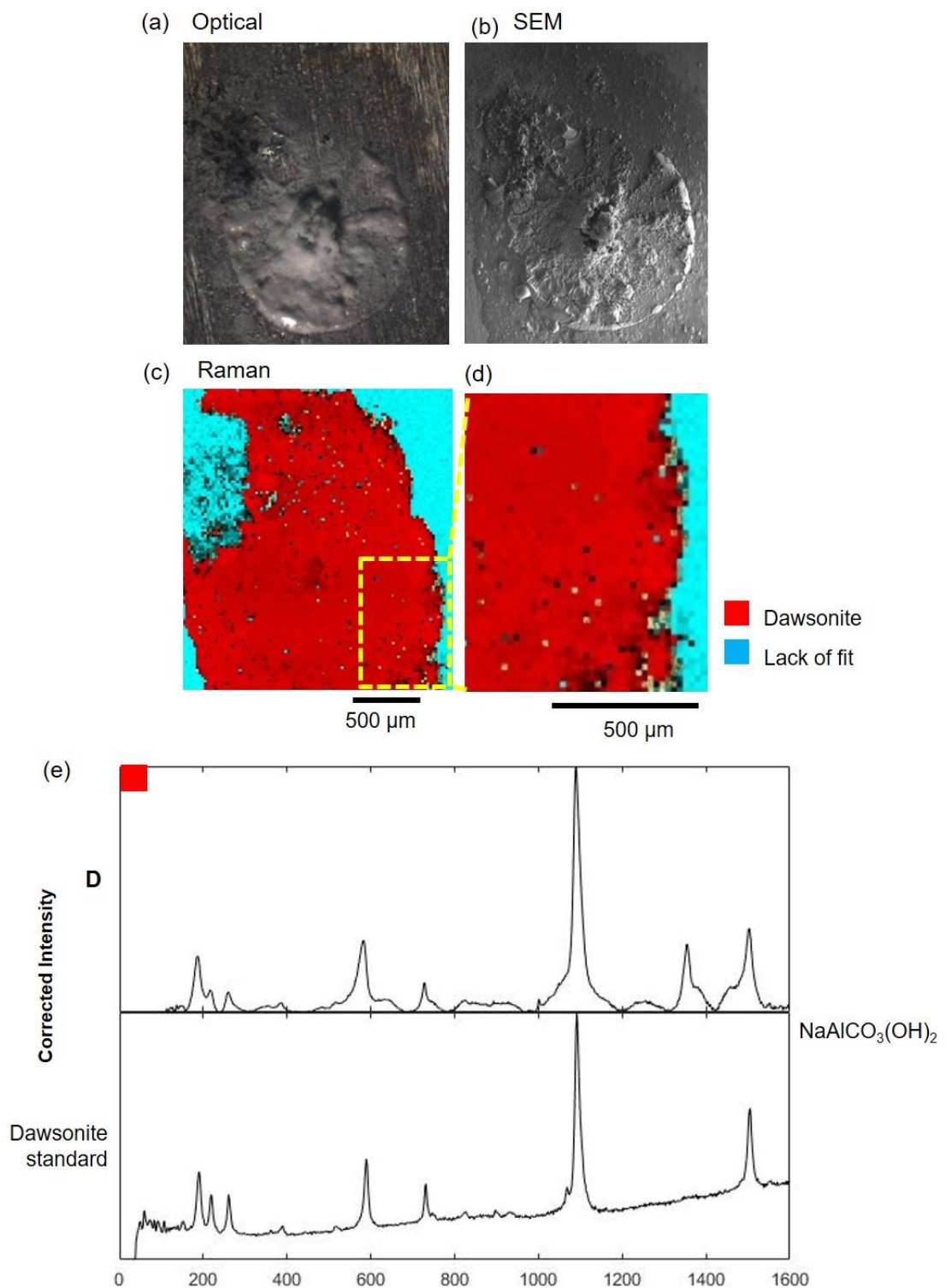
Figure 5-16 Graph stack of Raman spectra and map of AA2024-T3 sample shown in Figure 5-5, of corrosion products formed under 1000 µg/cm^2 NaCl droplets exposed at 85 ± 3% relative humidity and at 30 ± 1 °C for 4 weeks (shown in Table 3-8). Raman data was collected with a 488 nm. A DCLS component map (section 3.4.1.4) of Dawsonite (NaAlCO$_3$(OH)$_2$) is shown in red, DLSC map of a lack of best fit is shown in blue. Dawsonite standard was: synthesised Dawsonite (Appendix 4 - section 9.2.1).

Figure 5-16 displays optical, SEM and Raman maps of the NaCl droplet which was introduced in Figure 5-5 and Figure 5-13. Figure 5-16 (a) shows the optical image where white corrosion product are visible. (b) shows an SEM image. (c) shows a Raman map, where red regions show a fit from the DCLS mapping (section 3.4.1.4) to the Dawsonite standard, and light blue highlights where a fit to the Dawsonite standard could not be made. (d) shows a magnified image of (c). (e) shows a stack plot of Dawsonite measured using DCLS compound analysis where 'D' is all red data points summed and then averaged. This spectrum shows a strong correlation to Dawsonite. There is an additional peak seen within the averaged data at 1350 cm^{-1} Raman shift.

Other NaCl droplets exposed at 85 ± 3% relative humidity and at 30 ± 1 °C for 4 weeks were analysed using Raman point measurements. The average CDD of three droplets measured was 1000 µg/cm^2, the average of three additional droplets 3000 µg/cm^2 and average CDD of three saturated NaCl droplets measured was 6250 µg/cm^2. One single 1000 µg/cm^2 NaCl droplet was mapped while the droplet was at 80 ± 3% RH and therefore wet. Droplets of these varying CDD washed and unwashed were found to have all had the same three spectra found in Figure 5-14 including the additional peak at 1350 cm^{-1}. These three spectra also covered the same regions as the typical sample presented, with Dawsonite covering all but the anodic sites of these samples. The NaCl samples are shown in Figure 5-5, Figure 5-6, Figure 5-7, Figure 5-8, Figure 5-12 and Figure 5-14 is a representative of all samples measured.
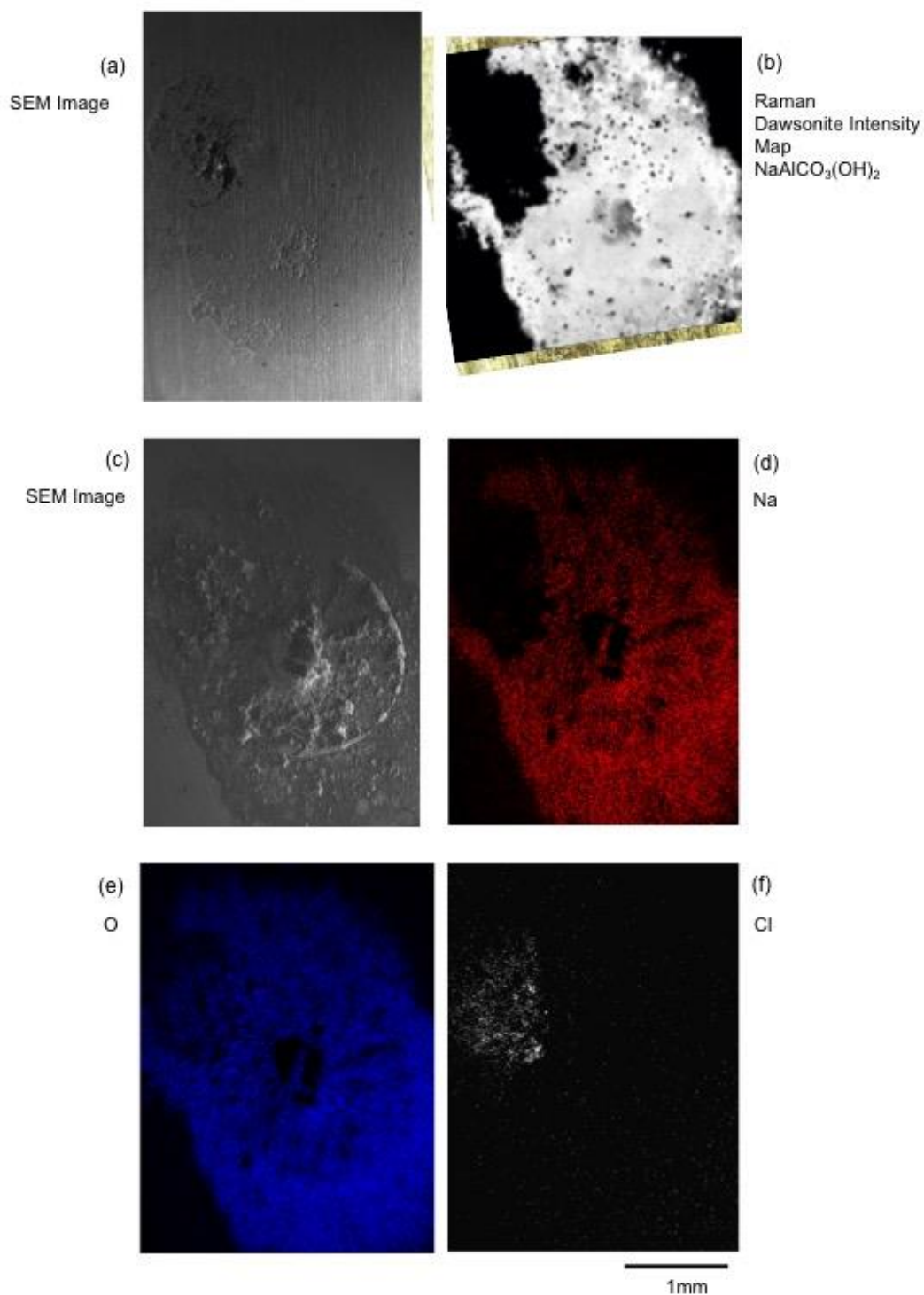
Figure 5-17 a series images taken from Raman also shown in Figure 5-16 and SEM. EDX maps of oxygen, sodium and chlorine alongside a Raman intensity map of the corroded 1000 µg/cm^2 CDD NaCl droplet on a AA2024-T3 sample shown in Figure 5-5 exposed at 85 ± 3% relative humidity and at 30 ± 1 °C for 4 weeks (shown in Table 3-8). (a) is a SEM of the sample in with the corrosion products (c) is and SEM of the sample after being immersed nitric acid (protocol shown in section 3.4.3. (b) is used a Dawsonite standard collected using 488 nm laser (Appendix 2) to map spectrum and generate a DCLS intensity map (section 3.4.1.4). (d)-(f) show EDX maps of Na, O and Cl.

129

Figure 5-17 shows a series of images, which include SEM EDX maps indicated by their elemental abbreviation and Raman DCLS map as indicated by Dawsonite chemical formula and name. These images show the NaCl water droplet introduced in Figure 5-5. EDX maps and Raman map shows where the main elements Na, O and Cl reside. Dawsonite contains Na and shows correlation to the regions of the droplet and spread droplet where Na is present in the EDX map. Other EDX maps show the presence of Cl. Cl is seen in the same vicinity as at the intersecting the edge and main droplet where the corrosion site is observed on this sample as shown in (a) Figure 5-7. Dawsonite is absent in regions where EDX mapping shows the presence of Cl. O is seen throughout the surface measured including regions such as the droplet, spreading region and location the corrosion site is seen. An SEM of corrosion products are shown in Figure 5-17 (c) for reference.
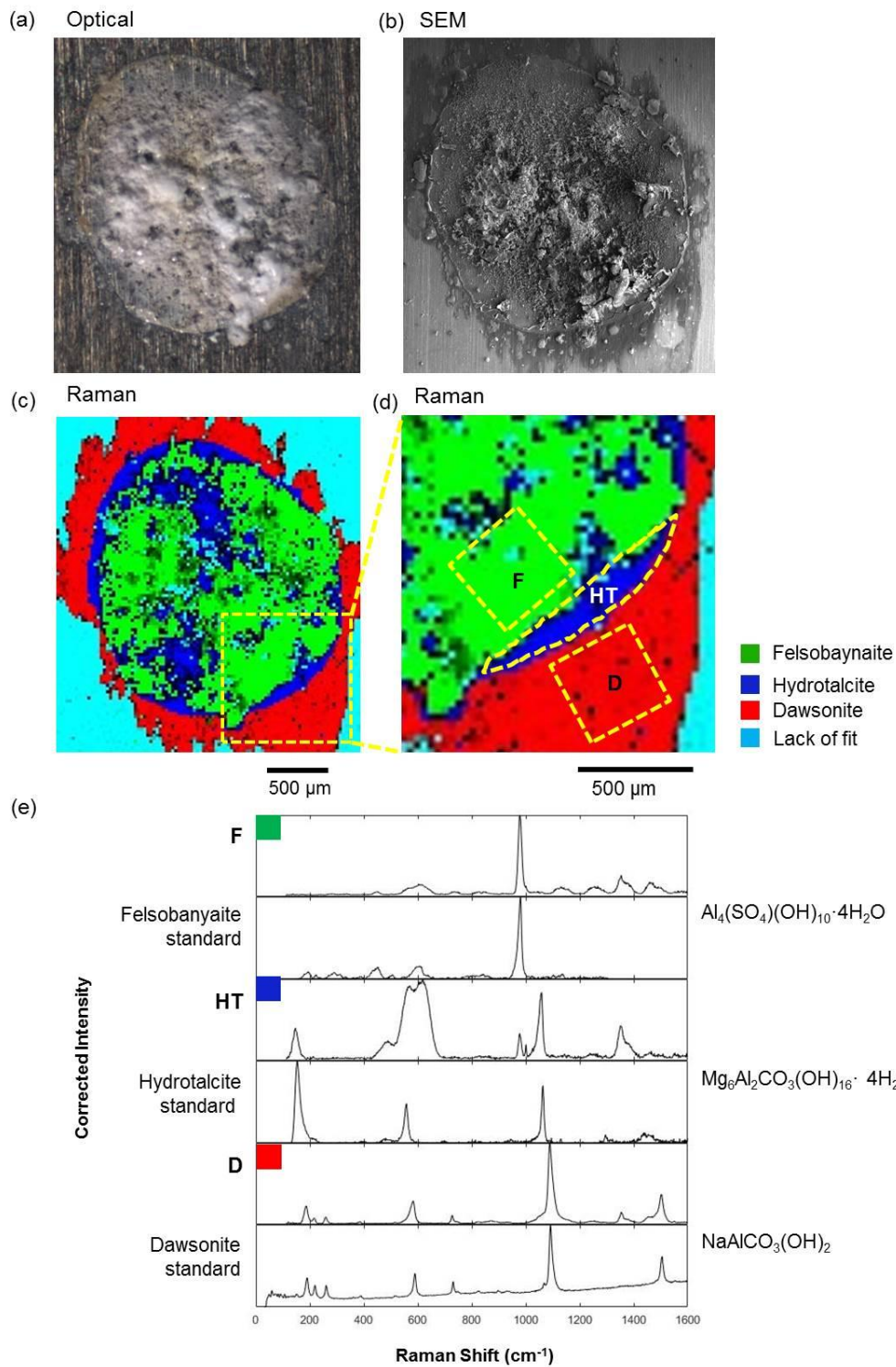
Figure 5-18 a graph stack of Raman spectra used in DCLS component mapping on corroded 430 µg/cm^2 CDD ASTM ocean water droplets shown in Figure 5-5 on AA2024-T3 exposed at 85 ± 3% relative humidity and at 30 ± 1 °C for 4 weeks (shown in Table 3-8). Measurements shown are from Figure 5-15. A DCLS maps (section 3.4.1.4) of Felsöbányaite is shown in green. A DCLS component map of Dawsonite is shown in red. A DCLS component map of Hydrotalcite is shown in navy blue. The DLSC map of the lack of best fit is shown in light blue. Average spectra are plotted in a stack with standard spectra (Appendix 2) immediately below in (e).

Figure 5-18 shows optical (a), SEM (b) and Raman maps (c) and (d) of the ASTM ocean water droplet shown in Figure 5-5. (a) shows the optical image where white corrosion product is visible. (b) shows an SEM image. (c) shows a Raman map where highlighted regions confirmation the presence of Felsöbányaite in green, Hydrotalcite in navy blue and Dawsonite in red. Light blue highlights data with a lack of fit to these components. (e) shows a stack plot graph of all components mapped against their standard counterpart. Average data is derived from averaging highlighted regional data points confirmed by mapping. These are shown above their assumed standard. 'F' and its measured standard Felsöbányaite closely correlates with the addition of peaks at 1350 cm^{-1}. 'HT' which shows a spectrum of Hydrotalcite plus the addition of Felsöbányaite and 630 cm^{-1} and 1350 cm^{-1}. The higher intensity of the 'HT' peak shows that this is the more dominant compound in the region revealed by DCLS. The spectrum 'D' shows a close correlation to the Dawsonite standard spectrum along with a peak at 1350 cm^{-1}.

A total of 5 other ASTM droplets with an average of 400 µg/cm^2 CDD corroded at 85 ± 3% relative humidity and at 30 ± 1 °C for 4 weeks were measured using Raman. One other droplet was mapped and showed the same Raman map results and distribution of corrosion products as the fully mapped droplet in Figure 5-18. Further point measurements were made on 4 droplets from the same sample set. All droplets measured contained all three corrosion products. Dawsonite was found in the spreading region, Felsöbányaite inside the footprint of the droplet, and Hydrotalcite surrounding the perimeter of the droplet.
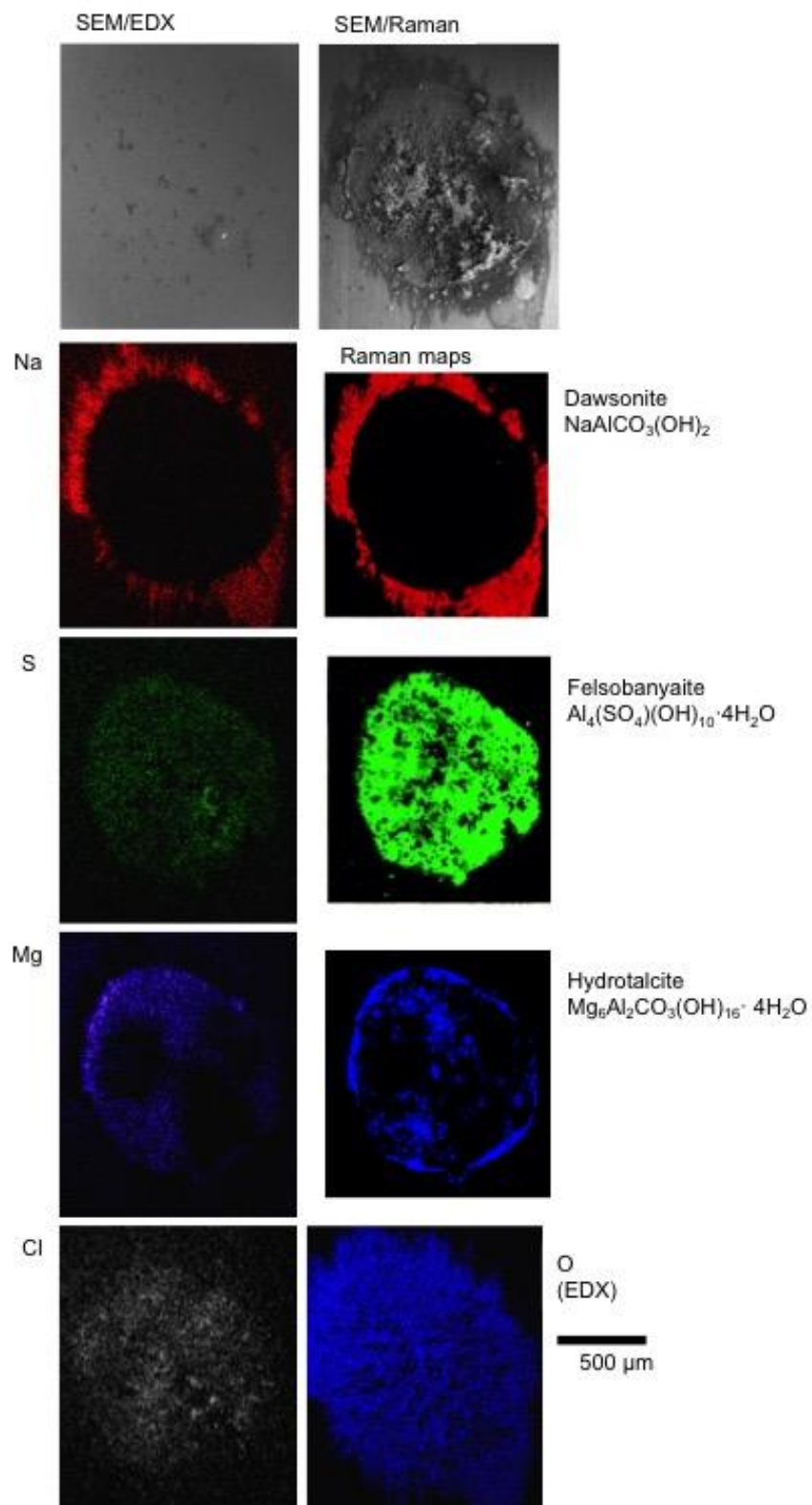
Figure 5-19. EDX maps of oxygen, sodium, sulphur, magnesium and chlorine alongside Raman DCLS maps (section 3.4.1.4) maps of a corroded 430 μg/cm^2 CDD ASTM ocean water droplet as shown in Figure 5-5 on AA2024-T3 corroded at 85 ± 3% relative humidity and at 30 ± 1 °C for 4 weeks maps (shown in Table 3-8). Felsöbányaite and Dawsonite and Hydrotalcite Raman maps have been presented with their name and chemical composition.

133

Figure 5-19 shows the results of the experiment using ASTM ocean water droplets from Figure 5-5. EDX and Raman maps show where the main elements and chemicals reside, correlating findings from the Raman mapping. The majority of elements are seen where the corresponding corrosion product is observed. Na was seen in the exterior to the droplet and shows good correlation to Dawsonite shown in red. S and Felsöbányaite shown in green are found in the interior of the droplet and it can be seen that Felsöbányaite correlates well to S. Mg and Hydrotalcite shown in blue are seen around the perimeter and interior of the droplet. The pattern shown by mapping shows a good correlation between Mg and Hydrotalcite. Other EDX maps show the presence of O and Cl. Cl is seen in the same vicinity as the droplet foot print. The distribution of corrosion sites shown in Figure 5-10 correlates to the Cl map. O is found in the entire region of the droplet and spread region.

5.2.6 Corrosion Product Confirmation
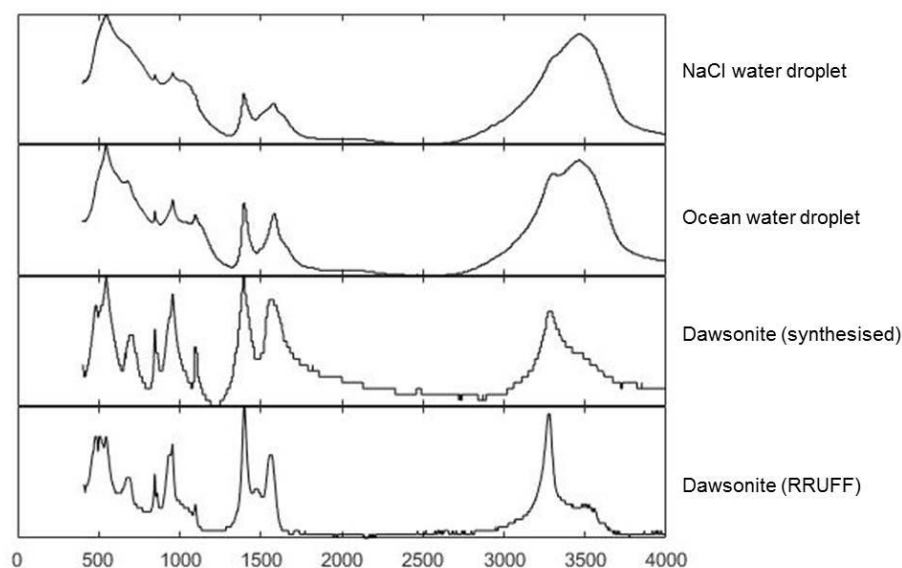
Figure 5-20 FTIR taken from 4000 µg/cm^2 CDD NaCl and 400 µg/cm^2 CDD ASTM ocean water corroded on AA2024-T3 at 85 ± 3% relative humidity and at 30 ± 1 ^{o}C for 4 weeks maps (protocol shown in 3.4.4). Corrosion products were removed by scraping the sample with glass slide and suspended in KBr for imaging in IR maps.

Figure 5-20 shows a stacked graph plot of FTIR for both NaCl and ASTM ocean water corrosion products after four weeks exposure to 85% RH ± 2 at 30 ±1 °C. Protocol for the removal of corrosion products is shown in (protocol shown in 3.4.4). IR shows that the dominant IR active corrosion product in both NaCl and ASTM ocean water is Dawsonite. This was confirmed by also measuring a Dawsonite standard, as used in the Raman measurements made in accordance with Raman Microscopy section 3.4.1.
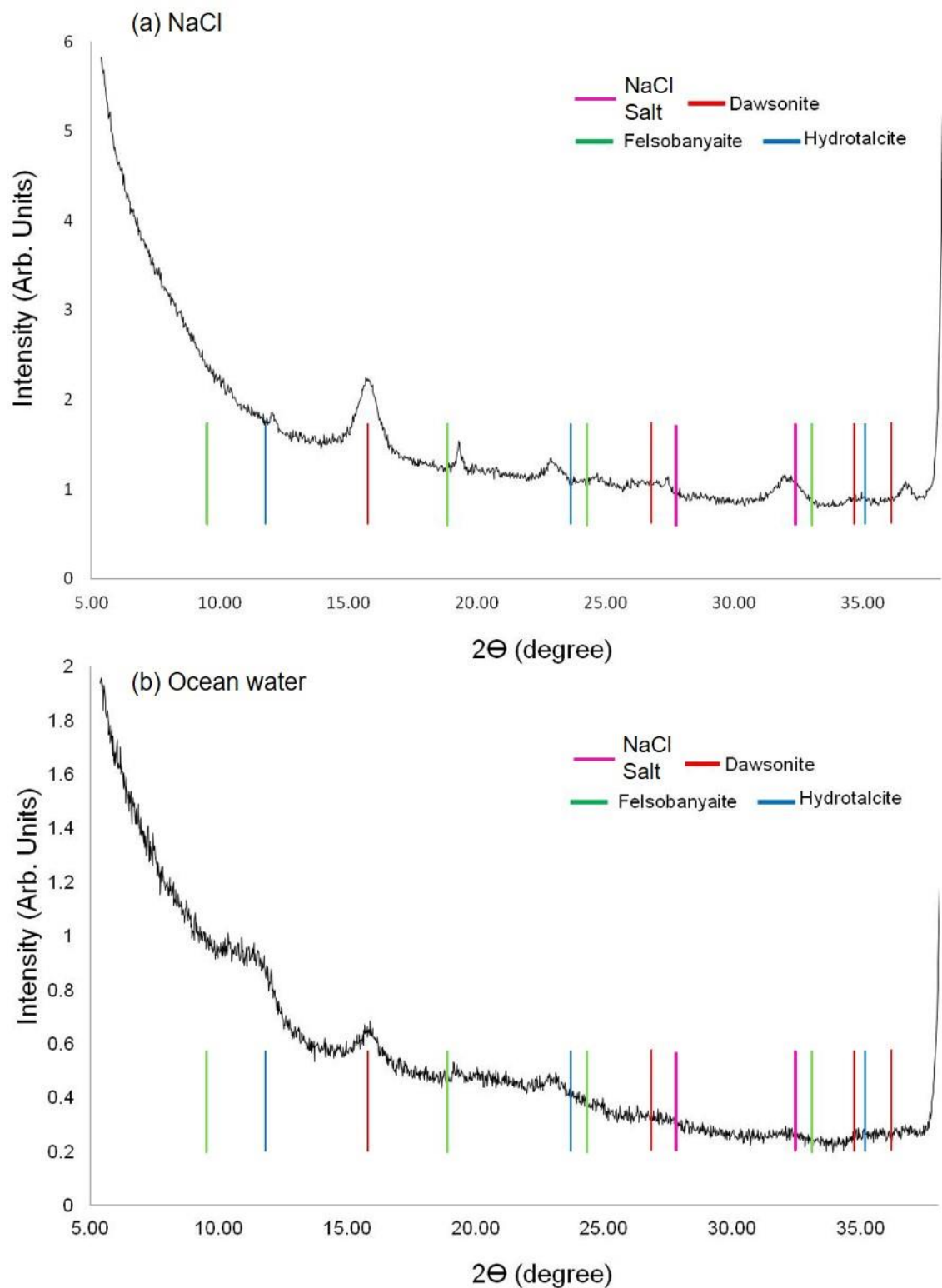
Figure 5-21 Grazing angle XRD patterns of a 4000 μg/cm² CDD NaCl (a) and 400 μg/cm² CDD ASTM ocean water (b) droplets on AA2024-T3 exposed at 85 ± 3% relative humidity and at 30 ± 1 °C for 4 weeks maps (protocol shown in 3.4.3). Coloured bars indicate dominant peaks from control spectrum: NaCl [181] Dawsonite [179] Felsöbányaite [180] Hydrotalcite [181].

Figure 5-21 shows a graph of grazing angle XRD patterns collected from corrosion products taken from a 4000 µg/cm^2 CDD NaCl (a) and a 400 µg/cm^2 CDD ASTM ocean water on AA2024-T3 exposed at 85 ± 3% relative humidity and at 30 ± 1 ^{o}C for 4 weeks (protocol shown in section 3.4.3). XRD patterns show Dawsonite as the dominant corrosion product present.

NaCl Droplet AA2024:
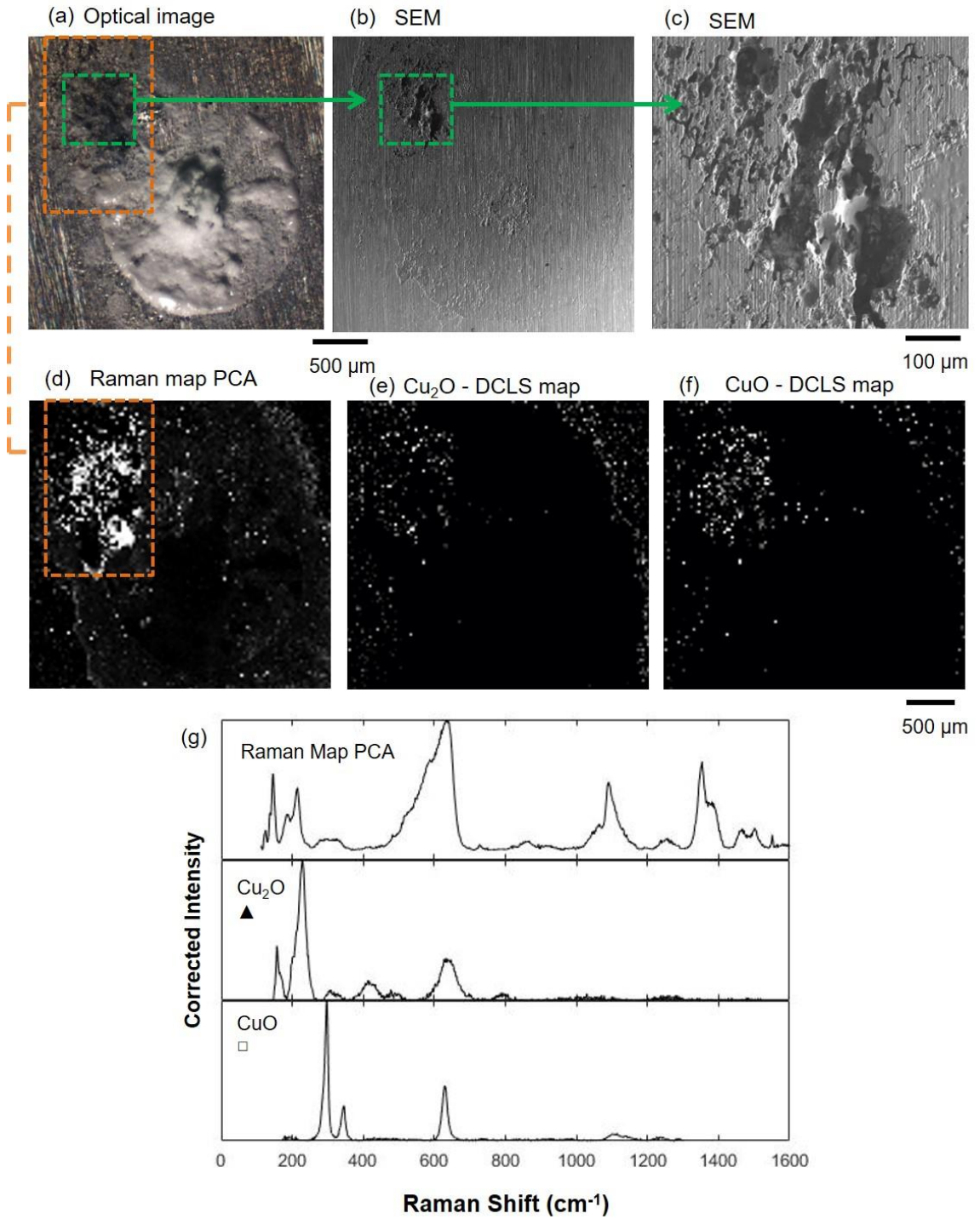
Figure 5-22 Graph stack of Raman spectra used in DCLS component mapping of corroded AA2024-T3 plate sample shown in Figure 5-5 with a 1000 µg/cm^2 CDD NaCl exposed at 85 ± 3% relative humidity and at 30 ± 1 °C for 4 weeks. (a) optical image of the dried droplet. (b) SEM images of the sample after cleaning. (c) SEM of (b) at higher magnification. Green boxes highlight the corrosion site. Raman data was collected with a 488 nm laser. DCLS maps show (d) 'Raman map PCA' taken from 2 Averaged in Figure 5-13, (e) DCLS Cu$_2$O and (f) DCLS CuO. (g) shows a stack plot the Raman spectrum mapped in (d)-(f) and can be found in (Appendix 2).

Figure 5-22 shows optical, SEM and Raman maps of the NaCl sample. Optical and SEM images show the corroded site highlighted by green and orange boxes. In (a), an optical image of the corroded droplet, white corrosion product can be seen, while the dark region on the top left of the droplet shows the corrosion site. (b) and (c) shows an SEM image of the sample following cleaning. The corrosion site is highlighted by a green box. (d) shows a Raman map introduced in Figure 5-13 as map 2 where unidentified spectral features were found. Graphs (e) and (f) show maps of Cu_2O and CuO. (g) shows a stack plot of the data highlighted by maps. Peaks shown in the spectrum (g) 'Raman Map PCA' are also seen on the ASTM ocean water sample which can be seen in Figure 5-15 at 160 cm^{-1}, 210 cm^{-1}, 630 cm^{-1}, and 1350 cm^{-1}. However, due to their thin distribution and low peak intensities these were harder to map. Using the large region seen corresponding to the corrosion site on NaCl, with the same peaks found sparsely on ASTM ocean water droplets, maps of spectra can be summed and averaged. A loose correlation can be seen of the corrosion site and both Cu_2O and CuO. A closer correlation of Cu_2O is seen than CuO.

5.2.7 Visualisation and Observations Corrosion Products on AA1050

There are a number of unidentified corrosion products in the spectra for AA2024-T3. It is possible that these arise from the minor alloying elements. Therefore study of an alloy of a different composition could be helpful; particularly to identify products containing Mg or Cu. Figure 5-23 shows optical and Raman maps of a AA1050 sample.
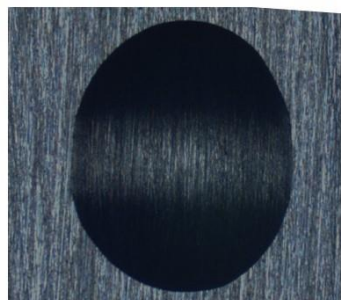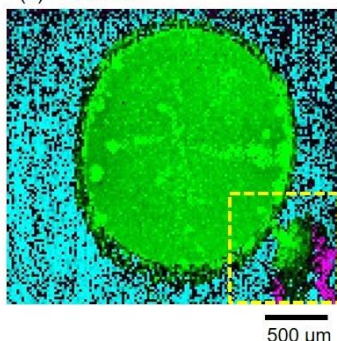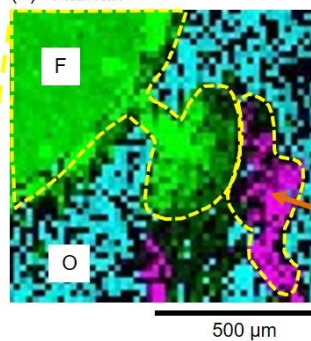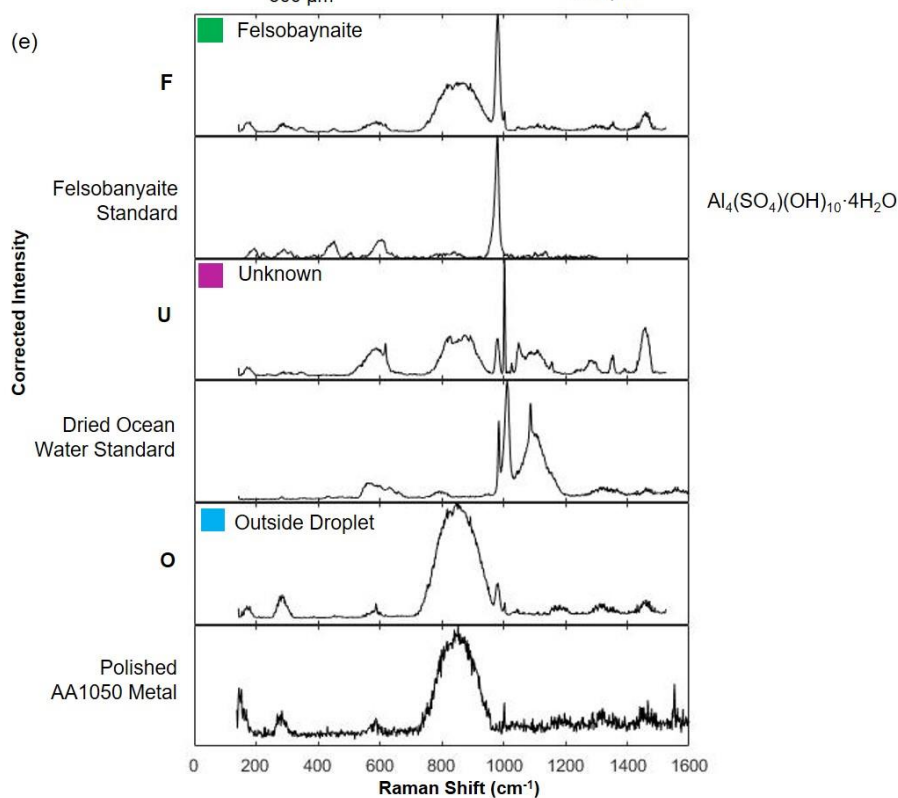
Figure 5-23 Raman spectrum used in DCLS component mapping of AA1050 sheet sample with 400 µg/cm^2 CDD ASTM ocean water droplets exposed at 96 ± 3% relative humidity and at 30 ± 1 °C for 8 weeks (shown in Table 3-8). The sample was scanned by Raman mapping post methanol rinsing and dried for 12 hours. DCLS component maps are shown in (c) and (d) of Felsöbányaite is shown in green. A DCLS component map of an unknown is shown in pink. A DCLS component map of the outside of the droplet is shown in light blue. Average spectra of these maps are plotted in a stack with standard spectra (Appendix 2 – section 9.2.1) immediately below in (e).

140

An ASTM ocean water droplet was exposed at 96 ± 3% relative humidity at 30 ± 1°C for 8 weeks. A higher relative humidity and exposure time was required to obtain corrosion products precipitation due to the corrosion resistance of AA1050. Figure 5-23 (a) shows an optical image of the initially deposited droplet. (b) shows the optical image of the corroded droplet post rinsing and drying with methanol where a white corrosion product is visible. (c) shows a Raman map where regions of corrosion products are shown in colour. The following maps are shown: Felsöbányaite (F) in green, an unknown (U) spectrum in fuchsia, and the spectrum gathered from outside the droplet (O) in light blue. (e) shows a stack plot of this data after the spectra from each highlighted region has been averaged together. The data is then matched to standards averaged from mapping. (F) data is shown to closely correlate to the Felsöbányaite standard. The measured spectrum shows additional peaks to the standard, with a broad peak at 800 cm^{-1} and a low intensity sharp peak at 1000 cm^{-1}. The broad peak is also seen in (O) and related to the bare metal of AA1050. An unknown (U) Raman spectrum is found in the outside of the droplet. The spreading region is not seen surrounding the entire droplet (comparable in AA2024-T3 Figure 5-20) but a small isolated region as highlighted in image (d). The main peak of this spectrum is 1000 cm^{-1}. This 1000 cm^{-1} peak is also found in the Raman spectrum gathered from a dry ASTM ocean water droplet standard as shown in (Figure 5-3). The outside of the droplet (O) has a broad peak at 800 cm^{-1}. A Raman measurement was taken from another sample of the same AA1050, polished with 800 grit SiC paper, in order to gather a standard for 1050 bare metal shown in (e), this

shows the same 800 cm^{-1} broad peak as seen throughout all Raman spectra on the AA1050 sample.
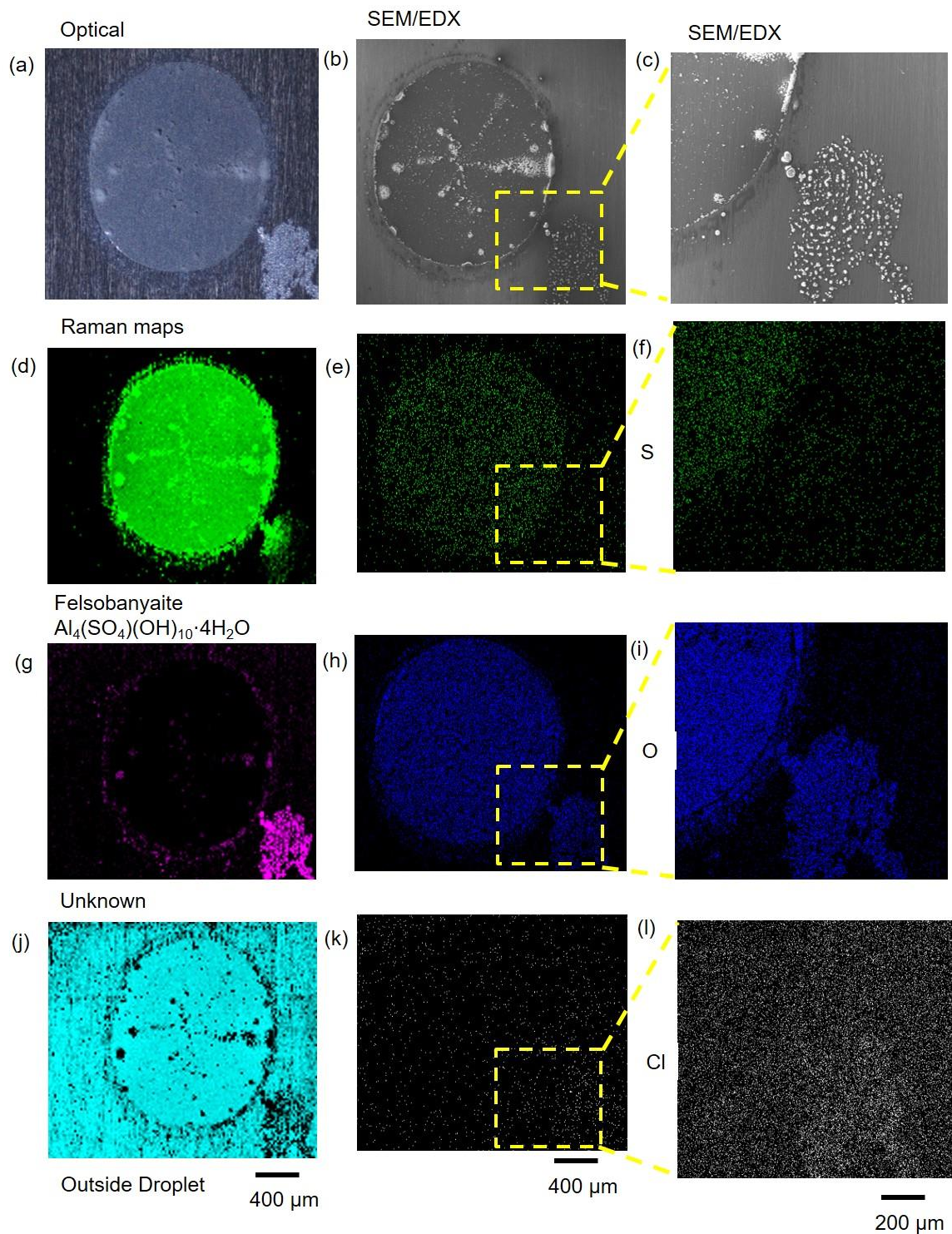
Figure 5-24 A series images taken from Raman and SEM images, of a 400 µg/cm^2 CDD ASTM ocean water droplet on AA1050 (as shown in Figure 5-23) exposed at 96 ± 3% relative humidity and at 30 ± 1 °C for 8 weeks. EDX maps of sulphur (S), oxygen (O) and chlorine (Cl) at two different length scales alongside Raman DCLS maps. (a) an optical image of the dried corroded droplet. (b) a SEM image of this droplet. (c) a higher magnification of yellow box outlined in (b). (d) a Raman map of a Felsöbányaite standard. (g) a map of unknown compound. (j) a map of the outside of the droplet. (e) (h) (k) all show EDX maps. (f) (i) (l) all show higher magnification maps of EDX of the region highlighted by the yellow boxes.

Figure 5-24 shows a series of images of an AA1050 sample obtained with the use of Raman and SEM. Comparisons between EDX maps and Raman maps show where the main elements reside with respect to findings from the Raman mapping. Where the majority of an element is seen, the corresponding corrosion product is observed. S and Felsöbányaite is shown in green, sulphur is a constituent of Felsöbányaite. Other EDX maps show the presence of O and Cl. Cl is seen in the same vicinity as the small spreading region. O is found throughout the footprint of the droplet and the spreading region. Na maps are not shown as data was not obtained. This could be due to the lack of Dawsonite present on the sample following atmospheric exposure.

5.3 Discussion

5.3.1 The Influence of Salt Type on Atmospheric Corrosion

Experiments were carried out on AA2024-T3 to identify and quantify the corrosion products present after exposure to NaCl and ASTM ocean water salt droplets. Tests on AA2024-T3 samples were carried out at 85 ± 3% relative humidity and at 30 ± 1 °C for 4 weeks. The observations of these droplets are found in Figure 5-5. Experiments carried out on AA1050 plate 96 ±3% relative humidity and at 30 ± 1°C for 8 weeks (shown in Table 3-8). Due to the corrosion resistance of AA1050, a longer exposure to atmospheric conditions was required to accumulate enough corrosion products for measurements to be made. Initial observations of this experiments are seen in Figure 5-23. An investigation of corrosion products was done using SEM, Raman mapping, EDX, XRD and FTIR.

Following the removal of the top surface of the initial P800 grit finish of the NaCl sample, Figure 5-7 and Figure 5-8 reveal attacked features such as localised corrosion sites, grooving and trenching of intermetallic particles. Similar features are seen following atmospheric exposure of the ASTM ocean water droplet in Figure 5-10 and Figure 5-11.

The NaCl sample has one large anodic region which is intersecting the main body and the droplets original footprint. The corrosion site shown in Figure 5-5, Figure 5-7, Figure 5-8 are is highlighted clearly by a red boxes in Figure 5-12. In contrast, the ASTM ocean water droplet; seen in Figure 5-5, Figure 5-10, Figure 5-11 and highlighted by red circles in Figure 5-12, exhibits multiple smaller sites

which are seen only within the droplet's original footprint, contrasting to the large singular site seen intersecting the main droplet and droplet edge under the NaCl droplet (see Figure 5-12).

EDX maps show differences in location of important elements associated with anodic and cathodic sites of corrosion under NaCl droplets (Figure 5-17) and ASTM ocean water droplets (Figure 5-19). Using EDX anodic sites are shown by the presence of Cl, in the case of the NaCl droplet, and Cl and S demonstrating sulphate ions, in the ASTM ocean water sample. Al^{3+} formed from the corroded metal is expelled from the anodic sites along with H^+ formed by hydrolysis of water which will lower the pH and generate an aggressive environment. To balance charge as a result of localised attack, Cl^- and SO_4^{2-} will be drawn to these regions. This action will lower the interfacial potential and further promote the dissolution of aluminium in these regions [74]. Under the NaCl droplet, Cl^- is concentrated to one location (Figure 5-17) whereas the ASTM ocean water shows Cl^- and SO_4^{2-} over the entire foot print of the originally deposited droplet (Figure 5-19). The difference between the distribution of Cl^- and corrosion behaviour could be due to the presence of sulphates present in ocean water. S and Cl have been seen previously within corrosion pits, using EDX, following coastal and industrial exposures [12, 22, 24]. This phenomenon has previously been investigated on stainless steels and sulphates were found residing in corroded crevices [190]. Multiple sites seen on the ASTM ocean water AA2024-T3 sample could be explained by competitive ion migration. Whereby the aggressive ion moves towards corrosions sites in order to balance the production of Al^{3+} and H^+. The effects of Cl^- ions migration is reduced due

sulphate being more easily adsorbed into the passive oxide film than Cl⁻ [191]. This could result in a larger distribution of anodic sites as Cl⁻ migration is reduced. Sulphate is also a known ion inhibitor [24, 191-193]. This inhibition could cause easier passivation and as a consequence lead to many smaller sites in ASTM ocean water droplets.

Sodium sulphate precipitates out of solution at 90%, and its presence can be seen in a dried droplet in Figure 5-1 using XRD. At 85% RH used for these experiments (shown in Table 3-8) sodium sulphate will effloresce out of solution and is thus unlikely to reduce the rate of corrosion processes in environmental conditions studied [133] (ASTM ocean water constituents Table 3-2). This suggests cathodic processes could play a role in the differences in corrosion site number and distribution.

Further analysis of anodic sites on NaCl, using Raman mapping in the regions Cl⁻ is found using EDX, revealed the spectrum of anodic region 'Average 2' in Figure 5-14 on the NaCl droplet and 'Average 3' Figure 5-15 on the ASTM ocean water droplets. Raman peaks are seen at 630 cm^{-1} and 1350 cm^{-1} under both droplets. These spectra are for AA2024-T3 strongly under NaCl and less so under ASTM ocean water droplets, however are not seen under ASTM ocean water droplets on AA1050 corroded. Figure 5-22 is used to analyse these peaks in more detail, due to their abundance under the anodic region of NaCl highlighted by a green and orange boxes. Figure 5-22 (g) shows the average spectrum and the correlating region on a Raman PCA map in (d) compared to Raman spectrum and maps of CuO and Cu$_2$O. Other Raman experiments have measured similar peaks in Cu rich particles on AA2024-T3 at 630 cm^{-1} [109].

Cu is likely to form in anodic regions as dealloying of AA2024-T3 can leave copper rich zones [15, 84, 88, 150, 194]. Cu ion formation has been previously documented under full immersion conditions in AlCu alloys [195]. The oxidation of Cu^+ and Cu^{2+} is dependent on pH and local potential. These can be dictated by the amount of metal ions produced, more metal ions would result in a lower pH. During the corrosion of Cu a higher pH has shown oxidise CuO and lower pH oxidise Cu_2O [196]. The low pH found in the large corrosion site may lead to the production of Cu_2O.

NaCl samples (Figure 5-7 (a)) after immersion in nitric acid and after P4000 grit polish (Figure 5-8 (i)), ASTM ocean water droplets before (Figure 5-10(a)) and after immersion in nitric acid (Figure 5-11 (d)), and after P4000 grit polish all show grooving around intermetallic particles. Grooving can be used to identify these regions as cathodic. Trenching/grooving is seen in both salt types outside the original footprint. This happens in a region that appears to have secondary spreading of the deposited droplet, suggesting these were region where pH is high owing to an abundance of OH^- ions. OH^- ions present are produced during cathodic reactions. Trenching/grooving is associated with preferential dissolution next to cathodic particles in cathodically-charged regions under and at the edge of the droplet. Uniform dissolution of the passive film is caused by locally high pH around intermetallic particles. Due to aluminium's amphoteric nature, intermetallic particles are attacked less by the high pH. This phenomenon is very well documented in AA2024-T3 in alkaline regions [83, 103, 197].

Spreading behaviour in the two salts is explained by the distribution of anodic and cathodic regions. OH⁻ ions in the cathodic regions draw in and promote the movement on Na^+ ions in the solution [198]. Spreading and the corrosion behaviour observed in the NaCl droplet agrees with observations seen in AA7075-T6 [136], where initiation close to the droplet edge in drying droplets results in a high concentrations of ions in this region. These ions diffuse to the edge of the droplet where, in high concentrations, they absorb water from the atmosphere and form secondary droplets outside the initial droplet footprint as NaOH is soluble [133]. EDX maps of both NaCl (Figure 5-17) with Na found in both the droplet and spreading region and ASTM ocean water (Figure 5-19) with Na in its spreading regions, confirms the migration of Na to cathodic areas.

The OW spreading region is smaller due to the insolubility of Mg-OH hydroxides as they react with CO_2 to form regions of Hydrotalcite at the droplet edge [133, 199]. The evidence of Mg in these regions in OW can be seen in Figure 5-19. The precipitation of insoluble Mg-OH hydroxides could restrict the propagation of the spreading region and thus reduce the droplets cathodic area reducing the drive for corrosion. Corrosion products have been shown to reduce corrosion over time, as they are formed their literature has shown a porous morphology which slows the movement of ions in solution [13, 121]. This physical barrier between anodic and cathodic regions on OW may reduce corrosion.

5.3.2   The Nature of Corrosion Products of AA2024-T3

The presence of aluminium oxy-hydroxides is well established in the field of aluminium corrosion. However, few investigations have focused on the chemical compounds which are formed. Many assume, due to the presence of Al, O and

H identified by methods such as EDX, that the corrosion products formed are mainly Boehmite (γ-AlO(OH)) [118], Nordstrandite (Al(OH)$_3$) and Bayerite (β-Al(OH)$_3$) [105]. Other methods such as FTIR [12, 22, 24] and XRD [12, 55, 111, 112, 145]have been able to yield more detailed compositions without looking at an entire droplet. Although looked at and speculated upon in atmospheric conditions, little work on the specific composition of corrosion products has been done under ASTM ocean water droplets and thus the processes around how they are formed.

5.3.2.1 Corrosion Products Under NaCl Water Droplets

Using a combination of investigation methods (Raman, XRD, FTIR and EDX), neither sample (NaCl Figure 5-16 and ASTM ocean water Figure 5-18) exhibited well documented aluminium based corrosion products such as Boehmite, PsudoBoehmite and Bayerrite [110, 118]. Corrosion products are seen to differ between NaCl and ASTM ocean water samples. Figure 5-14 shows three averaged regions of three main Raman signals found on the NaCl sample taken from Raman mapping scans. In Figure 5-16 one signal was confirmed to match that of Dawsonite (NaAlCO$_3$(OH)$_2$), while the other distinct signal is speculated to be either Cu$_2$O or CuO a more closely analysed in Figure 5-22. Separating anodic sites to possible copper constituents and Dawsonite to the cathodic regions, Dawsonite is seen in the spreading region and main bulk of the droplet, where Na is also seen using EDX (Figure 5-17). The effects of atmospheric CO$_2$ are shown most prominent in regions Dawsonite is seen, owing to the formation of this carbonate-based corrosion product via the incorporation of CO$_2$ into the droplet forming HCO$_3$. This HCO$_3$ reacts with OH$^-$

and $AlOH^{2+}$ along with Na^+ present in the solution to form Dawsonite. The influence of environment and thermodynamics on the precipitation of Dawsonite has been proposed using FTIR, GIXRD on AA1060 [108]. Other studies have seen the presence of Dawsonite and established the role of Na, using EDX maps and FTIR to confirm its abundance [108], along with the effects of atmospheric CO_2 on its precipitation over commonly recorded precipitates such as Boehmite [112]. Neither studies mapped the precipitation of Dawsonite related to droplet corrosion sites.

5.3.2.2 Corrosion Products Under ASTM Ocean Water Droplets

Raman mapping of corroded ASTM ocean water on AA2024-T3 shows three corrosion products with clear regions between the main bulk of the droplet, the edge of the main droplet and some inside regions as well as the spreading regions (Figure 5-15). These regions have confirmed compounds associated to them (Figure 5-18). The main body of the droplet is dominated by Felsöbányaite - $(Al_4(SO_4)(OH)_{10} \cdot 4H_2O)$, the edge and some of the main droplet body is Hydrotalcite – $Mg_6Al_2CO_3(OH)_{16} \cdot 4(H_2O)$ and the spreading region is confirmed to be Dawsonite $(NaAlCO_3(OH)_2)$. EDX of elements in these regions help confirm these findings from Raman mapping. Figure 5-19 shows Na within the spreading region caused by ion balance of Na^+ migration, similar behaviour to that seen in the NaCl experiment in Figure 5-16. The presence of Dawsonite can be mostly associated to the droplet's spreading region. With the centre of the droplet likely to be the net anode, the edges and spreading regions of the droplet are left to become the net cathode. The cathodic reactions produce OH^- ions. Cations presented in the solution, such as Na^+, are attracted towards

these negative anions. This coupled with the morphology of the edge of the droplet allowing for easy access of gases such as CO_2 [112], which will result in the precipitation of Dawsonite [108]. The corrosion product Felsöbányaite is seen in the main body of the droplet, where sulphur is confirmed with EDX in Figure 5-19 and is confined to just the middle region of the droplet. It is common to see aluminium sulphate hydrates in the corrosion products of aluminium in marine atmospheres [104], and Felsöbányaite has previously been identified in atmospheric conditions [200] and is owed to atmospheric SO_2. Theories consider that sulphur from the droplet environment is incorporated into the surface layer of aluminium oxide and then into the corrosion products produced [104, 112, 191, 201]. Mechanisms of absorption of Cl^- into the oxide film is believed to be weaker than SO_4 [191, 193, 201, 202] promoting the precipitation of Felsöbányaite over other aluminium hydroxides in these anodic areas. Hydrotalcite is seen at the edge of the droplet between the main body of the initially deposited droplet and the spreading region.

Magnesium is seen mirroring the same pattern of deposition in both Raman and EDX as seen in Figure 5-19. It is not uncommon to see Mg-OH based deposit at the edge of atmospheric droplets due to their insoluble nature [133, 199]. Mg-OH based deposits usually causes droplets to halt spreading [147, 198, 203]. Hydrotalcite is a naturally occurring mineral and is usually identified during the Bayer processing of refining bauxite [204]. Hydrotalcite forms when ocean water, Mg and Al salts come into contact. The presence of Mg^{2+} and $Al(OH)^{4-}$ will result in the formation of Hydrotalcite. Hydrotalcite usually forms over the more commonly expected Bayerite and Boehmite in environments that are

152

alkaline [205, 206]. The formation of Hydrotalcite outcompetes the more thermodynamically stable anions such as CO_3^{2-} and Cl^- for bonding sites [124]. A Raman peak at 1350 cm^{-1} across both AA2024-T3 samples is observed. This is likely to be a O-C-O v_3 symmetric stretch.

5.3.3 Corrosion Products on AA1050

Figure 5-23 shows Raman mapping of ASTM ocean water on AA1050. The main body of the droplet is dominated by Felsöbányaite - $(Al_4(SO_4)(OH)_{10}\cdot 4H_2O)$, and an unknown spectrum in a small region where spreading is seen. From Figure 5-3 the sharp peak at 1000 cm^{-1} of a dried droplet on a glass slide, shows a close correlation for the Raman peak at 1000 cm^{-1} found in this spreading region of the corroded droplet. This suggests that the Raman signal from this area could be due to salt residue left on the sample after cleaning with methanol. The broad peak at approximately 700- 990 cm^{-1} is seen throughout the gathered spectra from the corrosion products and is the Raman signal collected from the AA1050 metal surface. Other Raman studies on aluminium alloys have seen similar background metal spectra in these ranges [109]. EDX maps in Figure 5-24 agree with the Raman signal gathered. EDX maps showing primarily the presence of sulphur correlate to the Felsöbányaite Raman map in Figure 5-23. Oxygen is present on all the corrosion products seen on the sample, and chlorine signals are observed in the small spreading region. The higher magnified EDX images highlight the region of chloride in the spreading region. Unlike on the AA2024-T3 sample, AA1050 shows no evidence of the presence of Dawsonite or Hydrotalcite. It is well established that due to the different alloying additions of AA1050 vs

AA2024-T3, corrosion rates and susceptibly is reduced in the AA1050 alloy. A reduction in the production of OH^-, due to a reduced rate of corrosion, could contribute to the reduced amount of spreading seen in the AA1050 sample. Na^+ ions would be less compelled to migrate to less cathodically charged regions. The droplet edge being thicker will slow the diffusion of gases such as CO_2 will also contribute to the lack of Dawsonite seen on this sample compared to corrosion products found on AA2024-T3.

5.3.4 Summary

The dominant species of corrosion product found in both NaCl droplet and ASTM ocean water droplets on corroded AA2024-T3 is Dawsonite. FTIR spectrum plotted in Figure 5-20 and grazing angle XRD patterns seen in Figure 5-21 both confirm the dominant precipitation of Dawsonite. However it is not seen in AA1050 and therefore Dawsonite precipitation is attributed to high corrosion rates.

The knowledge of Dawsonite being present during high rates of corrosion on aluminium alloy, along with it being both Raman and FTIR active make its detection useful for application into CBM [25-27].

5.4 Conclusions

The atmospheric corrosion products formed on AA2024-T3 and AA1050 were investigated with Raman mapping, FTIR, EDX and XRD.

1. Under NaCl droplets there are fewer larger sites of corrosion where Cl is predominantly detected by EDX.

2. Under ASTM ocean water droplets on AA2024-T3 there are multiple small corrosion sites found where Cl and S is prominently detected by EDX.

3. Under NaCl droplets on AA2024-T3 Dawsonite is the dominant corrosion product in both the main droplet region and the spreading region.

4. Under ASTM ocean water droplets on AA2024-T3 Dawsonite and Felsöbányaite are the dominant corrosion products. Dawsonite is found in the spreading region and Felsöbányaite is found under the main body of the droplet. Other corrosion products are seen including Hydrotalcite.

5. The corrosion products present on AA2024-T3 are dominated by Dawsonite. This has been confirmed by FTIR, grazing angle XRD and supported by Raman mapping.

6. Under ASTM ocean water droplets on AA1015 Felsöbányaite is prominently and detected by the presence of S in EDX.

7. Dawsonite was not seen in corroded droplets of AA1050 alloy and was attributed to a reduce rate of corrosion.

6. WET-DRY ATMOSPHERIC CYCLING OF AA2024-T3

6.1 Introduction

Wet-dry cycling is a natural environmental phenomenon that aircraft are subject to throughout their service lifetime. Atmospheric corrosion tests are often carried out in constant RH conditions. Wet-dry cycling leads to variation in parameters that control atmospheric corrosion such as, droplet height, electrolyte concentration [128, 132]. A growing and shrinking droplet will have constantly changing diffusion distances for an inner anodic and outer cathodically dominant regions [14]. These factors in turn altering the diffusion distance within a droplet of gases such as O_2, dramatically effecting corrosion behaviour. Consequently, it would be unreasonable to expect corrosion processes to be the same as with those found in steady state conditions. A small handful of studies have shown that damage accumulation under cyclic testing is greater than that found under steady state for AA2024-T3 [23] and other aluminium alloys [24]. Despite this, very limited work has been carried out under realistic atmospheric cyclic conditions [21]. Previous work has looked at accumulated corrosion damage at the end of a wet/dry cycling tests. The aim of this chapter is to show how this damage evolves in real time using high resolution synchrotron XMT to improve knowledge associated with kinetics, such as propagation and volume loss rates taking place on AA2024-T3.

6.2 Results

6.2.1 General Observations of Wet-Dry Cycling ASTM Ocean Water and NaCl Droplets
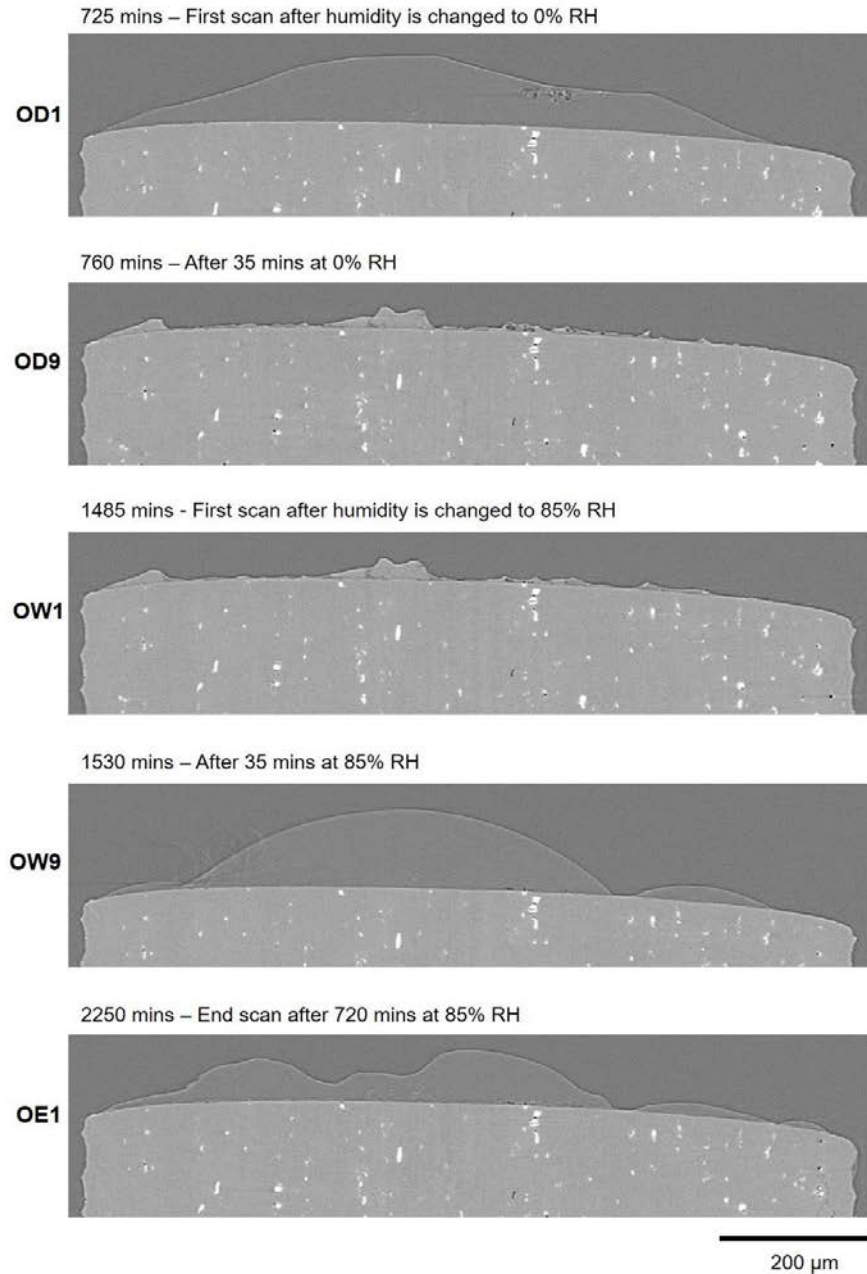
Figure 6-1 tomographic sections of the droplet behaviour on a 1mm diameter AA2024-T3 pin exposed to a 0.2 µL droplet of ASTM ocean water, giving a CDD of 1400 µg/cm^2 at a temperature of 21±2 °C (shown in Table 3-5) as it is cycled through humidity shown in Figure 3-4. OD1 is the scan taken in the first dry cycle collected at 725 mins. OD9 the last scan of the dry cycle collected at 760 mins. OW1 the first wet scan of the wet cycle collected at 1485 mins. OW9 the last wet scan of the wet cycle collected at 1530 mins. OE1 the end scan after 12 hours of wet exposure collected at 2250 mins

Figure 6-1 shows vertical tomographic sections through a 1 mm diameter AA2024-T3 pin exposed to a 0.2 µL droplet of ASTM ocean water, giving a CDD of 1400 µg/cm^2 cycled through humidity shown in Figure 3-4. The sample was scanned at the point of which humidity was changed. Each vertical section is located in the middle of the 1 mm pin. The droplet has been initially wet at 85%RH, and the first scan (OD1) shows this wet droplet 10 minutes after a change in humidity to ~3±3.0 % using silica gel orange. The droplet is not hemispherical, but is inhomogeneous in shape probably controlled by the presence of corrosion products. The second image (OD9) shows the same section after 35 minutes in a dry ~3±3.0 % RH. The droplet has evaporated, and salt crystals can be seen formed on the surface of the pin. The droplet remains absent after 12 hours in ~3±3.0 % RH and after 5 minutes in 85% RH as shown in image OW1. Salt crystals have not changed since the scan, OD9, 12 hour previously. After 45 minutes of the sample being held at 85% RH, scan OW9 shows that an irregular droplet has reformed. The droplet in OW9 has formed in two dome shaped droplets. The sample was then held at 85% RH for 12 hours. A final scan, (OE1), was collected after 2250 mins of exposure. The droplet though still present, can been seen to have formed an irregular geometry rather than a dome.
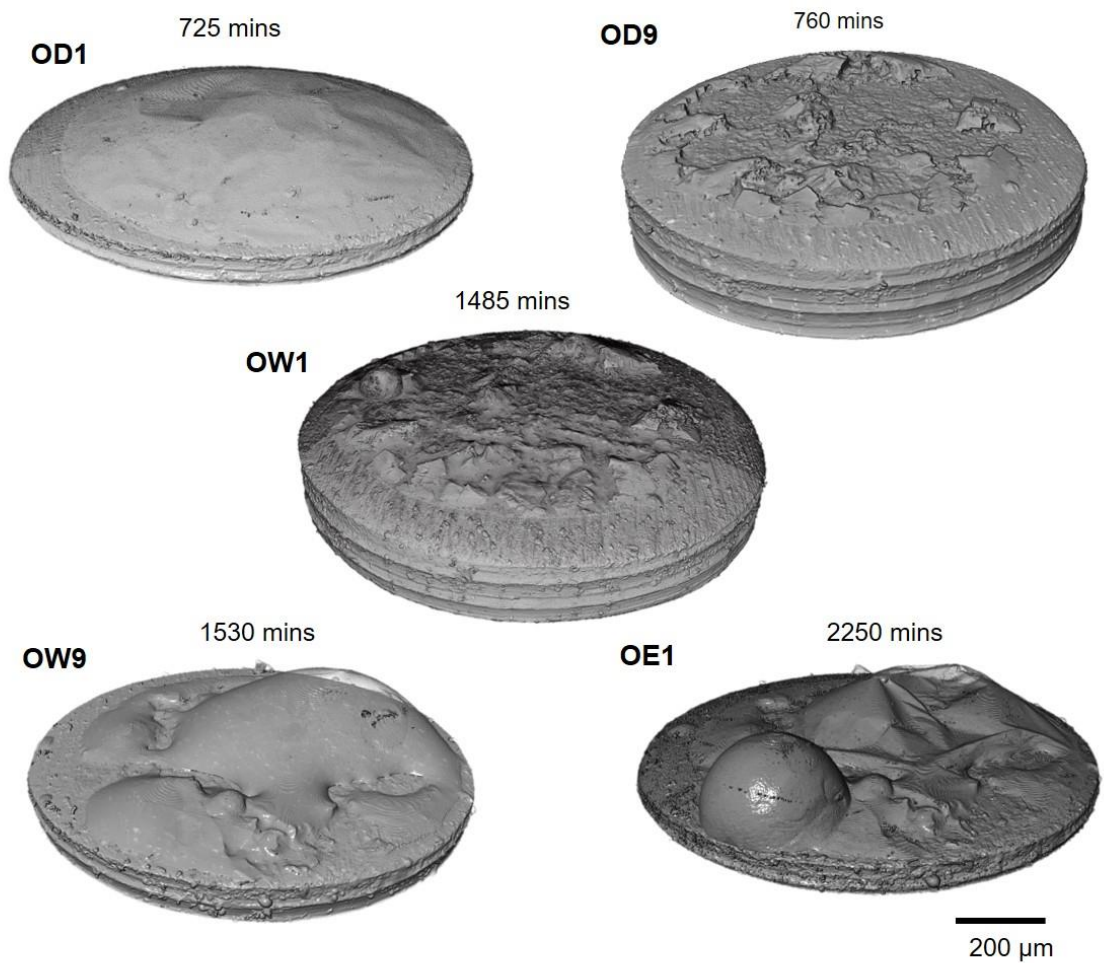
Figure 6-2 3D image of the droplet behaviour on a 1 mm diameter AA2024-T3 pin exposed to a 0.2 µL droplet of ASTM ocean water shown in Figure 6-1, giving a CDD of 1400 µg/cm^2 at a temperature of 21±2 °C (shown in Table 3-5) as it is cycled through humidity shown in Figure 3-4, introduced Figure 6-1. OD1 is the scan taken in the first dry cycle collected at 725 mins. OD9 the last scan of the dry cycle collected at 760 mins. OW1 the first wet scan of the wet cycle collected at 1485 mins. OW9 the last wet scan of the wet cycle collected at 1530 mins. OE1 the end scan after 12 hours of wet exposure collected at 2250 mins. Time in mins is shown above each droplet image.

159

Figure 6-2 shows 3D images of the droplet presented Figure 6-1. 3D images allow for the entire droplet to be seen in each dry or wet cycle. OD1 shows an inhomogeneous shaped droplet retreating from the edge of the pin probably as a result of corrosion products present in the droplet. OD9 and OW1 show surface deposits assumed to be corrosion products and efflorescence salts on the surface of the pin. OW9 shows the re-wetted pin, with irregular regions in the droplet where the maximum height is displaced away from the original centre of the as-deposited droplet.
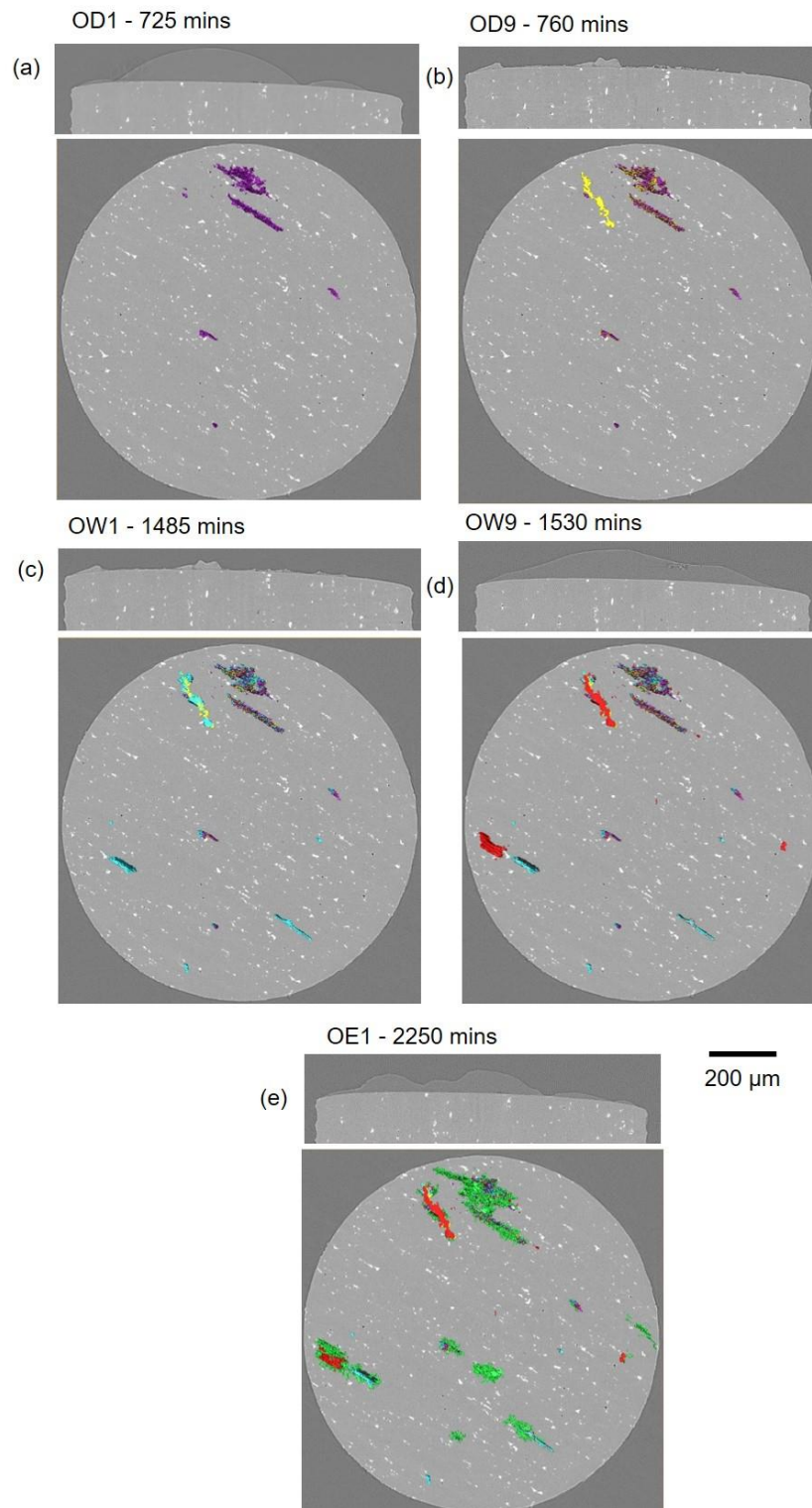
Figure 6-3 tomographic sections of the sample shown in Figure 6-1 and Figure 6-2. Vertical sections are through the centre of the pin and horizontal sections are just below the surface of the pin. Each colour change reveals additional material loss at each time interval. (a) OD1 is the scan taken in the first dry cycle at 725 mins, material loss is shown in purple. (b) OD9 the last scan of the dry cycle at 760 mins, material loss is shown in yellow. (c) OW1 the first wet scan of the wet cycle at 1485 mins, material loss is shown in cyan. (d) OW9 the last wet scan of the wet cycle at 1530 mins, material loss is shown in red. (e) OE1 the end scan after 12 hours of wet exposure at 2250 mins, material loss is shown in green.

161

Figure 6-3 shows a series of vertical sections through the centre of the pin and horizontal sections just below the top of a pin shown Figure 6-1 and Figure 6-2. In each successive image, the newly visible corrosion damage is presented in a different colour. Following 12 hours of exposure to 85% RH (a) OD1 shows the first scan following a change in RH to ~3±3.0 % RH. After 45 minutes of exposure to ~3±3.0 % RH Figure 6-2 (b), OD9 shows a new corrosion site shown in yellow. The sample was then left in ~3±3.0 % RH for 12 hours. The relative humidity was changed back to 85% RH and scan OW1, in Figure 6-2 (c) shows the first wet scan after the RH was changed. Three additional corrosion sites can be seen. Figure 6-2 (d) shows scan OW9 taken 45 mins after the sample was held at 85% RH. Current sites are seen to grown, as well as additional sites having initiated during this wet phase. Figure 6-2 (e) OE1 shows growth of existing sites following a 12 hour wet phase of cycling. Additional corrosion sites have also initiated.

725 mins – First scan after humidity is changed to 0% RH

NaD1

750 mins – After 35 mins at 0% RH

NaD5

1485 mins - First scan after humidity is changed to 85% RH

NaW1

1520 mins – After 35 mins at 85% RH

NaW7

2250 mins – End scan after 720 mins at 85% RH

NaE1
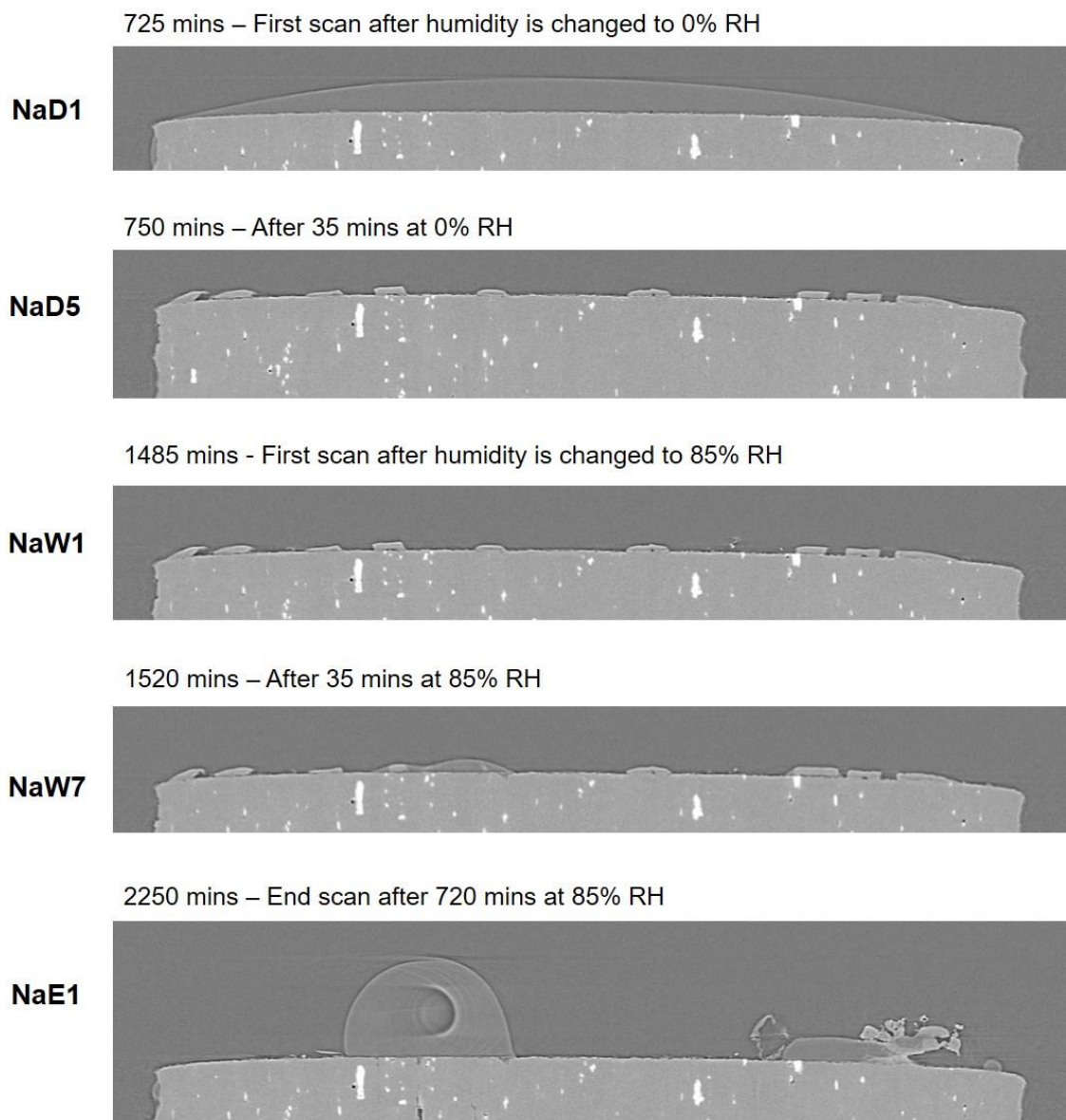
Figure 6-4 tomographic sections of the droplet behaviour on a 1mm diameter AA2024-T3 pin exposed to a 0.2 μL droplet of NaCl, giving a CDD of 500 μg/cm^2 at a temperature of 21±2 °C (shown in Table 3-5) as it is cycled through humidity shown in Figure 3-5. NaD1 is the scan taken in the first dry cycle at 725 mins. NaD9 the last scan of the dry cycle at 760 mins. NaW1 the first wet scan of the wet cycle at 1485 mins. NaW9 the last wet scan of the wet cycle at 1530 mins. NaE1 the end scan at 2250 mins after 12 hours of wet exposure.

Figure 6-4 shows vertical sections through a 1mm diameter AA2024-T3 pin exposed to a 0.2 µL droplet of NaCl, giving a CDD of 500 µg/cm^2 at a temperature of 21±2 °C as it is cycled through humidity as shown in Figure 3-5. Tomographic imaging of the sample started 5 minutes after a change in humidity and continued at 5-minute intervals for a period of 45 minutes. In each vertical section intercepting the middle of the 1mm pin white intermetallic particles can be seen. Following the initial 12 hours of exposure to a wet cycle (85% RH) the first scan 5 minutes after a humidity change to a dry cycle (~3±3.0 % RH) NaD1 shows the droplet uniformly spanning the surface of the pin, and as the humidity reduces over the 45 minutes at ~3±3.0 % RH the droplet undergoes drying and cubic salt crystals form as seen in NaD5. The sample is then held at ~3±3.0 % RH for a further 12 hours. The scan 5 minutes after a change to 85% RH (NaW1) shows that the droplet remains absent and the salt crystals have not changed since the previous NaW1 scan. Following exposure of the sample for 30 minutes at 85% RH, (NaW7) the droplet has not still fully reformed however a small wet region in the centre of the pin showing a salt crystal deliquesces/experience deliquescence. After exposure to these wet conditions of 85% RH for 12 hours (NaE1) shows that 2 smaller droplets are now present but which are irregular in shape.
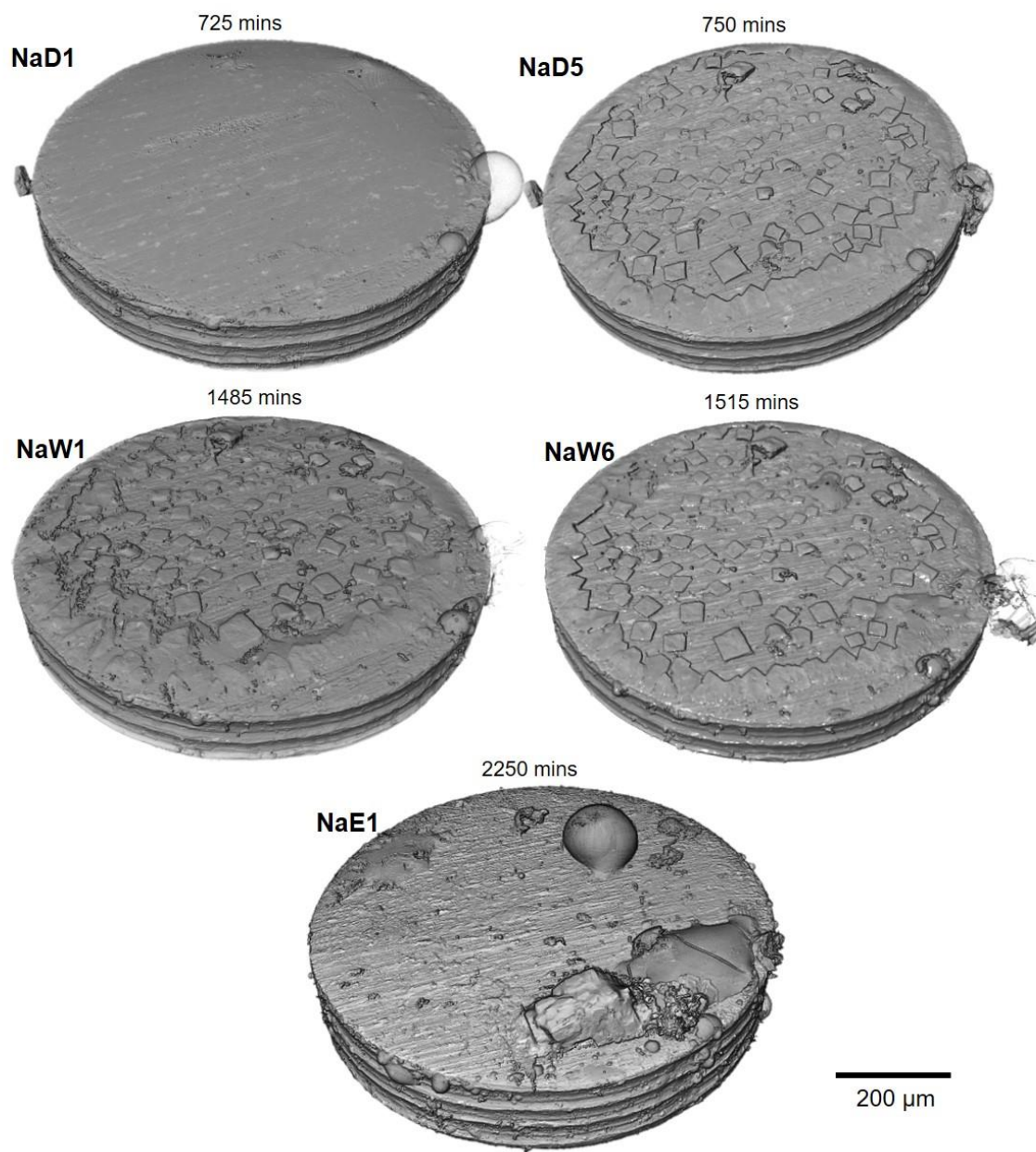
Figure 6-5 3D images of the droplet behaviour of the sample introduced in Figure 6-4. NaD1 is the scan taken in the first dry cycle. NaD9 the last scan of the dry cycle. NaW1 the first wet scan of the wet cycle. NaW9 the last wet scan of the wet cycle. NaE1 the end scan after 12 hours of wet exposure. The relative time interval for each wet or dry scan type are shown above the 3D images.

Figure 6-5 shows 3D images of the sample shown in Figure 6-4. 3D images allow for the entire droplet to be seen in each dry or wet cycle. NaD1 shows the droplet after 12 hours exposure to 85% RH and 5 minutes following a humidity change to ~3±3.0 %RH for a dry cycle. A regular shaped droplet can be seen on top of the along with larger droplet to the edge of the pin which is not seen in tomographic sections presented in Figure 6-4. After 45 minutes at ~3±3.0 % RH in the dry cycle (NaD5) and 12 hours after being held at ~3±3.0 % RH and 5 minutes of 85% (NaW1) cubic surface deposits assumed to be NaCl salts can be seen on the surface of the pin. The small droplet seen at the beginning of the drying cycle is shrivelled and dehydrated. After 45 minutes of exposure to a wet cycle (85% RH) environment NaW6 the pin shows, unclear, or only partial reformation of the droplet. The small droplet from NaD1 remains dried out. NaE1 shows the pin after being held for 12 hours in a wet cycle (85% RH) has partially reformed into two main droplet bodies. The small droplet from NaD1 is gone.
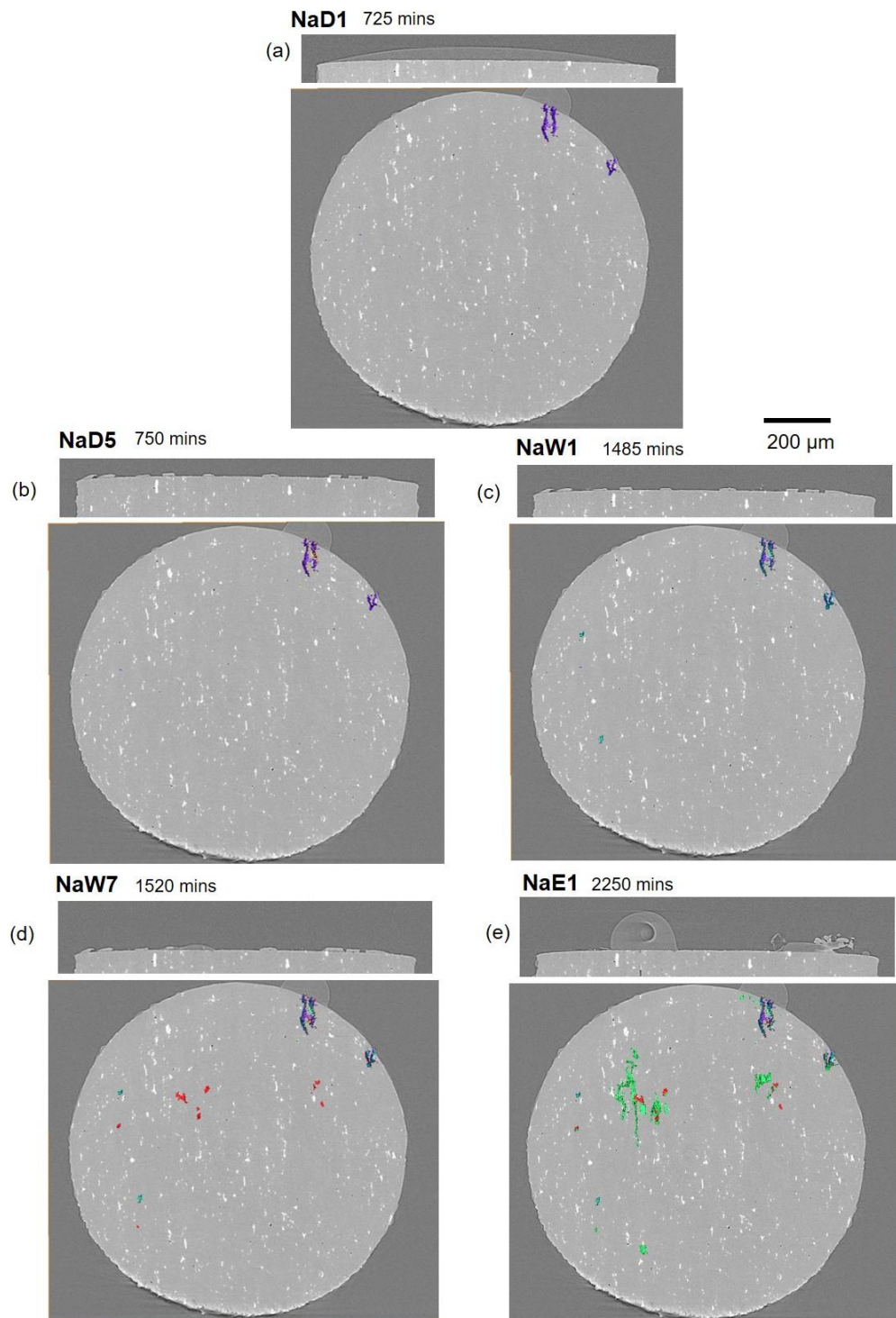
Figure 6-6 tomographic sections of the corrosion sites of the sample shown in Figure 6-4 and Figure 6-5. Each colour change reveals additional material loss at each time interval. (a) NaD1 is the scan taken in the first dry cycle, material loss is shown in purple. (b) NaD9 the last scan of the dry cycle, material loss is shown in yellow. (c) NaW1 the first wet scan of the wet cycle, material loss is shown in cyan. (d) NaW9 the last wet scan of the wet cycle, material loss is shown in red. (e) NaE1 the end scan after 12 hours of wet exposure, material loss is shown in green.

167

Figure 6-6 presents horizontal and vertical tomographic sections of the sample shown in Figure 6-4 and Figure 6-5. Corrosion sites are shown at the start and end of dry and wet cycles are shown using additional colour segmentation. Each tomographic section is shown with one vertical section of the middle of the pin and a top down horizontal section. The horizontal section highlights corrosion sites. Following 12 hours exposure to a wet (85% RH) environment Figure 6-6 (a) NaD1 shows corrosion sites present after 5 minutes of exposure to a dry ~3±3.0 % RH. After 45 minutes being held in a dry environment Figure 6-6 (b) NaD5 showed no new corrosion sites. During 12 hours of being held in a dry cycle at ~3±3.0 % RH Figure 6-6 (c) NaW1 shows the initiation of two corrosion sites. The samples was then held in a wet environment of 85% RH for 45 mins (Figure 6-6 (d) NaW7). More corrosion sites initiated during this wet phase in 45 mins at 85% RH. The sample was then held in this wet (85% RH) environment and scanned after 12 hours (Figure 6-6 (e) NaE1) shows that the sites initiated during the second wet phase had grown.

6.2.2 Corrosion Site Observations Using High Temporal Resolution XTM

6.2.2.1 Corrosion Behaviour of a Wet-dry Cycled ASTM ocean water Droplet
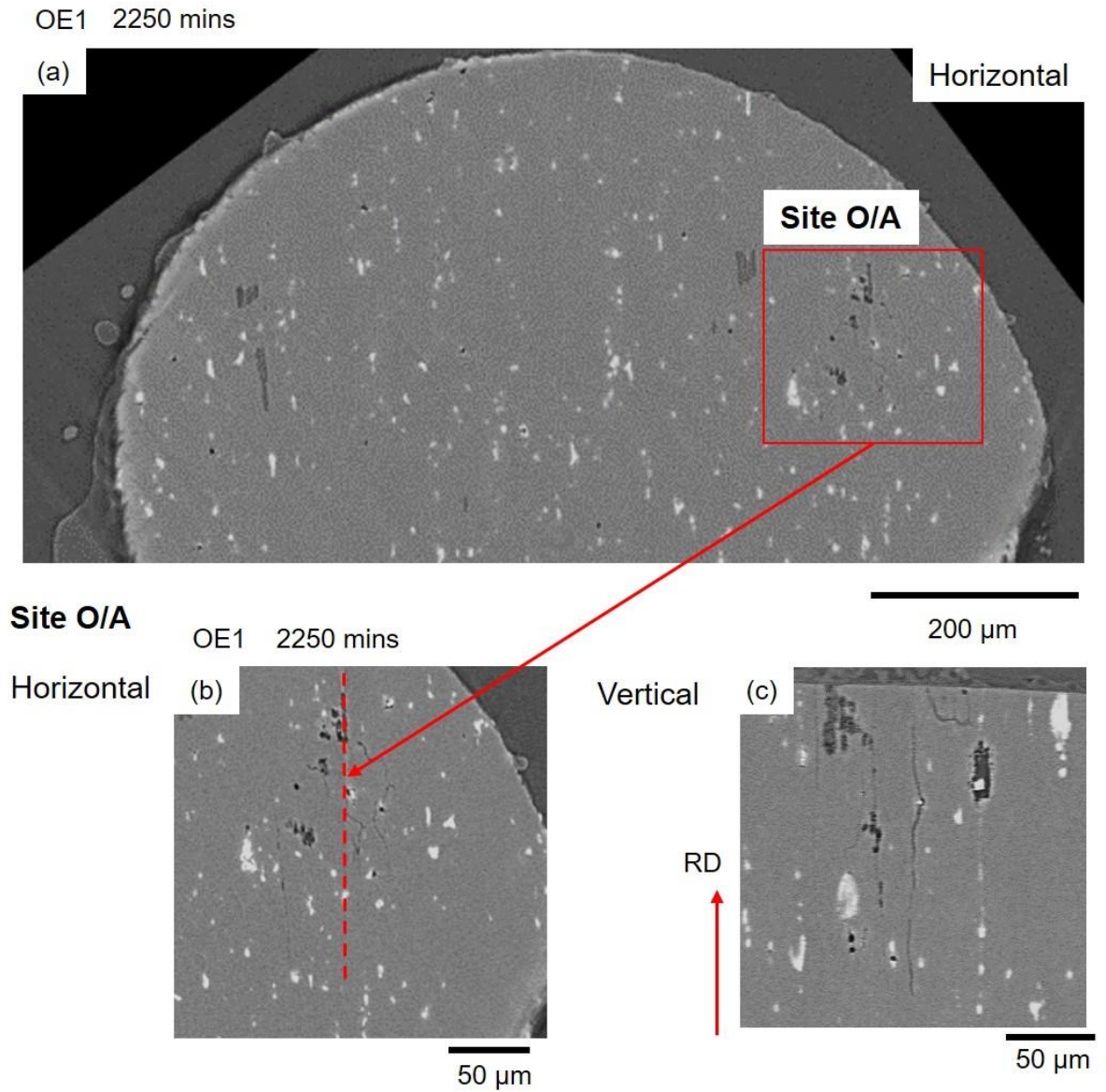
Figure 6-7 tomographic sections of sample shown in Figure 6-1 and Figure 6-2 and Figure 6-3 of a corrosion site O/A (located in red box) at the end of 2250 mins of exposure (OE1). (a) shows a top down horizontal section of the corroded pin sample. (b) shows a magnified section of (a). (c) shows a vertical section of site O/A the location of which the vertical section is taken from is highlighted by a red dotted line.

Figure 6-7 shows vertical sections through a 1mm diameter AA2024-T3 pin exposed to a 0.2 µL droplet of ASTM ocean water, giving a CDD of 1400 µg/cm^2 at a temperature of 21±2 °C as it is cycled through humidity shown Figure 3-4. (a) shows tomographic sections of a corrosion site labelled O/A which is located in red box at the end of 2250 mins of exposure to a wet-dry-wet cycle (OE1). A section of this site is taken from the dotted red line in (b) and is shown in (c). Three morphologies of corrosion sites can be seen in vertical slice (c). From left to right, a pit like corrosion site ascending into a long, thin intergranular like in corrosion morphology. Next to this site a predominantly intergranular like corrosion site is seen, snaking back towards the surface and down adjacent to the rolling direction. The final site seen is narrow at the metal surface and has propagated towards and intermetallic particle where it is seen expanding up around this particle.
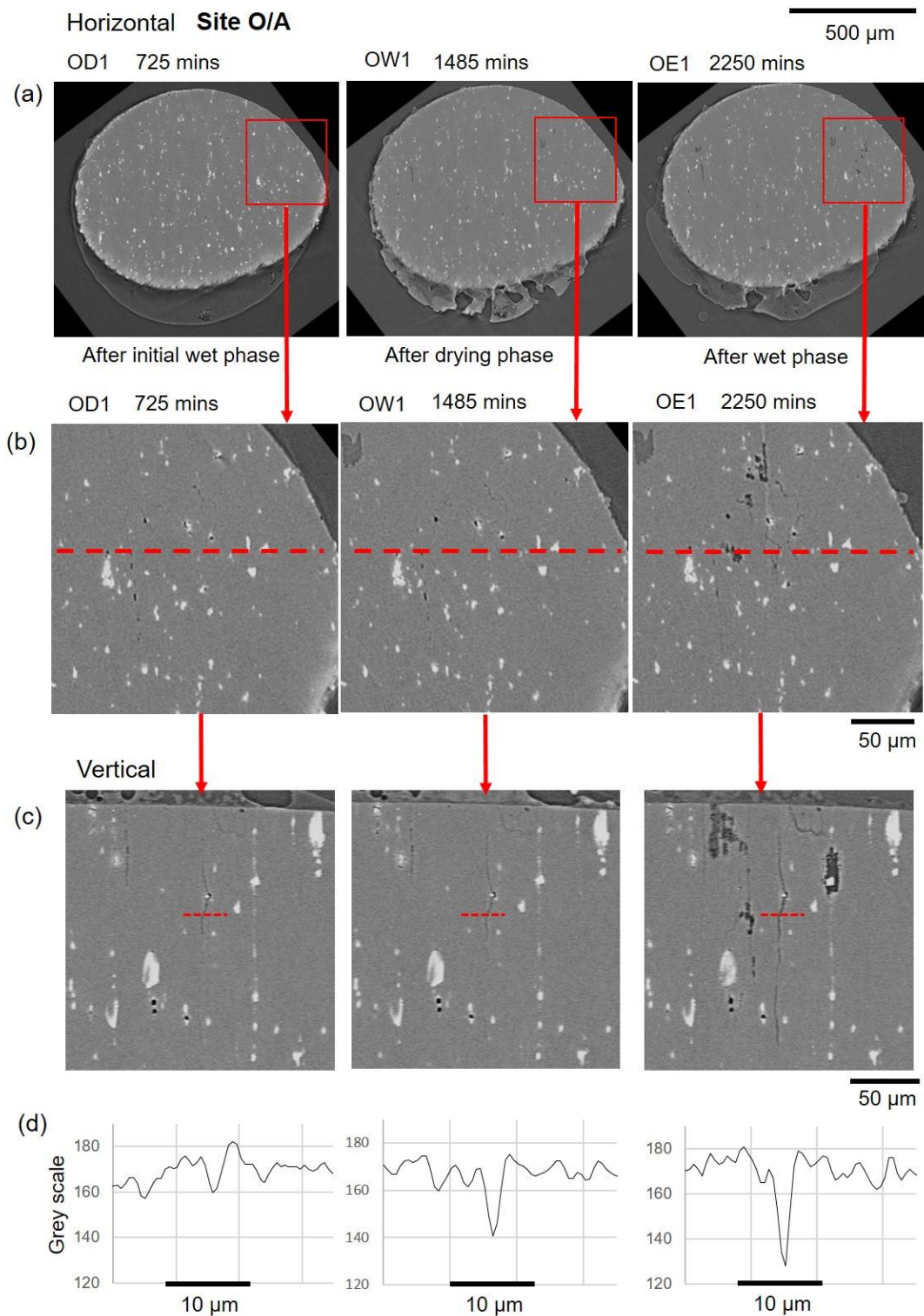
Figure 6-8 tomographic sections of the corrosion site shown in Figure 6-7 of the sample shown in Figure 6-1, Figure 6-2 and Figure 6-3. The corrosion site O/A (located in red box) is shown at the end of 2250 mins of exposure (OE1). Each row shows three time intervals at 725 mins, 1486 mins and 2250 mins. (a) shows a top down horizontal section of the top surface of the pin. The corrosion site O/A is highlighted with a red box. (b) shows a magnified section of site O/A at each time interval. (c) shows a vertical section of site O/A, the region of this section is highlighted by a red dotted line in (b). (d) row of graphs plotting the grey scale values of the corrosion site shown in (c) the location of the 10 μm measurement is shown in red.

171

Figure 6-8 shows site O/A from Figure 6-7. The three rows show different time intervals within the wet-dry-wet scan to show the development if the site over time; part (a) shows a horizontal section of the top of the pin, (b) shows a magnified image of site A/O as highlighted by the red boxes in (a). The vertical sections seen in (c) are taken from along the dotted red line shown in image (b). The deepest corrosion site is observed in image (c) and is seen to increase in thickness from 725 mins to 2250 mins. The graphs presented in (d) show a 10 µm line scan where grey scale has been measured through the corrosion site; the grey scale values are seen to increase during each time. The increase in darkness of the grey scale values is consistent with an increase in fissure width.
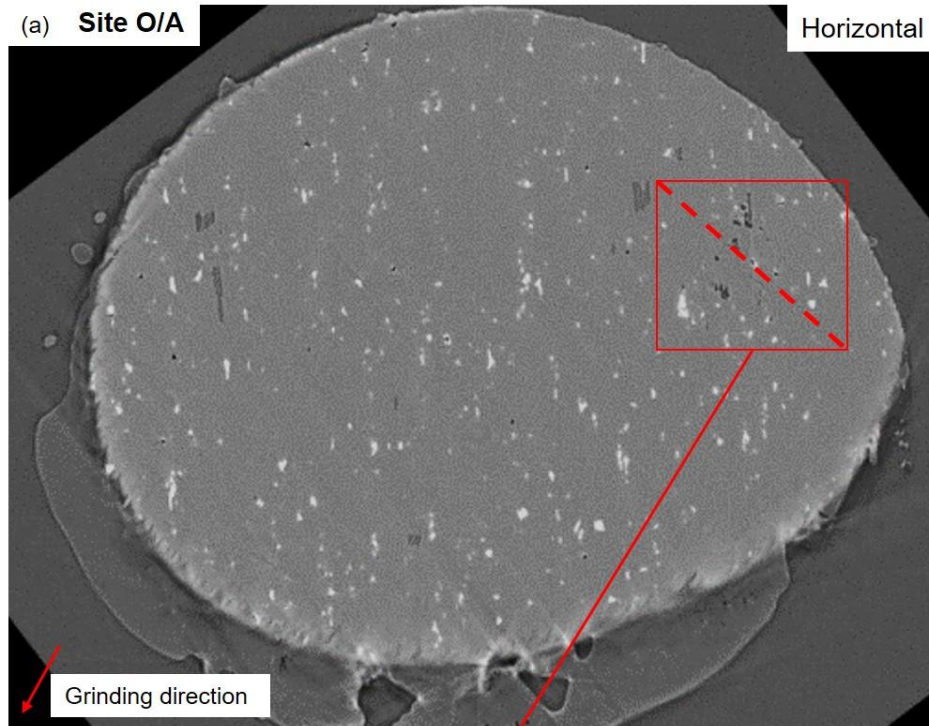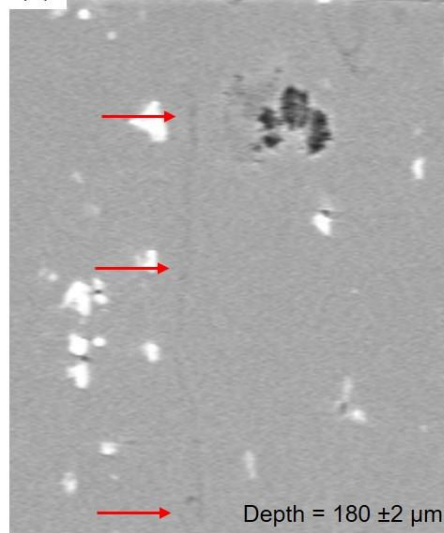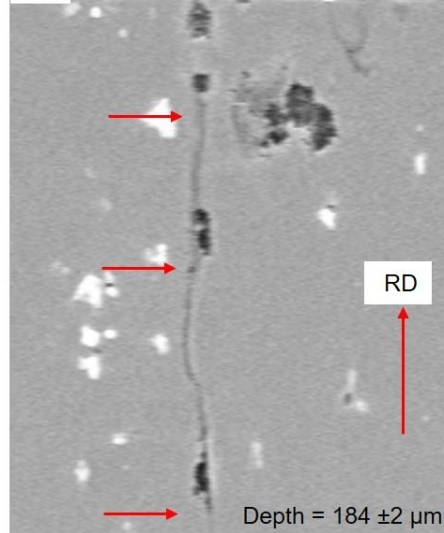
Figure 6-9 tomographic sections of a corrosion site O/A (located in red box) at two intervals of exposure (OD1 and OE1) shown in Figure 6-7 and Figure 6-8. (a) shows a horizontal tomogram of the site O/A. The corrosion site is located in red box. Rolling and grinding line directions are indicated using arrows. (b) and (c) show resections of corrosion site O/A adjacent to the grinding lines at 725 mins and 2250 mins. Arrows indicate the location of the corrosion site. Depth of the site is indicated in μm, mean ± standard deviation is determined (protocol shown in section 3.3.5 via section 3.3.5.1).

Figure 6-9 shows site O/A from Figure 6-7 at two different time intervals. The Figure 6-9 (a) shows the sample after 2250 mins exposure to a wet-dry-wet cycle and the developed corrosion site O/A is highlighted by a red box. The rolling and grinding directions are also shown with red arrows. The dotted line illustrates where the site has been re-sectioned; in this case the site has been re-sectioned perpendicular to the grinding lines. The images taken at time intervals, 725 mins and 2250 mins illustrate the growth of a corrosion site thickness at the start and end of tomography scans. Figure 6-9 (b) (OD1), taken after 720 mins of wet exposure (85% RH) next to and Figure 6-9 (c) taken after 2250 mins after 12 hours or dry (~3±3.0 % RH) and 12 hours of wet (85% RH) exposure. The corrosion site in (b) and (c) is indicated by red arrows. The corrosion site is seen to widen over time. An insignificant depth increased is seen from 180 μm ±2 to 184 μm ±2.
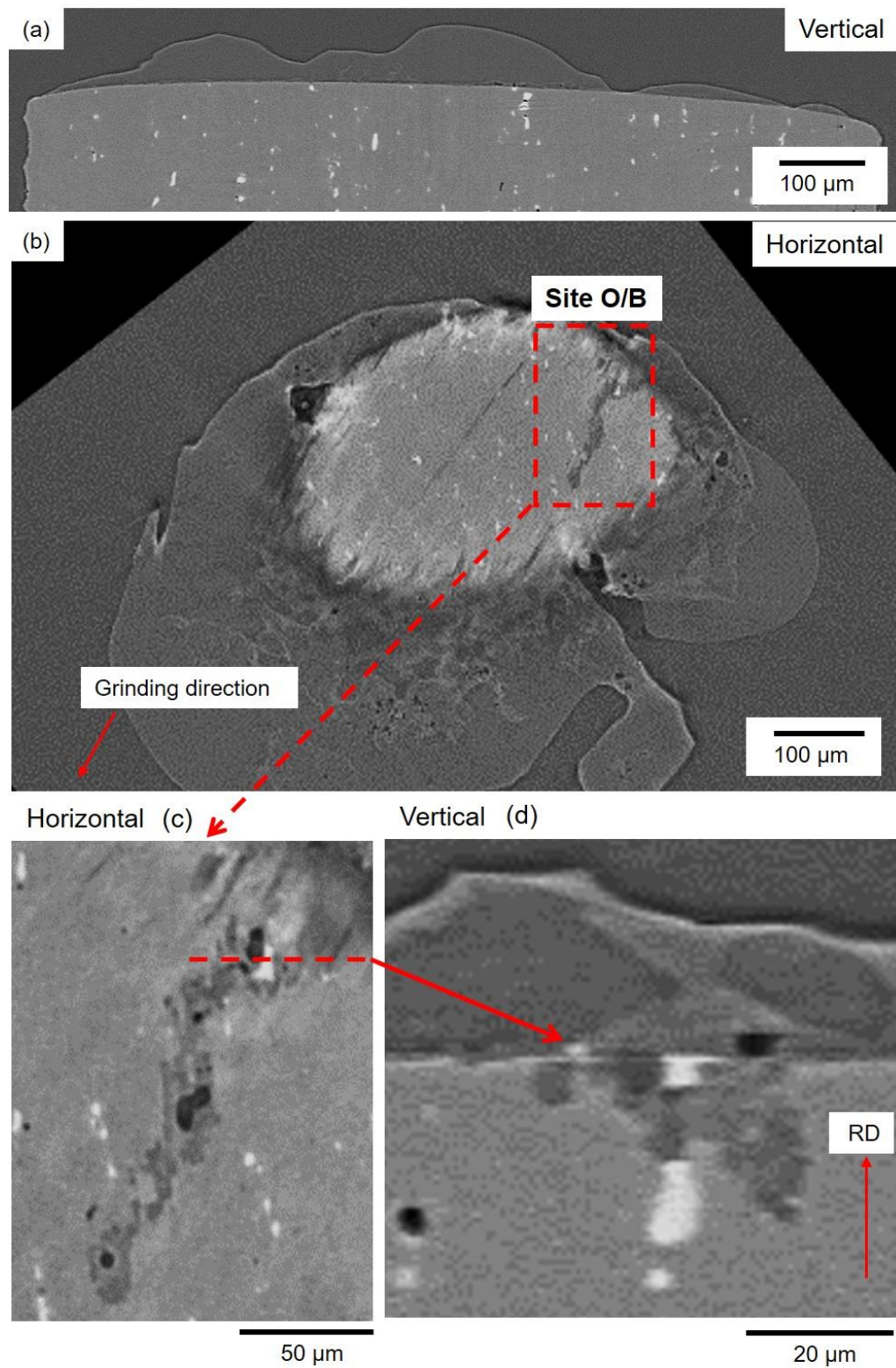
Figure 6-10 tomographic sections of a corrosion site O/B (located in red box) at the end of 2250 mins of exposure (OE1). The sample was a 1 mm diameter AA2024-T3 pin show in Figure 6-1, Figure 6-2 and Figure 6-3. Site O/B is highlighted by a red box. (c) shows a magnified tomogram of site O/B. (d) shows a vertical section of site O/B indicated by a red dotted line.

Figure 6-10 shows vertical sections through a 1mm diameter AA2024-T3 pin exposed to a 0.2 µL droplet of ASTM ocean water, giving a CDD of 1400 µg/cm^2 at a temperature of 21±2 °C as it is cycled through humidity shown in Figure 3-4 for 2250 mins. Figure 6-10 (a) shows a vertical tomographic sections of the pin, and the shape of the droplet at the end of the dry wet cycle after 2250 mins of exposure. Figure 6-10(b) shows a horizontal section of the top of the pin. The development of one corrosion site is considered here. This corrosion site is labelled O/B which is located in red box at the end of 2250 mins of cyclic exposure (OE1). Figure 6-10(c) shows a magnified horizontal tomogram of site O/B. It can be seen that the corrosion site is wide and shallow following the orientation of the grinding direction. Figure 6-10(d) shows a vertical section taken from the dotted red line shown in Figure 6-10 (c) where the site is at its deepest. The site can be seen intersecting two white intermetallic particles. The time development of this corrosion site is now considered in detail.
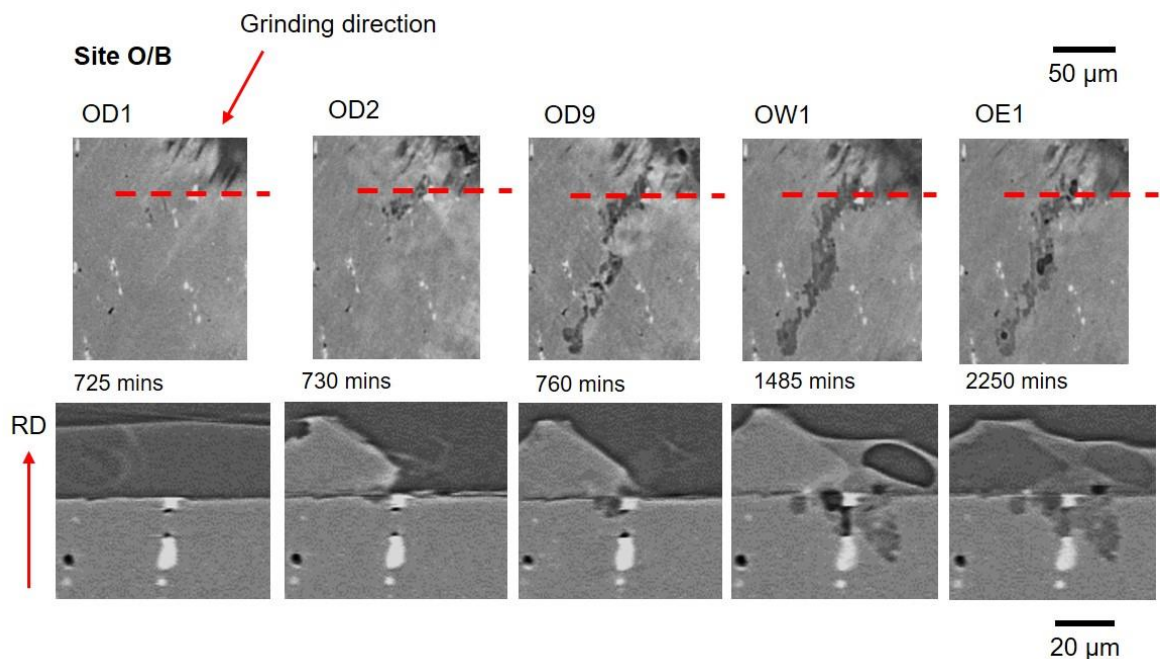
Figure 6-11 tomographic sections of a corrosion site O/B shown in Figure 6-10 (located in red box) at the end of 2250 mins of exposure (OE1). The sample was a 1 mm diameter AA2024-T3 pin show in Figure 6-1, Figure 6-2 and Figure 6-3. Grinding and rolling direction are indicated by red arrows. Horizontal (top group of images) and vertical (bottom group of images) the five time-intervals are shown; OD1 – 725 mins after 5 mins of ~3±3.0 %, OD2 – 730 mins, OD9 – 760 mins following 45 mins at ~3±3.0 %, OW1 – 1485 mins, 5 mins after RH is changed to 85% and OE1 – 2250 mins following wet-dry-wet exposure. Each vertical section shows the deepest section of the corrosion site.

Figure 6-11 shows site O/B from Figure 6-10 at five time-intervals. The rolling and grinding direction are indicated by red arrows. The top row shows horizontal tomograms and the bottom row shows vertical tomograms of scans; OD1 - 725 mins after 5 mins of ~3±3.0 %, OD2 – 730 mins (plus 5 mins in dry), OD9 – 760 mins following 45 mins at ~3±3.0 %, OW1 at 1485 mins (5 mins after RH is changed to 85%) and OE1 – 2250 mins wet-dry-wet exposure. Each vertical section shows the deepest segment of the corrosion site. In the vertical sections, initiation of a corrosion site O/B at 730 mins is seen next to an intermetallic particle under a cubic salt crystal. The site is seen to grow under this cubic crystal in 30 minutes between 730-760 minutes during exposure to

~3±3.0 % RH. The sample was left for 12 hours in ~3±3.0 % RH and the first scan 5 minutes after the droplet was put in a wet environment (85%) at 1485 mins shows that the corrosion site has grown. The salt crystal seen in previous scans is still present. A hydrogen bubble is seen in the vicinity the corrosion site at 1485 mins. The sample was then held at 85% RH for 12 hours. After this duration scan OE1 at 2250 mins showed no further corrosion growth of this sample had occurred since 1485 mins.
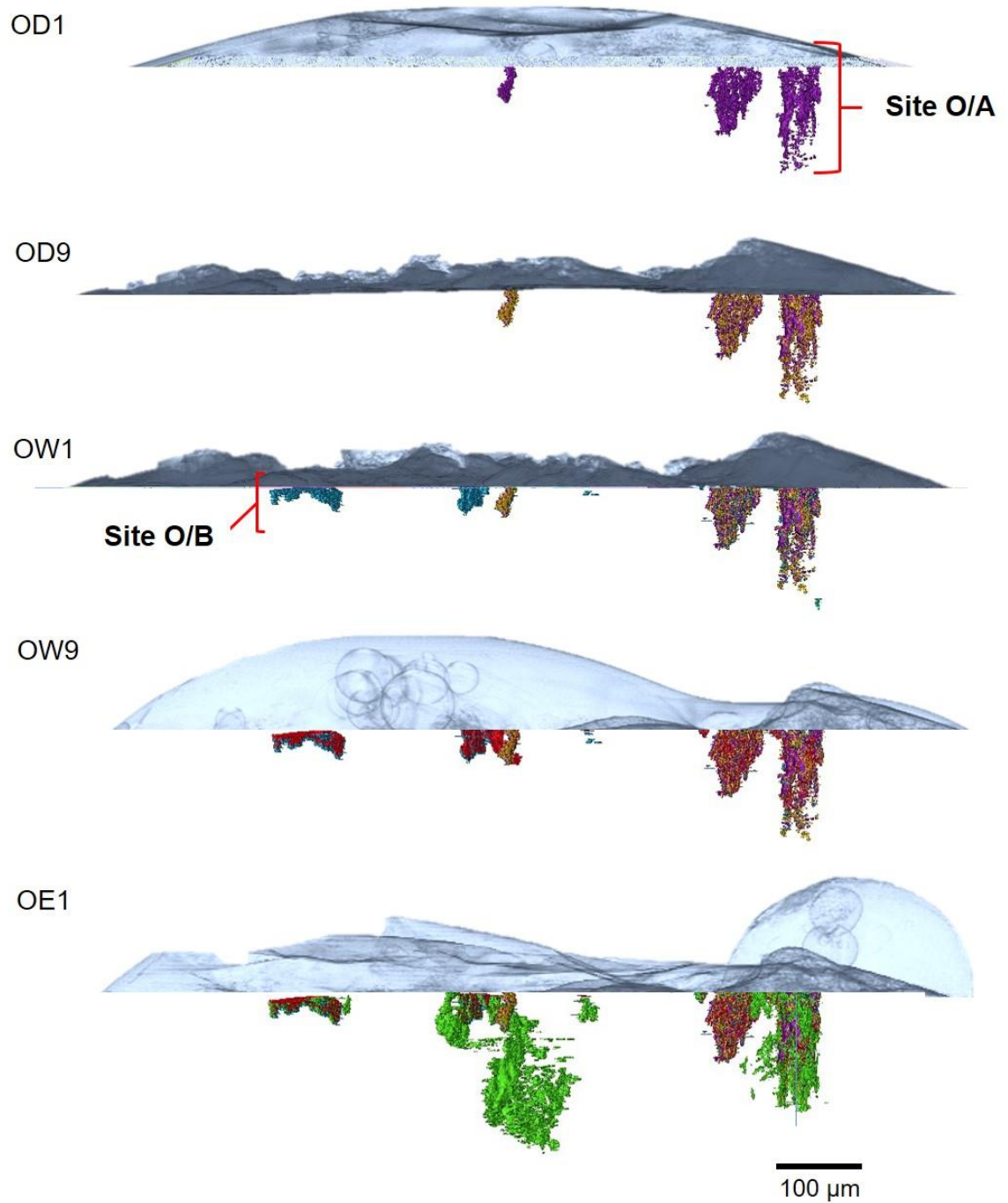
Figure 6-12 3D images a corrosion on sample introduced in Figure 6-1, Figure 6-2 and Figure 6-3 at the start and end of all wet and dry cycles (OD1-9 and OW1-7 and OE1). Each colour change reveals additional material loss at each time interval. OD1 is shown in purple. OD9 material loss is shown in yellow. OW1 material loss is shown in cyan material loss is shown in red. OE1 material loss is shown in green. Site O/A and O/B are highlighted by red brackets.
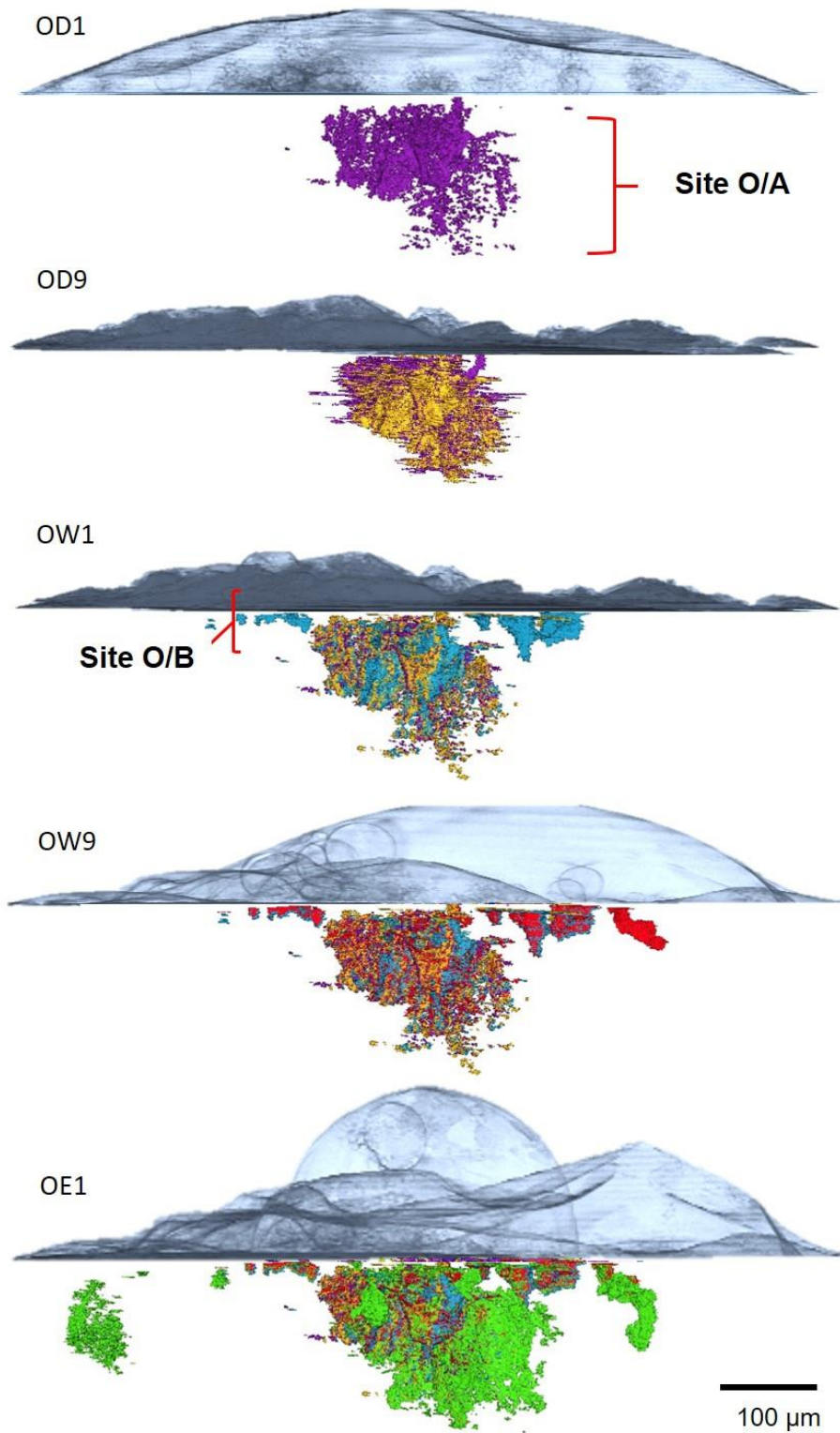
Figure 6-13 A 90º rotation of corrosion sites shown in Figure 6-12. 3D images a corrosion at the start and end of all wet and dry cycles (OD1-9 and OW1-7 and OE1). The sample introduced in Figure 6-1, Figure 6-2 and Figure 6-3. Each colour change reveals additional material loss at each time interval. OD1 is shown in purple. OD9 material loss is shown in yellow. OW1 material loss is shown in cyan material loss is shown in red. OE1 material loss is shown in green. Site O/A and O/B are highlighted by red brackets.

Figure 6-12 shows 3D images of all the corrosion sites after wet-dry cycling (OD1-9 and OW1-7 and OE1). From the sample shown in Figure 6-1, Figure 6-2 and Figure 6-3. OD1 shows corrosion sites were present after 5 minutes of exposure to a dry ~3±3.0 % RH. Site O/A is highlighted by red brackets. After 45 minutes being held in a dry ~3±3.0 % RH environment OD9 shows no new corrosion sites had initiated. Hydrogen bubbles are present in the droplet. Site O/A shows some additional material loss. After 12 hours being held in a dry cycle at ~3±3.0 % RH and then a RH change to 85% the scan OW1 taken after 5 mins shows the initiation of multiple corrosion sites. The samples was then held in a dry environment of 85% RH for 45 minutes. OW9 shows the last scan following the wet-dry-wet cycle. Corrosion sites initiated during the initial 5 minutes of the wet phase can be seen to have grown. The sample was then held in a wet (85% RH) environment and scanned after 12 hours (OE1) new sites initiated during this time and the already established corrosion sites had also grown. Hydrogen can be seen in the highest region of the second dome shaped droplet.

Figure 6-13 further highlights the results presented in Figure 6-12 but the images are rotated by 90º. As in Figure 6-12 the difference in colour change indicates the loss of additional material. Corrosion sites are seen to be elongated. The largest site is be seen to have grown during the 12 hour wet cycle between OWD9 and OE1.

## 6.2.2.2 *Corrosion Behaviour of a Wet-dry Cycled NaCl Water Droplet*
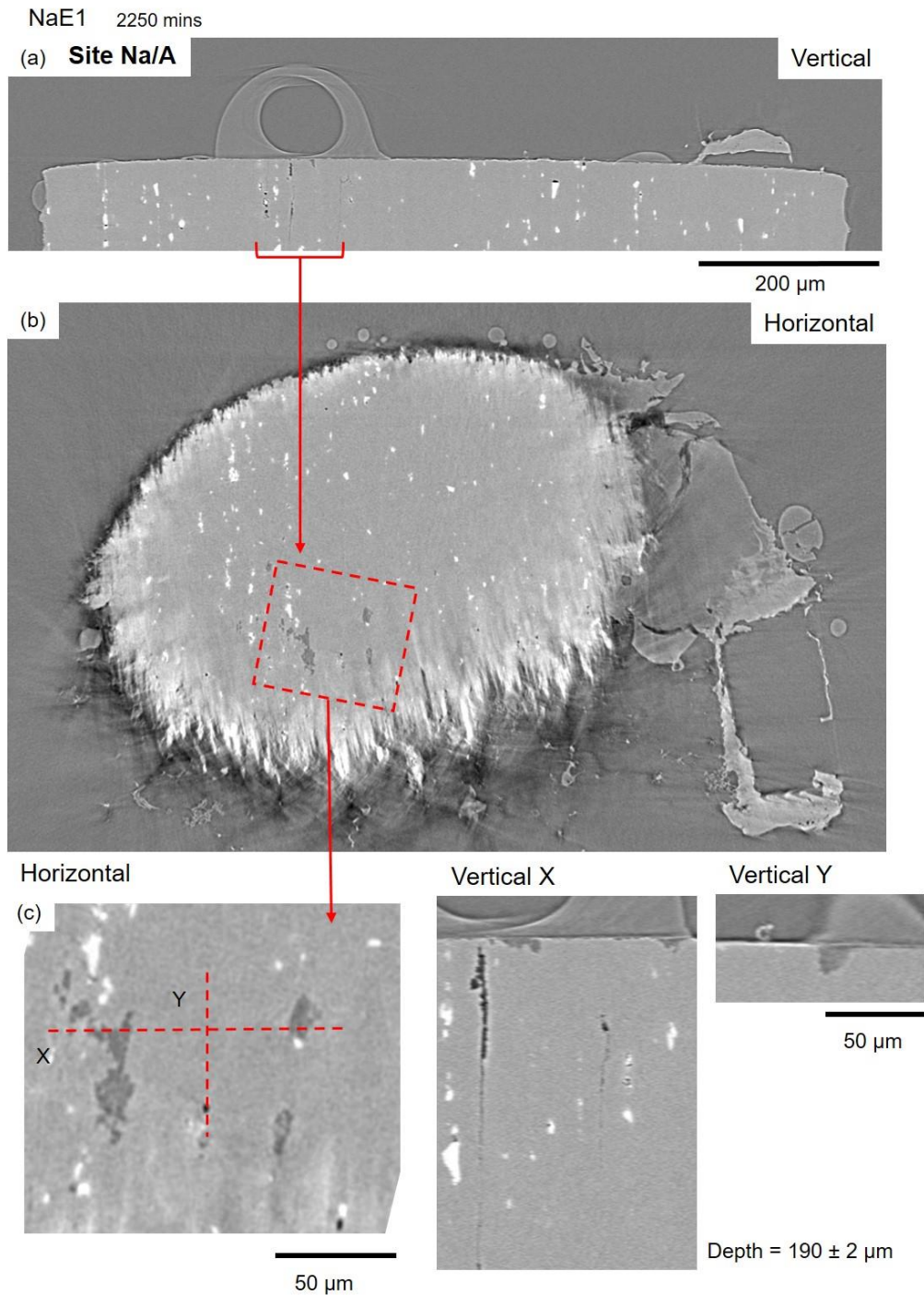
Figure 6-14 tomographic sections of a corrosion site Na/A (located in red box) at the end of 2250 mins of exposure (NaE1) 2250 from the sample shown in Figure 6-4, Figure 6-5, and Figure 6-6. (a) shows a vertical section of the middle of the pin. NaCl solution and a bubble can be seen (b) shows a top down horizontal section of the pin. Site Na/B is highlighted by a rotated red box. The red box is rotated in orientation or rolling direction (c) shows a magnified tomogram of site Na/A. Vertical X and Vertical Y shows a vertical section of site Na/A indicated by a red dotted lines X and Y. Maximum depth of this site is noted.

Figure 6-14 shows tomographic sections of the sample introduced in Figure 6-4, Figure 6-5, and Figure 6-6. Image Figure 14(a) shows a vertical section through the middle of the pin, the pin in which and inhomogeneous droplet can be seen and below which a corrosion site had developed. Figure 6-14 (b) shows a horizontal section of the top down view of the pin and solution droplet. The pin is not flat so a partial section of both the pin and droplet can be seen; the red box indicates the region of corrosion site Na/A. Figure 6-14 (c) shows a magnified tomogram section of site Na/A with the vertical sections taken in the X and Y planes represented by the red lines. Vertical X shows an elongated thin corrosion site fissure like in morphology. Vertical Y shows a shallow corrosion site, pit like in morphology. The evolution of corrosion site Na/A is considered in more detail in Figure 6-15.
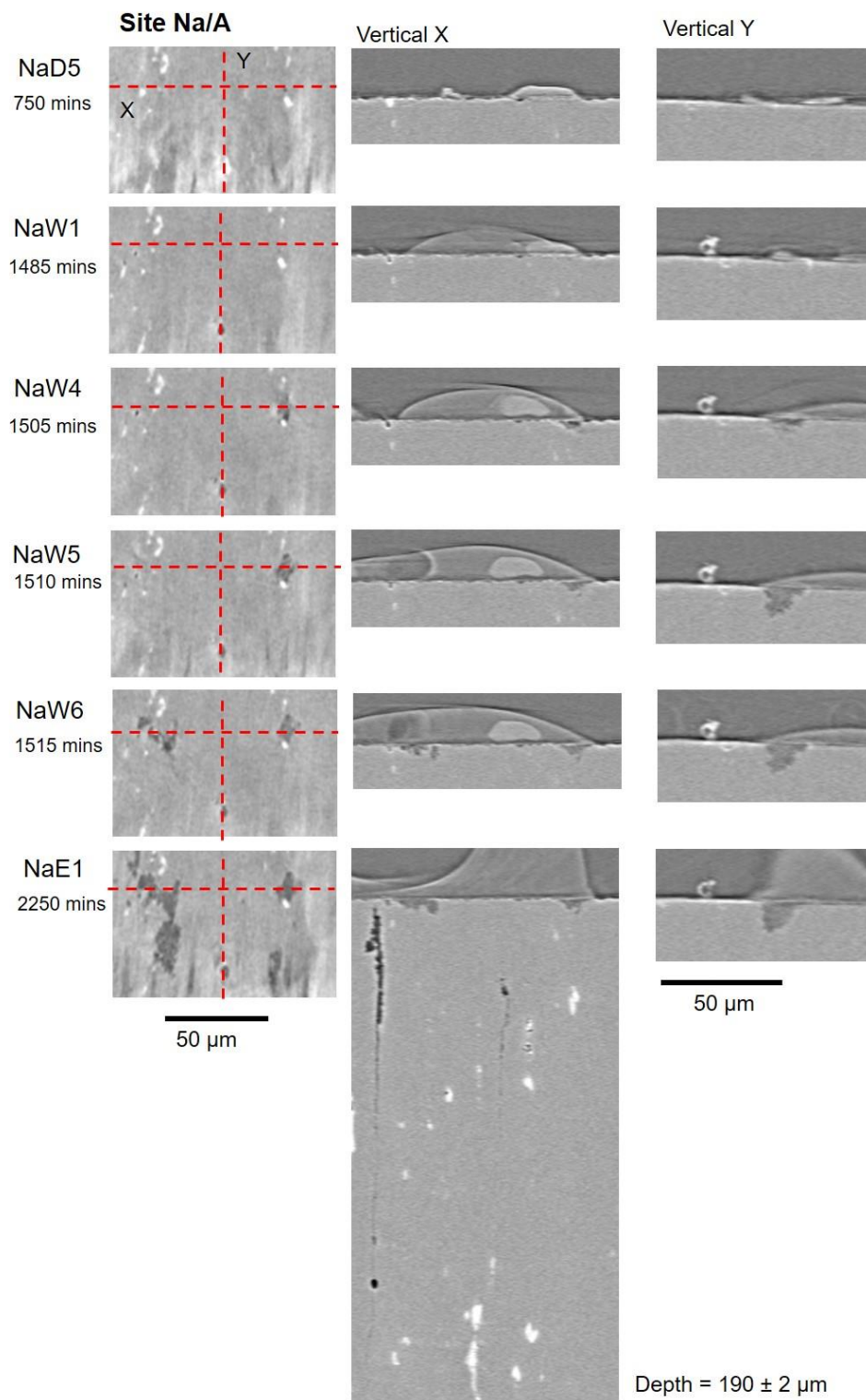
Figure 6-15 tomographic sections of a corrosion site Na/A (Figure 6-14) multiple time intervals. The sample was introduced in Figure 6-4, Figure 6-5, and Figure 6-6. The first column shows a horizontal section of the site, the second and third column a vertical section of the red dotted line labelled as Vertical X and Y.

Figure 6-15 shows the initiation and growth of site Na/A (introduced in Figure 6-14). The first column shows top down sections of the pin sample. Line X and Y highlights the location site Na/A which has been intersected for vertical slicing. Corrosion site initiation is seen in the vertical Y during NaW4 at 1505 minutes of exposure. The corrosion site can be seen initiating at a small white intermetallic particle where a droplet had begun to deliquesce during the first 5 minutes in 85% RH in NaW1. This site continues to grow during exposure to 85% RH for 10 minutes until NaW6 where growth ceases. The site is not seen to change during 12 hours in 85% RH between NaW6 and NaE1. A second site initiates during the first scan the sample is in 85% RH (NaW1) as a separate droplet which deliquesces at the salt crystal seen in the dry scan (NaD5). During 12 hours of exposure to 85% relative humidity the site increases in depth by 190 µm.
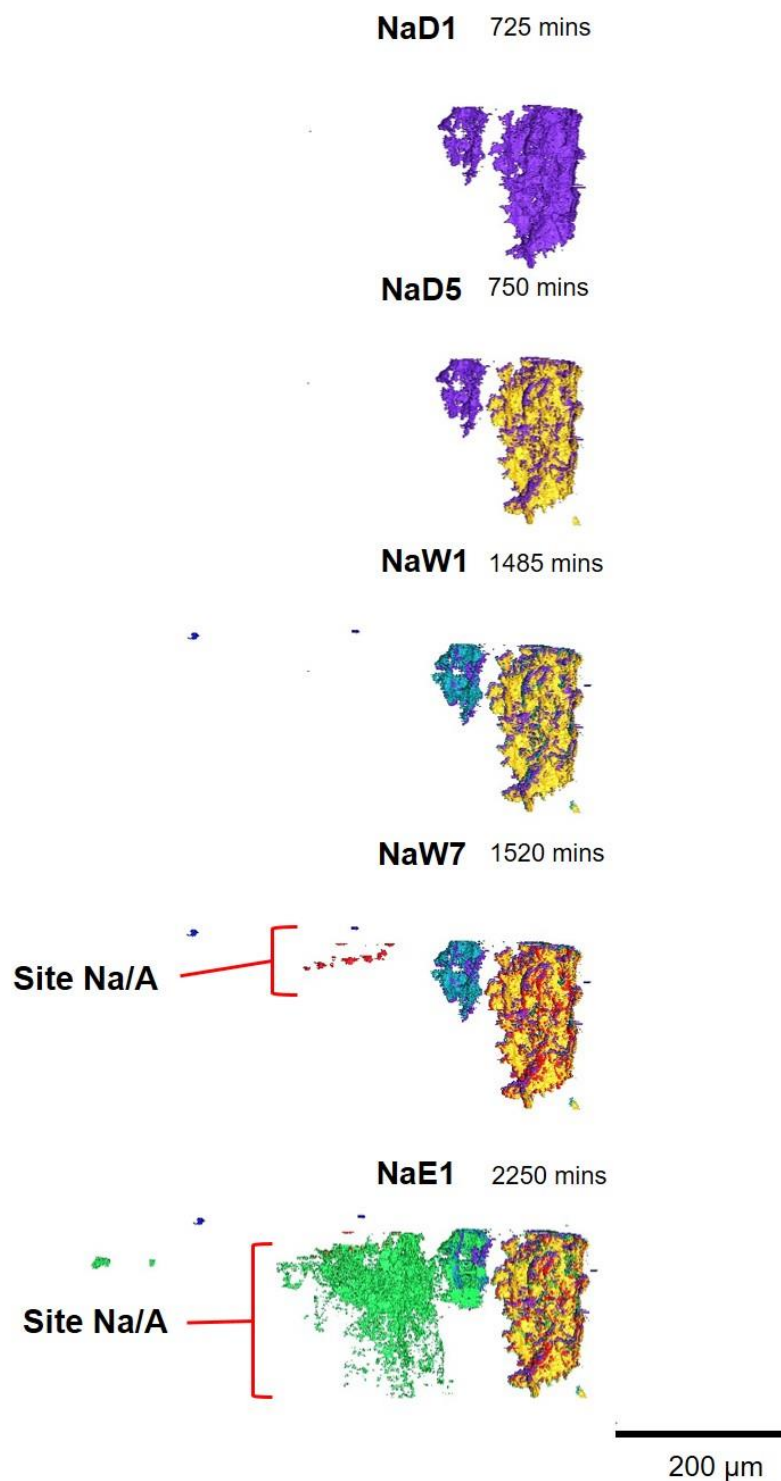
Figure 6-16 3D images a corrosion at the start and end of dry cycles (NaD1-5 and NaW1-7 and NaE1). The sample was a 1mm diameter AA2024-T3 pin exposed to a 0.2 µL droplet of NaCl giving a CDD of 500 µg/cm^2 at a temperature of 21±2 °C after it is cycled through humidity's shown in Figure 3-5. Each colour change reveals additional material loss at each time interval. NaD1 is shown in purple. NaD9 material loss is shown in yellow. NaW1 material loss is shown in cyan material loss is shown in red. NaE1 material loss is shown in green. Site Na/A is highlighted by red brackets.

186

Figure 6-16 shows 3D images of all the corrosion sites after wet-dry cycling (NaD1-5 and NaW1-7 and OE1). The sample was a 1mm diameter AA2024-T3 pin exposed to a 0.2 µL droplet NaCl, giving a CDD of 500 µg/cm^2 at a temperature of 21±2 °C after it is cycled through humidity's shown in Figure 3-5. NaD1 shows corrosion sites present after 5 minutes of exposure to a dry ~3±3.0 % RH. After 25 minutes being held in a dry ~3±3.0 % RH environment NaD5 shows no new corrosion sites have initiated. After 12 hour being held in a dry cycle at ~3±3.0 % RH and then a RH change to 85% from 5 mins scan NaW1 shows the initiation of two small corrosion sites. The samples is then held in a dry environment of 85% RH for 35 minutes. NaW7 shows the last scan following wet-dry-wet cycles. Multiple small corrosion sites have initiated. The sample is then held in this wet (85% RH) environment and scanned after 12 hours (NaE1) where multiple corrosion sites initiated during the initial 5 minutes of the wet phase have grown.

6.2.3 Effects of Wet-Dry Cycling on the Initiation, Growth and Accumulation of Corrosion
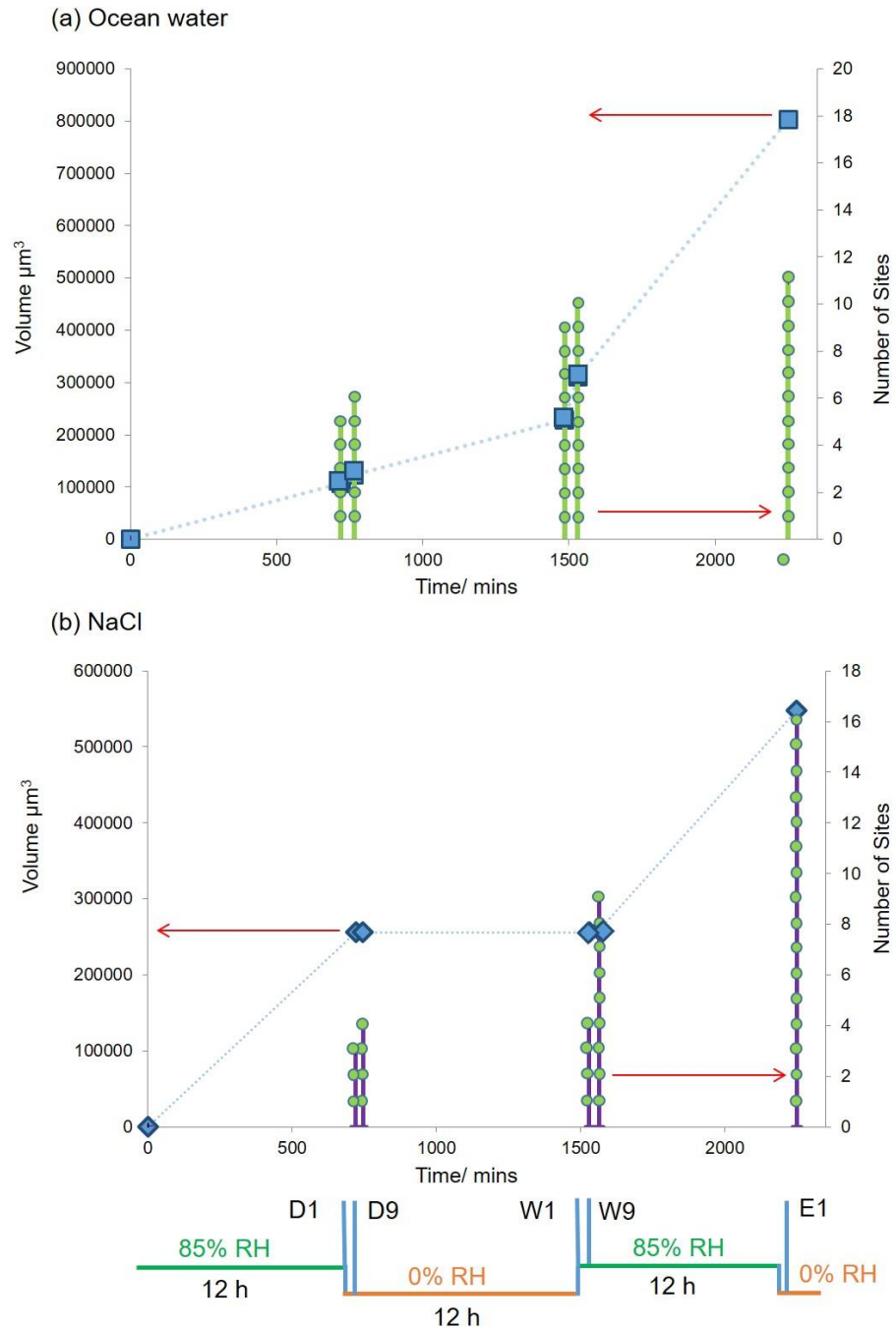
Figure 6-17 A series of graphs showing the total volume loss at the beginning and end of each dry, wet and end cycle. (a) Corresponds to the 3D images shown in ASTM ocean water sample shown in Figure 6-12. Sample follow wet-dry cycling as shown in Figure 3-4. (b) Corresponds to 3D images of a NaCl corroded droplet shown in Figure 6-16. Sample follow wet-dry cycling as Figure 3-5. In both cases (a) and (b) blue points shown indicate volume loss. Green dots indicate the number of individual corrosion sites.

Figure 6-17 shows graphs (a) and (b) summarising the total volume loss and number of pits seen from the two data sets wet-dry cycled sample of ASTM ocean water and NaCl shown in Figure 6-12 and Figure 6-16. The blue points indicate the total loss of material from the sample, the green dots highlight the number of corrosion sites present at each time interval for both ASTM ocean water and NaCl samples. The total volume loss was greater under the ASTM ocean water droplet then the NaCl droplet. From the two data sets it appears the volume of corrosion in the ASTM ocean water sample is seen to increase more during the wet cycle. NaCl droplet sees no increase in volume during the dry phase and increased in volume when in the wet phase. The number of corrosion site total is similar between both ASTM ocean water and NaCl droplets. The number of corrosion sites increases at a steady rate under the ASTM ocean water droplets. Whereas the number of sites only increases during wet cycles under the NaCl droplet.

Samples explored so far have had periods of long exposure to X-rays. In order to investigate the effects of X-rays samples exposed to the same wet-dry protocol shown in Figure 3-4 and Figure 3-5 where examined at the end of exposure with a single tomographic scan ('Control E1'). In addition the effects of wet-dry, exposed to a constant RH are also examined at the end of exposure (Constant RH control E1). Due to the inherent variability of corrosion likely to occur in the two samples analysed thus far Figure 6-18 compares the validity of results using controls.
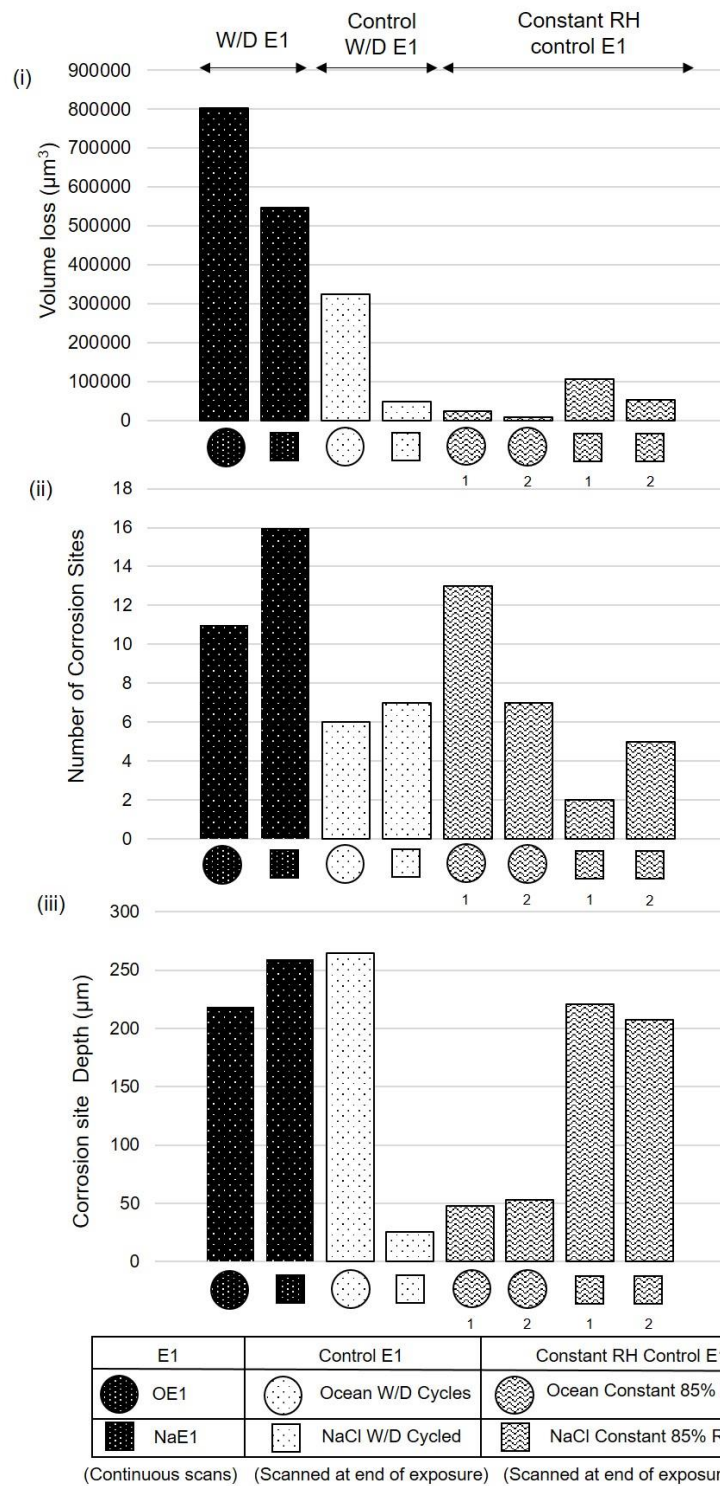
Figure 6-18 showing the (i) total volume loss, (ii) number of corrosion sites, and (iii) corrosion site depth. Data points include; OE1 wet-dry cycling and number of scans as shown in Figure 6-1, Figure 6-2 and Figure 6-3; NaE1 wet-dry cycling and scans as shown in Figure 6-4, Figure 6-5 and Figure 6-6; One other ASTM ocean water and NaCl samples are shown. These undergo the same wet and dry cycles but have only been scanned at the end of 2250 mins exposure ('Control E1'); Two Ocean and two NaCl samples exposed to a constant RH of 85% and are scanned at the end of 2250 mins exposure. These conditions are seen in a key below the plotted graphs ('Constant RH Control E1').

190

Figure 6-18 shows a number of graphs in succession which summarise the growth profile for a range of samples following 2250 mins of exposure to atmospheric conditions. The samples plotted are ASTM ocean water droplets as shown in Figure 6-12, NaCl sample that has under gone wet-dry cycling as shown in Figure 6-16. The samples for ASTM ocean water (OE1) and NaCl (NaE1) droplet samples which underwent wet-dry-wet cycling analysed throughout this chapter were scanned multiple times during atmospheric exposure. Additional ASTM ocean water and NaCl samples exposed to the same conditions were only 'scanned at the end of exposure' as indicated in the key below the graph plots. These are plotted along with two ASTM ocean water and two NaCl samples exposed to constant 85% RH for 2250 mins also 'scanned at the end of exposure'. Different scanning numbers were made to compare beam damage. Each bar chart represents a different variable measured (i) the total volume lost, (ii) the total number of corrosion sites and (iii) corrosion site depth.

Comparing the effects of beam damage, wet-dry OE1 and NaE1 can be compared with the wet-dry controls. In both salt droplets corrosion volume and site number are all greater than the controls measured. The depth measured in OE1 was similar to the control wet-dry ASTM ocean water measured. The NaE1 samples largest pit was deeper than the control sample measured.

As beam damage from exposure to x-rays is apparent, control wet dry and control constant RH exposure samples are compared. Results from these 6 samples shows some scatter across the data with no clear trends. In the ASTM ocean water droplets, the wet-dry cycled sample shows a great loss in volume

that the constant RH. The number of corrosion sites of the constant exposure are either equal or greater than the wet-dry cycled sample. However the depth obtained in the wet-dry cycled samples is much deeper than the constant exposure. NaCl droplets exposed to wet-dry cycles have similar losses in volume to constant exposure samples. The number of corrosion sites are more and approximately the same in the two exposures. Unlike in the wet-dry ASTM ocean water sample the depth of the wet-dry NaCl droplet is very low. This may be due to the method used to change the RH knocking the droplet off the top of the pin. In the X-ray exposed wet-dry samples, the higher humidity exposure saw the depth of corrosion sites increase in the NaCl sample in Figure 6-17. If the droplet is removed before the humidity is allowed to increase. An increase in depth is likely to be seen in this NaCl sample. This was an issue seen in 5 other wet-dry samples measured at the TOMCAT beamline where data is not included.

Comparing ASTM ocean water and NaCl, samples look at, X-ray exposed wet-dry, control X-ray, and constant RH. In OE1 and NaE1, ASTM ocean water has a higher loss in volume, a reduced number of corrosion sites and a shallower corrosion site when compare to NaCl. In the control wet-dry cycles ASTM ocean water has a higher loss in volume, and approximately the same number of corrosion sites. A discrepancy is seen in the depth of the corrosion sites. With the NaCl droplet having very shallow sites. This is thought to be due to the accidental removal of the droplet during a RH change. In constant exposure samples, similar results to section 5 where ASTM ocean water lost less volume

192

than the NaCl sample. The ASTM ocean water sample had a larger number of corrosion sites which were shallower than the NaCl sample.

6.3 Discussion

6.3.1 Initiation of Corrosion Sites During Wet-Dry Cycles

The deliquescence of the salt crystals is seen to result in initiation of corrosion under both ASTM ocean water droplets (Figure 6-11) and NaCl (Figure 6-15). Initiation occurred during the either the drying of salt solution in dry phases or during the deliquescence of salts in the initial wet phase. This will happen due to reduced availability of free water. During each phase both solution will equilibrate with the atmosphere and become saturated. Saturated salt will occupy all solvated shells of water, therefore it is more difficult for passivation to occur as water from the solution will need to adsorb onto the metal surface as deprotonation removes an H^+ [42, 207]. Consequently during either wet or dry phases an increase in likelihood for corrosion initiation under NaCl and ASTM ocean water droplets will occur.

Corrosion site O/B on the ASTM ocean water sample (introduced in Figure 6-10 and explored in Figure 6-11) can be seen to initiate during the dry cyclic phase of exposure. During this dry phase a cubic shaped salt crystal grows and forms a crevice. At the edge of this salt crystal, a corrosion site can be seen to initiate at an intermetallic particle (shown in bright white) as shown in Figure 6-11 (OD2). The corrosion site is wide and shallow. This crevice like corrosion site grows during the dry phase of the wet-dry cycle under the ~3±3.0 % RH

193

conditions. Once the salt deposit deliquesces, the site ceases to grow; this site death can be seen in Figure 6-11 between tomograms at 1485 mins and 2250 mins.

Figure 6-15 shows the growth of the deepest site from the NaCl sample (site Na/A). Initiation is seen under a NaCl crystal as it deliquesces. The droplet can be seen forming in NaW1 vertical X under this deposit, likely creating a crevice trapping the escape of metal ions produced and creating a region of high acidity making it the net anode. The second pit like site in Vertical Y is seen initiating at the edge of the newly formed droplet where O_2 diffusion will be easiest [208]. Hydrolysis within the corrosion site will result in acidification thus drawing Cl^- to balance the charge, favouring dissolution of the crevice over passivation.

In both cases in the ASTM ocean water and NaCl droplets, the crevice is seen to stop growing after re-wetting likely due to deliquescence of salt crystal which forms the mouth of the corrosion site. Once the salt has dissolved the corrosion site mouth is exposed, metal ions can escape faster than they are produced, promoting passivation and leading to corrosion site death [75, 76].

6.3.1.1 Corrosion Morphology

Site O/B in Figure 6-10 and Figure 6-11 grows with the direction of grinding lines rather than metallographic features such as grain boundaries. The surface topography of grinding lines is likely to cause deformation in the form of labial overhangs of metal. This surface topography will trap metal ions, thus dictating directional corrosion propagation.

Deep penetrating corrosion sites are seen across both samples and can be seen in Figure 6-7, Figure 6-14 and has previously been captured by tomography on AA2024-T3 in steady state environments [19, 20].

Figure 6-18 shows the range of depths of both wet-dry cycled and stead state corrosion sample. Corrosion site O/A in Figure 6-7 shows a deep corrosion site after 2250 mins of cyclic exposure. During the initial 12 hour the sample was held at 85% RH the corrosion site is seen to grow and insignificant amount from 180 to 184 ±2 µm. Figure 6-8 shows this sample at the three cyclic intervals measured. The width of this site was analysed using a line scan to show a change in grey scale. Grey scale is seen across a 10 µm section of the corrosion site and is seen to reduce in brightness intensity. During the wet-dry cycles this corrosion site thickens in width to accumulate volume loss rather than continuing to deepen. Corrosion site grow at the fastest rate in the longitudinal direction and lowest in the short transverse [19, 20].

Corrosion site depth could be limited. Limited current as large corrosion sites grow has been previously observed using XRT [20]. In order for multiple large corrosion sites to grow at once they must share current. During the rewetting of the droplets samples exhibit unevenly. In both cases reducing the cathodic area covered by the droplet. The ocean waters first corrosion site ceases to grow in depth as other sites initiate across the sample (Figure 6-12 and Figure 6-13). Suggesting current is being shared [16].

Increases in humidity has shown corrosion sites widening [19, 20, 23]. Similar behaviour is observed in Figure 6-8 and Figure 6-9. It can be hypothesised that

the increase in humidity will increase the conductivity within the droplet [209]. As a result the electrical potential (IR) between the corrosion site tip and the solution will drop. This will increase the interfacial potential and result in higher current to drive corrosion during higher humidities. Lateral growth will occur as the distance for Cl⁻ to travel to the corrosion site tip will increase. Similar behaviour to this has been seen in X-ray tomography [23].

6.3.2 Corrosion During Wet-Dry Cycles

Figure 6-17 highlights the number of corrosion sites and total loss of volume of the ocean and NaCl droplet samples over the 2250 mins experiment. The ASTM ocean water sample (Figure 6-17 (a)) shows a steady corrosion volume loss increases from the initial wet phase to the drying phase. This increase can be attributed to the steady addition of a new corrosion site growing between D1 to D9. During exposure at ~3±3.0 % RH four more corrosion sites can be seen to have initiated and material loss continued to accumulate as a result. A larger loss of metal is seen once the sample is rehydrated (W1 to W9). Corrosion loss continues to accumulate until scan E1 during this 12 hour period as established pits continue to grow. Sites which have initiated are shown clearly in 3D image as additional colour change shows volume loss. For the ASTM ocean water sample these new sites are shown by Figure 6-3, Figure 6-12 and Figure 6-13 respectively.

Conversely the behaviour seen for the NaCl droplet as shown in Figure 6-17 (b) is the opposite of this. Corrosion sites number does not increases steadily over the duration of the dry cycles. Five new sites and a consequential large increase in volume loss are seen between W1 and W9 once the sample is

reintroduced to a wet environment at 85% RH. 3D visualisation of the nature of this growth and volume measurements shown in Figure 6-6 and Figure 6-16.

Similar findings of this rapid volume loss upon rewetting has been seen previously [21] and is common under NaCl droplets [141]. Further evidence of this phenomenon is shown in AA7XXX series under NaCl droplets [23].

6.3.3 *The Impact of Droplet Behavior on Corrosion*

Both sample droplets of ASTM ocean water and NaCl were scanned at 300s intervals at the onset of a relative humidity change. The nature of the scanning method allowed for the droplet shape to be captured. Upon drying both sample droplets recede in height and width in a short space of time. The ASTM ocean water droplet appears to be dry at 35 mins as shown in Figure 6-1 and OW9 Figure 6-4. However, the droplet may not fully dry during these phase, but may form a thin droplet along with salt crystals due to the mixtures of salts in ASTM ocean water having various DRH. This is suggested by the initiation of a corrosion site in Figure 6-11, occurring and growing during the dry phase of cycled RH which is not possible without a small layer of solution. The NaCl droplet evaporates and forms crystal structures as shown in Figure 6-4 after 25 minutes exposure to a dry RH. Both droplets rehydrate following rewetting however the droplets do not reform in a uniform way, instead form irregular droplets geometry. These irregularities are better highlighted by 3D image in Figure 6-2 and Figure 6-5. This behaviour may vary as only two samples were visualised continuously during RH changes, unlike the control samples examined in Figure 6-18.

During a drying phase the droplet concentration would be expected to increase as the reducing RH drives away water leaving behind a higher concentration of Cl$^-$. This in turn will increase the effective chloride concentration, as well as leaving surface obstructions in the form of corrosion product deposits and salt precipitates on the sample surface. Deposits such as these are clear in tomograms (Figure 6-1 and Figure 6-4) and 3D images (Figure 6-2 and Figure 6-5) on both ocean and NaCl samples. An increase in chloride concentration will increase the corrosive nature of the droplet along with a reducing droplet thickness to allow for an increase in oxygen reduction as a result of the reduced diffusion distance. In the case of the ASTM ocean water droplet this increase in corrosion rate is seen during the dry phase in line with literature on evaporation [1, 68, 74], with the growth of new sites and increase of metal loss as shown in Figure 6-17 (a). This is not similar in the NaCl droplet. Although ASTM ocean water mostly consists of NaCl, the addition of salts with lower efflorescence points will slow the evaporation of water from the sample. This would result in a very thin layer of $MgCl_2$ (DHR 33%) and $CaCl_2$ (DHR 12%) [133] solution mixture maintaining an ion pathway as the sample dries. This thin solution later allows for corrosion processes to continue, shown by the continual increase in the initiation of corrosion sites in Figure 6-17. Unlike the NaCl droplet where having a high EHR of 45-55% depending on particulate size [210] therefore efflorescence would happen more rapidly. This rapid loss in solution would halt corrosion processes due to a lack of ion transport in dry phases of wet-dry cycles shown in Figure 6-17.

6.3.4 Corrosion during Cyclic Relative Humidity and Constant Relative Humidity

Steady state samples exposed to constant RH have been measured to analyse if wet-dry cycling has an effect on damage accumulation. Figure 6-18 shows a series of bar charts comparing volume loss (i), number of corrosion sites (ii) and corrosion site depth (iii). Wet-dry cycled OE1 and NaE1 samples show the highest volume loss in both ASTM ocean water and NaCl samples screened. Corrosion is characteristically variable so additional samples were analysed to assess the validity of data collected from the wet-dry ASTM ocean water and NaCl droplets. Corrosion volume, corrosion site number and corrosion depth of wet-dry samples continually exposed to X-rays were compared to wet-dry control exposed once to X-rays. All features analysed showed samples that underwent multiple scans had greater values in volume, site number and approximately similar values in corrosion site depths. This result suggests X-ray damage may attribute to accelerate corrosion processes and will be discussed in section 6.3.5.

Comparisons of wet-dry controls and constant relative humidity controls are made in Figure 6-18. ASTM ocean water samples which underwent wet-dry cycles saw a much greater loss in material volume than samples under constant RH. Which could be attributed to a deep corrosion site forming during wet-dry cycles. This finding suggests the roll of sulphates as inhibitors may be impaired by wet-dry cycles as during constant RH a greater number of shallow corrosion sites initiated. Similar to findings observed in lab based experiments in chapter 5 and was attributed to the presence of S and Mg.

In NaCl samples corrosion depth data may be invalid during wet dry cycles as the droplet may have been knocked off during a change in RH. This was a common occurrence during these experiments. In X-ray exposed samples, the rehydration phase in wet cycles saw the greatest accumulation of growth in the NaCl droplet (as shown in Figure 6-17). The accidental removal of the droplet may have resulted in no propagation past the dry phase of exposure without the reformation of a droplet.

Comparing constant RH, the NaCl samples had more volume loss than constant RH ocean water. The constant NaCl had less but deeper corrosion sites than ASTM ocean water contributing to its larger loss in material volume. Similar findings of this behaviour in lab based conditions were found under ASTM ocean water and NaCl samples in Chapter 5.

6.3.5 Limitation of X-ray Tomography

The effects of X-ray scans between wet-dry cycles can be examined and found to worsen the effects of corrosion, as in both droplet examples volume loss, site number and corrosion site depth are higher than that seen in the same environment with only one exposure to X-rays shown in Figure 6-18. However samples scanned multiple times by X-rays saw the same well-known corrosion morphology with sites initiating at intermetallic particles and surface deposits. As well as propagating down metallographic features such as along grain boundaries which have been elongated by the rolling direction and fissured expand around intermetallic particles.

Exposure to X-rays is known to cause radiolysis of water; whereby the formations of radiolysis products such as oxidising (such as H_2O_2, HO_2, H^+, O_2, OH^-) and reducing agents (such as H_2 can lower solution pH and produce accelerated corrosion processes increasing the damage accumulated [168-170].

6.4 Conclusions

XMT was used to investigate corrosion kinetics during wet-dry cycles. Visualisation of corrosion of aluminium has been achieved *in-situ*.

1. AA2024-T3 exposed to ASTM ocean water and NaCl droplets during wet-dry cycling showed similar corrosion site initiation and morphology. Sites initiated in both droplets under salt crystals which were adjacent to intermetallic particles. Corrosion morphologies observed under both droplets were shallow pits and intergranular-like fissures which propagated deep into the metal surface. These sites propagated down into the metal surface and expanded around intermetallic particles. Over time fissure-like corrosion sites are seen to widen.

2. During wet-dry cycles the rate of ASTM ocean water and NaCl droplets, evaporation and rewetting was dependent on the deliquescence of the constituent salts. Ocean water, which contains salt constituents with lower deliquescence relative humidities such as $MgCl_2$ (33% RH) and $CaCl_2$ (12% RH) showed initiation of new corrosion sites in both in wet and "dry" phases. This was due to the continuing presence of a thin droplet resulting in more metal volume loss. NaCl has a deliquescence of 75% resulting in faster evaporation in "dry" phases. Corrosion sites as a consequence were seen to only initiate and grown during wet phases as no droplet was present in dry phases. The deepest site for both NaCl and ASTM ocean water droplets continually scanned was similar, however NaCl contained more corrosion sites.

3. Control samples were imaged with X-rays only at the end of exposure to either constant or wet-dry RH cycles showed a difference in corrosion development. The number of corrosion sites on control wet-dry samples was greater than or similar to those exposed at constant RH for both ASTM ocean water droplets. Volume loss was greater in ASTM ocean water samples which underwent wet-dry cycles compared with constant exposure. However it was not possible to compare the behaviour for a wet-dry exposed NaCl droplet as the droplet appeared to have fallen off during the experiment.

4. Grinding direction was seen to influence the propagation of a corrosion site under the ASTM ocean water droplet. The abraded surface topography is thought to trap metal ions and thus favour growth orientated along the grinding direction.

5. Samples wet-dry cycled which were imaged with X-rays multiple times were compared with control samples that were imaged once at the end of the experiment. Increased exposure to X-rays appeared to increase the total volume of material lost, however the number of corrosion sites and depth of sites were similar. The morphology of corrosion sites did not change with increased exposure to X-rays.

7. GENERAL DISCUSSION, CONCLUSIONS AND FUTURE WORK

During this work different aspects of atmospheric corrosion of AA2024-T3 have been studied. Comparisons of behaviour of NaCl and ASTM ocean water droplets have been made. In particular initiation and growth of corrosion has been studied by means of XMT and detection of corrosion via the analysis of corrosion products has been undertaken.

7.1 Initiation of Corrosion Under ASTM Ocean Water and NaCl Droplets

7.1.1 Initiation Sites

It has been possible to capture the initiation and propagation of corrosion under atmospheric droplets shown in chapter 4 and chapter 6 by improving the temporal resolution of the XMT. It is commonly accepted that corrosion sites initiate at intermetallic particles on AA2024-T3 [1, 15, 183]. Due to AA2024-T3 the passive being thinner over such particles along with their cathodic nature [73, 86, 151]. In chapter 4 and chapter 6 corrosion sites initiation was captured within the 300 s that a tomography scan was collected. In both experimental conditions NaCl and ASTM ocean water samples corrosion sites initiated at intermetallic particles, under crevices formed by surface deposits and salt crystals and at unresolvable surface heterogeneities shown in Figure 4-5, Figure 6-10 and Figure 6-14.

During exposure to wet-dry cycles both NaCl and ASTM ocean water droplets, initiation of sites was visualised during changing RH in both solution droplets under salts crystals adjacent to intermetallic particles. The RH initiation was seen, be that dry conditions for ASTM ocean water and wet conditions for the

NaCl droplet this mechanism of initiation was similar. Comparable behaviour was seen in chapter 4 where the largest site was seen to grow under a surface deposit (Figure 4-5). These surface obstructions under both droplet types and under very different environmental conditions of steady state and wet-dry cycling of RH exposure, to facilitate the corrosion sites to grow and become stable.

7.1.2 Hydrogen Evolution

The phenomenon of H_2 evolution from aluminium alloys is well explored [4, 20, 80, 188]. It is usually a result of one of the two cathodic reactions which most commonly occurs at intermetallic particles. In the case of this study chapter 4 Figure 4-4, Figure 4-5 sites grew one at a time and were accompanied by a gas bubble. Hydrogen is also seen within all solution droplets with no clear association to corrosion sites. The quantity of H_2 evolved from sites as they initiated was measured to be 0.01% and 3.4% of the cathodic reaction taking place; suggesting the major cathodic reaction taking place was that of oxygen reduction in these conditions. It should be highlighted that excess H_2 evolution seen within the droplet may be as a result of 'beam damage', a process whereby X-rays cause radiolysis of water and the formation of radiolysis products. Both oxidising and reducing agents are formed which include H_2. This could generate excessive amounts of H_2 during these experiments.

Figure 6-18 shows samples which were exposed to the same environmental conditions and visualised to a single tomographic scan following exposure (to reduce the exposure of the sample to X-rays) saw results of corrosion site depth, similar to samples exposed to X-rays multiple times. However material

volume loss and corrosion site number were fewer in all cases of samples exposed to less X-ray radiation. Suggesting X-ray radiation accelerated metal loss but did not change the initiation processes or morphology of corrosion seen in both NaCl and ASTM ocean water droplets.

7.2 Propagation and Morphology of Corrosion Under ASTM Ocean Water and NaCl Droplets

With the introduction of X-ray tomography and the use of sectioning, the morphology of AA2024-T3 corrosion is well established [19, 42, 91]. Exposure to constant RH and wet-dry cycling of ASTM ocean water and NaCl droplets has observed this well-known corrosion morphology. Pit like corrosion sites initiated during both the early stages of exposure to a constant RH are shown Figure 4-4 and Figure 4-5 alongside a larger IGC like narrow fissure which continues to develop during exposure shown in Figure 4-8. The analysis of longer exposed wet-dry atmospheric corrosion under ASTM ocean water and NaCl both exhibited similar corrosion morphologies. Figure 6-7 shows wide pit like, elongated IGC propagating directionally parallel to the rolling direction and fissure widening around intermetallic particles as they penetrate through the metal.

Corrosion site propagation has previously been presented using XMT on large length scales to assess the directionality of IGC [19, 20]. IGC growth in these studies was seen to be disjointed and irregular with the greatest rate growth occurring in the L orientation. Growth rates are thought to be highly dependent on mechanical processing; resulting in the SL direction being the slowest when compared to L and LT [17, 19, 20, 98]. Similar directional behaviour was also

seen in during wet dry cycling experiments presented in Figure 6-8 and Figure 6-9, where corrosion sites propagate deep into the metal surface. These deep sites initially grow in the LT and L directions are then seen to laterally expand. It has been hypothesised that this is a way of sustaining a large enough surface area for the cathodic reactions to occur. These findings show corrosion depth could be limited under solution droplets of a fixed diameter, however still leave a risk of stress corrosion cracking due to the generation of H_2 when oxygen reduction reaction is limited beyond a specific depth [75, 80]. In chapter 4 corrosion samples were not exposed for long enough for corrosion sites reach a limited depth. However the early stages of growth was observed and measured. Growth was seen to be irregular and random, with bursts of growth in varying directions (Figure 4-6 and Figure 4-7). Most growth occurred along the longitudinal orientation. High temporal resolution of directional growth lengths have allowed for estimations of current density during initiation and propagation. The largest current density was estimated to be 0.44 A/cm^2 (shown in Figure 4-8) in the L direction agreeing with previous studies of growth observation during the initial phases of corrosion site growth.

7.3   Atmospheric Corrosion Experimental Factors

7.3.1   Tomographic Experiments Compared to Lab Based Experiments

In both XMT and lab based experiments differences in corrosion behaviour can be seen between NaCl and ASTM ocean water atmospheric droplets. In constant RH shown in Figure 5-12 and constant RH XMT experiments in Figure 6-18 show similar trends in corrosion site number in NaCl and ASTM ocean water samples. NaCl was found to have a fewer number or deep corrosion sites

opposing to the ASTM ocean water is found to have multiple and shallow corrosion. Multiple methods were used to study the corrosion and corrosion products that precipitate under atmospheric droplets in chapter 5. Anodic sites in lab based experiments are shown to correlate with Cl and S found in EDX maps shown in Figure 5-17 and Figure 5-19. Where Cl is confined to one region on NaCl samples and Cl and S are found under the entire droplet footprint of ASTM ocean water droplets. Corrosion products are shown to correlate with anodic sites under NaCl and ASTM ocean water droplets as expected and previously shown in pits on aluminium alloys [211].

Due to the precipitation of S and Mg based corrosion products such as Felsöbányaite and Hydrotalcite under ASTM ocean water droplets on AA2024-T3 shown in Figure 5-18. The addition of sulphates have been documented to reduce the migration of ions within solution, slowing the movement of Cl⁻ towards anodic regions [73, 74]. Additionally sulphates are known inhibitors [24, 191-193] resulting in easier passivation suggesting reasons for multiple smaller corrosion sites in both XMT and lab experiments. Along with the presence of insoluble Mg-OH based corrosion precipitates causing reduction in droplet spreading area was observed in lab conditions.

Na was only found in the spreading region under ASTM ocean water droplets maps shown in Figure 5-17. Unlike under NaCl droplets where Na was found in both the main droplet region and spreading regions shown in Figure 5-19. This Na was found to correlate with the corrosion product Dawsonite. The production of Dawsonite was hypothesised to precipitate under both NaCl and ASTM ocean water droplets on AA2024-T3 samples droplets due to the presence of

Na$^+$ ions which are compelled to migrate towards OH$^-$ ions [108]. In AA1050 alloy corrosion rates are lower than that found on AA2024-T3 alloys suggesting a high concentration of OH$^-$ is required along with access of CO_2 to the droplet for Dawsonite to precipitate. No spreading region or Dawsonite as a result were seen on AA1050 samples shown in Figure 5-23. Showing the presence of Dawsonite indicates a high rate of corrosion has taken place for applications into CBM.

A comparison and lab based experiments should therefore be made cautiously. The size of XMT samples was selected to maximise spatial resolution, and consequentially reduced the cathodic area of the samples used. A reduction in cathodic area will reduce the rate of corrosion occurring on XMT samples.

7.3.2 Wet-Dry Cycling Compared to Constant Atmospheric Exposure

In service conditions aircraft will be exposed to cyclic RH changes from wet to dry. Wet dry cycling as a process within corrosion is rarely studied, however the current literature suggests that corrosion is worse under such conditions [21, 24].

Corrosion volume loss is higher following control wet-dry cycles than volume loss in constant exposure conditions investigated by XMT experiments in shown in Figure 6-18 agreeing with previous literature [21, 24].

As previously discussed in section 7.1 and 7.2 the droplet type and condition exhibit the same corrosion initiation processes and morphology. Equally results shown in chapter 6 highlight the difference in corrosion behaviour between NaCl and ASTM ocean water droplets as they undergo wet-dry cycling. The numerous salts that make up ASTM ocean water drastically affects their deliquescence and efflorescence rates. The ASTM ocean water droplet was seen to dry at a slower rate than NaCl leaving the sample exposed to highly concentrate salt solutions for longer durations during dry cycles. This contributed to the droplets steady increase in corrosion sites and volume loss. The NaCl droplet dried quickly and resulted in corrosion to cease during dry phases. In both cases the presence of highly concentrated solutions saw pit initiation occur, due to the inability of aluminium to re-passivate under a saturated solution [42, 207] either during drying of early stages of wetting. Pit growth then arose when the solutions were less saturated as free water becomes available for the transport of ions in solution during wet cycles of higher RH.

Steady state experiments carried out as a control for wet-dry cycling experiments showed similar findings to lab based corrosions experiments shown in Figure 6-18. Although there was a degree of scatter in X-ray data, constant RH NaCl droplets contained a smaller number of large corrosion sites, whereas ASTM ocean water samples show a higher number of shallow pits. In lab based experiments this was owed to the presence of S and Mg. Which unlike during wet-dry cycles were varying DRH effected corrosion site initiation and propagation, the migration of ions such as S and Cl under constant RH were found affect the corrosion rate in lab based experiments.

7.4   General Conclusions

X-ray micro tomography was used for the visualisation of corrosion of AA2024-T3 and has been achieved *in-situ*.

1. Initiation visualised and occurred at expected locations on AA2024-T3 in constant and varied exposure to RH, around and adjacent to intermetallic particles, under surface deposits such as dirt and salt crystals and at spatially unresolvable heterogeneities in the metal matrix.

2. Various morphology of corrosion sites was observed. These included shallow pits, deep fissures. Morphology was not affect by salt species or environmental conditions as similarities were seen across all experiments carried out.

3. During constant RH humidity corrosion sites were observed to grow one at a time. Once a corrosion site became stable it grew with irregular and random surges of growth in varying directions with the most growth occurring along the microstructural orientation.

4. The rate of initiation and propagation was different for NaCl and ASTM ocean water samples exposed to wet-dry cycles. Lower DRH of constituents salts in ASTM ocean water such as $MgCl_2$ and $CaCl_2$ created thin and constant solution layers where corrosion is seen to continuously develop under both wet and dry conditions. Unlike under the NaCl where no growth occurs in dry cycles. In both salts corrosion sites increase in volume the most during wet cycles.

5. In steady state lab and tomography experiments site numbers was similar. NaCl droplets contained fewer, but deeper corrosion sites. ASTM ocean water droplets contained many smaller corrosion sites. The study of corrosion products formed under the two types of salt droplets contributed to the difference in the number of corrosion sites to the presence of sulphate and magnesium in ocean water. Sulphate are thought to reduce ion migration increasing the distribution of anodic sites, while Mg is reduced droplet spreading and resultantly reduced the cathodic area.

6. The atmospheric corrosion products formed on AA2024-T3 and AA1050 were investigated with Raman mapping, FTIR, EDX and XRD. Corrosion products showed corrosion is affected by salt species. Salt constituents were found to be integrated into corrosion precipitates. Precipitates were controlled by anode and cathode distribution. Ocean waters anodic regions were dominated by Felsöbányaite and cathodic regions by Dawsonite, Hydrotalcite was also precipitated. NaCl anodic region was speculated to be Cu_2O (however not confirmed). Dawsonite was identified in cathodic regions in NaCl.

7. Tomography results show evidence of X-ray damage. Excessive hydrogen evolution and an increased volume loss during highly exposed wet-dry cycles compared to samples scanned at the end of exposure was observed.

7.5 Summary and Context of Work

Propagation and morphology was similar under NaCl and ASTM ocean water droplets. However environmental conditions such as wet-dry cycling were found to effects the rate of initiation and development of corrosion under NaCl and ASTM ocean water droplets. DRH of constituent salts in ASTM ocean water allowed for solution to remain on the metal surface which maintained corrosion during both wet and dry exposure. Unlike NaCl where dry exposed terminated corrosion. The presence of salts such as $MgCl_2$ and $CaCl_2$ should be taken into account when monitoring in service conditions.

NaCl may not be a good proxy for ASTM ocean water in corrosion experiments. Despite NaCl being a main constituent of ASTM ocean water the corrosion behaviour during the investigations in this thesis were found to be dissimilar. The inclusion of sulphates and magnesium in ASTM ocean water effect both anodic and cathodic processes in ASTM ocean water shown by the distribution of corrosion products and corrosion site number and location. These differences should be noted when carrying out experiments when using NaCl as a proxy to ASTM ocean water in accelerated testing and application to CBM.

The detection of Dawsonite indicates a high rate of corrosion has taken place. This finding could be applied in such applications as CBM.

7.6 FUTURE WORK

7.6.1 Further Tomographic Studies to Understand Growth Kinetics

The work undertaken in this thesis has left many opportunities open for the further study of atmospheric corrosion on AA2024-T3. Due to the improvements in the capabilities of synchrotron based experiments taken advantage of during this body of work, areas for possible investigations have been highlighted. These include, additional visualisation of H_2 to observe its evolution and assess the extent of beam damage to calculate its evolution as an accurate percentage of the two cathodic reactions; along with evaluation of maximum pit depth over longer atmospheric exposure. During this PhD data was gathered as a proof of concept for a new data collection method used at Diamond Light Source I13 [212], where samples were measured using a high-throughput system [213]. The new method allowed for developments in improving temporal resolution whilst maintaining enough spatial resolution to obtain bubble volume measurements. Analysis of this data would aid in obtaining knowledge about H_2 evolution as a ratio of the cathodic reactions on AA2024-T3. Further experiments using tomography could be carried out in order to establish depth and directional propagation of corrosion under atmospheric conditions for both steady state and wet-dry cycled samples.

During the data collection at the TOMCAT beamline at the Swiss Light Source (SLS) [174] data with high temporal resolution was gathered of corroded AA2024-T3 samples with various polymer coatings. This was done to simulate realistic aircraft conditions. Analysis of this data would allow for *in-situ* insight into the mechanisms of failure in realistic environment to those found on aircraft.

215

7.6.2 Accelerated Testing using Mix Salts Lab Based Studies

Due to the qualitative nature of the XTM data, statistical studies are required. XTM has shown that wet dry cycling for both NaCl and ASTM ocean water droplets results in a greater metal volume loss. Further statistical investigations into a comparison of steady state and wet and dry cycling behaviour is required to support these findings. A comprehensive break down of mixtures of salts and quantities using an automated deposition of droplets (previously used on 304L stainless steel [214]) could show the effects of DHR and EHR on corrosion accumulation. This will then be applicable for use in accelerated testing models.

7.6.3 Corrosion Product Precipitation

A comprehensive break down of salt mixtures needs to be investigated in order to understand the thermodynamics of precipitated corrosion products relative to anions and cations formed in atmospheric droplets. Sulphates within ASTM ocean water droplets have already shown to have an effect on corrosion accretion; therefore other abundant anthropogenic and natural aerosols such as nitrates, phosphates and sulphates, and salts needs to be introduced into the corrosion system systematically to investigate their affect atmospheric corrosion precipitates.

Production of Cu_2O or CuO in pitted regions was not confirmed in this body of work. Due to the excitation energy used during EDX of the corrosion products or the likelihood that the particle size is less than the resolution limit using Raman accurate conclusions could not be obtained. Further GIXRD analysis will enable the identification of the phases precipitated at anodic regions.

8. REFERENCES

1. Szklarska-Smialowska, Z., *Pitting corrosion of aluminum.* Corrosion Science, 1999. **41**(9): p. 1743-1767.
2. Hashimoto, T., X. Zhou, C. Luo, K. Kawano, G. Thompson, A. Hughes, P. Skeldon, P. Withers, T. Marrow, and A. Sherry, *Nanotomography for understanding materials degradation.* Scripta Materialia, 2010. **63**(8): p. 835-838.
3. Liao, C.-M., J. Olive, M. Gao, and R. Wei, *In-situ monitoring of pitting corrosion in aluminum alloy 2024.* Corrosion, 1998. **54**(6): p. 451-458.
4. Frankel, G.S., *The growth of 2-D pits in thin film aluminum.* Corrosion Science, 1990. **30**(12): p. 1203-1218.
5. Leblanc, P. and G.S. Frankel, *A Study of Corrosion and Pitting Initiation of AA2024-T3 Using Atomic Force Microscopy.* journal of the Electrochemical society, 2002. **149**(6): p. B239-B247.
6. Boag, A., A. Hughes, A. Glenn, T. Muster, and D. McCulloch, *Corrosion of AA2024-T3 Part I: Localised corrosion of isolated IM particles.* Corrosion Science, 2011. **53**(1): p. 17-26.
7. Hughes, A., T.H. Muster, A. Boag, A.M. Glenn, C. Luo, X. Zhou, G.E. Thompson, and D. McCulloch, *Co-operative corrosion phenomena.* Corrosion Science, 2010. **52**(3): p. 665-668.
8. Hughes, A.E., A. Boag, A.M. Glenn, D. McCulloch, T.H. Muster, C. Ryan, C. Luo, X. Zhou, and G.E. Thompson, *Corrosion of AA2024-T3 Part II: Co-operative corrosion.* Corrosion Science, 2011. **53**(1): p. 27-39.
9. Glenn, A.M., T.H. Muster, C. Luo, X. Zhou, G.E. Thompson, A. Boag, and A.E. Hughes, *Corrosion of AA2024-T3 Part III: Propagation.* Corrosion Science, 2011. **53**(1): p. 40-50.
10. King, P.C., I.S. Cole, P.A. Corrigan, A.E. Hughes, and T.H. Muster, *FIB/SEM study of AA2024 corrosion under a seawater drop: Part I.* Corrosion Science, 2011. **53**(3): p. 1086-1096.
11. King, P.C., I.S. Cole, P.A. Corrigan, A.E. Hughes, T.H. Muster, and S. Thomas, *FIB/SEM study of AA2024 corrosion under a seawater drop, part II.* Corrosion Science, 2012. **55**(0): p. 116-125.
12. Sun, S., Q. Zheng, D. Li, and J. Wen, *Long-term atmospheric corrosion behaviour of aluminium alloys 2024 and 7075 in urban, coastal and industrial environments.* Corrosion Science, 2009. **51**(4): p. 719-727.
13. Cheng, Y.L., Z. Zhang, F.H. Cao, J.F. Li, J.Q. Zhang, J.M. Wang, and C.N. Cao, *A study of the corrosion of aluminum alloy 2024-T3 under thin electrolyte layers.* Corrosion Science, 2004. **46**(7): p. 1649-1667.
14. Gunasegaram, D., M. Venkatraman, and I. Cole, *Towards multiscale modelling of localised corrosion.* International Materials Reviews, 2014. **59**(2): p. 84-114.
15. Buchheit, R., R. Grant, P. Hlava, B. McKenzie, and G. Zender, *Local Dissolution Phenomena Associated with S Phase (Al2CuMg) Particles in Aluminum Alloy 2024-T3.* Journal Of The Electrochemical Society, 1997. **144**(8): p. 2621-2628.
16. Zhou, X., C. Luo, T. Hashimoto, A. Hughes, and G. Thompson, *Study of localized corrosion in AA2024 aluminium alloy using electron tomography.* Corrosion Science, 2012. **58**: p. 299-306.
17. B. J. Connolly, D.A.H., S. J. Fox, A. J. Davenport, C. Padovani,, A.T. S. Zhou, M. Preuss, N. P. Stevens, T. J. Marrow, J.-Y. Buffiere,, and A.G.a.M.S. E. Boller, *X-ray microtomography studies of localised corrosion and transitions to*

stress corrosion cracking. Materials Science and Technology, 2006. **22**: p. 1076-1085.

18.   Eckermann, F., T. Suter, P.J. Uggowitzer, A. Afseth, M. Stampanoni, F. Marone, and P. Schmutz, *In Situ Microtomographically Monitored and Electrochemically Controlled Corrosion Initiation and Propagation in AlMgSi Alloy AA6016.* Journal of The Electrochemical Society, 2009. **156**(1): p. C1-C7.

19.   Knight, S.P., M. Salagaras, and A.R. Trueman, *The study of intergranular corrosion in aircraft aluminium alloys using X-ray tomography.* Corrosion Science, 2010. **53**: p. 727-734.

20.   Knight, S.P., M. Salagaras, A.M. Wythe, F.D. Carlo, A.J. Davenport, and A.R. Trueman, *In Situ X-Ray Tomography Of Intergranular Corrosion Of 2024 And 7050 Aluminium Alloys.* Corrosion Science, 2010: p. 1-7.

21.   Larignon, C., J. Alexis, E. Andrieu, C. Blanc, G. Odemer, and J.-C. Salabura, *Corrosion damages induced by cyclic exposure of 2024 aluminum alloy in chloride-containing environments.* Journal Of The Electrochemical Society, 2011. **158**(9): p. C284-C295.

22.   Dan, Z., S. Takigawa, I. Muto, and N. Hara, *Applicability of constant dew point corrosion tests for evaluating atmospheric corrosion of aluminium alloys.* Corrosion Science, 2011. **53**(5): p. 2006-2014.

23.   du Plessis, A., *Studies on Atmospheric Corrosion Processes in AA2024*, in *Metallurgy and Materials* 2015: University of Birmingham. p. 232.

24.   Dan, Z., I. Muto, and N. Hara, *Effects of Environmental Factors on Atmospheric Corrosion of Aluminium and Its Alloys under Constant Dew Point Conditions.* Corrosion Science, 2012(0).

25.   Hontelez, J.A., H.H. Burger, and D.J. Wijnmalen, *Optimum condition-based maintenance policies for deteriorating systems with partial information.* Reliability Engineering & System Safety, 1996. **51**(3): p. 267-274.

26.   Dieulle, L., C. Bérenguer, A. Grall, and M. Roussignol, *Sequential condition-based maintenance scheduling for a deteriorating system.* European Journal of Operational Research, 2003. **150**(2): p. 451-461.

27.   Bai, F., H. Zuo, and S. Ren. *Average life prediction for aero-engine fleet based on performance degradation data*. in *Prognostics and Health Management Conference, 2010. PHM '10.* 2010.

28.   Vaughan, F.O.H., *Standard ISA temperatures at 36000 ft altitude above sea level* S. Glanvill, Editor. 2014.

29.   Starke, E.A. and J.T. Staley, *Application of modern aluminum alloys to aircraft.* Progress in Aerospace Sciences, 1996. **32**(2-3): p. 131-172.

30.   Williams, J.C. and E.A. Starke, *Progress in structural materials for aerospace systems.* Acta Materialia, 2003. **51**(19): p. 5775-5799.

31.   Harlow, D.G. and R.P. Wei, *Probabilities of occurrence and detection of damage in airframe materials.* Fatigue & Fracture of Engineering Materials & Structures, 1999. **22**(5): p. 427-436.

32.   Scanff, E., K.L. Feldman, S. Ghelam, P. Sandborn, M. Glade, and B. Foucher, *Life cycle cost impact of using prognostic health management (PHM) for helicopter avionics.* Microelectronics Reliability, 2007. **47**(12): p. 1857-1864.

33.   Roemer, M.J., E. Nwadiogbu, and G. Bloor. *Development of diagnostic and prognostic technologies for aerospace health management applications*. in *Aerospace Conference, 2001, IEEE Proceedings.* 2001: IEEE.

34.   Trueman, T., Trathen, P., Begbie, K., Davidson, L., Hinton, B.,, *The Development of a Corrosion Prognostic Health Management System for Australian Defence Force Aircraft.* Advanced Materials Research (volume 38), 2008. **Corrosion in the Military II**: p. 182-200.

35. Ofsthun, S., *Integrated vehicle health management for aerospace platforms.* Instrumentation & Measurement Magazine, IEEE, 2002. **5**(3): p. 21-24.

36. Deyao, M., L. Chuan, S. Jianming, Z. Yingzhi, and G. Zhiqi. *Research of the military aircraft maintenance support mode based on the prognostics and health management.* in *Prognostics and Health Management Conference, 2010. PHM '10.* 2010.

37. Kim, N.-H., D. An, and J.-H. Choi, *Introduction*, in *Prognostics and Health Management of Engineering Systems: An Introduction*, N.-H. Kim, D. An, and J.-H. Choi, Editors. 2017, Springer International Publishing: Cham. p. 1-24.

38. Wan, F., X. Yu, and Q. Yu. *Research on Optimal Sensor Placement for Aircraft Structural Health Management.* in *Prognostics and Health Management (ICPHM), 2017 IEEE International Conference on.* 2017: IEEE.

39. Demo, J., F. Friedersdorf, C. Andrews, and M. Putic. *Wireless corrosion monitoring for evaluation of aircraft structural health.* in *Aerospace Conference, 2012 IEEE.* 2012: IEEE.

40. Xie, C., F. Wei, P. Wang, and H. Huang. *Modeling of corrosion pit growth for prognostics and health management.* in *Prognostics and Health Management (PHM), 2015 IEEE Conference on.* 2015: IEEE.

41. Bauccio, M., *ASM Metal Reference Book.* 3rd ed. Vol. 3rd Edition. 1993, Ohio: SM Internatioal. 614.

42. Polmear, I.J., *Light Alloys: Metallurgy of Light Metals.* 3rd ed. Vol. 3rd Edition. 1995: J.Wiley & Sons (New York) 416.

43. Schmitz, C., *Handbook of aluminium recycling.* 2006: Vulkan-Verlag GmbH.

44. Downs, A.J., *Chemistry of aluminium, gallium, indium and thallium.* 1993: Springer Science & Business Media.

45. Heinz, A., A. Haszler, C. Keidel, S. Moldenhauer, R. Benedictus, and W.S. Miller, *Recent development in aluminium alloys for aerospace applications.* Materials Science and Engineering A, 2000. **280**(1): p. 102-107.

46. Vargel, C., M. Jacques, and M.P. Schmidt, *Corrosion of Aluminium* ed. E. Amsterdam. 2004.

47. Guillaumin, V. and G. Mankowski, *Localized corrosion of 2024 T351 aluminium alloy in chloride media.* Corrosion Science, 1998. **41**(3): p. 421-438.

48. Wilson, R.N. and P.G. Partridge, *The nucleation and growth of S' precipitates in an aluminium-2.5% copper-1.2% magnesium alloy.* Acta Metallurgica, 1965. **13**(12): p. 1321-1327.

49. Adachi, H., K. Osamura, S. Ochiai, J. Kusui, and K. Yokoe, *Mechanical property of nanoscale precipitate hardening aluminum alloys.* Scripta Materialia, 2001. **44**(8–9): p. 1489-1492.

50. Dwight, J., *Aluminium design and construction.* 1999: Routledge.

51. Chandler, H., *Heat treater's guide: practices and procedures for nonferrous alloys.* 1996: ASM International (OH).

52. aluSelect. *Wrought Alloy Compositions* [cited 2014 13.05.14]; Available from: http://aluminium.matter.org.uk/aluselect/06_wrought_comp.asp.

53. Suter, T. and R.C. Alkire, *Microelectrochemical studies of pit initiation at single inclusions in Al 2024-T3.* Journal of the Electrochemical Society, 2001. **148**(1): p. B36-B42.

54. Wang, S. and M. Starink, *Two types of S phase precipitates in Al–Cu–Mg alloys.* Acta Materialia, 2007. **55**(3): p. 933-941.

55. Wei, R., C.-M. Liao, and M. Gao, *A transmission electron microscopy study of constituent-particle-induced corrosion in 7075-T6 and 2024-T3 aluminum alloys.* Metallurgical and Materials Transactions A, 1998. **29**(4): p. 1153-1160.

56. Boag, A., A.E. Hughes, N.C. Wilson, A. Torpy, C.M. MacRae, A.M. Glenn, and T.H. Muster, *How complex is the microstructure of AA2024-T3.* Corrosion Science, 2009. **51**(8): p. 1565-1568.

57. Polmear, I., *Light alloys: from traditional alloys to nanocrystals.* 2005: Butterworth-Heinemann.

58. Hughes, A.E.T., R. J.; Nelson, K. J. H.; Hinton, B. R. W.; Wilson, L., *Characterisation of surface preparation of 2024 aluminium alloy for conversion coating.* Materials Science and Technology, 1996. **12**: p. 928-936.

59. Grard, C., H.W.L. Phillips, and C.M. Phillips, *Aluminium and Its Alloys.* 1922.

60. Davenport, A.J., *Year 2 Corrosion Lectures.* 2010, University of Birmingham

61. Winkelman, G.B., K. Raviprasad, and B.C. Muddle, *Orientation relationships and lattice matching for the S phase in Al–Cu–Mg alloys.* Acta Materialia, 2007. **55**(9): p. 3213-3228.

62. Charai, A., T. Walther, C. Alfonso, A.M. Zahra, and C.Y. Zahra, *Coexistence of clusters, GPB zones, S″-, S′- and S-phases in an Al–0.9% Cu–1.4% Mg alloy.* Acta Materialia, 2000. **48**(10): p. 2751-2764.

63. Torsten, E.M.S., K. Benedikt, K. Iris, K. Björn, H. Matz, D. Esther, and M. Karl, *Atomic structure of pre-Guinier-Preston and Guinier-Preston-Bagaryatsky zones in Al-alloys.* Journal of Physics: Conference Series, 2011. **265**(1): p. 012018.

64. Kovarik, L., S.A. Court, H.L. Fraser, and M.J. Mills, *GPB zones and composite GPB/GPBII zones in Al–Cu–Mg alloys.* Acta Materialia, 2008. **56**(17): p. 4804-4815.

65. Staab, T.E., B. Klobes, I. Kohlbach, B. Korff, M. Haaks, E. Dudzik, and K. Maier. *Atomic structure of pre-Guinier-Preston and Guinier-Preston-Bagaryatsky zones in Al-alloys.* in *Journal of Physics: Conference Series.* 2011: IOP Publishing.

66. Davies, J.R., *Corrosion of Aluminium and Aluminium Alloys.* 1999: ASM International. 313.

67. Pourbaix, M., *Atlas of electrochemical equilibria in aqueous solutions.* 1974.

68. Vargel, C., *Corrosion of Aluminium.* Materials & Mechanical. 2004: Elsevier Science. 1-658.

69. Marcus, P., *Corrosion mechanisms in theory and practice.* 2011: CRC PressI Llc.

70. Armstrong, R.D. and V.J. Braham, *The mechanism of aluminium corrosion in alkaline solutions.* Corrosion Science, 1996. **38**(9): p. 1463-1471.

71. Onuchukwu, A.I. and A.A.I. Adamu, *The Kinetics And Mechanism Of Hydrogen Evolution On Corroding Aluminum In Alkaline-Medium.* Materials Chemistry and Physics, 1990. **25**(3): p. 227-235.

72. Frankel, G., *Pitting corrosion.* ASM Handbook, 2003. **13**: p. 236-241.

73. Tomcsányi, L., K. Varga, I. Bartik, H. Horányi, and E. Maleczki, *Electrochemical study of the pitting corrosion of aluminium and its alloys—II. Study of the interaction of chloride ions with a passive film on aluminium and initiation of pitting corrosion.* Electrochimica Acta, 1989. **34**(6): p. 855-859.

74. McCafferty, E., *Sequence of steps in the pitting of aluminum by chloride ions.* Corrosion Science, 2003. **45**(7): p. 1421-1438.

75. Galvele, J.R., *Transport Processes and the Mechanism of Pitting of Metals.* Electrochemical Science and Technology, 1976. **123**(4): p. 11.

76. Frankel, G., *Pitting corrosion of metals a review of the critical factors.* Journal Of The Electrochemical Society, 1998. **145**(6): p. 2186-2198.

77. Glenn, A., T. Muster, C. Luo, X. Zhou, G. Thompson, A. Boag, and A. Hughes, *Corrosion of AA2024-T3 Part III: propagation.* Corrosion Science, 2011. **53**(1): p. 40-50.

78. Trueman, A.R., *Determining the probability of stable pit initiation on aluminium alloys using potentiostatic electrochemical measurements.* Corrosion Science, 2005. **47**(9): p. 2240-2256.

79. Wood, G.C., *Role Of Flaws In Breakdown Of Passivity Leading To Pitting Of Aluminum And Crevice Corrosion Of Stainless Steel.* Cor. & Coatings 1980.

80. Pride, S., J. Scully, and J. Hudson, *Metastable pitting of aluminum and criteria for the transition to stable pit growth.* Journal Of The Electrochemical Society, 1994. **141**(11): p. 3028-3040.

81. McCafferty, E., *The electrode kinetics of pit initiation on aluminum.* Corrosion Science, 1995. **37**(3): p. 481-492.

82. Amin, M.A., *Metastable and stable pitting events on Al induced by chlorate and perchlorate anions--Polarization, XPS and SEM studies.* Electrochimica Acta, 2009. **54**(6): p. 1857-1863.

83. Boag, A., R.J. Taylor, T.H. Muster, N. Goodman, D. McCulloch, C. Ryan, B. Rout, D. Jamieson, and A.E. Hughes, *Stable pit formation on AA2024-T3 in a NaCl environment.* Corrosion Science, 2010. **52**: p. 90-103.

84. Frankel, G.S., *Pitting corrosion of metals: A review of the critical factors.* Journal Name: Journal of the Electrochemical Society; Journal Volume: 145; Journal Issue: 6; Other Information: PBD: Jun 1998, 1998: p. Medium: X; Size: pp. 2186-2197.

85. Baumgärtner, M. and H. Kaesche, *Aluminum pitting in chloride solutions: morphology and pit growth kinetics.* Corrosion Science, 1990. **31**(0): p. 231-236.

86. Edeleanu, C. and U.R. Evans, *The Causes Of The Localized Character Of Corrosion On Aluminium.* Transactions of the Faraday Society, 1951. **47**(10): p. 1121-1135.

87. Zhao, S., D.A. Wolfe, T.-S. Huang, and G.S. Frankel, *Generalized model for IGC growth in aluminum alloys.* Journal of Statistical Planning and Inference, 2007. **137**(7): p. 2405-2412.

88. Schweitzer, P.A., *Fundamentals of metallic corrosion :: atmospheric and media corrosion of metals.* 2006, Taylor & Francis.

89. Galvele, J.R. and S.M. de De Micheli, *Mechanism of intergranular corrosion of Al-Cu alloys.* Corrosion Science, 1970. **10**(11): p. 795-807.

90. Liu, X., G.S. Frankel, B. Zoofan, and S.I. Rokhlin, *Transition from Intergranular Corrosion to Intergranular Stress Corrosion Cracking in AA2024-T3.* Journal of The Electrochemical Society, 2006. **153**(2): p. B42-B51.

91. Augustin, C., E. Andrieu, C. Blanc, G. Mankowski, and J. Delfosse, *Intergranular corrosion of 2024 alloy in chloride solutions.* Journal of The Electrochemical Society, 2007. **154**(11): p. C637-C644.

92. Zhao, X., G.S. Frankel, B. Zoofan, and S.I. Rokhlin, *In situ X-ray radiographic study of intergranular corrosion in aluminum alloys.* Corrosion, 2003. **59**(11): p. 1012-1018.

93. Ruan, S., D.A. Wolfe, W. Zhang, and G.S. Frankel, *Statistical modeling of minimum intergranular corrosion path length in high-strength aluminum alloy.* Technometrics, 2004. **46**(1): p. 69-75.

94. Zhang, W. and G.S. Frankel, *Anisotropy of Localized Corrosion in AA2024-T3.* Electrochemical and Solid-State Letters, 2000. **3**(6): p. 268-270.

95. Zhang, W., S. Ruan, D.A. Wolfe, and G.S. Frankel, *Statistical model for intergranular corrosion growth kinetics.* Corrosion Science, 2003. **45**(2): p. 353-370.

96. Hunkeler, F. and H. Bohni, *Determination of Pit Growth Rates on Aluminum Using a Metal Foil Technique.* Corrosion, 1981. **37**(11): p. 645-650.

97. Sehgal, A., G.S. Frankel, B. Zoofan, and S. Rokhlin, *Pit Growth Study in Al Alloys by the Foil Penetration Technique.* Journal of The Electrochemical Society, 2000. **147**(1): p. 140-148.

98. Fox, S., *An In Situ X-Ray Tomography Study of the Growth and Development of Localised Corrosion in Friction Stir Welded AA2024-T351*, in *Metallurgy and Materias.* 2006, University of Birmingham: Birmingham (UK). p. 231.

99. Rafla, V., A. Davenport, and J.R. Scully, *Determination of Cathodic and Anodic Charge from Operando X-Ray Tomography Observation of Galvanic Corrosion of Aluminum Alloy 7050-T7451 and 304 Stainless Steel in a Simulated Fastener.* Corrosion, 2015. **71**(11): p. 1300-1303.

100. Rafla, V., A.D. King, S. Glanvill, A. Parsons, A. Davenport, and J.R. Scully, *Operando Observation of Galvanic Corrosion Between Aluminum Alloy 7050-T7451 and 304 Stainless Steel in a Simulated Fastener Arrangement Using X-Ray Tomography.* Corrosion, 2015. **71**(10): p. 1171-1176.

101. Brunner, J.G., N. Birbilis, K.D. Ralston, and S. Virtanen, *Impact of ultrafine-grained microstructure on the corrosion of aluminium alloy AA2024.* Corrosion Science, 2012. **57**(0): p. 209-214.

102. Oltra, R., B. Malki, and F. Rechou, *Influence of aeration on the localized trenching on aluminium alloys.* Electrochimica Acta, 2010. **55**(15): p. 4536-4542.

103. Schneider, O., G. Ilevbare, J. Scully, and R. Kelly, *In situ confocal laser scanning microscopy of AA 2024-T3 corrosion metrology II. Trench formation around particles.* Journal Of The Electrochemical Society, 2004. **151**(8): p. B465-B472.

104. Graedel, T.E., *Corrosion Mechanisms for Aluminum Exposed to the Atmosphere.* Journal of The Electrochemical Society, 1989. **136**(4): p. 204C-212C.

105. Phambu, N., *Adsorption of carboxylic acids on submicrocrystalline aluminum hydroxides in aqueous solution. Part 1: Qualitative study by infrared and Raman spectroscopy.* Applied Spectroscopy, 2002. **56**(6): p. 756-761.

106. Zhang, J., M. Klasky, and B.C. Letellier, *The aluminum chemistry and corrosion in alkaline solutions.* Journal of Nuclear Materials, 2009. **384**(2): p. 175-189.

107. Ruan, H., R. Frost, and J. Kloprogge, *Comparison of Raman spectra in characterizing gibbsite, bayerite, diaspore and boehmite.* Journal of Raman Spectroscopy, 2001. **32**(9): p. 745-750.

108. Schaller, R.F., C.F. Jove-Colon, J.M. Taylor, and E.J. Schindelholz, *The controlling role of sodium and carbonate on the atmospheric corrosion rate of aluminum.* Materials Degradation, 2017. **1**(1): p. 20.

109. Hurley, B.L., S. Qiu, and R. Buchheit, *Raman spectroscopy characterization of aqueous vanadate species interaction with aluminum alloy 2024-T3 surfaces.* Journal of The Electrochemical Society, 2011. **158**(5): p. C125-C131.

110. Huang, I.W., B.L. Hurley, F. Yang, and R.G. Buchheit, *Dependence on Temperature, pH, and Cl− in the Uniform Corrosion of Aluminum Alloys 2024-T3, 6061-T6, and 7075-T6.* Electrochimica Acta, 2016. **199**: p. 242-253.

111. Wang, B.B., Z.Y. Wang, W. Han, and W. Ke, *Atmospheric corrosion of aluminium alloy 2024-T3 exposed to salt lake environment in Western China.* Corrosion Science, 2012. **59**(0): p. 63-70.

112. Blucher, D.B., J.E. Svensson, and L.G. Johansson, *The influence of CO2, ACl(3), 6H(2)O, MgCl2 6H(2)O, Na2SO4 and NaCl on the atmospheric corrosion of aluminum.* Corrosion Science, 2006. **48**(7): p. 1848-1866.

113. Ramsey, J.D. and R.L. McCreery, *In situ Raman microscopy of chromate effects on corrosion pits in aluminum alloy.* Journal of the Electrochemical Society, 1999. **146**(11): p. 4076-4081.

114. Zhao, J., G. Frankel, and R.L. McCreery, *Corrosion Protection of Untreated AA-2024-T3 in Chloride Solution by a Chromate Conversion Coating Monitored with Raman Spectroscopy.* Journal of the Electrochemical Society, 1998. **145**(7): p. 2258-2264.

115. Buchheit, R.G., S.B. Mamidipally, P. Schmutz, and H. Guan, *Active Corrosion Protection in Ce-Modified Hydrotalcite Conversion Coatings.* CORROSION, 2002. **58**(1): p. 3-14.

116. Zhang, W. and R.G. Buchheit, *Hydrotalcite Coating Formation on Al-Cu-Mg Alloys from Oxidizing Bath Chemistries.* CORROSION, 2002. **58**(7): p. 591-600.

117. Lee, H.-S., J. Singh, M. Ismail, and C. Bhattacharya, *Corrosion Resistance Properties of Aluminum Coating Applied by Arc Thermal Metal Spray in SAE J2334 Solution with Exposure Periods.* Metals, 2016. **6**(3): p. 55.

118. Kreta, A., M. Rodošek, L.S. Perše, B. Orel, M. Gaberšček, and A.Š. Vuk, *In situ electrochemical AFM, ex situ IR reflection–absorption and confocal Raman studies of corrosion processes of AA 2024-T3.* Corrosion Science, 2016. **104**: p. 290-309.

119. Calderón, J.A. and C.E. Arroyave, *A Laboratory Approach to the Mechanism of Attack on the Wire-on-Bolt Device Used for Atmospheric Corrosion Studies.* CORROSION, 2005. **61**(2): p. 99-110.

120. Le Bozec, N., D. Persson, A. Nazarov, and D. Thierry, *Investigation of filiform corrosion on coated aluminum alloys by FTIR microspectroscopy and scanning Kelvin probe.* Journal of The Electrochemical Society, 2002. **149**(9): p. B403-B408.

121. Dan, Z., I. Muto, and N. Hara. *Role of Corrosion Products in the Suppression of Atmospheric Corrosion of Aluminum and its Alloys.* in *Meeting Abstracts.* 2009: The Electrochemical Society.

122. Phambu, N., *Characterization of aluminum hydroxide thin film on metallic aluminum powder.* Materials Letters, 2003. **57**(19): p. 2907-2913.

123. Frost, R.L. and J.M. Bouzaid, *Raman spectroscopy of dawsonite NaAl (CO3)(OH) 2.* Journal of Raman Spectroscopy, 2007. **38**(7): p. 873-879.

124. Kloprogge, J.T., L. Hickey, and R.L. Frost, *FT-Raman and FT-IR spectroscopic study of synthetic Mg/Zn/Al-hydrotalcites.* Journal of Raman Spectroscopy, 2004. **35**(11): p. 967-974.

125. Cole, I.S.G., W. D.; Paterson, D. A.; King, G. A.; Furman, S. A.; Lau, D., *Holistic model for atmospheric corrosion: Part 2 - Experimental measurement of deposition of marine salts in a number of long range studies.* Corrosion Engineering, Science and Technology, 2003. **38**: p. 259-266.

126. Wang, H., X. Wang, X. Yang, W. Li, L. Xue, T. Wang, J. Chen, and W. Wang, *Mixed Chloride Aerosols and their Atmospheric Implications: A Review.* Aerosol and Air Quality Research, 2017. **17**(4): p. 878-887.

127. Leygraf, C., *New fundamental and environmental aspects of atmospheric corrosion.* Revista De Metalurgia, 2009. **45**(3): p. 223-227.

128. Wright, M.R., *An Introduction to Aqueous Electrolyte Solutions.* 1 ed, ed. Wiley. 2007: Wiley. 604.

129. Greenspan, L., *Humidity fixed points of binary saturated aqueous solutions.* Journal of research of the National Bureau of Standards. A, Physics and chemistry, January 1977. **81a** (1): p. 89-96

130. Smart, N. and J.O.M. Bockris, *Effect of water activity on corrosion.* Corrosion, 1992. **48**(4): p. 277-280.

131. Cook, A.B., S.B. Lyon, N.P. Stevens, R.C. Newman, M. Gunther, G. McFiggans, and D.L. Engelberg, *Under-deposit chloride-induced stress corrosion cracking in austenitic stainless steels: aspects associated with deposit type, size and composition.* ECS Transactions, 2014. **58**(29): p. 25-39.

132. Zemaitis Jr, J.F., D.M. Clark, M. Rafal, and N.C. Scrivner, *Handbook of Aqueous Electrolyte Thermodynamics: Theory & Application.* 2010: Wiley-AIChE.

133. Lide, D. and Cleveland, *Hand book of Chemistry and Physics* CRC, 1994. **75**.

134. Chen, Z. and R. Kelly, *Computational modeling of bounding conditions for pit size on stainless steel in atmospheric environments.* Journal Of The Electrochemical Society, 2010. **157**(2): p. C69-C78.

135. Li, C., Y. Ma, Y. Li, and F. Wang, *EIS monitoring study of atmospheric corrosion under variable relative humidity.* Corrosion Science, 2010. **52**(11): p. 3677-3686.

136. Morton, S.C. and G.S. Frankel, *Atmospheric pitting corrosion of AA7075-T6 under evaporating droplets with and without inhibitors.* Materials and Corrosion, 2014. **65**(4): p. 351-361.

137. Shi, Y.Y., Z. Zhang, J.X. Su, and J.Q. Zhang, *EIS study on 2024-T3 aluminum alloy corrosion in simulated acid rain under cyclic wet-dry conditions.* Materials and Corrosion, 2005. **56**(10): p. 701-706.

138. Evans, U., *The ferroxyl indicator in corrosion research.* The Metal Industry, 1926: p. 507-508.

139. Jia, W. and H. Bao-rong, *Characteristics of the oxygen reduction in atmospheric corrosion.* Chinese Journal of Oceanology and Limnology, 1997. **15**(1): p. 36-41.

140. He, K., H. Cheng, Y. Zhu, L. Wang, and Y. Zhang, *Measurement of electric properties of the single supersaturated aerosol droplet.* Chinese Science Bulletin, 2008. **53**(11): p. 1773-1776.

141. El-Mahdy, G.A. and K.B. Kim, *AC impedance study on the atmospheric corrosion of aluminum under periodic wet–dry conditions.* Electrochimica Acta, 2004. **49**(12): p. 1937-1948.

142. Chiba, M., S. Saito, K. Nagai, H. Takahashi, and Y. Shibata, *Effect of NaCl concentration on corrosion of Al alloy during repeated wet–dry cycle tests at 323 K—comparing with corrosion in immersion tests-.* Surface and Interface Analysis, 2016. **48**(8): p. 767-774.

143. Shi, Y., Z. Zhang, J. Su, F. Cao, and J. Zhang, *Electrochemical noise study on 2024-T3 Aluminum alloy corrosion in simulated acid rain under cyclic wet–dry condition.* Electrochimica Acta, 2006. **51**(23): p. 4977-4986.

144. Ul-Hamid, A., A. Ul-Hamid, L.M. Al-Hems, L.M. Al-Hems, A. Quddus, A. Quddus, A.I. Muhammed, A.I. Muhammed, H. Saricimen, and H. Saricimen, *Corrosion performance of aluminium in atmospheric, underground and seawater splatter zone in the northeastern coast of Arabian Peninsula.* Anti-Corrosion Methods and Materials, 2017. **64**(3): p. 326-334.

145. Blücher, D.B., J.E. Svensson, and L.G. Johansson, *The influence of CO2, AlCl3 · 6H2O, MgCl2 · 6H2O, Na2SO4 and NaCl on the atmospheric corrosion of aluminum.* Corrosion Science, 2006. **48**(7): p. 1848-1866.

146. Bian, L., Y. Weng, and X. Li, *Observation of micro-droplets on metal surface in early atmospheric corrosion.* Electrochemistry Communications, 2005. **7**(10): p. 1033-1038.

147. Tsuru, T., K.-I. Tamiya, and A. Nishikata, *Formation and growth of micro-droplets during the initial stage of atmospheric corrosion.* Electrochimica Acta, 2004. **49**(17-18): p. 2709-2715.

148. Li, J., B. Maier, and G. Frankel, *Corrosion of an Al–Mg–Si alloy under MgCl 2 solution droplets.* Corrosion Science, 2011. **53**(6): p. 2142-2151.

149. Zhang, J., J. Wang, and Y. Wang, *Micro-Droplets Formation during the Deliquescence of Salt Particles in Atmosphere.* Corrosion, 2005. **61**(12): p. 1167-1172.

150. Lacroix, L., C. Blanc, N. Pébère, G.E. Thompson, B. Tribollet, and V. Vivier, *Simulating the galvanic coupling between S-Al2CuMg phase particles and the matrix of 2024 aerospace aluminium alloy.* Corrosion Science, 2012. **64**(0): p. 213-221.

151. Sato, N., *Anodic Breakdown of Passive Films on Metals.* Journal of The Electrochemical Society, 1982. **129**(2): p. 255-260.

152. Knight, S., M. Salagaras, and A. Trueman, *The study of intergranular corrosion in aircraft aluminium alloys using X-ray tomography.* Corrosion Science, 2011. **53**(2): p. 727-734.

153. Liao, C.M., J.M. Olive, M. Gao, and R.P. Wei, *In-situ monitoring of pitting corrosion in aluminum alloy 2024.* Journal Name: Corrosion; Journal Volume: 54; Journal Issue: 6; Other Information: PBD: Jun 1998, 1998: p. Medium: X; Size: pp. 451-458.

154. Baruchel, J., J.-Y. Buffiere, and E. Maire, *X-ray tomography in material science.* 2000.

155. Flannery, B.P. and W.G. Roberge, *observational strategies for 3-dimensional synchrotron microtomography.* Journal of Applied Physics, 1987. **62**(12): p. 4668-4674.

156. Kinney, J.H. and M.C. Nichols, *X-Ray Tomographic Microscopy (XTM) Using Synchrotron Radiation.* Material Science, 1992. **Annual Review**(22): p. 121-52.

157. Landis, E.N. and D.T. Keane, *X-ray microtomography.* Materials Characterization, 2010. **61**(12): p. 1305-1316.

158. Salvo, L., M. Suéry, A. Marmottant, N. Limodin, and D. Bernard, *3D imaging in material science: Application of X-ray tomography.* Comptes Rendus Physique. **11**(9-10): p. 641-649.

159. Stock, S.R., *X-ray microtomography of materials.* International materials reviews, 1999. **44**(4): p. 141-164.

160. Cloetens, P., W. Ludwig, E. Boller, F. Peyrin, M. Chlenker, and J. Baruchel, *3d imaging using coherent synchrotron radiation.* 2011. Vol. 21. 2011.

161. Willmott, P., *An introduction to synchrotron radiation: Techniques and applications.* 2011: John Wiley & Sons.

162. Institute, P.S. *TOMCAT Source Characteristics.* [24/01/18]; Available from: https://www.psi.ch/sls/tomcat/source.

163. Thompson, S.P., J.E. Parker, J. Marchal, J. Potter, A. Birt, F. Yuan, R.D. Fearn, A.R. Lennie, S.R. Street, and C.C. Tang, *Fast X-ray powder diffraction on I11 at Diamond.* Journal of synchrotron radiation, 2011. **18**(4): p. 637-648.

164. Grossmann, J.G., R.W. Strange, and V.P. Suller, *Synchrotron Radiation (Production and Properties). By Philip John Duke. Oxford Science Publications, 2000. Pp. 251. Price (hardback) [pound sign]70.00. ISBN 0 19 851758 0.* Journal of Synchrotron Radiation, 2001. **8**(1): p. 38.

165. Banhart, J., *Advanced Tomographic Methods in Materials Research and Engineering.* 2008, Berlin: Oxford University Press.

166. Marone, F., Stampanoni, M., *Regridding reconstruction algorithm for real time tomographic imaging.* Journal of Synchrotron Radiation, 2012 (accepted manuscript).

167. Feldkamp, L.A., L.C. Davis, and J.W. Kress, *Practical cone-beam algorithm.* Optical Science of America, 1984. **1**(6): p. 612-620.

168. Nagy, Z. and H. You, *Radiolytic Effects On The In Situ Investigation Of Buried Interfaces With Sychrotron X-Ray Techniques*.* Electroanalytical Chemistry, 1994. **381**: p. 275-279.

169.   Whillock, G.O.H., S.E. Worthington, and C.J. Donohoe, *Localized Corrosion of Stainless Steel in a Nuclear Waste Cooling Water System— Part 1: Crevice Corrosion Studies.* Corrosion Science, 2012. **68**(8): p. 677-688.

170.   Song, T.H., I.S. Kim, and S.K. Rho, *Effects of H2O2 on the corrosion behaviour of 304L stainless steel.* journal of the Korean Nuclear Society, 1995. **27**(4): p. 453-463.

171.   Vander Voort, G.F., S.R. Lampman, B.R. Sanders, G.J. Anton, C. Polakowski, J. Kinson, K. Muldoon, S.D. Henry, and W.W. Scott Jr, *ASM handbook.* Metallography and microstructures, 2004. **9**: p. 44073-0002.

172.   ASTM, *D1141-98(2008) Standard Practice for the Preparation of Substitute Ocean Water*. 2008, ASTM International: West Conshohocken.

173.   Schindelin, J., I. Arganda-Carreras, E. Frise, V. Kaynig, M. Longair, T. Pietzsch, S. Preibisch, C. Rueden, S. Saalfeld, B. Schmid, J.-Y. Tinevez, D.J. White, V. Hartenstein, K. Eliceiri, P. Tomancak, and A. Cardona. *Fiji: an open-source platform for biological-image analysis*. [Software] 2012 [cited 2013 26 march 2013]; Available from: http://fiji.sc/Fiji.

174.   Marone, F., C. Hintermüller, S. McDonald, R. Abela, G. Mikuljan, A. Isenegger, and M. Stampanoni, *X-ray Tomographic Microscopy at TOMCAT.* Journal of Physics: Conference Series, 2009. **186**(1): p. 012042.

175.   Rasband, W.S., *Image J*. 1997, U.S National Institute of Health: Bethesda, Maryland, USA.

176.   Europe, A., *Certificate of Conformity* Wilsons, Editor. 2013: Windover Road, Huntington, Cambridge

177.   Lafuente, B., R.T. Downs, H. Yang, and N. Stone, *The power of databases: the RRUFF project.* Highlights in Mineralogical Crystallography, 2015.

178.   Zhang, X., Z. Wen, Z. Gu, X. Xu, and Z. Lin, *Hydrothermal synthesis and thermodynamic analysis of dawsonite-type compounds.* Journal of Solid State Chemistry, 2004. **177**(3): p. 849-855.

179.   Corazza, E., C. Sabelli, and S. Vannucci, *Dawsonite: new mineralogical data and structure refinement*. 1977: E. Schweizerbart.

180.   Farkas, L. and F. Pertlik, *Crystal structure determinations of felsöbányaite and basaluminite, Al4 (SO4)(OH) 10· 4H2O.* Acta Mineral Petrogr Szeged, 1997. **38**: p. 5-15.

181.   Kabekkodu, D.S. *ICDD PDF-4+ 20xx (Database)*. Available from: http://www.icdd.com/index.htm.

182.   Stratmann, M. and H. Streckel, *On the atmospheric corrosion of metals which are covered with thin electrolyte layers—I. Verification of the experimental technique.* Corrosion Science, 1990. **30**(6-7): p. 681-696.

183.   Szklarska-Smialowska, Z., *Progress in understanding pitting corrosion*. Corrosion Science: A Retrospective and Current Status in Honor of Robert P Frankenthal, ed. G.S. Frankel, H.S. Isaacs, J.R. Scully, and J.D. Sinclair. Vol. 2002. 2002. 251-265.

184.   Zavadil, K.R., J. Ohlhausen, and P. Kotula, *Nanoscale void nucleation and growth in the passive oxide on aluminum as a prepitting process.* Journal Of The Electrochemical Society, 2006. **153**(8): p. B296-B303.

185.   Zahavi, J. and M. Metzger, *Electron Microscope Study of Breakdown and Repair of Anodic Films on Aluminum.* Journal of The Electrochemical Society, 1972. **119**(11): p. 1479-1485.

186.   Baumgärtner, M. and H. Kaesche, *Microtunnelling during localized attack of passive aluminum: The case of salt films vs oxide films.* Corrosion Science, 1989. **29**(2–3): p. 363-378.

187. Pride, S.T., J.R. Scully, and J.L. Hudson, *Metastable Pitting of Aluminum and Criteria for the Transition to Stable Pit Growth.* Journal of The Electrochemical Society, 1994. **141**(11): p. 3028-3040.

188. Pourbaix, M., *Thermodynamics and corrosion.* Corrosion Science, 1990. **30**(10): p. 963-988.

189. Kelly, R., J. Scully, D. Shoesmith, and R. Buchheit, *Electrochemical techniques in corrosion science and engineering* Corrosion technology (New York, N.Y.) 18 2003, New York: Marcel Dekker. 426.

190. Brossia, C.S. and R.G. Kelly, *Influence of Alloy Sulfur Content and Bulk Electrolyte Composition on Crevice Corrosion Initiation of Austenitic Stainless Steel.* CORROSION, 1998. **54**(2): p. 145-154.

191. Kolics, A., J.C. Polkinghorne, and A. Wieckowski, *Adsorption of sulfate and chloride ions on aluminum.* Electrochimica Acta, 1998. **43**(18): p. 2605-2618.

192. Bohni, H., *Ugligs Corrions Handbook.* Second Edition ed, ed. R.W. Revie. 2000: John Wiley & Sons, Inc.

193. Böhni, H. and H.H. Uhlig, *Environmental factors affecting the critical pitting potential of aluminum.* Journal of The Electrochemical Society, 1969. **116**(7): p. 906-910.

194. Li, J., B. Hurley, and R. Buchheit, *Effect of Temperature on the Localized Corrosion of AA2024-T3 and the Electrochemistry of Intermetallic Compounds During Exposure to a Dilute NaCl Solution.* CORROSION, 2016. **72**(10): p. 1281-1291.

195. Buchheit, R.G., M.A. Martinez, and L.P. Montes, *Evidence for Cu ion formation by dissolution and dealloying the Al{sub 2}CuMg intermetallic compound in rotating ring-disk collection experiments.* Journal of the Electrochemical Society, 2000: p. Medium: X; Size: page(s) 119-124.

196. Feng, Y., K.-S. Siow, W.-K. Teo, K.-L. Tan, and A.-K. Hsieh, *Corrosion Mechanisms and Products of Copper in Aqueous Solutions at Various pH Values.* CORROSION, 1997. **53**(5): p. 389-398.

197. Ilevbare, G., O. Schneider, R. Kelly, and J. Scully, *In situ confocal laser scanning microscopy of AA 2024-T3 corrosion metrology I. Localized corrosion of particles.* Journal Of The Electrochemical Society, 2004. **151**(8): p. B453-B464.

198. Neufeld, A.K., I.S. Cole, A.M. Bond, and S.A. Furman, *The initiation mechanism of corrosion of zinc by sodium chloride particle deposition.* Corrosion Science, 2002. **44**(3): p. 555-572.

199. Hänchen, M., V. Prigiobbe, R. Baciocchi, and M. Mazzotti, *Precipitation in the Mg-carbonate system—effects of temperature and CO_2 pressure.* Chemical Engineering Science, 2008. **63**(4): p. 1012-1028.

200. Sommers, A.D. and A.M. Jacobi, *Wetting phenomena on micro-grooved aluminum surfaces and modeling of the critical droplet size.* Journal of Colloid and Interface Science, 2008. **328**(2): p. 402-411.

201. Kolics, A., J.C. Polkinghorne, A.E. Thomas, and A. Wieckowski, *Sorption of Sulfate and Chloride Anions on a Well-Characterized Al 2024 Electrode.* Chemistry of Materials, 1998. **10**(3): p. 812-824.

202. Pyun, S.-I. and S.-M. Moon, *The inhibition mechanism of pitting corrosion of pure aluminum by nitrate and sulfate ions in neutral chloride solution.* Journal of Solid State Electrochemistry, 1999. **3**(6): p. 331-336.

203. Na, M., M. Ghahari, T. Rayment, and A.J. Davenport, *Use of inkjet printing to deposit magnesium chloride salt patterns for investigation of atmospheric corrosion of 304 stainless steel.* Corrosion Science, 2011. **53**(10): p. 3114-3122.

204. Palmer, S.J. and R.L. Frost, *Use of Hydrotalcites for the Removal of Toxic Anions from Aqueous Solutions.* Industrial & Engineering Chemistry Research, 2010. **49**(19): p. 8969-8976.

205. Drewien, C., M. Eatough, D. Tallant, C. Hills, and R. Buchheit, *Lithium-aluminum-carbonate-hydroxide hydrate coatings on aluminum alloys: Composition, structure, and processing bath chemistry.* Journal of materials research, 1996. **11**(06): p. 1507-1513.

206. Austing, C.E., A.M. Pritchard, and N.J.M. Wilkins, *The formation and properties of Al/Mg scales on Al heat- exchange surfaces in desalination plant.* Desalination, 1973. **12**(2): p. 251-272.

207. Street, D.S., M.A. Cook, D.H. Mohammed-Ali, P.T. Rayment, and D.A. Davenport, *The effect of deposition conditions on atmospheric pitting corrosion location under Evans droplets on 304L stainless steel.* CORROSION. **0**(0): p. null.

208. Evans, U.R., *Oxygen Distribution as a Factor in the Corrosion of Metals.* Industrial & Engineering Chemistry, 1925. **17**(4): p. 363-372.

209. Yang, L.T., R.T. Pabalan, and L. Browning, *Experimental determination of the deliquescence relative humidity and conductivity of multicomponent salt mixtures*, in *Scientific Basis for Nuclear Waste Management Xxv*, B.P. McGrail and G.A. Cragnolino, Editors. 2002, Materials Research Society: Warrendale. p. 135-142.

210. Gao, Y., S.B. Chen, and E.Y. Liya, *Efflorescence relative humidity of airborne sodium chloride particles: A theoretical investigation.* Atmospheric Environment, 2007. **41**(9): p. 2019-2023.

211. Foley, R. and T. Nguyen, *The chemical nature of aluminum corrosion v. energy transfer in aluminum dissolution.* Journal of the Electrochemical Society, 1982. **129**(3): p. 464-467.

212. Bodey, A. and C. Rau. *Launch of the I13-2 data beamline at the Diamond Light Source synchrotron*. in *Journal of Physics: Conference Series*. 2017: IOP Publishing.

213. Atwood, R.C., A.J. Bodey, S.W. Price, M. Basham, and M. Drakopoulos, *A high-throughput system for high-quality tomographic reconstruction of large datasets at Diamond Light Source.* Phil. Trans. R. Soc. A, 2015. **373**(2043): p. 20140398.

214. Cook, A.J., C. Padovani, and A.J. Davenport, *Effect of Nitrate and Sulfate on Atmospheric Corrosion of 304L and 316L Stainless Steels.* Journal of The Electrochemical Society, 2017. **164**(4): p. C148-C163.

215. Rowley, W. *Raman averaging from WiRE*. 2018 [30/01/18]; Available from: https://uk.mathworks.com/matlabcentral/fileexchange/65909-raman-averaging-from-wire?s_tid=gn_loc_drop#feedbacks.

9. APPENDICES

9.1 Appendix 1

9.1.1 Tomography Scripts

```
for(i=210; i<1000; i++){
run("DMP Reader", "choose=E:\\disk4\\OWD1_2d\\rec_DMP\\OWD1_2d0"+i+".rec.DMP");
run("Brightness/Contrast...");
setMinAndMax(-0.0017, 0.0018);
call("ij.ImagePlus.setDefault16bitRange", 0);
run("Close");
run("8-bit");
saveAs("Tiff", "X:\\Sarah\\SLS DATA\\SLS_Data\\OWD1\\OWD1_2d\\rectiff\\OWD1_2d0"+i+".rec.tif");
close();
}

for(i=1000; i<1600; i++){
run("DMP Reader", "choose=E:\\disk4\\OWD1_2d\\rec_DMP\\OWD1_2d"+i+".rec.DMP");
run("Brightness/Contrast...");
setMinAndMax(-0.0017, 0.0018);
call("ij.ImagePlus.setDefault16bitRange", 0);
run("Close");
run("8-bit");
saveAs("Tiff", "X:\\Sarah\\SLS DATA\\SLS_Data\\OWD1\\OWD1_2d\\rectiff\\OWD1_2d0"+i+".rec.tif");
close();
}
```

Figure 9-1 Fiji macro script used to edit brightness and contract and resave in .DMP files in .Tif data format.
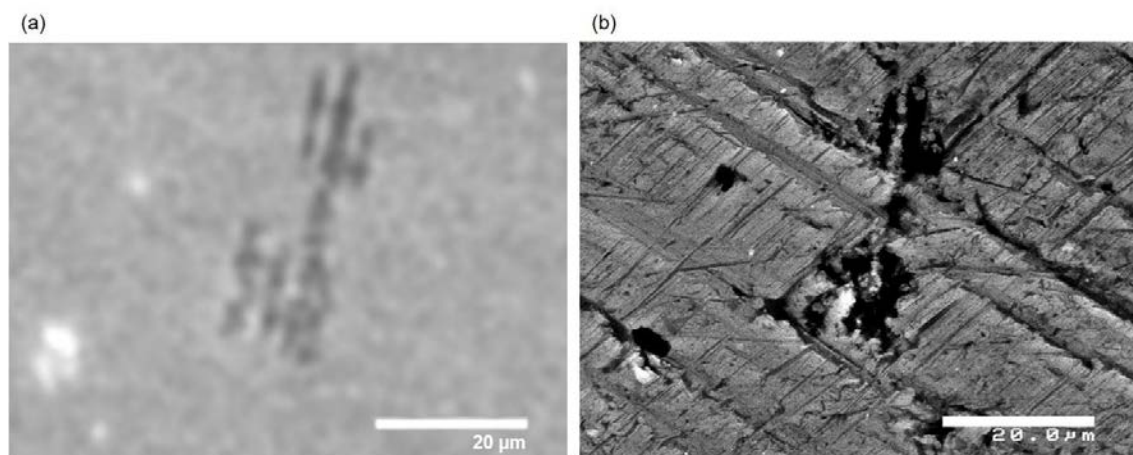
9.1.2 Verification of Scale Between Instruments

Figure 9-2 (a) Tomogram of corrosion site with scale as analysed based on 0.74 μm pixel size. (b) SEM image of corrosion site.

229

9.2 Appendix 2

9.2.1 Raman Standards

Standard Spectrum	Reference laser	Reference number
Alum (Na)	532	R110204
boehmite	532	R120133
Boracite	532	R070317
brucite	532	R040077
corundum	785	X050042
diaspore	785	X050055
Felsőbányaite	532	R060565.2
Kurnakovite	514	R050393
mendozite	532	R070315
Natroalunite	532	R060406
nordstandite	532	R050592
Quintinite	532	R070709
Rostite	532	R061001
Tamarugite	532	R061060
CuO	532	R120076
Trembathite	532	R070756
tamarugite	532	R061060

Figure 9-3 reference numbers for standard Raman spectrum collected from the Rruff.com database [177].

9.2.1 Dawsonite Synthesis Protocol

'The hydrothermal synthesis of Dawsonite-type compounds was carried out in a stainless steel autoclave with a Teflon liner under autogenous pressure. The $Al(OH)_3$ suspension freshly precipitated by the addition of $AlCl_3$ solution (2 mol/L) to $NH_3 \cdot H_2O$ solution (28%) was used as the aluminium source for the synthesis of Dawsonite.

The mixture of supersaturated $NaHCO_3$ solution/$Al(OH)_3$ suspension ($NaHCO_3$/Al=16:1) was stirred vigorously when a 10 M solution of NaOH was added slowly until pH 9-10 (no higher than 10.5). Then the solution was transferred to an autoclave (45 cm^3 in capacity) and heated at 150 °C for 5 h. Finally, the product was washed with DI-water to remove excess Na^+ ions and dried at 60 °C.'

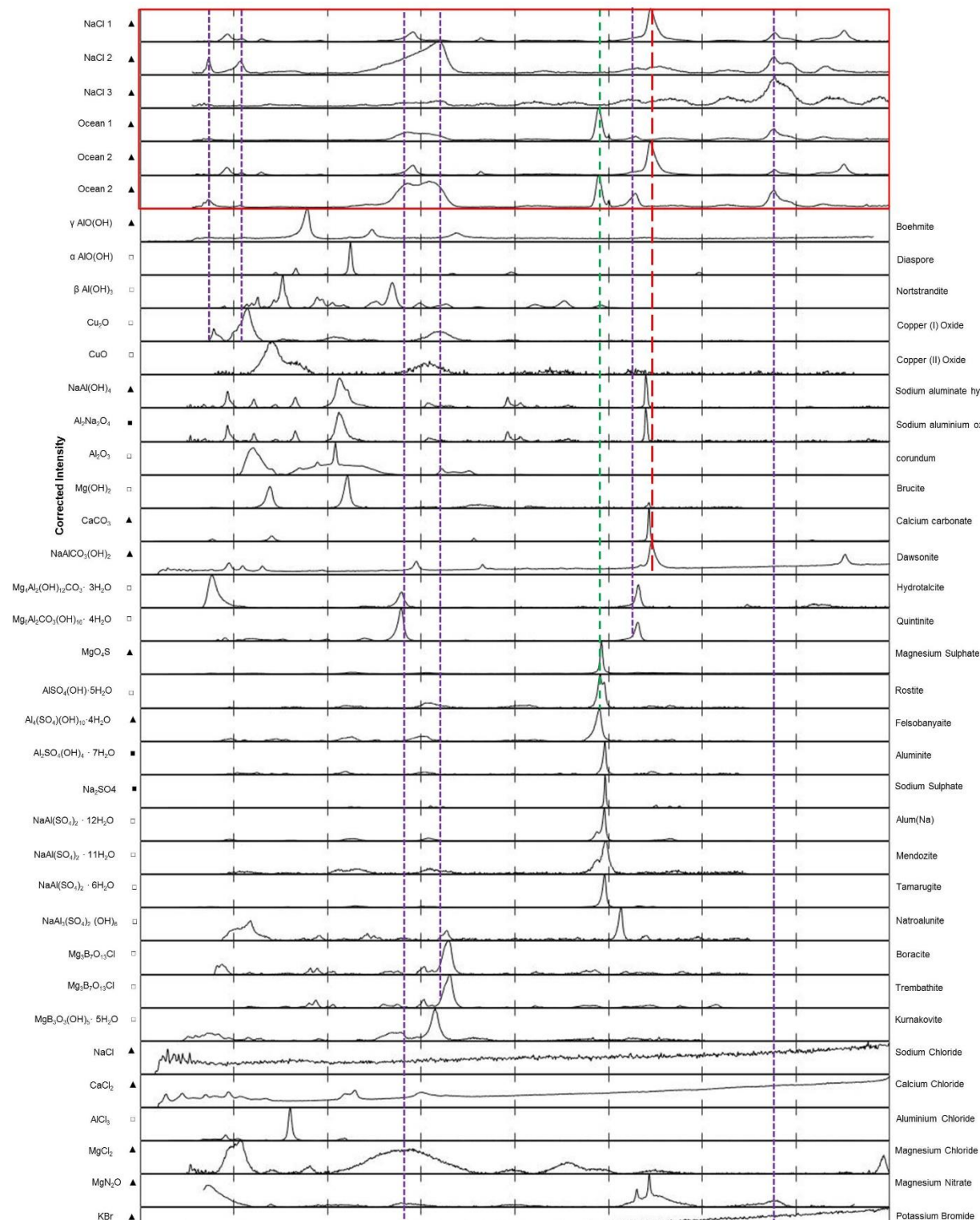Protocol 1 – Modified prep of Dawsonite [178]

Figure 9-4 shows a graph stack of Raman spectrum of possible corrosion products. Dotted lines represent correlation of the main peaks found in both salt spectrum taken. Red = NaCl match with Dawsonite. Green = match with Felsöbányaite. Purple = the main peaks in Hydrotalcite.

▲ - measured 488 nm laser. ■ - measured 532 nm laser. □ - Rruff 532nm laser (rruff.info).
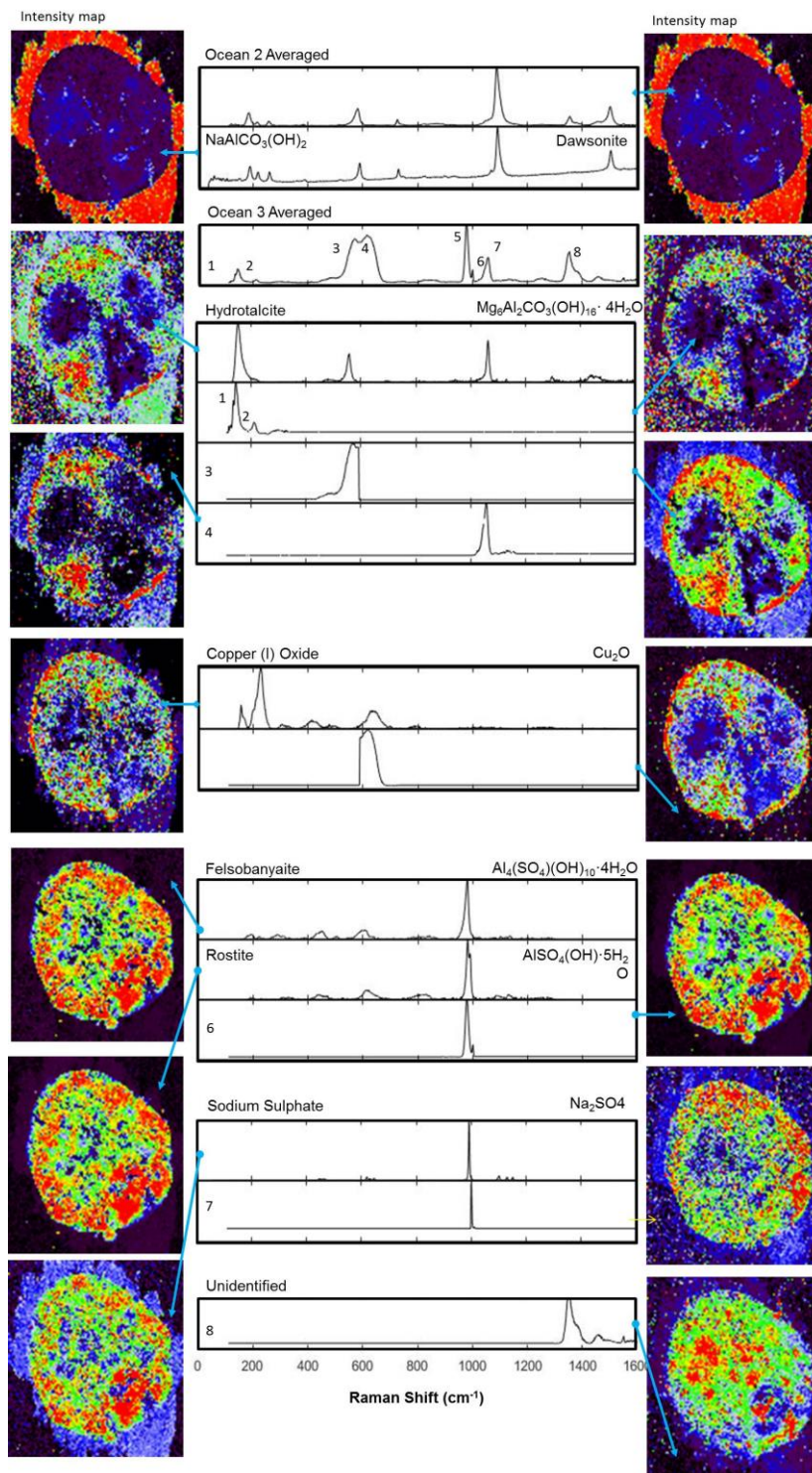
Figure 9-5 Shows a graph of corroded ASTM ocean water droplets corroded at 85 ±3% relative humidity and at 30 ±1oC. The graphs collected from the Raman with a 488nm laser at 100% power, 20 acquisitions and 2 second exposure and have been baseline subtracted. All Data points with matching components with graphs (a) to (f) are shown on the right in the form of Raman DCLS maps. Intensity maps show all related pixels which have matching peaks to graphs.

9.3 Appendix 3

9.3.1 Matlab Scripts

```matlab
%Script for averaging raman mapping data based on greyscale thresholds generated by Wire
DCLS maps
%Written by W.G.Rowely
%%Takes a directory of tab seperated variable text files and an image
%%corresponding to a map produced by WiRE Raman software. It will average
%%all spectra corresponding to pixels above a set intensity value in the
%%map image (set with thresh variable).


function [xout, yout] = RMNAVG(dirvar, Im)

%Threshold for including spectrum in averaging | N.B. this is a pixel
%intensity value ranging from 1-255, so 0.5 is 128, 0.75 is 191 etc.
thresh = 245;
%%process
%read spectra
%average spectra
%output (display)
%% Initialise
Im = Im(:,:,1)';%delete pointless colour channels & transpose
k=0;
j=0;
ImIndexLength = size(Im,1)*size(Im,2);                      %Get total # of expected spectra
fnames = dir(strcat([dirvar,'\*.txt']));                %Get file name list
if length(fnames) == 0
    dis;
    return
end
[xout,~] = readspec(fnames(1).name);                        %Extract list of wavenumbers (x axis)

Indexlist = zeros(ImIndexLength, 1);                       %Initialise list of indices
speclist = zeros(ImIndexLength,size(xout,1));              %Initialise list of spectra for averaging
if ImIndexLength ~= size(fnames)                          %Check to make sure that your image
size is the same as the number of spectra in the folder
    disp('Image dimensions do not match length of file list');
    return
end

%%  extract the spectrum indices from the filenames as they don't line up with array indices
when imported
for i = 1:ImIndexLength
    Indexlist(i) = cell2mat(textscan(fnames(i).name, '%*s %*s %*s %*s %*s %*s %*s %*s %*s
%u %*s %*s %*s %*s %*s %*s %*s', 'delimiter', '_'));  %oceanwater
end
% A1 = figure;
% title('included stuff');
% set(gca, 'xlim',[0,1600])
% A2 = figure;
% title('not included stuff');
% set(gca, 'xlim',[0,1600])
%% read the spectra for relevant indices (Image intensity over threshold set at start of script)
for i=1:ImIndexLength
```

```matlab
    clear tempname
    tempname = fnames(Indexlist == i-1).name;
    if exist('tempname','var') ~= 0
        if Im(i) >= thresh
            [~,tempy] = readspec(tempname);
            tempy = abs(tempy./max(tempy));
            if isnan(tempy)
                tempy = zeros(size(xout,1),1);
            end

%           figure(A1);
%           hold on
%           plot(xout, tempy,'b');
            %Im(i)=255;
          % disp(strcat([num2str(i), ' of ', num2str(ImIndexLength), ' spectra scanned']));
            %else Im(i) =0;
            if tempy == 0       %sometimes there will be error spectra (all zeroes), ignore them.
                k=k-1;
                i
            end
            speclist(i,:) = tempy;
            k=k+1;
        else
%           [~,tempy] = readspec(tempname);
%           figure(A2);
%           hold on
%           plot(xout, tempy,'r');
            j = j+1;
        end
    end
end
%imshow(Im)
speclist(speclist==0)=[];
speclist=reshape(speclist,k,size(xout,1));
yout = mean(speclist,1);                              %Actually average the spectra
figure;plot(xout,yout, 'k')                            %plot it
set(gca, 'ylim',[0,inf]);
disp(strcat(['Averaged ', num2str(k) ,' spectra']));
end
```

Figure 9-6 – Matlab script for averaging Raman mapped data [215].